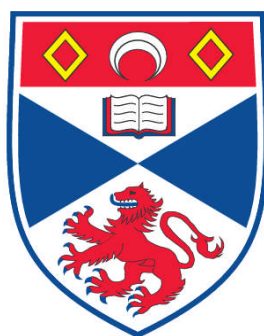


**NOVEL ELECTROCATALYTIC MEMBRANE FOR AMMONIA
SYNTHESIS**

Sujitra Klinsrisuk

**A Thesis Submitted for the Degree of PhD
at the
University of St. Andrews**



2010

**Full metadata for this item is available in
Research@StAndrews:FullText
at:**

<https://research-repository.st-andrews.ac.uk/>

Please use this identifier to cite or link to this item:

<http://hdl.handle.net/10023/1294>

This item is protected by original copyright

**This item is licensed under a
Creative Commons License**

**Novel Electrocatalytic Membrane for
Ammonia Synthesis**

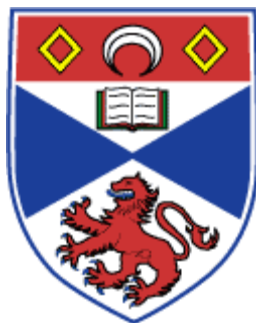
A thesis submitted for the degree of Ph.D.

by

Sujitra Klinsrisuk

University of St. Andrews

Supervised by Prof. John T. S. Irvine



Submitted August 2010

Abstract

Novel ceramic membrane cells of $\text{BaCe}_{0.5}\text{Zr}_{0.3}\text{Y}_{0.16}\text{Zn}_{0.04}\text{O}_{3-\delta}$ (BCZYZ), a proton-conducting oxide, have been developed for electrocatalytic ammonia synthesis. Unlike the industrial Haber-Bosch process, in this work an attempt to synthesise ammonia at atmospheric pressure has been made. The membrane cell fabricated by tape casting and solution impregnation comprises of a 200 μm -thick BCZYZ electrolyte and impregnated electrode composites.

Electrocatalysts for anode and cathode were investigated. For the anode, the co-impregnation of Ni and CeO_2 provided excellent electrode performance including high catalytic activity, sintering stability and compatibility with the BCZYZ electrolyte. The best composition was the mixture of 25wt% NiO and 10 wt% CeO_2 . A symmetrical cell prepared with this electrode composition revealed low polarisation resistances of 1.0 and 0.45 Ωcm^2 in humidified 5% H_2/Ar at 400 and 500 $^\circ\text{C}$, respectively. For the cathode, 25 wt% of impregnated Fe oxide provided a satisfactory performance in non-humidified N_2 atmosphere.

Significant amounts of ammonia were produced from the single cell with Ni- CeO_2 anode and Fe oxide cathode at 400-500 $^\circ\text{C}$ under atmospheric pressure. Ammonia formation rate was enhanced by Pd catalyst addition and electrochemical performance was improved by Ru addition. The highest ammonia formation rate of 4×10^{-9} $\text{mol s}^{-1}\text{cm}^{-2}$ was attained using the cell with a Pd-modified Fe cathode at 450 $^\circ\text{C}$. The formation reaction of ammonia typically consumed around 1-2.5 % of total applied current while most of the applied current was employed in H^+ reduction. The total current efficiency of around 90-100 % could be obtained from the membrane cells.

Acknowledgements

There are so many people who I wish to acknowledge for their support and assistance that make the completion of this thesis become possible.

First of all, I gratefully acknowledge the Royal Thai Government Scholarship who sponsored my PhD study at University of St. Andrews and EPSRC for support.

I would like to show my gratitude to my supervisor, Prof. John T. S. Irvine. It is an honour for me to have a great chance working with him. Thanks for his guidance and advice, for showing me the right direction and for sharing me some of his knowledge. I am deeply grateful for all his kind support and encouragement.

I would like to thank my examiners: Assist. Prof. Georgios Marnellos and Dr. Richard T. Baker for their suggestions and insightful comments.

I am indebted to many of my former and present colleagues in JTSI group for their assistance, advice and fruitful discussion. Special thanks go to Julie Nairn for all of her help with lab facilities, Dr. Cristian Savaniu for his advice on electrochemical testing, Dr. Yuta Nabae for his help on the testing jig, Dr. Paul Connor for his assistance on testing instruments, Dr. Maarten Verbraeken for sharing his knowledge about the impedance, Dr. David Miller and Dr. George Tsekouras for correcting parts of my thesis, Dr. Jung-Hyun Kim for his help with the ceramic sealant. For many names that I have not written down here, I do appreciate their support that I have received.

I would like to thank all the staffs in School of Chemistry, especially Mrs. Sylvia Williamson for her help with TGA, Mr. George Antony and Robert E. Cathcart for their help on my experimental setup.

Many thanks to all my Thai friends in St Andrews and in Thailand for their friendship.

Finally, I would like to dedicate this work to my parents, Boonsong and Premrudee Klinsrisuk, and my family in Thailand. Without their endless love and support, I would not have made it.

Table of Contents

	Page
Abstract	i
Acknowledgements	ii
Table of Contents	iii
List of Tables	ix
List of Figures	x
List of Abbreviations and Symbols	xviii
Chapter 1	
Introduction, Background and Related work	1
1.1 Ammonia	2
1.1.1 Ammonia as a hydrogen carrier source	2
1.1.2 Synthesis of ammonia: Haber-Bosch process	4
1.1.3 Catalysts in Haber-Bosch process	6
1.2 Electrocatalytic ammonia synthesis at atmospheric pressure	9
1.2.1 Principle	10
1.2.2 Cell performance	13
1.2.2.1 Ohmic losses (η_{ohm})	14
1.2.2.2 Activation overpotential (η_{act})	15
1.2.2.3 Concentration overpotential (η_{conc})	16
1.3 Components of electrocatalytic membrane cell	17
1.3.1 Proton-conducting oxide electrolyte	17
1.3.2 Anode material	22
1.3.2.1 Anodic reactions	22
1.3.2.2 Kinetics of hydrogen oxidation	23
1.3.3 Cathode materials for ammonia formation in previous studies	25
1.3.4 Faradaic efficiency	27
1.3.5 Electrocatalytic ammonia synthesis conditions	28
References	30

Table of Contents (cont.)

	Page
Chapter 2	
Proton Conducting Oxide Electrolyte: Preparation and Characterisation	35
2.1 Overview	36
2.2 Preparation of oxide ceramic	36
2.2.1 Solid state synthesis	36
2.2.2 Densification of ceramics	37
2.3 Experimental	40
2.3.1 Powder preparation	40
2.3.2 Electrolyte sintering	40
2.3.3 Ex-situ characterisations	42
2.3.3.1 X-ray Diffraction (XRD)	42
2.3.3.2 Scanning Electron Microscopy (SEM)	44
2.3.3.3 Energy-dispersive X-ray spectroscopy (EDS)	46
2.3.3.4 Density of sintered ceramic	47
2.3.3.5 Thermogravimetric Analysis (TGA)	47
2.3.4 Electrochemical Measurements	48
2.3.4.1 Cell preparation	48
2.3.4.2 Experimental apparatus: Two-chamber apparatus	49
2.3.4.3 AC impedance spectroscopy	52
2.3.4.4 Current efficiency calculation	56
2.3.4.5 Mass spectrometry (MS)	57
2.4 Results and discussion	59
2.4.1 Physical properties of sintered BCZYZ pellet	59
2.4.2 Microstructure Characterisation	59
2.4.3 Phase Identification	61
2.4.4 TGA characterisation for water uptake	62
2.4.5 Electrochemical measurements	64
2.4.5.1 OCV measurements of Pt BCZYZ Pt cell	64
2.4.5.2 AC impedance spectra of 5% H ₂ /Pt BCZYZ Pt,O ₂ cell	65
2.4.5.3 Performances of Pt BCZYZ Pt cell in different cathode gases	68
2.4.5.4 Cell performance after electrode geometry modification	70

Table of Contents (cont.)

	Page
2.4.5.5 Performances of cells with different cathodes	72
2.4.5.6 Cell performances under closed-circuit condition	73
2.4.5.7 Ammonia formation rate	77
2.4.5.8 H ₂ evolution rate and overall current efficiency	80
2.5 Conclusions	85
References	86
Chapter 3	
Fabrication of Thin BCZYF Ceramic Membrane	87
3.1 Introduction	88
3.2 A brief overview of tape casting process	90
3.2.1 Tape slurry ingredients	91
3.2.1.1 Solvent	91
3.2.1.2 Dispersants/deflocculants	92
3.2.1.3 Binder	95
3.2.1.4 Plasticizers	96
3.2.2 Tape forming	98
3.2.3 Tape drying	99
3.2.4 Organics burnout	99
3.3 Experimental	101
3.3.1 Powder processing	101
3.3.2 Tape casting process	102
3.3.2.1 Lamination of ceramic green tape	103
3.3.2.2 Thermal decomposition of green tapes	105
3.3.2.3 Sintering support	106
3.3.2.4 Sintered body characterisation	107
3.4 Results and discussion	108
3.4.1 Thermal Analysis of green tapes	108
3.4.2 Optimum heating treatment	111

Table of Contents (cont.)

	Page
3.4.3 Dense electrolyte layer	112
3.4.3.1 Slurry formulation	112
3.4.3.2 Effect of organic additive: Binder	114
3.4.3.3 Final slurry formulation	116
3.4.3.4 Microstructure of green electrolyte tape surface	116
3.4.3.5 Sintering conditions	118
3.4.3.5.1 Effect of sintering temperature	118
3.4.3.5.2 Thickness of the electrolyte layer	120
3.4.3.5.3 Sintering duration and final microstructure	121
3.4.4 Porous substrate layer	123
3.4.4.1 Porous structure optimisation	124
3.4.4.2 Effect of sintering temperature	125
3.4.4.3 Influence of pore former morphology	127
3.4.4.4 Microstructure of porous green tape surface	130
3.4.4.5 Effect of dispersant and binder contents	132
3.4.4.6 Phase identification of sintered porous BCZYZ layer	135
3.5 Conclusions	138
References	139
Chapter 4	
Electrochemical Characterisations of Anode and Cathode Materials	141
4.1 Ion Impregnation of Electrode Materials	142
4.2 Experimental	143
4.2.1 Impregnation procedure	143
4.2.2 SEM and EDS elemental analysis	144
4.2.3 X-ray diffraction	145
4.2.4 Details of electrode materials and catalysts	145
4.2.5 Single-atmosphere testing apparatus	146
4.2.6 Cell with painted Pt electrode as a reference cell	148

Table of Contents (cont.)

	Page
4.3 Results and discussion	149
4.3.1 Decomposition temperature of metal nitrates	149
4.3.2 Phase compositions of impregnated electrodes	153
4.3.3 Performances of Ni impregnated anodes in H ₂ atmospheres	154
4.3.3.1 Ni electrodes without catalyst addition	155
4.3.3.2 Degradation of Ni impregnated electrodes	158
4.3.3.3 Ni electrodes with CeO ₂ addition	160
4.3.3.4 NiO-CeO ₂ electrodes in different H ₂ partial pressures	162
4.3.3.5 Stability of NiO-CeO ₂ electrodes	165
4.3.3.6 NiO-CeO ₂ electrode in different regimes of H ₂ O contents	168
4.3.3.7 Comparison of Ni impregnated electrodes and painted Pt electrode	169
4.3.3.8 Microstructure of Ni impregnated electrodes after testing	172
4.3.4 Cathode material: impregnated Fe oxide	175
4.3.4.1 Cell with 1:1 Fe oxide:BCZYZ electrode	175
4.3.4.2 Microstructure of Fe oxide impregnated electrode	177
4.3.4.3 Cell with 25 wt% Fe oxide-BCZYZ electrode	178
4.3.4.4 Behaviour of 25wt% Fe electrode in non-humidified atmospheres	181
4.3.5 Comparison between conductivities of cells with various electrodes	184
4.4 Conclusions	185
References	186
Chapter 5	
Electrocatalytic ammonia synthesis	188
5.1 Components of a membrane cell for electrocatalytic ammonia synthesis	189
5.2 Experimental	190
5.3 Results and discussion	192
5.3.1 Effect of cathode current collector on ammonia formation	192
5.3.2 Investigations of single cells with and without catalyst addition	194

Table of Contents (cont.)

	Page
5.3.2.1 AC impedance measurements under open-circuit condition	195
5.3.2.2 Polarisation properties under closed-circuit condition	198
5.3.2.3 The relationship between applied potential and cell resistance	202
5.3.2.4 Overall overpotentials of cells with and without catalyst addition	204
5.3.2.5 Changes in the gas compositions during V - I measurement	207
5.3.2.6 Microstructure of single cells with catalyst impregnated Fe	209
5.3.3 Ammonia production	212
5.3.3.1 Ammonia formation rate	216
5.3.3.2 H_2 evolution rate and overall current efficiency	221
5.4 Conclusions	225
References	226
Chapter 6	
Conclusions and Future Work	228
6.1 Conclusions	228
6.2 Future work	230

List of Tables

	Page
Table 1.1 Gravimetric and volumetric densities of selected H ₂ storage options	3
Table 1.2 A classification of metals according to their abilities in chemisorptions	25
Table 1.3 Summary of previous works on electrocatalytic ammonia synthesis with various experimental conditions	29
Table 2.1 Relationship between capacitance values and corresponding processes	54
Table 3.1 Physical and dielectric properties of ethanol and methyl ethyl ketone	92
Table 3.2 Formulations of green tapes for thermogravimetric analysis	110
Table 3.3 Starting formulation and modified formulations for BCZYZnO electrolyte slurries	113
Table 3.4 Selected formulations for porous BCZYZnO tape slurries	125
Table 3.5 Final formulation for the porous tape slurry	134
Table 4.1 List of electrode and catalyst precursors used in this experiment	146
Table 5.1 Gas composition from the cathode outlet stream under open circuit	198

List of Figures

	Page
Figure 1.1 Equilibrium constant of ammonia synthesis reaction as a function of temperature in the standard state	5
Figure 1.2 Operating principle of electrolytic ammonia synthesis cell using a proton conducting electrolyte	10
Figure 1.3 Schematic of a polarisation curve	14
Figure 1.4 Comparison of conductivities of typical proton conducting perovskite-type oxides in a hydrogen atmosphere	18
Figure 1.5 Cubic perovskite structure ABO_3	20
Figure 1.6 Schematic of reactions at the electrode-electrolyte- H_2 phase	23
Figure 2.1 Schematic of six mechanisms take place between the particles leading to densification of a powder system	37
Figure 2.2 Stages of liquid-phase sintering	39
Figure 2.3 Diagram of optimum sintering treatment for BCZYZ 1 mm thick pellet	42
Figure 2.4 Derivation of Bragg's law	43
Figure 2.5 (a) schematic of a typical SEM components and (b) possible signals emitted by an electron beam	45
Figure 2.6 Geometry of electrode on BCZYZ pellet for electrochemical testing	48
Figure 2.7 Electrode firing conditions	49
Figure 2.8 Two-chamber testing apparatus	51
Figure 2.9 An example of Nyquist plot with impedance vector	53
Figure 2.10 Impedance plot in the complex plane revealing factors controlled electrochemical reactions	55
Figure 2.11 Characteristic impedances for diffusive systems	55
Figure 2.12 Components of a mass spectrometer	57

List of Figures (cont.)

	Page
Figure 2.13 Typical sintered BCZYZ pellet	59
Figure 2.14 SEM images of fracture surface of samples sintered at (a) 1400 °C and (b) 1300 °C for 10 h	60
Figure 2.15 XRD spectra of $\text{BaCe}_{0.5}\text{Zr}_{0.3}\text{Y}_{0.16}\text{Zn}_{0.04}\text{O}_{3-\delta}$, BCZYZ	61
Figure 2.16 TGA data of sintered BCZYZ powder	63
Figure 2.17 Open circuit voltage measured at different temperatures and cathode gases	65
Figure 2.18 Nyquist plots of 1 mm thick Pt BCZYZ Pt cell in humidified 5% H ₂ and non-humidified O ₂ under open circuit at various temperatures	67
Figure 2.19 An equivalent circuit for the impedance from cell with Pt electrodes	67
Figure 2.20 Nyquist plots of 1 mm thick Pt BCZYZ Pt cell in different cathode gases under open circuit	69
Figure 2.21 Modification of Pt electrode pattern	70
Figure 2.22 Impedance spectra of Pt BCZYZ Pt cell with different electrode geometry	71
Figure 2.23 Impedance spectra under open circuit of cells with different cathodes in non-humidified N ₂	73
Figure 2.24 Polarisation curves from cells with different cathodes	75
Figure 2.25 Impedance spectra of cells with various cathodes under DC loading	76
Figure 2.26 NH ₃ production rate at different imposed currents and temperatures	78
Figure 2.27 Current efficiencies of NH ₃ formation versus current at various temperatures	79
Figure 2.28 H ₂ evolution rates at different imposed currents and temperatures	82

List of Figures (cont.)

	Page
Figure 2.29 Current efficiencies at various temperatures	84
Figure 3.1 Schematic illustration of steric forces occurring in the presence of uncharged polymer chains	94
Figure 3.2. Chemical structures of (a) DBP, (b) PEG and (c) PVB	97
Figure 3.3. Schematic of a tape casting machine	98
Figure 3.4. XRD pattern of BCZYZnO powder	101
Figure 3.5. Green electrolyte tape lamination	104
Figure 3.6. Geometric pattern of a three-layer green tape stack	105
Figure 3.7. Setup inside furnace chamber for sintering BCZYZnO green tapes	107
Figure 3.8. TG curves of green electrolyte and porous tapes with various pore former contents	110
Figure 3.9. Microstructures of (a) graphite and (b) glassy carbon pore formers	111
Figure 3.10. Optimum sintering treatment for laminated tapes	112
Figure 3.11. SEM images of cross section of dense BCZYZ layers	114
Figure 3.12. SEM images of dense electrolyte layer with different amounts of binder in the slurries	115
Figure 3.13. SEM images of the dried green tape surface	117
Figure 3.14. SEM image of BCZYZnO starting powder	117
Figure 3.15. SEM image of fracture surface of BCZYZ electrolyte sintered at different temperatures	119
Figure 3.16. Sintered specimens with different electrolyte thicknesses	120
Figure 3.17. SEM images of fracture cross section of 4-layer laminated dense layer	122

List of Figures (cont.)

	Page
Figure 3.18. SEM images of specimens prepared from tapes containing 30 wt% graphite sintered for 10 h at different temperatures	126
Figure 3.19. SEM images of fracture surface of sintered BCZYZ porous layers prepared from various amounts and types of pore formers	129
Figure 3.20. SEM images of green porous tape surfaces for tape containing 40 wt% graphite + 10 wt% glassy carbon	131
Figure 3.21. SEM images of fracture surface of samples prepared using various amounts of dispersant and binder	133
Figure 3.22. SEM image of fracture surface of sample prepared from final slurry formulation for both dense and porous layers	134
Figure 3.23. XRD patterns of sintered porous layers	136
Figure 3.24. XRD data of BCZYZ powder buffer layer after use as a sintering support at 1300 °C	137
Figure 3.25. XRD pattern of bottom porous layer sintered at 1300 °C for 10 h	137
Figure 4.1 Schematic of experimental set up for single atmosphere test	147
Figure 4.2 SEM images of fracture-cross section of three-layer BCZYZ membrane with an impregnated porous layer	150
Figure 4.3 SEM images of fracture surface of Ni impregnated sample after firing at 650 °C	152
Figure 4.4 XRD patterns of impregnated electrodes before testing	153
Figure 4.5 AC impedance data under open circuit from the cells with Ni impregnated electrodes in humidified 5% H_2 /Ar	157

List of Figures (cont.)

	Page
Figure 4.6 An equivalent circuit for the impedance from cells with Ni electrodes	158
Figure 4.7 Comparison of cell degradation of symmetrical cells with NiO:BCZYZ electrodes in humidified 5% H_2 /Ar	159
Figure 4.8 AC impedance data under open circuit from the cells with CeO ₂ -NiO co-impregnated electrodes at different temperatures in humidified 5% H_2 /Ar	161
Figure 4.9 Comparison of the impedance spectra of cells with 35Ni15Ce electrode and 25Ni10Ce electrode in humidified 5% H_2 and pure H_2	163
Figure 4.10 Temperature dependence of (a) the polarisation resistances and (b) the ohmic resistances for 35Ni15Ce cell (\square) and 25Ni10Ce cell (\circ) in humidified 5% H_2 (---) and pure H_2 (—)	164
Figure 4.11 Comparison of cell degradation as function of time and thermal cycle from 600 to 400 °C in cells with different NiO-CeO ₂ electrodes	166
Figure 4.12 Plots of R_s and R_p values versus time comparing electrode stabilities in humidified 5% H_2 of pure Ni electrode (1:1 NiO:BCZYZ) and NiO-CeO ₂ electrode (25Ni10Ce) at 400 and 600 °C	167
Figure 4.13 Behaviour of 25Ni10Ce electrode under the atmospheres with different water contents	169

List of Figures (cont.)

	Page
Figure 4.14 Impedance spectra of thin BCZYZ electrolyte cell with Pt electrodes tested as function of temperature in humidified 5% H ₂ /Ar	171
Figure 4.15 Comparison of polarisation resistances as a function of temperature tested in humidified 5% H ₂	171
Figure 4.16 SEM images of Ni and Ni-CeO ₂ impregnated electrodes after testing	174
Figure 4.17 EDS elemental analysis of 25Ni10Ce impregnated electrode after testing	174
Figure 4.18 AC impedance data of cell with 1:1 Fe:BCZYZ electrode in various H ₂ content atmospheres at 550 °C	176
Figure 4.19 SEM image of a fractured cross-section of 1:1 Fe:BCZYZ electrode	177
Figure 4.20 AC impedance spectra under open circuit of cell with 25 wt% Fe oxide electrode with Pt current collector in humidified atmospheres as a function of temperature.	179
Figure 4.21 AC impedance spectra under open circuit of cell with 25 wt% Fe oxide electrode with Pd current collector in humidified atmospheres as a function of temperature	180
Figure 4.22 Impedance spectra of cell with 25 wt% Fe oxide electrode in non-humidified atmospheres as a function of temperature	182
Figure 4.23 Stability of 25 wt% Fe oxide impregnated electrode at 600 °C in non-humidified atmosphere with various H ₂ contents	183

List of Figures (cont.)

	Page
Figure 4.24 SEM images of a fractured cross-section of 25 wt% Fe oxide impregnated electrode after testing	183
Figure 4.25 Arrhenius plots for ohmic conductivities of cells with various electrodes	184
Figure 5.1 Schematic of the components of a single cell prepared for electrocatalytic ammonia synthesis	189
Figure 5.2 Two-chamber testing apparatus	191
Figure 5.3 AC impedance spectra under open circuit of single cells, humidified 5% H ₂ , 25Ni10Ce BCZYZ 25Fe, N ₂ with Pd or Pt current collector on Fe cathode	193
Figure 5.4 AC impedance spectra under open circuit of humidified 5% H ₂ , 25Ni10Ce BCZYZ 25Fe, N ₂ cell with and without catalyst addition on the Fe cathode at different temperatures	197
Figure 5.5 Polarisation curves of humidified 5% H ₂ , 25Ni10Ce BCZYZ 25Fe, non-humidified N ₂ cells at various temperatures	201
Figure 5.6 AC impedance spectra of cell without catalyst addition at Fe cathode measured at OCV and under loading	201
Figure 5.7 Plots of dE/dI values evaluated from the slopes in polarisation curves	203
Figure 5.8 Plots of overpotentials (IR_{ohmic} -free) versus current density of cells with and without catalyst addition	206
Figure 5.9 Correlation between electrolytic current and changes in concentrations of gases in cathode outlet stream during potential sweep at 2mV/s	209

List of Figures (cont.)

	Page
Figure 5.10 SEM image of a fractured cross-section of 25Ni10Ce BCZYZ 25Fe cell without catalyst addition after testing	210
Figure 5.11 SEM images of fractured cross-section of Fe-BCZYZ impregnated electrode after testing	211
Figure 5.12 typical data obtained from the cathode outlet stream recorded by Mass spectrometer	214
Figure 5.13 Correlation between applied potential and corresponding current employed for ammonia synthesis in single cells	215
Figure 5.14 NH ₃ production rate at different imposed currents and temperatures	219
Figure 5.15 Current efficiency for NH ₃ formation versus current density	220
Figure 5.16 H ₂ evolution rate at different imposed currents and temperatures	222
Figure 5.17 Total current efficiency evaluated from (open symbol) H ₂ evolution rate and (closed symbol) total amount of H ₂ and H ₂ O formation rate including NH ₃ production rate	224

List of Abbreviations and Symbols

Abbreviations	Meaning
ASR	Area specific resistance
DBP	Dibutyl phthalate
EDS	Energy-dispersive X-ray spectroscopy
MEK	Methyl ethyl ketone
MS	Mass Spectrometry
OCV	Open circuit voltage
PEG	Polyethylene glycol
PVB	Poly(vinyl butyral)
SEM	Scanning Electron Microscope
SOFCs	Solid Oxide Fuel Cells
TGA	Thermogravimetric analysis
XRD	X-ray diffraction

Roman symbols

Symbol	Meaning
E	electrical potential
F	Faraday constant
G	Gibbs free energy
$\Delta_r G$	change in Gibbs free energy of a reaction
ΔH	change in enthalpy
i_r	the fraction of current used in a particular reaction
i_t	the total current across the cell
I	current
j	(a) current density (b) imaginary unit, $\sqrt{-1}$

List of Abbreviations and symbols (cont.)

Symbol	Meaning
j_0	exchange current density
j_L	limiting current density
K_{eq}	equilibrium constant
n	stoichiometric number of electrons involved in an electrode reaction
P	(a) absolute pressure (b) partial pressure
Q	charge passed in electrolysis
r	rate of reaction
R	(a) gas constant (b) resistance
R_{ohmic}	ohmic resistance
R_p	polarisation resistance
R_s	series resistance
s_0	sticking coefficient
t_{H^+}	transport number of protons
T	absolute temperature
V_{OC}	open circuit voltage
W_{elec}	electric work

Greek symbols

Symbol	Meaning
α	transfer coefficient
η	overpotential
η_{ohm}	ohmic overpotential

List of Abbreviations and symbols (cont.)

Symbol	Meaning
η_{act}	activation overpotential
η_{conc}	concentration overpotential
θ	incident angle
Λ	faradaic efficiency
λ	wavelength of the light
ρ	density
ω	angular frequency of a sinusoidal oscillation; $2\pi f$

Kröger-Vink notation for point defects used in this Thesis

Symbol	Type of defect
$\text{Ce}_{\text{Ce}}^{\times}$	Ce^{4+} ion on its normal lattice position
M'_{Ce}	M^{3+} dopant ion on Ce site with effective charge -1
$\text{V}_{\text{O}}^{\bullet\bullet}$	oxygen ion vacancy with effective charge +2
$\text{O}_{\text{O}}^{\times}$	oxygen ion on its normal lattice position
h^{\bullet}	(Quasi)-free electron hole in valence band
$\text{OH}_{\text{O}}^{\bullet}$	proton defect with effective charge +1
e'	(Quasi)-free electron in conduction band

Chapter 1

Introduction, Background and Related work

1.1 Ammonia	2
1.1.1 Ammonia as a hydrogen carrier source	2
1.1.2 Synthesis of ammonia: Haber-Bosch process	4
1.1.3 Catalysts in Haber-Bosch process	6
1.2 Electrocatalytic ammonia synthesis at atmospheric pressure	9
1.2.1 Principle	10
1.2.2 Cell performance	13
1.2.2.1 Ohmic losses (η_{ohm})	14
1.2.2.2 Activation overpotential (η_{act})	15
1.2.2.3 Concentration overpotential (η_{conc})	16
1.3 Components of electrocatalytic membrane cell	17
1.3.1 Proton-conducting oxide electrolyte	17
1.3.2 Anode material	22
1.3.2.1 Anodic reactions	22
1.3.2.2 Kinetics of hydrogen oxidation	23
1.3.3 Cathode materials for ammonia formation in previous studies	25
1.3.4 Faradaic efficiency	27
1.3.5 Electrocatalytic ammonia synthesis conditions	28
References	30

1.1 Ammonia

Ammonia has been synthesised commercially for nearly a century. The production capacity of ammonia has exceeded 100 million tons in 2000^[1]. The most important chemicals manufactured from ammonia are nitric acid, urea, ammonium sulphate and ammonium phosphate. The fertilizer industry is by far the most important consumer of ammonia and accounts for about 80% of the world production of ammonia. The plastics industry is the next consumer, accounting for 10% of the ammonia production^[2]. Recently, ammonia has been used in fuel cell application as an alternative hydrogen source.

1.1.1 Ammonia as a hydrogen carrier source

Alternative energy sources to fossil fuel have been intensively investigated. The hydrogen fuel cell is an attractive power generation option as it provides substantial power that can be used in transportation and power generation sectors. Considering the availability factor of a power plant from the amount of time that electricity is produced in a certain period, the fuel cell plant tends to provide higher power availability than renewable energy sources e.g. wind and solar power plants. This is because the power output generated by a fuel cell can be conveniently controlled by the supply of hydrogen fuel, whereas the others depend on climatic conditions^[3]. However, the use of hydrogen is restricted by the difficulty in storage and transport. Typically, hydrogen is stored under very low temperature (-253 °C) or high pressure (250 atm) leading to the requirement of a bulky gas cylinder. In addition, hydrogen is a flammable gas with flammability limits of 4-75 vol% in air^[4]. This wide range of

flammability limits raises concerns about safe handling and transportation in order to avoid explosion danger.

Ammonia contains hydrogen in a density of 17.6% by weight and can be easily liquefied under 1 atm at -33°C or 10 atm at 20°C . Apart from ammonia, there are many options for hydrogen storage. The comparison of various hydrogen sources considered from storage conditions, gravimetric densities and volumetric densities are shown in Table 1.1.

Table 1.1 Gravimetric and volumetric densities of selected H_2 storage options^[5].

Material	Special storage conditions	Gravimetric densities (wt% H)	Volumetric densities ($\text{mol l}^{-1}\text{H}_2$)
H_2 (gas)	250 atm	100	10
H_2 (liquid)	-253°C , 1 atm	100	35
CH_4 (gas)	250 atm	25	21
NH_3	-33°C , 1 atm or 20°C , 10 atm	17.6	60
CH_3OH	Normal T and P*	12.5	49
Mg_2NiH_x	Normal T and P	3.6	39
Gasoline, C_8H_{18}	Normal T and P	15.8	55

*T = temperature, P = pressure

According to the gravimetric densities, hydrogen is the best choice. However, its low volumetric density makes it difficult to store and transport. The volumetric density of a metal hydride is reasonable but the gravimetric density is too small. Hydrocarbons show superior properties to the hydride in both storage and transportation. However, the use of hydrocarbons in solid oxide fuel cells (SOFCs) causes a problem with carbon deposition on the Ni anode that significantly decreases cell performance^[6-8].

As an alternative option, ammonia which has the best volumetric density and a good gravimetric density of H₂ storage is of interest.

Comparing with hydrogen, ammonia offers significant advantages in cost and convenience as a vehicular fuel due to its higher density and its easier storage and distribution. Regarding its safety, although anhydrous ammonia is toxic and dangerous for the environment, it is lighter than air and tends to disperse in the atmosphere. However, the leakage of ammonia can be easily sensed by the human nose at low concentration, such as 5 ppm^[9].

1.1.2 Synthesis of ammonia: Haber-Bosch process

The synthesis of ammonia from gaseous nitrogen and hydrogen on a uranium catalyst at high pressure was firstly demonstrated by Fritz Haber and colleagues in 1909. However, it was Carl Bosch who carried on the industrial scale-up giving rise to the Haber-Bosch process for industrial ammonia synthesis^[10].

Nowadays, an Fe-based catalyst is well known as the industrial catalyst for ammonia synthesis. The reaction occurs at high pressure (150-300 bar) and in the temperature range of 450-500°C. The reason for working at moderate temperature and high pressure is considered from the nature of this reaction.



This reaction is exothermic and thermodynamically preferable at low temperature.

The values of equilibrium constant (K_{eq}) given by:

$$K_{\text{eq}} = \frac{P_{\text{NH}_3}^2}{P_{\text{H}_2}^3 \cdot P_{\text{N}_2}} \quad (1.2)$$

at various temperatures shown in Figure 1.1 indicate that the decomposition of NH_3 is significant at higher temperatures^[11]. Working at lower temperature can avoid the ammonia decomposition but the formation rate of ammonia will be relatively slow.

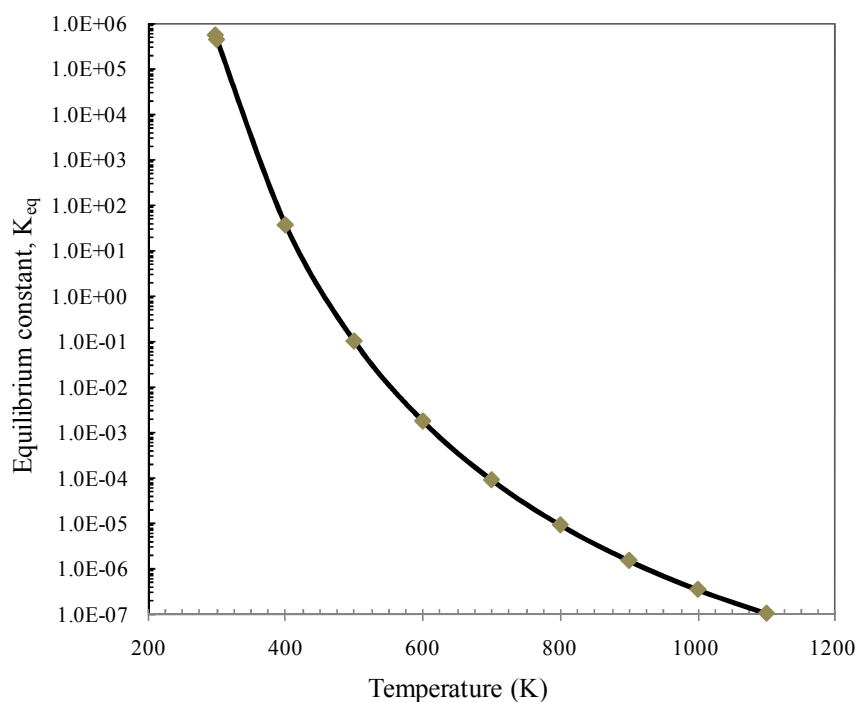


Figure 1.1 Equilibrium constant of ammonia synthesis reaction as a function of temperature in the standard state.

Under operating conditions, the evolution of ammonia decreases the total gas volume since 4 moles of reactant provides only 2 mole of product. According to the Le Chatelier's principle, an increase in pressure shifts the equilibrium towards the product side and yields a larger amount of ammonia.

In order to achieve industrially acceptable conversion, the pressure and temperature must be high enough to achieve a sufficiently fast rate of reaction but the equilibrium constant should not be too small. For example in order to achieve 100% conversion of reactants to ammonia product at 200°C, a pressure above 750 atm must be used. Since there are difficulties in working with high pressure, nowadays ammonia is

industrially synthesized at a temperature of about 500°C and a pressure of around 200 atm which provides 10-20% yield of ammonia^[2,12].

The conflict between thermodynamic and kinetic considerations brings on the need of an active catalyst which would help decrease the operating temperature and pressure. Together with the catalyst studies, new methods for ammonia synthesis have been investigated.

The synthesis of ammonia in an electrochemical cell has been suggested as an alternative process over the last decade. Marnellos et al. reported that ammonia was synthesized from gaseous hydrogen and nitrogen in a solid state proton conducting cell reactor. This cell provided greater than 78 % conversion of hydrogen to ammonia at 570 °C and atmospheric pressure^[13]. It is likely that electrocatalytic ammonia synthesis could be an effective method to avoid working with high pressure and the thermodynamic limitations in the conventional catalytic reactor.

1.1.3 Catalysts in Haber-Bosch process

It is well known that the active catalyst for ammonia synthesis is successfully derived from magnetite ore (Fe_3O_4) which contains a few percent of several promoters such as oxides of calcium, aluminium, potassium, etc. Nowadays, the composition of the catalyst employed in industry is still more or less identical to that demonstrated in a German patent in 1910^[14]. Interestingly, the continued use of this magnetite catalyst has been explained by the highly porous structure of metallic iron which occurs after the reduction of magnetite. The surface area of the iron catalyst after reduction could be up to $20 \text{ m}^2 \text{ g}^{-1}$ ^[15]. However, the presence of promoters on the iron catalyst is of utmost importance. The roles of promoters on the iron catalyst can be divided into two groups depending on their behaviours on iron catalyst^[15]. The presence of aluminium

oxide on the iron surface is believed to help prevent high surface area metallic iron from sintering during operation. Therefore, this kind of promotion is named structural promotion^[15,16]. The role of potassium oxide may be different as it is reported to enhance the rate of N₂ dissociative adsorption and decreases the adsorption energy of ammonia by transferring electronic charge from K to the Fe surface^[16,17]. However, Dahl et al. suggested that the K promoter on Fe catalyst may not take part in N₂ dissociation but tends to destabilise the intermediate NH* and increase the ammonia formation rate instead^[18].

Apart from promoters affecting the rate of reaction, the crystal structure of the Fe catalyst is also highly important. Surface science experiments on single crystals of metallic iron as present during the operating conditions suggest that Fe (111) is the most active surface among the structural surfaces such as Fe (110) and Fe (100), respectively^[19,20]. These results suggest that the ammonia synthesis reaction on iron surface is a structure-sensitive reaction.

The reaction between H₂ and N₂ on an iron surface is quite complicated. The mechanism of the reaction has been studied via the observation for intermediate species adsorbed on the iron surface. By using spectroscopic techniques, the intermediate species such as NH and NH₂ could be identified. Hence, the sequence of elementary steps has been proposed as follows;



It is well known that the dissociative chemisorption of N_2 is a very slow process and it could be the rate determining process for the overall reaction^[14].

The sticking coefficient for N_2 on the Fe catalyst is extremely low. The initial sticking coefficient (s_0) of N_2 on the active sites of industrial Fe-based catalyst has been proposed to be $s_0 = 10^{-5} \exp(-4\text{kJ/mol}/RT)$ ^[21] while H_2 has much higher sticking coefficient in order of 10^{-1} ^[14,22]. Although H atoms are mobile and can bond covalently with the Fe catalyst surface, the surface concentration of H atoms at temperature higher than 400 °C is rather small. Hence, the adsorption of nitrogen on the Fe surface may not be inhibited by the surface H atoms^[14]. Apart from hydrogen, the presence of an oxygenated poison (O_2 , CO and H_2O) causes rapid poisoning to the Fe catalyst. The oxygenated poison forms an oxide layer on the Fe surface leading to the expulsion of the adsorbed nitrogen from the surface^[12,23]. However, the poisoning effect tends to be reversible upon removing the oxygenated poison from H_2 and N_2 reactants^[24].

Osmium catalyst is one of the catalysts that can be applied in ammonia synthesis reaction. It used to be employed by the early experiments of Haber but the osmium metal was too expensive for the large-scale industrial plant^[25]. Ruthenium catalyst is one of the non-iron based catalysts that has been proposed as an active catalyst for ammonia synthesis^[26]. The ruthenium catalyst was found to be more active than the Fe catalyst, so it can perform at milder conditions (low temperature and pressure) compared to that for the Fe catalyst^[18, 27, 28]. However, Ru is more expensive than Fe and the lifetime of the Ru catalyst is shorter than that of the Fe catalyst.

1.2 Electrocatalytic ammonia synthesis at atmospheric pressure

Because of the disadvantages of working under high pressure and the thermodynamic limitations of the Haber-Bosch process, alternative methods for ammonia synthesis have been proposed. One of the most promising methods is the utilisation of an electrochemical cell. Various electrolytic cells have been employed with various electrolyte materials, such as aqueous electrolytes^[29] and molten salts^[30,31]. In aqueous electrolytes, the kinetics of the reaction is quite slow due to the low operating temperature. In the case of molten salt electrolytes, the operating temperature could be around 400 °C which is close to that for industrial ammonia synthesis but the difficulty in molten salt preparation is a major concern. Typically, a mixture of alkali salts such as LiCl, KCl and CsCl is usually used as the molten salt electrolyte. These air-sensitive molten salts require that the experiment must be operated in inert atmosphere which is not practical for large-scale synthesis. In 1981, an electrochemical cell with a proton conducting oxide electrolyte based on SrCeO₃ was reported by Iwahara et al.^[32]. Since then, several applications of cells utilising solid state H⁺ conductors, working at temperatures of 500-1000 °C, have been considered. Electrochemical devices utilising proton conducting oxides as electrolyte and involving both hydrogen and hydrogen-containing compounds, include hydrogen sensors, fuel cells, electrolyzers and hydrogen pumps^[33]. In particular, the application of solid oxide proton conductors in electrocatalytic ammonia synthesis has been investigated^[34-40].

1.2.1 Principle

The principle of ammonia synthesis via a proton conducting oxide electrolyte is shown in Figure 1.2.

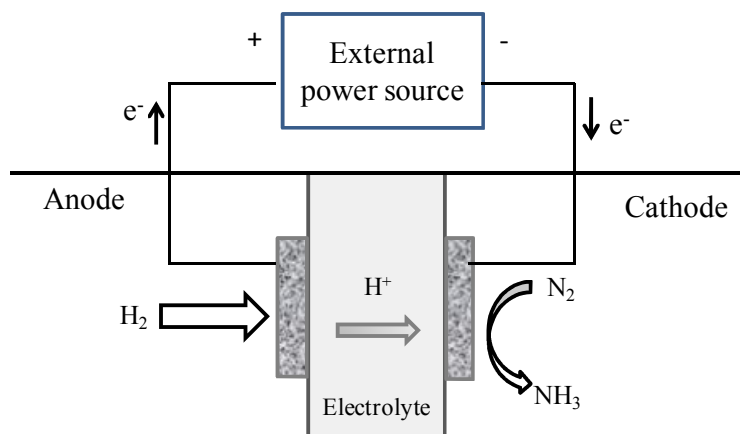


Figure 1.2 Operating principle of electrolytic ammonia synthesis cell using a proton conducting electrolyte.

The apparatus consists of two compartments separated by a proton conducting oxide ceramic membrane cell containing the anodic and cathodic electrocatalysts for hydrogen oxidation and ammonia formation, respectively.

At the anode, gaseous H_2 and H_2O passing over the anode is converted to protons.



Then protons are transported through the electrolyte membrane to the cathode where the reaction with gaseous N_2 is expected.



The overall reaction is



Thermodynamically, this reaction is a non-spontaneous reaction with the reaction Gibbs energy, $\Delta_r G^\circ > 0$ at temperature higher than 130 °C^[11].

Therefore, this reaction needs to be done under electrolysis condition by applying an electric current to the cell via an external power source.

Under Open circuit condition

The difference in chemical potentials of electro-active ionic species (which are protons in this case) between two electrodes induces some of the protons to move from the anode (higher concentration) to the cathode (lower concentration). However, the reactions at the cathode cannot be completed as the electrons cannot be transported through the electrolyte and the high resistance external source connected to the electrodes also forbids the flow of electrons. As the reaction between H₂ and N₂ should not occur under open circuit condition, the chemical potential difference between the electrodes will cause a potential called the open-circuit voltage (OCV or V_{oc}) which can be theoretically calculated from the Nernst equation based on hydrogen concentration cell consideration.

$$V_{oc} = E_c - E_a = \frac{RT}{2F} \ln \frac{P_{H_2}(\text{cathode})}{P_{H_2}(\text{anode})} \quad (1.12)$$

where E_c and E_a are the equilibrium potential of the cathode and anode, respectively, R is gas constant (8.314 J/K mol), T is absolute temperature (K) and F is the Faraday constant (96485 C)^[41].

Under closed circuit condition

During electrolysis conditions, a Galvanostat-Potentiostat will provide a constant potential or current to the membrane cell reactor and drive the reactions forward. The minimum energy or electrical work (W_{elec}) needed for the reaction is equal to the change in Gibbs free energy^[41].

$$W_{elec} = -\Delta_r G \quad (1.13)$$

while,

$$W_{elec} = EQ \quad (1.14)$$

E = electrical potential (V)

Q = charge passes in electrolysis (C)

If the charge is assumed to be carried by electrons, then

$$Q = nF \quad (1.15)$$

F = the Faraday constant, 96485 coulombs

n = stoichiometric number of electrons involved in the reaction

Therefore,

$$\Delta_r G = -nFE \quad (1.16)$$

where E refers to the minimum voltage needed for the formation of the desired product and is called the theoretical electrolysis voltage^[41].

For example at 700 K, ammonia should be theoretically synthesised by imposing a potential of at least 0.094 V.

However, Murakami et al.^[31] suggested that the ammonia synthesis rate may not depend on only the electrolysis potential. Other factors such as catalytic activity of electrode material, partial pressure of gaseous reactants, and temperature are crucial for the kinetics of ammonia synthesis^[31, 34, 42].

1.2.2 Cell performance

When the external power source supplies a current or potential to the cell, all the electrode reactions will be driven away from the equilibrium state. These irreversible processes, including charge transfer, conduction and diffusion of charge species, cause a decrease in operating voltage. Voltage losses or overpotential (η) can be classified into activation overpotential (η_{act}), concentration overpotential (η_{conc}) and ohmic overpotential (η_{ohm})^[43].

$$V_{operating} = V_{OC} - \eta_{act} - \eta_{ohm} - \eta_{conc} \quad (1.17)$$

The relation between potential and current density is expressed by a polarisation curve (I - V curve) as shown in Figure 1.3.

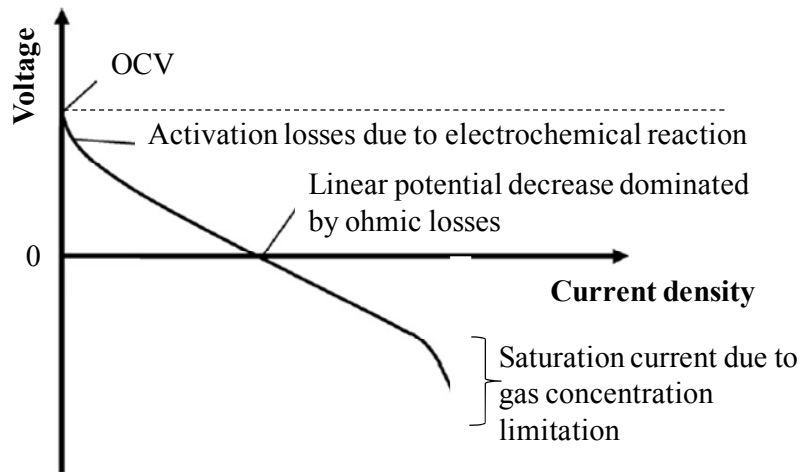


Figure 1.3 Schematic of a polarisation curve.

1.2.2.1 Ohmic losses (η_{ohm})

Ohmic losses attributed to electron and ion conduction processes exist in the electrodes, electrolyte, interconnects, current collectors and contact resistances at the electrode-electrolyte interface. Generally, the major contribution to the ohmic losses tends to arise from high ionic resistivity of the electrolyte rather than electronic resistivity of the electrodes. Ohmic losses are a linear function of current (i) and can be simply defined by Ohm's law:

$$\eta_{ohm} = iR \quad (1.18)$$

where R is the resistance.

1.2.2.2 Activation overpotential (η_{act})

Activation overpotential is the overpotential needed to overcome the activation barrier associated with the electrochemical reaction at the reaction site at the three phase boundary (TPB) between the electrode-electrolyte interface. The mechanism of the charge transfer reaction $A + ne^- \rightleftharpoons Z$ and the electrocatalytic activity of electrode material directly affect this overpotential. The relationship between current density (j) and η_{act} is expressed by the Butler-Volmer equation.

$$j = j_0 \left(e^{\alpha n F \eta_{act} / (RT)} - e^{-(1-\alpha) n F \eta_{act} / (RT)} \right) \quad (1.19)$$

where η is the activation overpotential, n is the number of electrons involved in the reaction, j_0 is the exchange current density and F , R and T have their usual meanings. Note that this equation applies to each individual electrode separately. The value of α is between 0 and 1 and refers to the symmetry of the activation barrier and expresses the change in size of the forward versus reverse activation barrier under applied potential. Thus, $\alpha = 0.5$ means the size of the forward activation barrier is equal to that of the reverse.

From the Butler-Volmer equation, it can be seen that the current produced by an electrochemical reaction increases exponentially with η_{act} .

The complication of the Butler-Volmer equation is simplified by using two approximations when the η_{act} in the Butler-Volmer equation is either very small or

very large. When η_{act} is very small, the current and the overpotential show linear correlation and are independent of α as exhibited in following equation;

$$j = j_0 \frac{nF\eta_{act}}{RT} \quad (1.20)$$

When η_{act} is large, the forward reaction is prominent and the process becomes completely irreversible. Thus, the second exponential term in the Butler-Volmer equation will be ignored, then

$$j = j_0 e^{\alpha n F \eta_{act} / (RT)} \quad (1.21)$$

or

$$\eta_{act} = - \frac{RT}{\alpha n F} \ln j_0 + \frac{RT}{\alpha n F} \ln j \quad (1.22)$$

This equation is known as *Tafel equation*^[41].

In details, η_{act} is also dependent upon the reactant concentration, temperature and the TPB length^[41].

1.2.2.3 Concentration overpotential (η_{conc})

Concentration overpotential is the loss due to the mass transport of charges and uncharged species from the reactant and product. This mass transport loss is concerned with the concentrations of reactant and product within the catalyst layer where the reaction takes place. The concentration overpotential is manifested as a rapid decrease of cell potential due to the reactant concentration falling to zero at a current density named the limiting current density (j_L). The concentration overpotential (η_{conc}) may be described as

$$\eta_{conc} = \frac{RT}{nF} \ln \left(1 - \frac{j}{j_L} \right) \quad (1.23)$$

The factors that govern the concentration loss are diffusivity of reactants and products in the porous electrode, electrode structure, the distribution of gaseous reactants and reactant concentration^[41].

1.3 Components of electrocatalytic membrane cell

1.3.1 Proton-conducting oxide electrolyte

The proton conducting oxide electrolytes that are used in ammonia synthesis applications are usually perovskite type oxides (ABO_3), as inspired by the first reported proton-conducting oxide, doped-SrCeO₃ from Iwahara et al^[44]. Hence, the application of SrCe_{0.95}Yb_{0.05}O₃ (SCY) for ammonia synthesis was proposed by Marnellos et al.^[13,34]. Apart from SCY, other perovskite-structured oxides were also employed such as SrZr_{0.95}Y_{0.05}O_{3- δ} ^[35], Y-doped BaCeO₃^[36,37] and complex perovskite-type oxides e.g. Ba₃(Ca_{1.18}Nb_{1.82})O₉^[38]. Other structure-type oxides such as La_{1.95}Ca_{0.05}M₂O_{7- δ} (M= Ce, Zr)^[39] and Ce_{0.8}M_{0.2}O_{2- δ} (M= La, Y, Gd, Sm)^[40], which have the fluorite structure, were also studied for the ammonia synthesis application.

In order to consider a proton conducting oxide electrolyte for electrolytic ammonia synthesis, the following requirements need to be fulfilled: (1) High ionic conductivity of the order of $10^{-2} - 10^{-3}$ S/cm in the operating temperature range in order to minimise the ohmic loss; (2) high transport number of protons, $t_{H^+} > 0.9$. (3) excellent chemical stability under the operating atmosphere. (4) good sinterability to a dense

ceramic and substantial mechanical strength, as to to prevent crossover of the reactants.

Comparing perovskite- and non-perovskite-type oxides, the ionic conductivity of the perovskite-structured oxides is much higher than the non-perovskite structure^[45]. Among the perovskite-based oxides, barium cerates showed the highest ionic conductivity especially Y-doped barium cerate, $\text{BaCe}_{1-x}\text{Y}_x\text{O}_{3-\alpha}$ ^[33]. Comparison of their conductivities is depicted in Figure 1.4.

Owing to copyright restrictions,
the electronic version of this thesis does not contain this image

Figure 1.4 Comparison of conductivities of typical proton-conducting perovskite oxides in a hydrogen atmosphere^[33]. “Reprinted from Solid State Ionics, Vol.77, H. Iwahara, Technological challenges in the application of proton conducting ceramics, p.290, (1995), with permission from Elsevier.”

Consequently, the physical and chemical properties of doped BaCeO₃ including ionic conductivity, transport properties and applications have been extensively investigated^[46-50].

According to the A²⁺B⁴⁺O₃ configuration of perovskite-type BaCeO₃, the substitution of B⁴⁺ (which is Ce⁴⁺ in this case) with a trivalent cation (M³⁺) creates oxygen vacancies (V_O^{••}) due to the depletion of positive charge within the crystal structure.



The oxygen vacancies in the structure lead to the formation of hydroxyl ions at their sites by taking protons from water vapour or hydrogen under humid atmosphere.



At elevated temperature, the proton transport is thermally activated. Two mechanisms for proton conduction have been proposed. One is the Grotthus-type mechanism based on the fact that protons travel or hop from one oxygen ion to the adjacent oxygen ion. Another is the vehicle mechanism in which protons migrate along with an oxygen ion^[51,52]. By the investigation of the H/D isotope effect, the transport of protons between stationary oxygen ions is likely to occur via the Grotthus mechanism^[53]. Hereby, the existence of Grotthus mechanism in solid oxide proton conductors has been confirmed by a number of techniques such as thermal gravimetric analysis and conductivity studies^[54], concentration cell measurements^[55] and quasielastic neutron scattering (QENS)^[56].

The perovskite structure (ABO_3) as shown in Figure 1.5 comprises of the large cation A coordinated to 12 oxygen atoms O at the A-site and the smaller cation B occupying the B-site which has a coordination number of 6. Ion A and atom O form a cubic close packing while ion B occupies the octahedral holes.

Owing to copyright restrictions,
the electronic version of this thesis does not contain this image

Figure 1.5 Cubic perovskite structure ABO_3 ^[57]. “Reprinted from Reports on Progress in Physics, Vol.67, J. B. Goodenough, Electronic and ionic transport properties and other physical aspects of perovskites, p.1917, (2004), with permission from IOP Publishing.”

Typically, the M^{3+} ion is a rare earth element such as Y^{3+} , Yb^{3+} , Nd^{3+} and In^{3+} [58,59]. The partial substitution of Ce^{4+} by M^{3+} results in the solid solution formation of $BaCe_{1-x}M_xO_{3-\delta}$ where x is usually less than 0.2 and δ is the number of oxygen vacancies per formula unit. According to eq. (1.24) and (1.25), the oxygen vacancy concentration is in proportion to the dopant content, x and the degree of hydration. Kruth et al. studied the incorporation of water in $BaCe_{1-x}Y_xO_{3-\delta}$ as a function of temperature and the dopant content. The results showed an almost linear correlation between the dopant content and the degree of hydration. However, loss of water does happen at high temperature. The sample with higher dopant content or oxygen

vacancy concentration was able to retain more water than the others at the same temperature^[60].

Although the high ionic conductivity of doped BaCeO₃ drew much attention, its chemical stability soon became a critical issue. It has been reported that BaCeO₃ readily reacts with CO₂ and H₂O forming undesired products, i.e barium carbonate and cerium oxides^[61,62]. Barium zirconate has higher chemical stability than barium cerate but its proton conductivity is relatively low. For compensation, the partial substitution of Ce⁴⁺ with Zr⁴⁺ seems to be a solution. It has been reported that the chemical stability of doped BaCeO₃-BaZrO₃ solid solutions is greater than doped BaCeO₃. The increase of Zr content improves the chemical stability of the solid solution but has an adverse effect on proton conductivity^[63-67]. In addition, the substitution of Zr in BaCeO₃ dramatically increases its sintering temperature. In order to achieve dense microstructure with reasonable grain boundary conductivity, the Zr-substituted BaCeO₃ ceramic needs to be sintered at very high temperature, around 1550-1700 °C^[64, 66,67]. This high sintering temperature makes it unsuitable for low cost preparation and it would furthermore be difficult to find a compatible electrode material for a thin-electrolyte membrane cell using an oxide electrode as a support. Therefore, sintering aids have played an important role in decreasing the sintering temperature without impairing conductivity. ZnO has been used for this purpose. The addition of Zn in small amounts did decrease the sintering temperature significantly^[68-71].

Recently, Tao et al. reported a new protonic conductor, BaCe_{0.5}Zr_{0.3}Y_{0.16}Zn_{0.04}O_{3-δ}, which has total conductivity in wet 5% H₂ of 3.14 mS cm⁻¹ at 400 °C and over 10 mS cm⁻¹ above 600 °C. Moreover, the chemical stability testing of this oxide under pure

CO₂ by thermal gravimetric analysis (TGA) also provided a satisfactory result as compared to the other doped BaCeO₃ materials^[69].

1.3.2 Anode material

1.3.2.1 Anodic reactions

At the anode, a mixture of hydrogen and water vapour will be used. It has been reported that the presence of water vapour at the anode can improve the area specific resistance (ASR) of the cell^[72,73]. The reason should be the additional proton incorporation into the electrolyte through the following equation:



Moreover, proton defects will be formed by the reaction with hydrogen as follows.



This is in the case where electron holes (h[•]) are present.

In some cases, the oxidation of hydrogen may cause the formation of free electrons according to the following equation^[52]



As a result, a gas mixture of hydrogen and water vapour is always used at the anode in order to prevent the reduction of the electrolyte^[72,74]. Concerning the catalytic effect

of water on H₂ oxidation, it was found that an appropriate amount of water vapour can improve the polarisation resistance of the cermet anode containing a proton-conducting ceramic phase^[73,75]. However, the explanation for this effect is still unclear.

1.3.2.2 Kinetics of hydrogen oxidation

The oxidation of hydrogen is rather simple. It includes at least three steps i.e. the dissociation, adsorption and charge transfer steps.



Figure 1.4 illustrates the details of reactions that occur at the three phase boundary (TPB) of a cell with a metal electrode and proton conductor electrolyte.

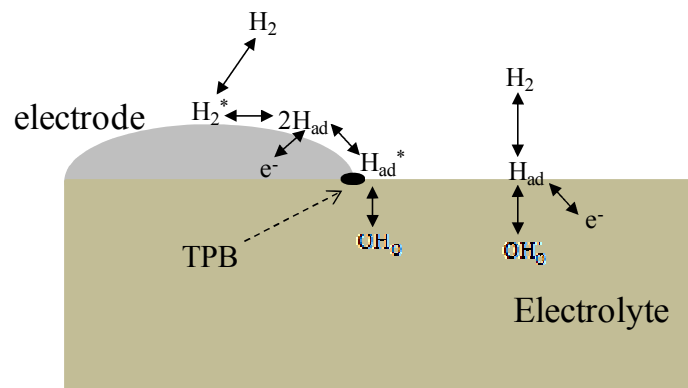


Figure 1.6 Schematic of reactions at the electrode-electrolyte-H₂ phases.

Kek et al. has proposed that the reaction mechanism of hydrogen oxidation depends on the nature of the electrode and hydrogen partial pressure. According to their experiment, non-dissociative adsorption or diffusion of hydrogen molecules is likely to be the rate determining step for a point contact Ni metal electrode using $\text{Sr}_{0.995}\text{Ce}_{0.95}\text{Y}_{0.05}\text{O}_{2.970}$ (SCY) proton conducting oxide electrolyte^[76]. From Figure 1.4, there is a chance that adsorbed species like H_{ad} have to diffuse on the electrode surface to the TPB site. This transport process has been considered as one of the possible rate limiting steps by Akoshima et al.^[77] while another possible step could be the dissociative adsorption of H_2 on the electrode surface at the TPB. In their experiment, both models of possible rate limiting steps for H_2 oxidation at Pt/ $\text{BaCe}_{0.95}\text{Y}_{0.05}\text{O}_{3-\delta}$ interface are presented.

1.3.2.3 Anode materials in previous studies

When using hydrogen as a reactant for electrocatalytic ammonia synthesis, several metal electrodes including Pd^[34,42], Ag^[35], Ag-Pd^[39, 40], Ni cermet^[37] were anticipated as an anode material. In those studies, less attention was paid to the anodic reaction of hydrogen oxidation as compared to the cathodic reaction of ammonia formation, which is quite sluggish. Although metals in the same group as Pd and Pt have very good catalytic activity for hydrogen oxidation, their costs discourage the usage of these metals in a cost-efficient device. Ni is also considered as electrode material for hydrogen oxidation, as it is commonly used in solid oxide fuel cell applications, with excellent catalytic activity for hydrogen oxidation.

1.3.3 Cathode materials for ammonia formation in previous studies

For the cathode reaction, protons from the anode will transport through the electrolyte and readily react with nitrogen, which is either molecularly or atomically adsorbed on the surface of the cathode catalyst, to form ammonia as mentioned in equation 1.10.

The ammonia formation reaction at the cathode may look simple but in the real situation many factors that have to be considered. As a surface-catalysed reaction, the factors that are involved in reaction kinetics could be the adsorption of the reactants on the catalyst or into the structure of the catalyst. Only a few metal catalysts can induce chemisorption of N_2 on their surfaces. A classification of metals according to their abilities in chemisorption is presented in Table 1.2.

Table 1.2 A classification of metals according to their abilities in chemisorption^[15]

Group Metals		Gases						
		O ₂	C ₂ H ₂	C ₂ H ₄	CO	H ₂	CO ₂	N ₂
A	Ti, Zr, Hf, V, Nb, Ta, Cr, Mo, W, Fe, Ru, Os	+	+	+	+	+	+	+
B ₁	Ni, Co	+	+	+	+	+	+	-
B ₂	Rh, Pd, Pt, Ir	+	+	+	+	+	-	-
B ₃	Mn, Cu	+	+	+	+	±	-	-
C	Al, Au	+	+	+	+	-	-	-
D	Li, Na, K	+	+	-	-	-	-	-
E	Mg, Ag, Zn, Cd, In, Si, Ge, Sn, Pb, As, Sb, Bi	+	-	-	-	-	-	-

(+ strong chemisorption, ± weak chemisorption and – unobservable)

From Table 1.2, it is obvious that N_2 is the most difficult molecule to form chemisorbed nitrogen on the metal surface and quite a limited number of metals can be anticipated to work. However, the adsorption strength of each type of molecule on the metal still depends on the adsorption coefficient.

Practically, it was reported that metallic Pd can be used as electrocatalyst for electrocatalytic ammonia synthesis at atmospheric pressure by Marnellos et al.^[13,34] and Pd-Ag alloy was also employed in several experiments^[36,38-40,78]. Apart from Pd metal electrodes, the modifications of a metal electrode with a catalyst such as Fe or Ru catalyst were also investigated with an attempt to extend the active site for N_2 dissociation and NH_3 formation. For example, Ouzounidou et al. employed an Fe metallic electrode with an industrial Fe catalyst as an electrocatalyst^[35]. A similar experiment was performed by Skodra et al. who applied an industrial Ru catalyst over metallic Ag^[42]. Comparing Pd metal electrode with the combinations of the metal electrode and the additional catalyst, the Pd metal electrode showed superior performance despite the adsorption and dissociation of N_2 on Pd metal being relatively limited with regard to the information in Table 1.2. The reason for poor performance in metallic electrode-catalyst combination must come from the difficulty in proton transport from the electrolyte to the active site in the electrode phase. The layer of the metallic electrode (Ag or Fe) on the electrolyte surface may block the diffusion of protons, so the reaction cannot take place at the catalyst surface since the reactant in this case is protons instead of H_2 . Consequently, the formation rate of ammonia is limited by the inadequate number of protons on the catalyst surface.

In the case of Pd metal, which has high capability for hydrogen adsorption, the metal may act as an anchor for N₂ to adsorb and initiate the reaction without the need of N₂ dissociation as happens in some biological processes^[34].

Considering previous works, the key factor for electrocatalytic ammonia synthesis could be the number of TPB sites at the cathode in order to facilitate the reaction between protons from the electrolyte, N₂ from the gas phase and electrons from the external power source.

1.3.4 Faradaic efficiency

Under the closed-circuit condition, the correlation between imposed current (I) and the formation rate of product or the consumption rate of reactant (r) is expressed in terms of Faradaic efficiency (A).

$$A = r / (I/nF) \quad (1.32)$$

where r is the formation rate of ammonia, I is the imposed current, F is Faraday's constant, n is the number of electrons involved in the reaction and (I/nF) is the theoretical rate of ammonia production related to flux of protons through the electrolyte. If $A=1$, it means that protons pumped through the electrolyte by the imposed current are all used in the reaction. This reaction obeys Faraday's law and has Faradaic effect. In some cases, the A value can be higher than unity leading to a phenomenon called Non-Faradaic Electrochemical Modification of Catalytic Activity (NEMCA)^[13,34,35,79]. This phenomenon is beyond the scope of this study. However, the details about NEMCA can be found elsewhere^[80,81].

1.3.5 Electrocatalytic ammonia synthesis conditions

At atmospheric pressure, the decomposition of ammonia begins at about 450-500 °C. With the presence of catalyst, the decomposition starts at 300 °C and is nearly complete at 500-600 °C^[2,12]. The fact that the proton conductivity of the electrolyte increases with the temperature leads to compensation in the increase of H⁺ flux of the ammonia decomposition rate.

Typical operating temperatures of electrocatalytic ammonia synthesis via a cell with proton conducting solid oxide electrolyte are around 400-700 °C corresponding to the working temperature of the proton conductor electrolyte. A volcano-shape dependence of ammonia formation rates on temperature is observed in most cases. The formation rate of ammonia increases with temperature due to the increase of the H⁺ flux, then the formation rate reaches maximum value at a certain temperature which varies between 450 and 650 °C depending on experimental setup, proton conductivity of electrolyte, type of catalyst and partial pressure of the reactants. When the temperature is further increased, the ammonia formation rate then turns downhill due to the decomposition of ammonia becoming prominent. The maximum formation rates of ammonia from previous works and their experimental conditions are summarised in Table 1.3. So far, the highest formation rate of ammonia of 8×10^{-9} mols⁻¹cm⁻² was reported by Liu et al.^[40]. Surprisingly, doped ceria electrolyte, which is known as an oxide-ion conductor, can provide high ammonia formation rates. According to their results, the authors of this study claimed the coexistence of proton and electron conduction in doped ceria under a hydrogen-containing atmosphere. However, one must be aware that under higher oxygen partial pressure oxide ion conduction may become pronounced and undesirable NO_x gases could be synthesised.

Table 1.3 Summary of previous works on electrocatalytic ammonia synthesis with various experimental conditions.

Electrolyte	Anode	Cathode	Temperature range (°C)	Optimum temperature (°C)	Rate of NH ₃ formation (mol s ⁻¹ cm ⁻²)	Applied V or I	Ref
SrCe _{0.95} Yb _{0.05} O ₃	Pd	Pd	-	570	4.6 x 10 ⁻⁹	1.5 mA cm ⁻²	[13]
SrCe _{0.95} Yb _{0.05} O ₃	Pd	Pd	550-750	570	1.5 x 10 ⁻⁹	2.3 mA cm ⁻²	[34]
Ba ₃ (Ca _{1.18} Nb _{1.82})O _{9-δ}	Ag-Pd	Ag-Pd	550-680	620	2.16 x 10 ⁻⁹	0.6 V	[38]
La _{1.95} Ca _{0.05} Zr ₂ O _{7-δ}	Ag-Pd	Ag-Pd	460-560	520	2.0 x 10 ⁻⁹	0.6 V	[39]
Ce _{0.8} Sm _{0.2} O _{2-δ}	Ag-Pd	Ag-Pd	400-800	650	8.2 x 10 ⁻⁹	0.6 V	[40]
SrZr _{0.95} Yb _{0.05} O _{3-δ}	Ag	Fe metal	450-700	450	6.3 x 10 ⁻¹²	2 V	[35]
BaCe _{0.85} Gd _{0.15} O _{3-δ}	Ni-BCGO	Ag-Pd	400-480	480	4.63 x 10 ⁻⁹	1.9 mA cm ⁻²	[37]
BaCe _{0.85} Y _{0.15} O _{3-δ}	Ag-Pd	Ag-Pd	440-570	500	2.1 x 10 ⁻⁹	0.75 mA	[36]

References

1. <http://www.chemlink.com.au/ammonia-summary.htm>
2. W. Büchner, R. Schliebs, G. Winter, K. H. Büchel, *Industrial inorganic chemistry*, Weinheim, Federal Republic of Germany (1989).
3. J. T. S. Irvine, *J. Power Sources* 136 (2004) 203-207.
4. Basic hydrogen properties, Internet source
<http://hydrogen.pnl.gov/cocoon/morf/hydrogen/article/701>
5. Q. Ma, J. Ma, S. Zhou, R. Yan, J. Gao, G. Meng, *J. Power Sources* 164 (2007) 86-89.
6. J. H. Koh, Y. S. Yoo, J. W. Park, H. C. Lim, *Solid State Ionics* 149 (2002) 157-166.
7. V. Alzate-Restrepo, J. M. Hill, *Appl. Catal. A* 342 (2008) 49-55.
8. N. Laosiripojana, S. Assabumrungrat, *J. Power Sources* 163 (2007) 943-951.
9. G. Thomas, G. Parks, Potential roles of ammonia in a hydrogen economy. Internet source http://www.hydrogen.energy.gov/pdfs/nh3_paper.pdf
10. K. L. Manchester, *Endeavour* 26 (2002) 64-69.
11. D. R. Lide, *Handbook of Chemistry and Physics*, 76th edition, CRC Press, Florida (1995) p. 5-68.
12. R. Kirk, D. Othmer, *Encyclopedia of chemical technology*, John Wiley & Sons. Inc, USA (1985).
13. G. Marnellos, M. Stoukides, *Science* 282 (1998) 98-100.
14. J. M. Thomas, W. J. Thomas, *Principle and practice of heterogeneous catalysis*, VCH, the Federal Republic of Germany (1997).

15. G. C. Bond, *Heterogeneous catalysis: Principles and application*, 2nd edition, Oxford University Press, New York (1987).
16. D. R. Strongin, G. A. Somorjai, *Catal. Lett.* 1 (1988) 61-66.
17. G. Ertl, M. Weiss, S. B. Lee, *Chem. Phys. Lett.* 60 (1979) 391-394.
18. S. Dahl, A. Logadottir, C. J. H. Jacobsen, J. K. Nørskov, *Appl. Catal. A* 222 (2001) 19–29.
19. N. D. Spencer, R. C. Schoonmaker, G. A. Somorjai, *J. Catal.* 74 (1982) 129.
20. G. Ertl, in: J. R. Jennings (ED.), *Catalytic Ammonia Synthesis Fundamentals and Practice*, Plenum Press, New York (1991) p. 109.
21. S. Dahl, E. Törnqvist, C. J. H. Jacobsen, *J. Catal.* 198 (2001) 97-102.
22. B. C. Gates, *Catalytic chemistry*, John Wiley & Sons, Inc., New York (1992).
23. K. C. Waugh, D. Butler, B. E. Hayden, *Catal. Lett.* 24 (1994) 197.
24. K. C. Waugh, D. A. Butler, B. E. Hayden, *Top. Catal.*, 1 (1994) 295-301.
25. F. Haber, *Z. Elektrochem.*, 16 (1910) 244.
26. M. V. Twigg, *Catalyst Handbook*, Manson, London, 1996.
27. I. Rossetti, N. Pernicone, F. Ferrero, L. Forni, *Ind. Eng. Chem. Res.* 45 (2006) 45, 4150-4155
28. A. Logadottir, T. H. Rod, J. K. Nørskov, B. Hammer, S. Dahl, C. J. H. Jacobsen, *J. Catal.* 197 (2001) 229.
29. F. Köleli, D. B. Kayan, *J. Electroanal. Chem.* 638 (2010) 119–122.
30. T. Murakami, T. Nishikiori, T. Nohira, Y. Ito, *J. Am. Chem. Soc.* 125 (2003) 334-335.
31. T. Murakami, T. Nishikiori, T. Nohira, Y. Ito, *J. Electrochem. Soc.* 152 (2005) D75-D78.

32. H. Iwahara, T. Esaka, H. Uchida, N. Maeda, *Solid State Ionics* 3-4 (1981) 359-363.
33. H. Iwahara, *Solid State Ionics* 77 (1995) 289-298.
34. G. Marnellos, S. Zisekas, M. Stoukides, *J. Catal.* 193 (2000) 80-87.
35. M. Ouzounidou, A. Skodra, C. Kokkofitis, M. Stoukides, *Solid State Ionics* 178 (2007) 153-159.
36. Y. Guo, B. Liu, Q. Yang, C. Chen, W. Wang, G. Ma, *Electrochem. Commun.* 11 (2009) 153-156.
37. C. Chen, G. Ma, *J. Alloys Compd.* 485 (2009) 69-72.
38. Z. J. Li, R. Q. Liu, Y. H. Xie, S. Feng, J. D. Wang, *Solid State Ionics* 176 (2005) 1063–1066.
39. J. D. Wang, Y. H. Xie, Z. F. Zhang, R. Q. Liu, Z. J. Li, *Mater. Res. Bull.* 40 (2005) 1294–1302.
40. R. Q. Liu, Y. H. Xie, J. D. Wang, Z. J. Li, B. H. Wang, *Solid state Ionics* 177 (2006) 73-76.
41. R. O'Hayre, S. W. Cha, W. Colella, F. B. Prinz, *Fuel cell fundamentals*, John Willey & Sons, New York (2006).
42. A. Skodra, M. Stoukides, *Solid State Ionics* 180 (2009) 1332-1336.
43. A. Huth, B. Schaar, T. Oekermann, *Electrochim. Acta* 54 (2009) 2774-2780.
44. H. Iwahara, T. Esaka, H. Uchida and N. Maeda, *Solid State Ionics* 3/4 (1981) 359.
45. T. Shimura, S. Fujimoto, H. Iwahara, *Solid State Ionics* 143 (2001) 117-123.
46. N. Bonanos, *J. Phys. Chem. Solids* 54 (1993) 867-870.
47. N. Bonanos, K. S. Knight, B. Ellis, *Solid State Ionics* 79 (1995) 161-170.

48. N. Zakowsky, S. Williamson, J. T. S. Irvine, *Solid State Ionics* 176 (2005) 3019-3026.
49. J. Wu, L. P. Li, W. T. P. Espinosa, S. M. Haile, *J. Mater. Res.* 19 (2004) 2366-2376.
50. T. Schober, *Solid State Ionics* 162-163 (2003) 277-281.
51. K. D. Kreuer, *Chem. Mater.* 8 (1996) 610-641.
52. P. J. Gellings, H. J.M. Bouwmeester, *Catal. Today* 58 (2000) 1–53.
53. K. D. Kreuer, A. Fuchs, J. Maier, *Solid State Ionics* 77 (1995) 157-162.
54. K. D. Kreuer, E. Schönherr, J. Maier, *Solid State Ionics* 70-71 (1994) 278-284.
55. D. P. Sutija, T. Norby, P. Bjiirnbom, *Solid State Ionics* 77 (1995) 167-174.
56. R. Hempelmann, *Physica B* 226 (1996) 72-77.
57. J. B. Goodenough, *Rep. Prog. Phys.* 67 (2004) 1915–1993.
58. K. S. Knight, *Solid State Commun.* 112 (1999) 73-78.
59. T. Shimada, C. Wen, N. Taniguchi, J. Otomo, H. Takahashi, *J. Power Sources* 131 (2004) 289–292.
60. A. Kruth, J. T. S. Irvine, *Solid State Ionics* 162-163 (2003) 83-91.
61. S. V. Bhide, A. V. Virkar, *J. Electrochem. Soc.* 146 (1999) 2038-2044.
62. F. Chen, O. T. Sørensen, G. Meng, D. Peng, *J. Mater. Chem.* 7 (1997) 481-485.
63. N. Taniguchi, C. Nishimura, J. Kato, *Solid State Ionics* 145 (2001) 349-355.
64. E. Fabbri, A. D’Epifanio, E. Di Bartolomeo, S. Licoccia, E. Traversa, *Solid State Ionics* 179 (2008) 558-564.
65. K. H. Ryu, S. M. Haile, *Solid State Ionics* 125 (1999) 355–367.
66. S. Ricote, N. Bonanos, G. Caboche, *Solid State Ionics* 180 (2009) 990-997.
67. Z. Zhong, *Solid State Ionics* 178 (2007) 213–220.
68. P. Babilo, S. M. Haile, *J. Am. Ceram. Soc.* 88 (2005) 2362-2368.

69. S. W. Tao, J. T. S. Irvine, *Adv. Mater.* 18 (2006) 1581-1584.
70. A. K. Azad, J. T. S. Irvine, *Solid State Ionics* 179 (2008) 678–682.
71. C. Zhang, H. Zhao, N. Xu, X. Li, N. Chen, *Int. J. Hydrogen Energy* 34 (2009) 2739-2746.
72. H. Taherparvar, J. A. Kilner, R. T. Baker, M. Sahibzada, *Solid State Ionics* 162-163 (2003) 297-303.
73. S. Klinsrisuk, J. T. S. Irvine, *Solid State Ionics* 181 (2010) 168-172.
74. N. Bonanos, F. W. Poulsen, *J. Mater. Chem.* 9 (1999) 431–434.
75. G. C. Mather, F. M. Figueiredo, J. R. Jurado, J. R. Frade, *Electrochim. Acta* 49 (2004) 2601–2612
76. D. Kek, N. Bonanos, M. Mogensen, S. Pejovnik, *Solid State Ionics* 131 (2000) 249-259.
77. S. Akoshima, M. Oishi, K. Yashiro, K. Sato, J. Mizusaki, *Solid State Ionics* 181 (2010) 240-248.
78. B. H. Wang, J. D. Wang, R. Q. Liu, Y. H. Xie, Z. J. Li, *J. Solid State Electrochem.* 11 (2006) 27-31.
79. C. G. Yiokari, G. E. Pitselis, D. G. Polydoros, A. D. Katsaounis, and C. G. Vayenas, *J. Phys. Chem. A* 104 (2000) 10600-10602.
80. C. G. Vayenas, S. Bebelis, C. Pliangos, S. Brosda, D. Tsiplakides, *Electrochemical Activation of Catalysis*, Kluwer/Plenum Publishers, New York (2001).
81. C. G. Vayenas, M. M. Jaksic, S. Bebelis, S. G. Neophytides, in: J. O'. M. Bockris, B. E. Conway, W. R. E. White (Eds.), *Modern Aspects in Electrochemistry*, vol. 29, Plenum (1996) p. 57.

Chapter 2

Proton Conducting Oxide Electrolyte: Preparation and Characterisation

2.1 Overview	36
2.2 Preparation of oxide ceramic	36
2.2.1 Solid state synthesis	36
2.2.2 Densification of ceramics	37
2.3 Experimental	40
2.3.1 Powder preparation	40
2.3.2 Electrolyte sintering	40
2.3.3 Ex-situ characterisations	42
2.3.3.1 X-ray Diffraction (XRD)	42
2.3.3.2 Scanning Electron Microscopy (SEM)	44
2.3.3.3 Energy-dispersive X-ray spectroscopy (EDS)	46
2.3.3.4 Density of sintered ceramic	47
2.3.3.5 Thermogravimetric Analysis (TGA)	47
2.3.4 Electrochemical Measurements	48
2.3.4.1 Cell preparation	48
2.3.4.2 Experimental apparatus: Two-chamber apparatus	49
2.3.4.3 AC impedance spectroscopy	52
2.3.4.4 Current efficiency calculation	56
2.3.4.5 Mass spectrometry (MS)	57
2.4 Results and discussion	59
2.4.1 Physical properties of sintered BCZYZ pellet	59
2.4.2 Microstructure Characterisation	59
2.4.3 Phase Identification	61
2.4.4 TGA characterisation for water uptake	62
2.4.5 Electrochemical measurements	64
2.4.5.1 OCV measurements of Pt BCZYZ Pt cell	64
2.4.5.2 AC impedance spectra of 5% H ₂ /Pt BCZYZ Pt,O ₂ cell	65
2.4.5.3 Performances of Pt BCZYZ Pt cell in different cathode gases	68
2.4.5.4 Cell performance after electrode geometry modification	70
2.4.5.5 Performances of cells with different cathodes	72
2.4.5.6 Cell performances under closed-circuit condition	73
2.4.5.7 Ammonia formation rate	77
2.4.5.8 H ₂ evolution rate and overall current efficiency	80
2.5 Conclusions	85
References	86

2.1 Overview

The properties of the proton-conducting oxide electrolyte, BCZYZ, which was used in this project, have been evaluated. The ceramic preparation, sintering conditions and characterizations including electrochemical measurements are summarised in this Chapter. Moreover, electrolytic ammonia synthesis was characterised to evaluate the possibility of using this electrolyte in ammonia synthesis.

2.2 Preparation of oxide ceramic

2.2.1 Solid state synthesis

Solid state reaction is the oldest and simplest method for preparing ceramics. This method involves physical mixing of powdered reactants then pressing or shaping them before sintering. This method is intrinsically slow as the reactants are mixed as individual particles while soft chemistry methods, e.g. sol-gel methods, provide mixing on the atomic level. The advantages of solid state reaction are the inexpensive reactants and the convenience for a large scale preparation. In solid state reaction, the reaction happens at the interface between grains of the reactants. First of all, nucleation of product crystals occurs at the interface by the diffusion of ions from the contacting reactants. The reaction is fast in the first stage due to a large chemical potential difference. In the second stage, the growth of product impedes the reaction as the reactants are no longer in contact. Hence, the reaction progresses slowly between the product and each reactant interface instead. Consequently, it is difficult to attain reaction completion even if very high temperatures and prolonged periods are applied. However, the problem with unreacted reactants can be solved by grinding the

partially reacted mixtures in order to break up reactant/product interfaces and allow the residual reactants into contact. Another way is the addition of a small amount of liquid or gaseous sintering aid into the mixture. This gas- or liquid-phase assists the transport of matter and accelerates the reaction rates^[1].

2.2.2 Densification of ceramics

Since an electrolyte ceramic membrane with high density is required, the densification and sintering processes need to be considered.

The sintering process happens at the interface between the particles and at least six mechanisms can be involved. Typically, the sintering is accompanied by the shrinkage of the ceramic body, the removal of interstitial porosity, grain growth and coarsening. The possible mechanisms of the sintering process are displayed in Figure 2.1.

Owing to copyright restrictions,
the electronic version of this thesis does not contain this image

Figure 2.1 Schematic of six mechanisms take place between the particles leading to densification of a powder system^[2]. “With kind permission of Springer Science and Business Media:<Ceramic materials science and engineering, 2007, p.431, Chapter 24, C. B. Carter and M. G. Norton, Fig. 24.8>”

There are several mathematic approaches for the theoretical analysis of sintering. Most of the models assume that the spherical particles and uniform packing and omit the change in shape of particles during sintering. The model that has been used widely is the analytical model. In this model, the sintering process is divided into three stages. At the initial stage, the growth of necks between the particles is rapid due to surface diffusion, lattice diffusion or vapour transport. Neck growth leads to bonding between the particles and substantial shrinkage (3-5%) of the powder compact. The initial stage lasts until the radius of the neck has approached half of the particle radius. The intermediate stage includes grain growth, shrinkage and the isolation of pores. At the end of this stage a density of 90% of the theoretical should be reached. In the final stage, the isolated pores at the grain corners are assumed to shrink continuously and are finally eliminated.

Often, solid-state sintering can be difficult to complete or require very high sintering temperatures, In some cases, a small amount of additive which has relatively low melting temperature can be added into the system to enhance the sintering rate by creating a liquid phase during sintering. The presence of liquid phase facilitates the transport of matter by producing a high diffusivity path between grains.

Liquid-phase sintering typically proceeds via the rearrangement of the particulate solid, solution-precipitation and Ostwald ripening (a coarsening process). The summary of stages of liquid phase sintering is depicted in Figure 2.2.

Owing to copyright restrictions,
the electronic version of this thesis does not contain this image

Figure 2.2 Stages of liquid-phase sintering^[3]. “With kind permission from Springer Science+Business Media: <Journal of Materials Science/Review: liquid phase sintering, 44, 2009, 3, R. M. German, P. Suri, and S. J. Park, Fig. 1>.”

In this experiment, a small amount of ZnO (4 wt%) was used as sintering aid. ZnO which has a lower melting point than the other oxides will form a liquid phase at the firing temperature and enhance the sintering. Tao and Irvine reported that the addition of ZnO lowered the sintering temperature of barium cerate/zirconate ceramic and dramatically improved density of the sintered body. In addition, a change in unit cell parameters was also observed. Hence, it was suggested that ZnO enters in the crystal lattice and forms a solid solution with the other reactants^[4].

2.3 Experimental

2.3.1 Powder preparation

The perovskite proton conducting oxide, $\text{BaCe}_{0.5}\text{Zr}_{0.3}\text{Y}_{0.16}\text{Zn}_{0.04}\text{O}_{3-\delta}$ (BCZYZ), was prepared by solid-state reaction. Starting oxides, CeO_2 (Sigma-Aldrich, 99.9%), ZrO_2 (Riedel-de Haen, 99%), ZnO (Hopkin and Williams, 99%) and Y_2O_3 (Alfa Aesar, 99.9%) were dried in air at 600 °C for 2 h to remove absorbed H_2O and CO_2 , while BaCO_3 (Aldrich, 99.9%) was dried at 300 °C due to its low melting point. All the dried powders were removed from the furnace at around 300 °C and weighted immediately. Stoichiometric amounts of all starting materials except ZnO were mixed in a planetary ball mill (Pulverisette 7, Fritsch) for 2 h using six zirconia balls (8.8 mm in diameter) in acetone medium. After ball milling, the powder was dried in an oven at 80 °C before being calcined in air at 1250 °C for 2 h. In the last step, a stoichiometric amount of ZnO was added into the calcined powder and followed by another ball-milling for 2 h. The finished powder appeared as fine and almost white particles. This calcined powder, called BCZYZnO, was used for both uniaxial pressing (in this chapter) and tape casting (in Chapter 3). Phase identification of this powder was performed by X-ray diffractometry (XRD).

2.3.2 Electrolyte sintering

Dense electrolyte ceramic for electrochemical measurements were prepared by uniaxial dry-pressing BCZYZnO powder at room temperature. About 1.9 g of BCZYZnO powder was placed into a 2.3 cm diameter steel die and pressed under a pressure of 1 ton. The pressed pellets were then transferred to a furnace using an

alumina plate as a support. The sintered BCZYZ pellets with ~ 1 mm thickness and ~ 19 mm diameter were attained after sintering under a stagnant air atmosphere. The sintering temperature was varied from 1300 to 1400 °C and the most suitable sintering temperature was determined from the microstructure of sintered samples. The sintering conditions also required careful attention. It was found that the BCZYZ pellet react with either alumina or zirconia support if they were in direct contact. Therefore, a layer of sintered BCZYZ powder derived from a sintered pellet was applied as a buffer layer between the alumina plate and the BCZYZnO pellet. This sintered powder layer worked effectively in preventing the highly reactive BCZYZnO from reacting with the alumina support.

Besides the undesired reaction, another problem for sintering this material came from the thermal stress that developed during sintering. Serious cracking of specimens occurred during heating and cooling when the heating/cooling rates were too high or too low. Consequently, the heating/cooling rates needed to be optimised. After trial and error tests, it was speculated that the cracks were likely to happen during the cooling step as a result of temperature gradients between the high heat capacity ceramic disk and the atmosphere above the ceramic. Therefore instead of cooling down directly to room temperature, the disks were held at 650 °C for 2 h. This was expected to reduce the thermal stress inside the ceramic disks. Finally, the electrolyte ceramic disks were successfully sintered by the sintering treatment as shown in Figure 2.3.

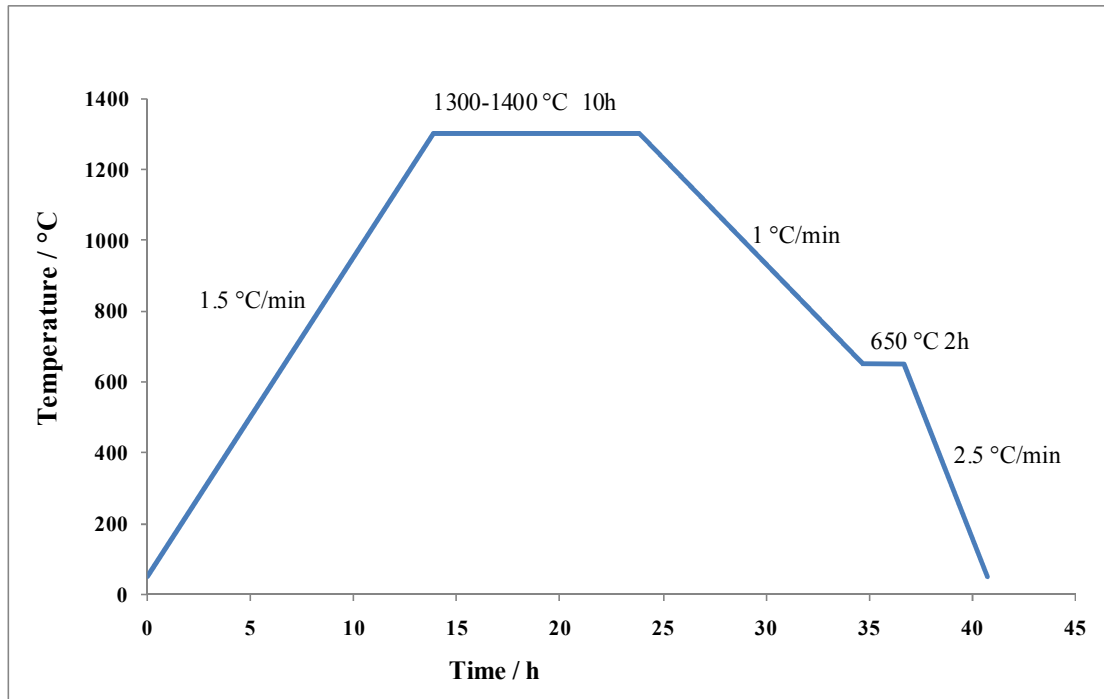


Figure 2.3 Diagram of optimum sintering treatment for BCZYZ 1 mm thick pellet

2.3.3 Ex-situ characterisation

2.3.3.1 X-ray Diffraction (XRD)

X-ray powder diffraction is a non-destructive method providing information about the crystallographic structure and crystalline phases or compounds in polycrystalline or powdered solid samples. The theory of diffraction is based on Bragg's law. A crystal structure consists of three-dimensional arrangements of atoms in a repeating pattern. This pattern is built up from a smallest unit called the *unit cell*. This array of atoms may be divided up into sets of lattice planes. These parallel planes are present in various orientations and directions with their individual interplanar distance, d . When the incoming beams of X-rays strike these lattice planes, they will be diffracted in all directions due to the interaction with atoms in the lattice plane. In a few specific

directions, the diffracted X-rays beams interfere constructively resulting in a set of intense reflection beams which can be detected. Theoretically, the constructive interference of two reflected beams occurs when Bragg's law is satisfied. Figure 2.4 exhibits the derivation of Bragg's law. For two incident beams with an angle Θ to the lattice planes, beam 22' has to travel the extra distance xyz comparing to beam 11'. For beam 2' to be still in phase with 1', the path difference xyz needs to be an integral number of wavelengths $(n\lambda)^{[1]}$.

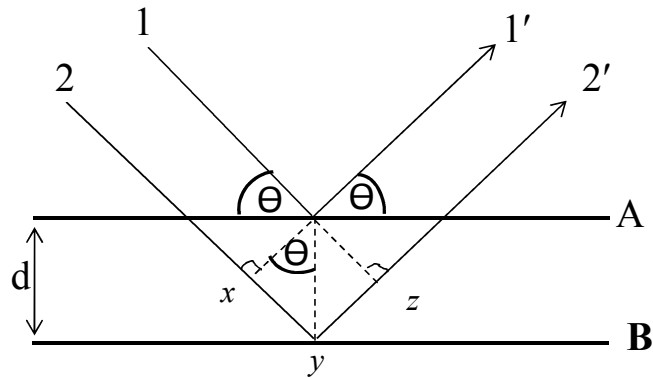


Figure 2.4 Derivation of Bragg's law.

From Figure 2.4,

$$xy = yz = d \sin\Theta \quad (2.1)$$

Then

$$xyz = 2d \sin\Theta \quad (2.2)$$

For constructive interference, the distance xyz must be equal to an integral number of wavelengths $(n\lambda)$. Therefore,

$$2d \sin\Theta = n\lambda \quad \text{Bragg's law} \quad (2.3)$$

The X-ray diffraction pattern of each crystalline solid represents its ‘fingerprint’ which can be used to identify unknown crystalline materials by comparing with a reference source, *Powder Diffraction File* (International Center for Diffraction Data, USA).

Instruments

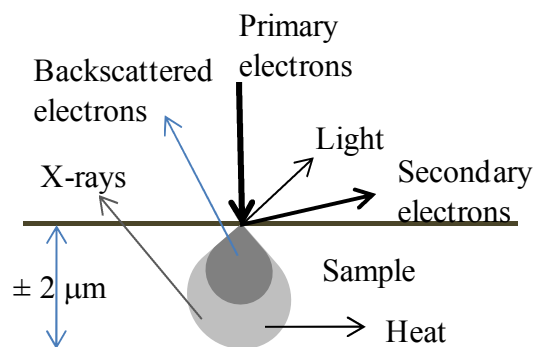
Phase purity of the starting powder and sintered ceramic were examined by two X-ray diffractometers with different working modes. The Philips PW 1710 diffractometer operates in reflection mode using $\text{CuK}\alpha$ radiation (1.5406 Å) and is suitable for the examination of bulk ceramic surfaces. The STOE Stadi-P Transmission X-ray diffractometer operates in transmission mode with $\text{CuK}\alpha 1$ radiation and provides data suitable for evaluating the lattice parameters of the powder. X-POW Software was employed for the lattice parameter calculation using least squares refinement method. The XRD data from the Philips diffractometer were collected using a continuous scan with a range of $2\theta = 15\text{-}100^\circ$, 0.02° step size and $1^\circ 2\theta\text{min}^{-1}$ scan rate. In the case of the STOE Stadi-P diffractometer, the same scan range was employed but a 0.01° step size and a 2000 sec/step slow scan rate were used instead.

2.3.3.2 Scanning Electron Microscopy (SEM)

Scanning electron microscopy (SEM) is a technique that provides information about the texture, topography and features of the sample surface. The narrow electron beam of the SEM provides excellent depth of field allowing the three-dimensional structure of the surface to be imaged. A schematic of a typical SEM is displayed in Figure 2.5a.

By scanning the sample surface with a high-energy beam of electrons thermionically generated from an electron gun equipped with a tungsten filament cathode, the interaction between electrons and the surface atoms emits several types of signals such as secondary electrons, back-scattered electrons, characteristic X-rays, light and heat as displayed in Figure 2.5b. For SEM imaging, secondary electrons (SE) with low energy (~ 5 eV) are commonly used. The secondary electron comes from the loosely bound electrons scattered from the surface. The resolution of SEM in SE mode is around 0.7 nm at 25 kV^[2].

Owing to copyright restrictions, the electronic version of this thesis does not contain this image



(a)

(b)

Figure 2.5 (a) schematic of a typical SEM components^{[2]*} and (b) possible signals emitted by an electron beam. *"With kind permission of Springer Science and Business Media:<Ceramic materials science and engineering, 2007, p.158, Chapter 10, C. B. Carter and M. G. Norton, Fig. 10.5>"

2.3.3.3 Energy-dispersive X-ray spectroscopy (EDS)

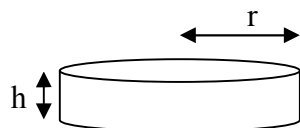
As mentioned above, it is possible to have characteristic X-rays emitted from the sample by the collision between electron beam and atoms at the sample surface. In this case, the inner shell electron is hit by a high-energy beam of electrons and ejected from its shell creating an electron hole. If the replacement electron is a higher energy electron from the outer shell, the excess energy may be released as an X-ray. The energy of this X-ray is related to the difference in energy between two shells and corresponds to the atomic structure of a particular element. Therefore, the elemental composition of the sample within a sampling depth of 1-2 microns can be revealed. This technique allows both qualitative and quantitative (standards are required) analysis. The advantage of EDS is the ability to indicate the distribution of elements on a sample surface by elemental mapping technique.

Instrument

SEM analysis was carried out on a JEOL 5600 scanning electron microscope with secondary electron image mode coupled to an EDS (Oxford Inca) analysis system. Working distance was set at 20 mm. The voltage in the range of 5-20kV was used with a spot size around 30.

2.3.3.4 Density of sintered ceramic

The actual density, ρ , of a sintered pellet can be calculated as follows;



$$\rho = \frac{\text{mass}}{\text{volume}} = \frac{m}{\pi r^2 h} \text{ (g cm}^{-3}\text{)} \quad (2.4)$$

where h is an average height of the specimen in cm, r is an average radius of the specimen in cm and m is the specimen weight in grams.

The actual density value will be compared with the theoretical density (TD or $\rho_{\text{theoretical}}$) which is calculated from the unit cell parameter as follows:

$$\rho_{\text{theoretical}} = \frac{M_w \times Z}{V \times 10^{-24} \times 6.02 \times 10^{23}} \text{ (g cm}^{-3}\text{)} \quad (2.5)$$

where M_w denotes relative molecular mass of material (g mol^{-1})

V is the unit cell volume calculated from unit cell parameter, a , b and c (\AA)

Z is the number of molecules per unit cell ($Z= 1$ in this case)

2.3.3.5 Thermogravimetric Analysis (TGA)

Thermogravimetry is a technique for studying physical and chemical properties of a substance as a function of temperature. A certain amount of sample is heated with constant rate and the change in mass of the sample is recorded continuously. A plot of mass against temperature indicates the initial temperature of a process and final temperature when the process has been completed. Those temperatures are dependent on the nature of the sample such as its particle size, heating rate and the testing

atmosphere. Typically, H₂O uptake of a proton conducting ceramic oxide can be characterised by this technique^[5, 6].

Instrument

The studies of hydrogen incorporation in BCZYZ ceramic were carried out on a Netzsch STA 449C Jupiter thermal analyser. The sample was prepared from a ground sintered BCZYZ pellet. The powder was heated up to 900 °C in argon with a heating rate of 5 °C/min and dwelled for 1 h before cooling down in 5% H₂ at the same rate. Once the temperature decreased to 50 °C, the sample was heated up in argon to 900 °C again in order to confirm the previous result.

2.3.4 Electrochemical Measurements

2.3.4.1 Cell preparation

Metal ink electrodes were employed as electrode and current collector on the 1 mm thick BCZYZ pellet. Three kinds of metal inks, either Pd (Metalor), Pt (G.E.M) or Au (Metalor), were employed in this experiment. The electrode ink was applied on the electrolyte pellet by hand-painting. The electrode was painted in full-circle pattern at the centre on both sides of the pellet creating a cell with two-electrode configuration as displayed in Figure 2.6. The superficial surface area of each electrode was 1.23 cm².

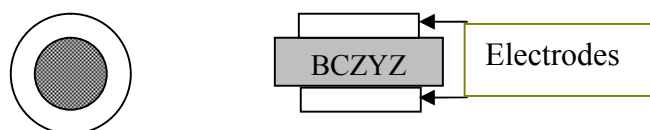


Figure 2.6 Geometry of electrode on BCZYZ pellet for electrochemical testing.

After painting, the electrode was fired at 900 °C, for Pd and Pt electrodes, and at 800 °C, for Au electrodes, in air for 1 h in order to attain good adhesion with the electrolyte. Cracking of the electrode was still a problem during the cooling step after firing . The solution of this problem was similar to the sintering treatment. A dwell step was applied during cooling. The pellets were held at 450 °C for 2 h before cooling to room temperature. The optimised heat treatment for electrode firing is shown in Figure 2.7.

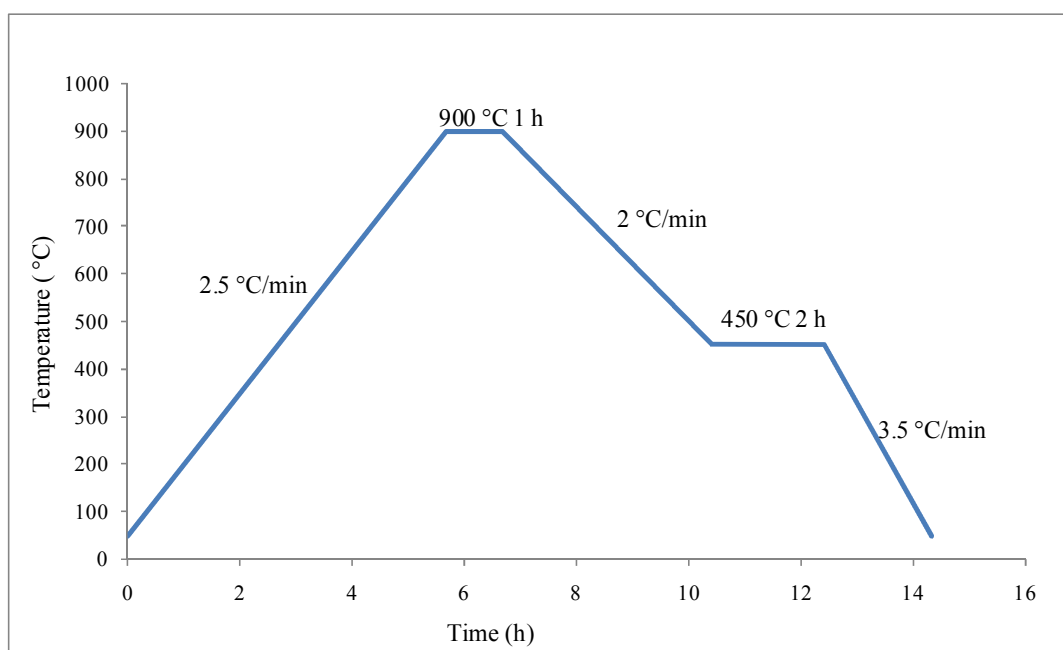


Figure 2.7 Electrode firing conditions.

2.3.4.2 Experimental apparatus: Two-chamber apparatus

Electrochemical measurements of BCZYZ cells were carried out in a two-chamber apparatus. A schematic representation of the apparatus is shown in Figure 2.8. The measurements were performed in the temperature range 400-750 °C. The sample was fixed between two alumina tubes by alumina sealant (P-24, To Ku ceramic) creating

two gas-tight compartments. The outlet tube with 0.25 mm diameter was placed centrally inside the 20 mm diameter tube. Both 20 mm and 0.25 mm diameter tubes were fitted with a Swagelok stainless steel T-shape fitting. Electrical connections were achieved by connecting the electrodes of the cell to the stainless steel fitting from inside the alumina tube using Au paste and Au wires. The schematic of the two-chamber setup is shown in Figure 2.8. Inside the furnace, the cell was dwelled at 150 °C for 1-2 h in order to cure the ceramic sealant. Then the temperature was raised with a heating rate of 2.5 °C/min to 750 °C. In this study, only humidified 5% H₂ was used as the anode gas. Humidified 5%H₂ was achieved by bubbling 5%H₂/Ar gas through room-temperature water resulting in a gas mixture of 3 % H₂O and 4 % H₂ in Ar. The flow rate of 5% H₂ of 30 ml/min was controlled by a needle flow meter. For the cathode, three kinds of gases i.e. O₂, N₂ and Ar were used.

The open circuit voltage (OCV) of the cell under testing condition was recorded as a function of time until the system reached the steady state before performing the electrochemical measurements. The electrochemical measurements were carried out using a frequency response analyzer (Solartron 1255, UK) coupled with an electrochemical interface (Solartron 1287, UK). The voltage-current (*V-I*) measurement was performed by sweeping potentials across the cell using a scan rate of 2 mV/sec with the applied potentials from 0-3 V with respect to the OCV. The AC-impedance measurement was obtained in a frequency range of 1 MHz to 0.1 Hz using a potential amplitude of 50 mV under open-circuit conditions. In some cases, the polarisation under applied potential was also investigated.

For ammonia synthesis, non-humidified N₂ was fed into the cathode, as it has been reported that the presence of moisture in the gas mixture would inhibit the formation of ammonia^[7]. During electrolysis, the gaseous products in the cathode outlet stream

were examined by a mass spectrometer (MS) (Prolab, Thermo Scientific). In order to determine the ammonia formation rate, a constant flow rate of N_2 was required. In this work, a mass flow controller (Model 5850S, Brooks instrument) was employed. However, the actual flow rate of the outlet stream was checked periodically by a glass soap bubble flow meter.

The electrolysis was done by applying a constant potential to the cell. The values of applied potentials were varied between 1.8 and 3.5 V depending on the cell resistance due to obtain a target current which was in the range of 10-30 mA. The transient period was set at 20 min and the concentrations of evolved products in mol% were taken from the concentration difference between open circuit and closed circuit.

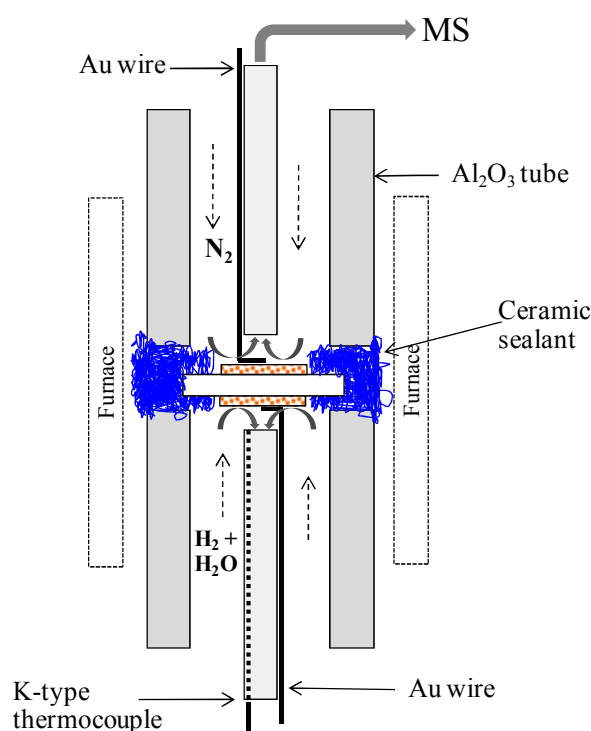


Figure 2.8 Two-chamber testing apparatus.

2.3.4.3 AC impedance spectroscopy

AC impedance spectroscopy is a powerful technique that is able to separate different contributions in an electrochemical cell. The information obtained from the impedance measurement concerns not only electrochemical processes but also physical or chemical transport limitations which can include electrolyte response, electrode response and transportation limitations of reactants and products.

The impedance measurement is performed by applying a small sinusoidal voltage perturbation to the cell expressed as a function of time:

$$V(t) = V_m \sin \omega t \quad (2.6)$$

So then the resultant current will also be a sinusoid at the same frequency but shifted in phase as expressed by:

$$I(t) = I_m \sin(\omega t + \phi).$$

V_m and I_m are the maximum amplitude of signal, ω is frequency in radians per second, ϕ is the phase shift in radians and equals to zero for purely resistive behaviour. The relationship between ω and frequency (f) is

$$\omega = 2 \pi f \quad (2.7)$$

From the above equations, the relationship between system properties and response to voltage or current excitation is very complex in the time domain. In general, the impedance (Z) can be expressed as

$$Z(\omega) = Z' + jZ'' \quad \text{where } j = \sqrt{-1} \quad (2.8)$$

When plot Z in the plane with rectangular coordinates;

$$\text{Re}(Z) = Z' = |Z| \cos(\phi) \quad \text{and} \quad \text{Im}(Z) = Z'' = |Z| \sin(\phi) \quad (2.9)$$

Since Z is frequency-dependent, a Nyquist plot, such as that shown in Figure 2.9., is a result of the impedance at individual frequencies. Normally, the sample is measured in a wide range of frequency of 10^7 to 10^{-2} Hz.

The impedance spectrum can be characterised as a arrangement of electrical circuits. For a ceramic sample, the impedance is usually characterised by a resistance (R) and a capacitance (C) placed in parallel as displayed in Figure 2.9. From the relationship between the characteristic relaxation time (τ) of each parallel RC component ($\tau = RC$) and the frequency at maximum loss, ω_{\max} , the different RC elements in different regions in the sample can be identified^[8].

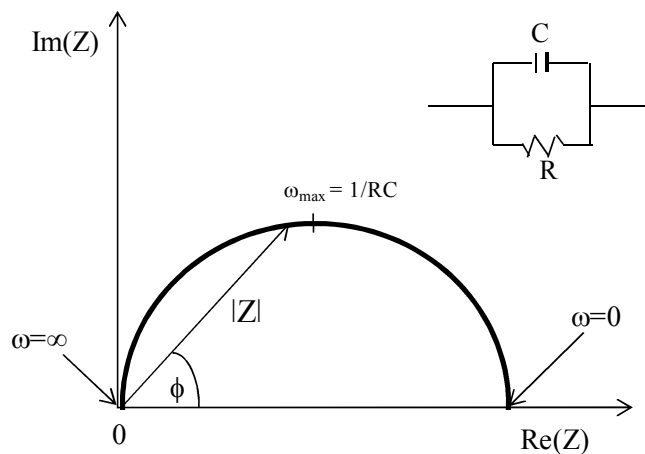


Figure 2.9 An example of Nyquist plot with impedance vector.

In a real sample, several semicircles may be attained. The capacitance from each semicircle provides information about the corresponding response that occurs in different regions in the sample. Some relationships between capacitance and corresponding response are shown in Table 2.1.

Table 2.1 Relationship between capacitance values and corresponding processes^[9].

Capacitance (F)	Corresponding processes
10^{-12}	Bulk
10^{-11}	Minor, second phase
10^{-11} - 10^{-8}	Grain boundary
10^{-9} - 10^{-7}	Surface layer
10^{-7} - 10^{-5}	Sample-electrode interface
10^{-4}	Electrochemical reactions

Considering electrochemical reactions at the electrode, there are two main processes which are normally seen by the impedance spectroscopy technique as shown in Figure 2.10. First, a charge transfer process which kinetically controls the electrochemical reaction. The speed of this process depends on the temperature, type of reaction and the concentration of reactants. Inevitably, a diffusion process also happens along with the charge transfer process. However this process controlled by mass transport, tends to appear at low frequency. In some cases, both charge transfer and diffusion features may not be well distinguished. If the electrochemical reaction rate is slow, the charge transfer resistance (R_{ct}) will be pronounced and the mass transfer may be negligible and vice versa. The characteristic impedance for diffusive systems is shown in Figure 2.11. Semi-infinite diffusion appears as a straight line with a slope of 0.5. This type of diffusion is known as the Warburg impedance (Z_w) and occurs when the diffusion layer has an infinite thickness. In some cases, the impedance tends to bend down into a semicircle due to the diffusion happens through a layer of finite thickness.

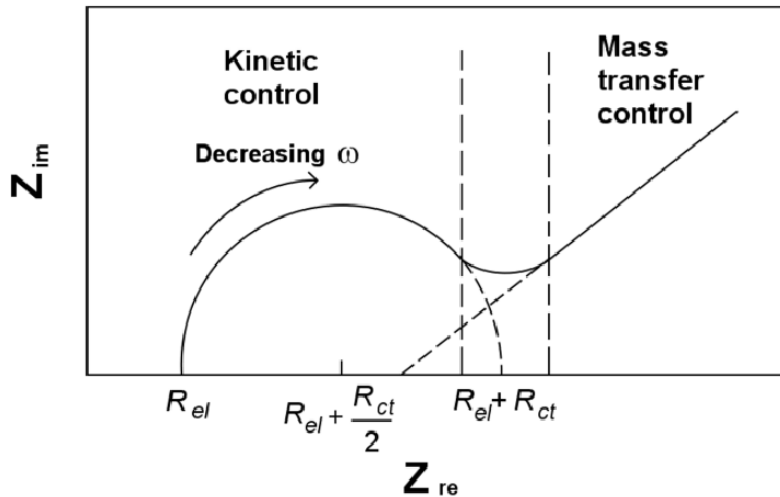


Figure 2.10 Impedance plot in the complex plane revealing factors controlling electrochemical reactions. Charge transfer process for kinetic control and diffusion process for mass transfer control. R_{el} is the resistance of electrolyte, R_{ct} is charge-transfer resistance^[10]. “With kind permission from Springer Science and Business Media: <Electrochemical Impedance Spectroscopy in PEM Fuel Cells: Fundamentals and applications, 2010, p. 117, Chapter 3, X.-Z.Yuan, C. Song, H. Wang, J. Zhang, Fig. 3.8>”

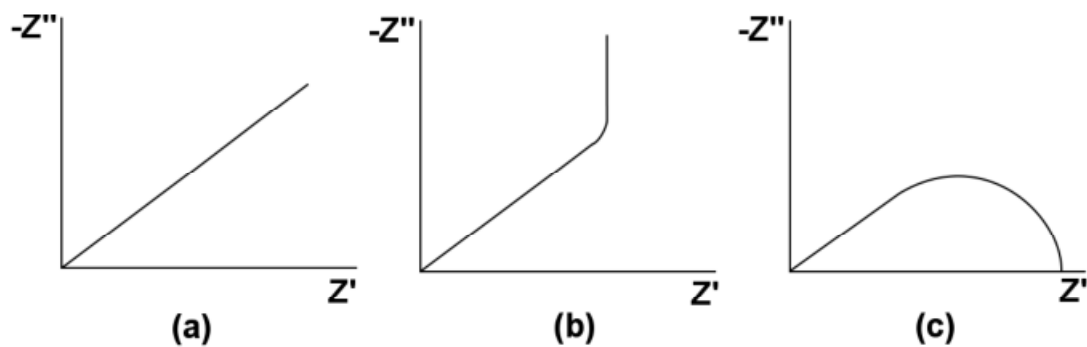


Figure 2.11 Characteristic impedances for diffusive systems: (a) semi-infinite diffusion, (b) reflective finite diffusion and (c) transmissive finite diffusion^[10]. “With kind permission from Springer Science and Business Media: < Electrochemical Impedance Spectroscopy in PEM Fuel Cells: Fundamentals and applications, 2010, p. 117, Chapter 3, X.-Z.Yuan, C. Song, H. Wang, J. Zhang, Fig. 3.9>”

2.3.4.4 Current efficiency calculation

Since there will be more than one faradaic reaction occurring at the cathode, the current efficiency for each reaction must be calculated individually from the fraction of current used in the particular reaction (i_r) to the total current that is imposed across the cell (i_{total})^[11]

$$\text{Current efficiency (\%)} = \frac{i_r}{i_{total}} \times 100 \quad (2.10)$$

Then i_r can be obtained from:

$$i_r \text{ (amperes)} = \frac{dQ}{dt} \text{ (coulombs/sec)} \quad (2.11)$$

and

$$\frac{Q}{nF} \frac{\text{(coulombs)}}{\left(\frac{\text{coulombs}}{\text{mol}}\right)} = N \text{ (mol electrolysed)} \quad (2.12)$$

where n is the stoichiometric number of electrons involved in the reaction and F is Faraday's constant, 96485 coulombs. From equation 2.11 and 2.12, moles of analysed gas (N) produced per second is equal to

$$\frac{dN}{dt} = \text{formation rate (mol/s)} = \frac{i_r}{nF} \quad (2.13)$$

Hence, the formation rate of each product relates to the amount of current consumed in the reaction (i_r) and the ratio of i_r to the total current (i_{total}) is referred to as the current efficiency.

By applying the ideal gas law, the molar flow rate of the outlet stream can be calculated from:

$$\text{Molar flow rate (mol/s)} = P \frac{(dV/dt)}{RT} \quad (2.14)$$

where dV/dt is the volumetric flow rate (cm^3/s); T and P values are regarding to standard conditions for temperature (298.15 K) and pressure (0.101 MPa), respectively based on the United Environmental Protection Agency (EPA) standard, and R is the gas constant ($8.314 \text{ cm}^3 \text{ MPa K}^{-1} \text{ mol}^{-1}$).

Because the amount of analysed gas detected by a mass spectrometer was presented in mol% of the molar flow rate, then its formation rate can be calculated as followed:

$$\text{formation rate (mol/s)} = \text{mol\% of analysed gas} \times \text{molar flow rate (mol/s)} \quad (2.15)$$

2.3.4.5 Mass spectrometry (MS)

Mass spectrometry is a technique for analysing gas compositions in the gaseous sample. Both quantitative and qualitative information can be provided via the determination of mass-to-charge ratio (m/z) of ions or fragments of analysed molecule. A mass spectrometer comprises of inlet system, ion source, mass analyser, detector and data analysis system as shown in Figure 2.12.

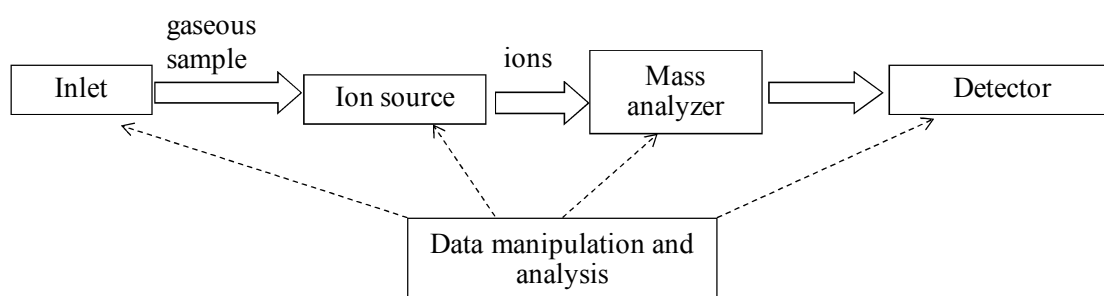


Figure 2.12 Components of a mass spectrometer.

First, the sample will be totally vaporised before passing through the ion source. At the ion source, the gaseous sample is then ionised by one of several ionisation methods, such as by bombarding gaseous molecules with an electron beam. This fragments those molecules into positively-charged ions. These positively-charged particles are then accelerated in an electric field before reaching a mass analyser. At the mass analyser, an electromagnetic field is applied to the charged particles while they are travelling across the mass analyser. Particles with different m/z values will be sorted by the electromagnetic field and sent into the detector in sequence. An electrical signal is generated when ions strike the detector. The signal is converted into a plot between intensity and m/z values and called a mass spectrum. Nowadays, all of the components are under computer control.

Instrument

The outlet gas stream from the cathode was analysed in a quadrupole mass spectrometer (Prolab 300, Thermo Scientific). The concentrations of gas compositions including H_2 , NH_3 , O_2 and H_2O were detected continuously especially under closed-circuit condition. The instrument contains an electron ionisation ion source and triple filter Quadrupole Mass Filter. The Faraday detector was set for recording mass channels of 2, 17, 18 and 28. The calibration gas was a mixture of 500 ± 10 ppm H_2 and 500 ± 10 ppm NH_3 with balance of N_2 . The operation and data analysis were controlled by GasWorks software. Because a significant amount of water may be present in the gas stream, the overlapping peaks at m/z 17 (NH_3^{*+} or OH^{*+}) and 18 ($^{15}NH_3^{*+}$ or H_2O^{*+}) will cause errors in both qualitative and quantitative analysis of ammonia. Therefore, the fragmentation patterns of water and ammonia needed to be

identified. From these patterns and their relative intensities, the fraction of a certain peak intensity related to a certain gas can be calculated.

2.4 Results and discussion

2.4.1 Physical properties of sintered BCZYZ pellet

After sintering, flat ceramic pellets with dark colour of the BCZYZ as shown in Figure 2.13 were obtained. The sample pellets used in this experiment had electrolyte thicknesses of 1.22 ± 0.02 mm and 95 ± 2 % of theoretical density.

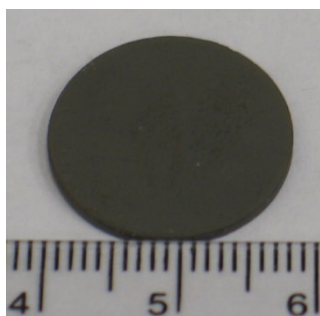


Figure 2.13 Typical sintered BCZYZ pellet.

2.4.2 Microstructure Characterisation

The microstructures of pellets sintered at various temperatures were investigated by SEM. Figure 2.14 displays a comparison between samples sintered at 1400 °C and 1300 °C. The SEM images of the fracture surfaces of both samples reveal dense microstructure with some isolated pores. The fracture path happens across the grains and is called transgranular fracture. This kind of fracture suggests good bonding between grain boundaries as a result of well-sintered ceramic which may be encouraged by the presence of a liquid phase during sintering. Samples sintered at

higher temperature tend to have larger grains but also larger pores. Large pores can more easily nucleate cracks than small pores. In addition, the distribution of porosity in the 1300 °C sample is better than the 1400 °C sample. The homogeneous grain size and pore distribution are preferred microstructure for good mechanical strength in ceramics.

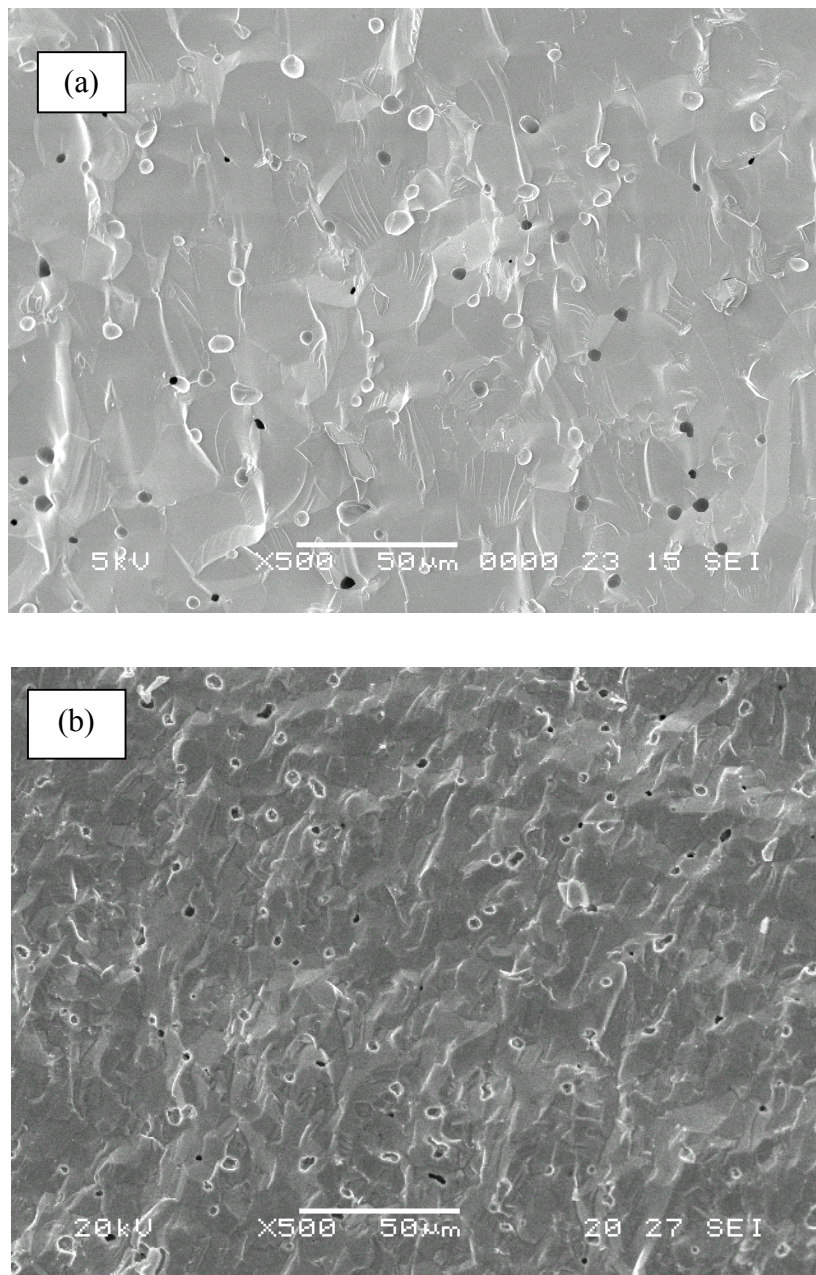


Figure 2.14 SEM images of fracture surface of BCZYZ pellets after sintered at (a) 1400 °C and (b) 1300 °C for 10 h.

2.4.3 Phase Identification

The X-ray diffraction patterns at room temperature of sintered BCZYZ and calcined BCZYZnO powder are shown in Figure 2.15. The XRD pattern of the calcined powder show a mixed phase of BaCeO₃ and BaZrO₃ (ICDD PDF card No. 22-74 and 6-399, respectively) but after sintering at 1300°C for 10 h, a single perovskite phase was obtained. By using X-POW software, refinement of the XRD data gave the sintered BCZYZ a cubic structure with unit cell parameter $a = 4.3376(6) \text{ \AA}$.

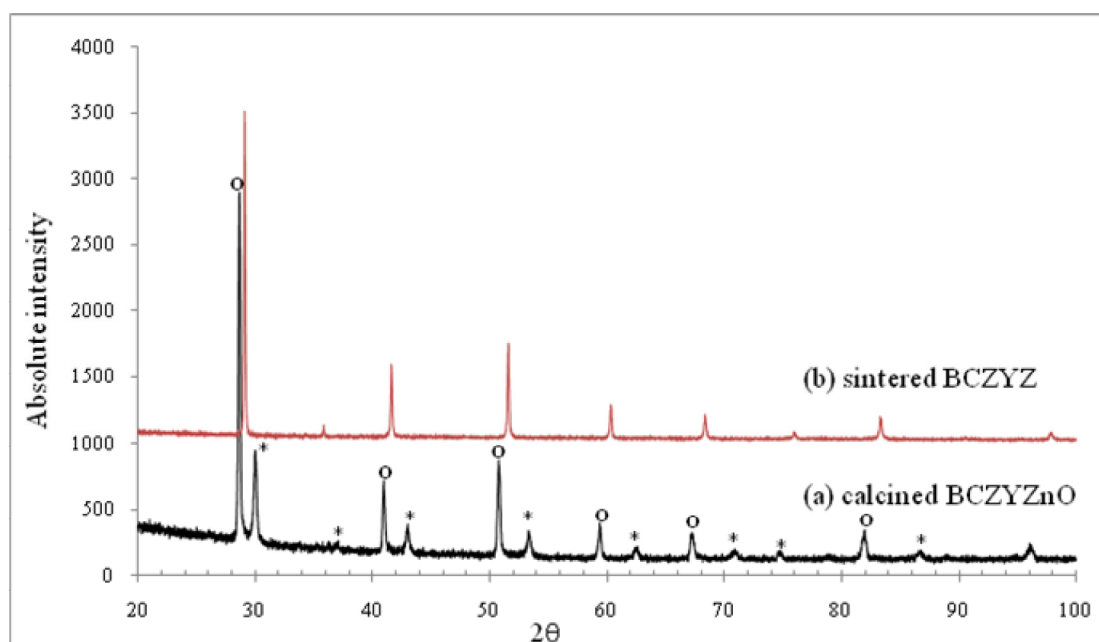


Figure 2.15 XRD results of BaCe_{0.5}Zr_{0.3}Y_{0.16}Zn_{0.04}O_{3-δ}, BCZYZ (a) BCZYZnO after calcining at 1250°C, (b) BCZYZ after sintering at 1300°C (o : BaCeO₃ peaks, * : BaZrO₃ peaks)

2.4.4 TGA characterisation for water uptake

The TGA data in Figure 2.16a of the powdered BCZYZ in Ar exhibits a sharp mass loss between the start of heating and 100 °C which could be a loss of adsorbed water from the powder surface. There is a gradual mass gain before a drastic weight loss between 500 °C and 800 °C. The loss at 500-800 °C is expected to be a loss of water bound within the crystal lattice. On cooling in 5%H₂/Ar (Figure 2.16b), the mass gain started at ~800 °C and finished at a lower temperature than that observed in the heating step. It is typical for a process to be slower on cooling than on heating. The uptake of water in 5% H₂ may arise from either H₂ or some moisture in the gas line. However, the result was confirmed again by continuously heating the sample in Ar atmosphere. On the 2nd heating round (Figure 2.16c), the mass loss was observed to occur in the same temperature range.

The weight difference derived from TGA data was 0.25 mass%. Assuming that the loss occurred from the uptake/loss of water from the crystal lattice, 0.045 moles of water per mole of BCZYZ was attained. Theoretically, the amount of oxygen vacancies (V_o^{••}) in BaCe_{0.5}Zr_{0.3}Y_{0.16}Zn_{0.04}O_{3-δ} (BCZYZ) is equal to 0.12 mol V_o^{••} per mol BCZYZ. According to;



Hence, the uptake of H₂O 0.045 moles by the BCZYZ crystal lattice claims that ~37.5 % of total V_o^{••} is filled by H₂O.

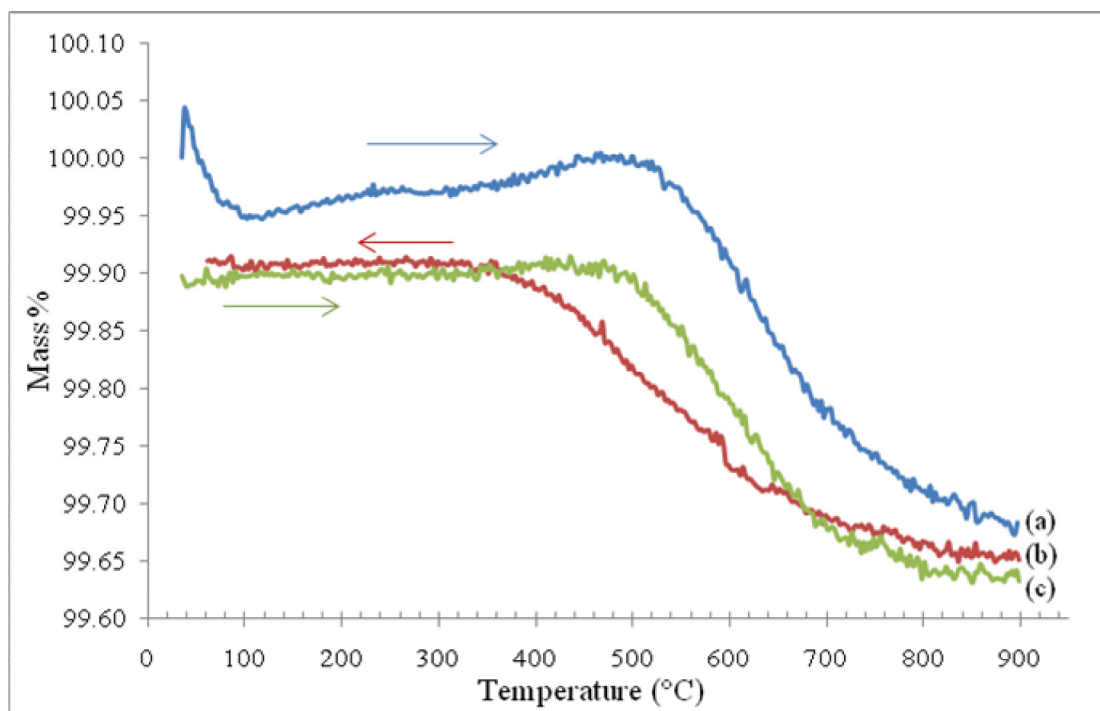


Figure 2.16 TGA data of sintered BCZYZ powder (a) on heating in Ar (b) on cooling in 5%H₂/Ar and (c) on 2nd heating in Ar.

2.4.5 Electrochemical measurements

2.4.5.1 OCV measurements of Pt|BCZYZ|Pt cell

Performances of the Pt|BCZYZ|Pt cell under humidified 5% H₂ (3%H₂O/Ar/4%H₂) in the anode chamber and non-humidified O₂ or N₂ or Ar gases in the cathode was investigated. In Figure 2.17, open circuit voltages (OCV) with various cathode gases are displayed. As expected, OCV values between humidified 5% H₂ and pure O₂ are higher than in the case of pure N₂ or Ar. According to the Nernst's equation,

$$E = E^{\circ} - \frac{RT}{2F} \ln \left[\frac{P_{H_2O}}{P_{H_2} \cdot P_{O_2}^{1/2}} \right] \quad (2.17)$$

where E° is standard cell potential (1.229 V) and R, T and F have their usual meanings.

From the Nernst's equation, theoretical OCV values for the cell operated in 5% H₂ and pure O₂ at various temperatures are present as a dashed line in Figure 2.17. The measured OCV is close to the theoretical value only at 450 °C then it decreases with increasing temperature. The reduction of the measured OCV may stem from the increasing of electronic conduction in BCZYZ electrolyte as usually observed in barium cerates. The ratio between measured OCV and theoretical OCV provides the ionic transport number (t_{ion}) that decreases from 1 (purely ionic) at 450 °C to 0.78 (mixed ionic/electronic) at 750 °C.

In cases of pure Ar and N₂, the unexpected high OCV may arise from some leakages within the testing apparatus. For example if 0.1% O₂ was present within the cathode gas, the theoretical OCV would be 1.02 V which is 0.1 V less than that of 100% O₂.

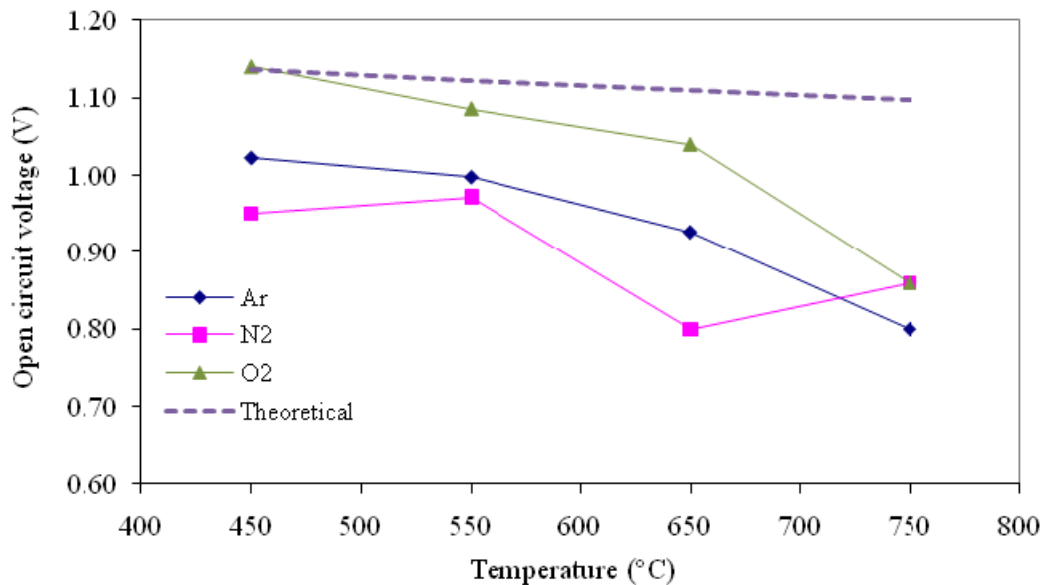


Figure 2.17 Open circuit voltage measured at different temperatures and cathode gases. Dashed line expresses theoretical OCV values in 5%H₂/Ar and pure O₂.

2.4.5.2 AC impedance spectra of 5% H₂,Pt|BCZY|Pt,O₂ cell

Figure 2.18 shows the impedance spectra of the BCZY cell with Pt electrodes in humidified 5% H₂ and non-humidified O₂ under open circuit conditions. The impedance comprises of at least two overlapping depressed semicircle arcs and the equivalent circuit fitting suggests that there are three possible electrode processes included in these spectra. The equivalent circuit is shown in Figure 2.19.

The series resistance, R_s, derives from the resistances of the electrolyte and the electrode materials and also the contact resistance at the electrode/electrolyte

interface. A set of parallel R_n and CPE_n (Constant Phase Element) is equivalent to an electrode process derived from the electrode polarisation. The CPE is employed in this study instead of the pure capacitance (C) due to the depression of the observed semicircle arcs. From the equivalent circuit, at least three electrode processes are suggested. The capacitances of the high frequency arc with peak frequency of 10^5 Hz are between 10^{-7} - 10^{-6} F/cm² which is associated to the charge transfer process at the electrode/electrolyte interface. The remaining electrode responses were assigned as medium- and low-frequency responses related to their summit frequencies. The medium-frequency contribution with peak frequency around 10^2 Hz possesses the capacitances of 10^{-6} - 10^{-5} F/cm² which corresponds to a combination of electrode reaction and charge diffusion processes. The low frequency contribution with peak frequency around 1 Hz may mainly relate to mass transfer process at the electrode surface.

With increasing temperature, the total polarisation resistance (R_p) calculated from the sum of R_1 , R_2 and R_3 tends to decrease as a result of the improvement of catalytic activity of the Pt electrode with temperature. Compared to the high frequency contribution, the contribution at medium frequency shows much stronger temperature dependence.

From R_s values, the conductivities of this cell are in the range of 2.5 – 3.9 mS cm⁻¹ for the temperature range of 450-650 °C, much lower than conductivities of the same material in humidified 5 % H₂ reported by Tao and Irvine^[4]. In their report, the conductivities of BCZYZ in wet 5% H₂ were 3.14 mS cm⁻¹ at 400 °C and > 10 mS cm⁻¹ above 600 °C. Smaller conductivities in this experiment may arise from the different atmospheres in two-chamber testing. The proton conductivity in non-humidified O₂ atmosphere should be very low.

Due to the limitation of two-electrode configuration, the impedance spectrum can provide only the overall processes occurring at both anode and cathode. However by fixing the anode condition and changing the cathode atmosphere, it is possible to notice the difference between anodic and cathodic polarisations by the AC impedance measurement.

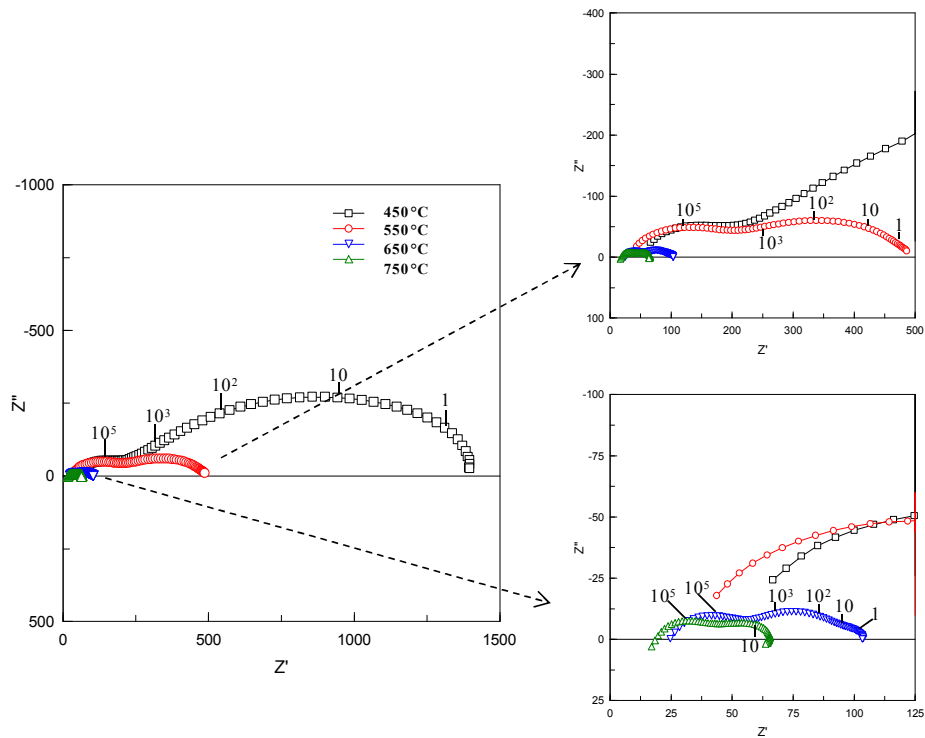


Figure 2.18 Nyquist plots of 1 mm thick Pt | BCZYZ | Pt cell in humidified 5% H₂ and non-humidified O₂ under open circuit at various temperatures where the number indicates frequency in Hz.

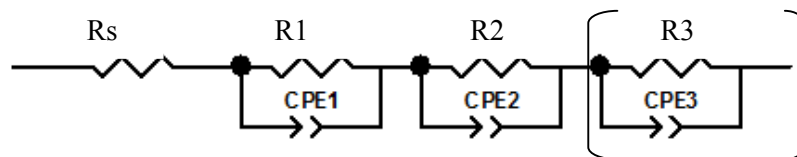


Figure 2.19 An equivalent circuit for the impedance from cell with Pt electrode.

2.4.5.3 Performances of Pt|BCZYZ|Pt cell in different cathode gases

In order to understand the electrode polarisation in the impedance spectrum, different cathode gases were employed. On the other hand, the purpose of this project is to find a cathode that can be used in pure N₂ atmosphere. Therefore, pure Ar or pure N₂ gases were introduced to the cathode instead of O₂. The impedance spectra are shown in Figure 2.20. Note that the impedance was taken in N₂ or Ar atmosphere which contained some O₂ from the leakage as seen from the OCV measurements. The impedance spectra at 450-650 °C indicate that the contributions at medium and low frequency are strongly affected by the change of gas types or oxygen partial pressure. It confirms that the oxygen partial pressure in the cathode controls the behaviours of the medium- and low-frequency responses.

It can be concluded that medium- and low-frequency processes stem from cathodic polarisation and the process that dominates the polarisation is the diffusion.

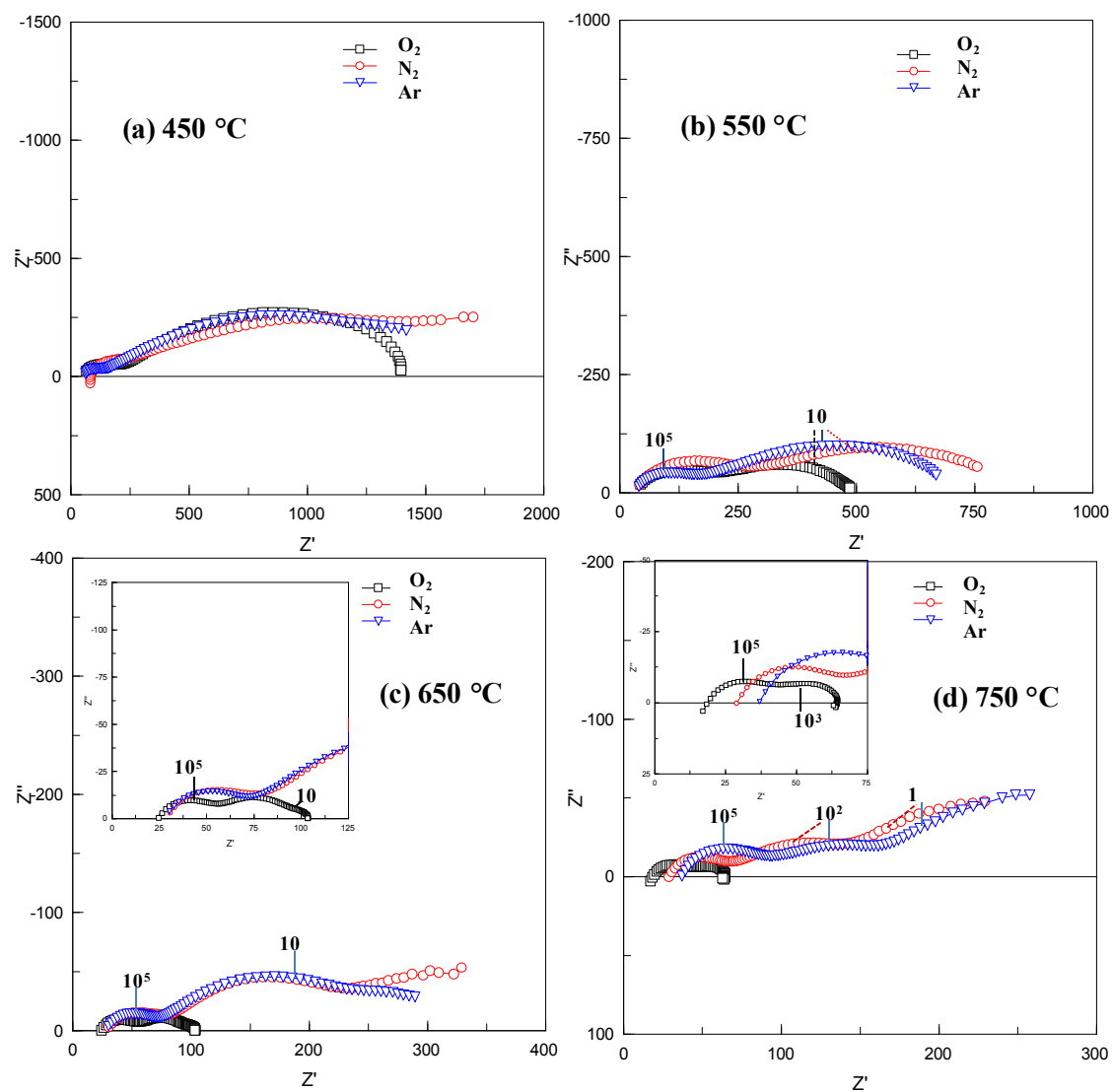


Figure 2.20 Nyquist plots of 1 mm thick Pt|BCZY|Pt cell in different cathode gases under open circuit (\square) O_2 , (\circ) N_2 , (Δ) Ar at (a) 450 °C, (b) 550 °C (c) 650 °C and (d) 750 °C.

2.4.5.4 Cell performance after electrode geometry modification

Problems due to poor adhesion of the electrode to the electrolyte are often found in cells with metal electrodes. In this experiment, the Pt electrode was quite dense and particles tended to agglomerate with each other rather than attach to the electrolyte surface after the firing step. The dense layer of Pt with poor adhesion and small three-phase boundary length are responsible for high R_p values. Therefore, electrode modification was necessary. The electrode was therefore painted in a grid pattern instead of painting in a full-circle as shown in Figure 2.21. By using the grid pattern, the adhesion with the electrolyte was improved and also the cell performance.

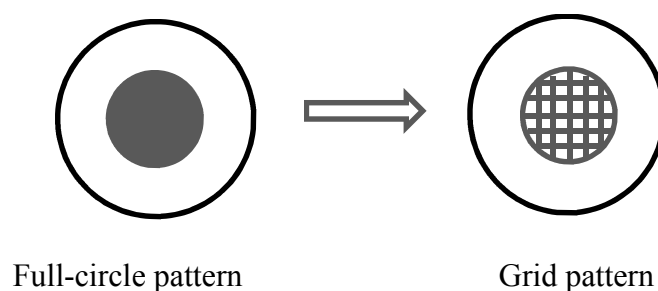


Figure 2.21 Modification of Pt electrode pattern

The comparison in cell performances for different electrode patterns was carried out in humidified 5 % H_2 and non-humidified N_2 . Examples of the impedance spectra of Pt | BCZY | Pt cells with different electrode patterns under open circuit are shown in Figure 2.22. Note that both pellets had similar densities and thicknesses. The results show that the Pt electrode with grid pattern provides much better performance. The R_p value of this grid electrode at 600 °C is smaller than the full-circle electrode by approx. 10 times. The shape of the high-frequency contribution was slightly changed and much smaller in size. The change in both shape and size was significant at the low

frequency arc which relates to the mass transfer process. It can be explained that Pt electrode may act as a dense layer on BCZYZ pellet instead of a porous electrode. Therefore, the activity of the Pt electrode did improve with the increase of TPB length in the grid pattern. Moreover, the improvement of ohmic resistance was also observed. This is probably due to the reduction of the contact resistance at electrode/electrolyte interface in the grid pattern. Hence, the conductivities of BCZYZ increase to the range of $2.4 - 5.4 \text{ mScm}^{-1}$ at $400\text{-}600 \text{ }^\circ\text{C}$ which are around 40% higher than the full-circle pattern.

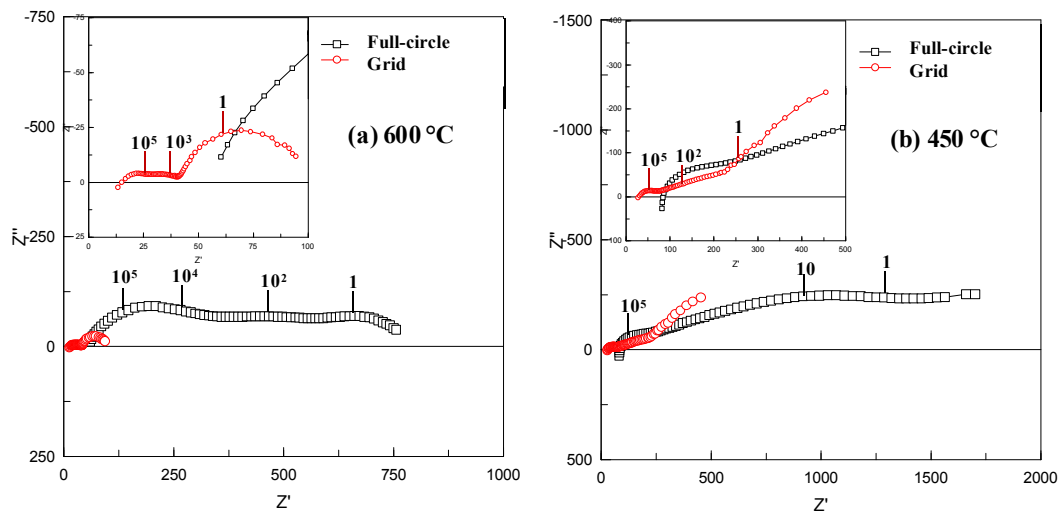


Figure 2.22 Impedance spectra of Pt|BCZYZ|Pt cell with different electrode geometry (□) full-circle pattern and (o) grid pattern at (a) 600 °C and (b) 450 °C in humidified 5% H_2 and non-humidified N_2 under open-circuit condition

2.4.5.5 Performances of cells with different cathodes

In order to find a proper cathode for operating in non-humidified N_2 , the performances of cells with various cathodes was investigated. The electrodes were painted in the grid pattern. The anode was kept in humidified 5% H_2 . The temperature range of the studies was varied from 400-600 °C in order to avoid the presence of electronic conduction and the decomposition of ammonia at temperature higher than 600 °C.

Examples of the impedance spectra of cells with different cathodes are displayed in Figure 2.23. At different temperatures, the behaviours of cells with different cathodes are quite distinct. However, the difference in performances of cells with different cathodes can be noticed clearly at high temperature. At 600 °C, cell with Au cathode provided a better performance than the others while Pd cathode exhibited a poor performance. It is likely that the impedance of all cells contains at least three electrode responses. The behaviours of high- and medium-frequency contribution are similar in most cases but the low-frequency contribution is different in the case of Au cathode. It seems that the mass transfer process is much better on the cell with Au cathode.

Considering R_s and R_p values, the cell with Pd cathode showed highest R_s and R_p values although the thicknesses of all cells are similar. The difference in R_s value may be attributed to the additional contact resistance at the electrode/electrolyte interface or the resistance of PdO which may form during operation in N_2 atmosphere. The presence of PdO could be a reason for the poor catalytic activity observed.

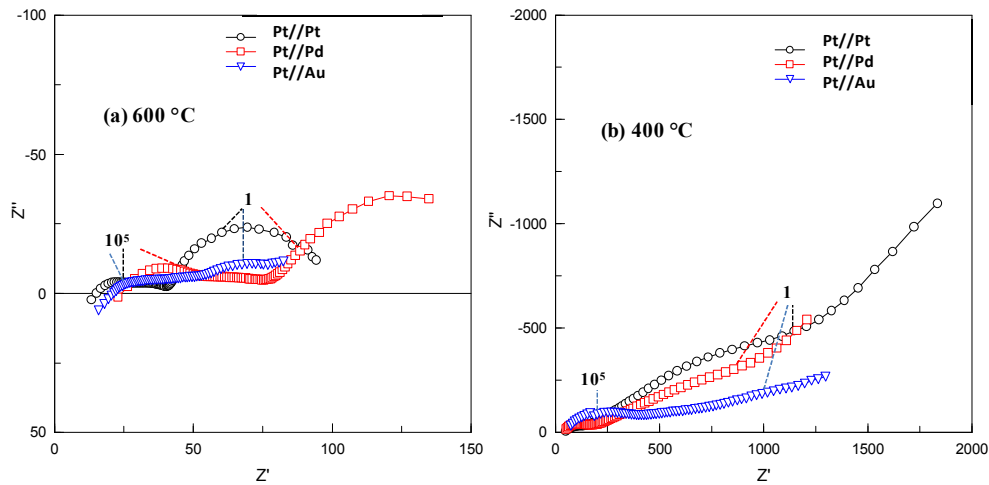


Figure 2.23 Impedance spectra under open circuit of cells with different cathodes in non-humidified N_2 at (a) 600 °C and (b) 400 °C. Pt was employed as anode and operated in humidified 5% H_2/Ar .

2.4.5.6 Cell performances under closed-circuit condition

It is important to characterise behaviour of cell under a potential or current loading. One method for characterisation is polarisation curve measurement or $V-I$ curve. From Figure 2.24, OCV values of all cells are close to -1 V. By applying positive potential to them, positive currents were driven across the cell. The amount of corresponding current is dependent on the total resistance of cell which can be roughly estimated from the slope of the $V-I$ curve. There is no significant difference in generated current among the three cells at 600 °C but at 400 °C the performance of the cell with Au cathode seems slightly better than the others. It could be a result of the catalytic activity of Au itself or the difference in metal paste properties such as particle size of metal.

In order to track the changes in cell performance during closed circuit, the impedance spectra of cells under voltage loading were investigated. As shown in Figure 2.25, the high frequency arcs were relatively constant under closed-circuit conditions especially at low temperature. When applying 1 V, the impedance at medium frequency became prominent. Then the increase of potential to 2 V definitely decreases the polarisation resistance of cells. Note that there are no changes in R_s values during closed-circuit conditions. This confirms that the applied potential results in changes only to the electrochemical reactions. The increase of the polarisation resistance when applying 1 V could be attributed to the resistances from the transport of electro-active species across electrode/electrolyte interfaces and the charge blocking effect due to the accumulation of protons at the cathode surface, since the amount of electrons to reduce them to H_2 was too small. The decrease of polarisation resistance when 2 V was applied is probably attributable to the reduction reaction of protons becoming feasible because of the higher availability of electrons.

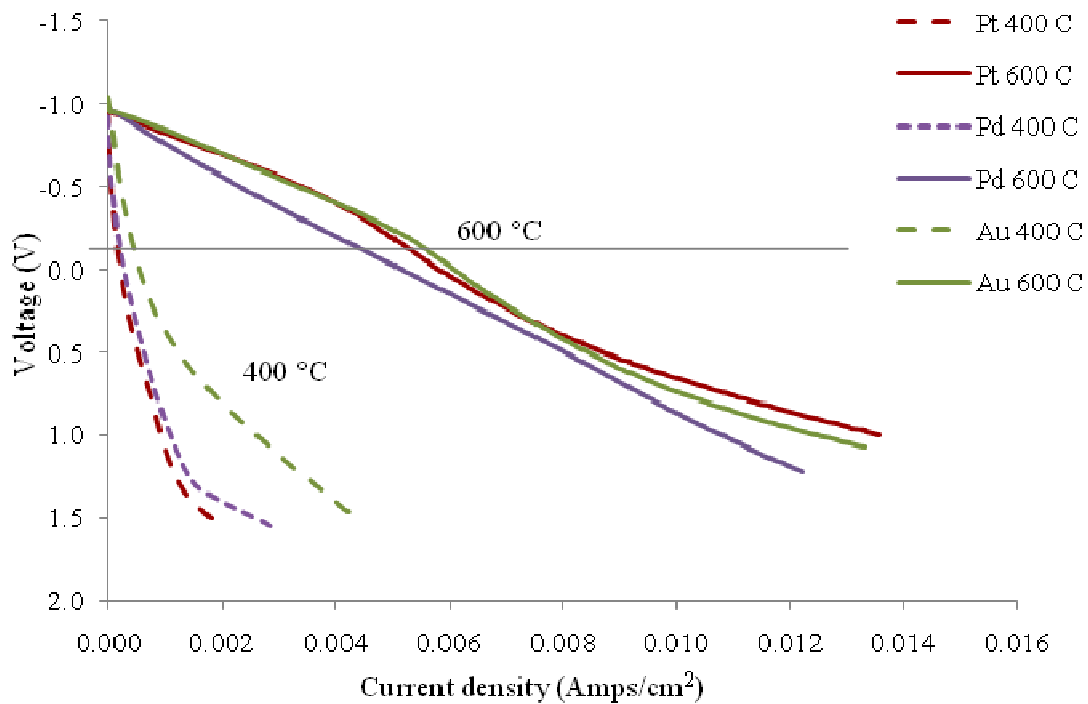


Figure 2.24 Polarisation curves from cells with different cathodes at 400 °C (dashed lines) and 600 °C (Solid lines). A sweep rate of 2 mV/s was employed when applying potential to the cell.

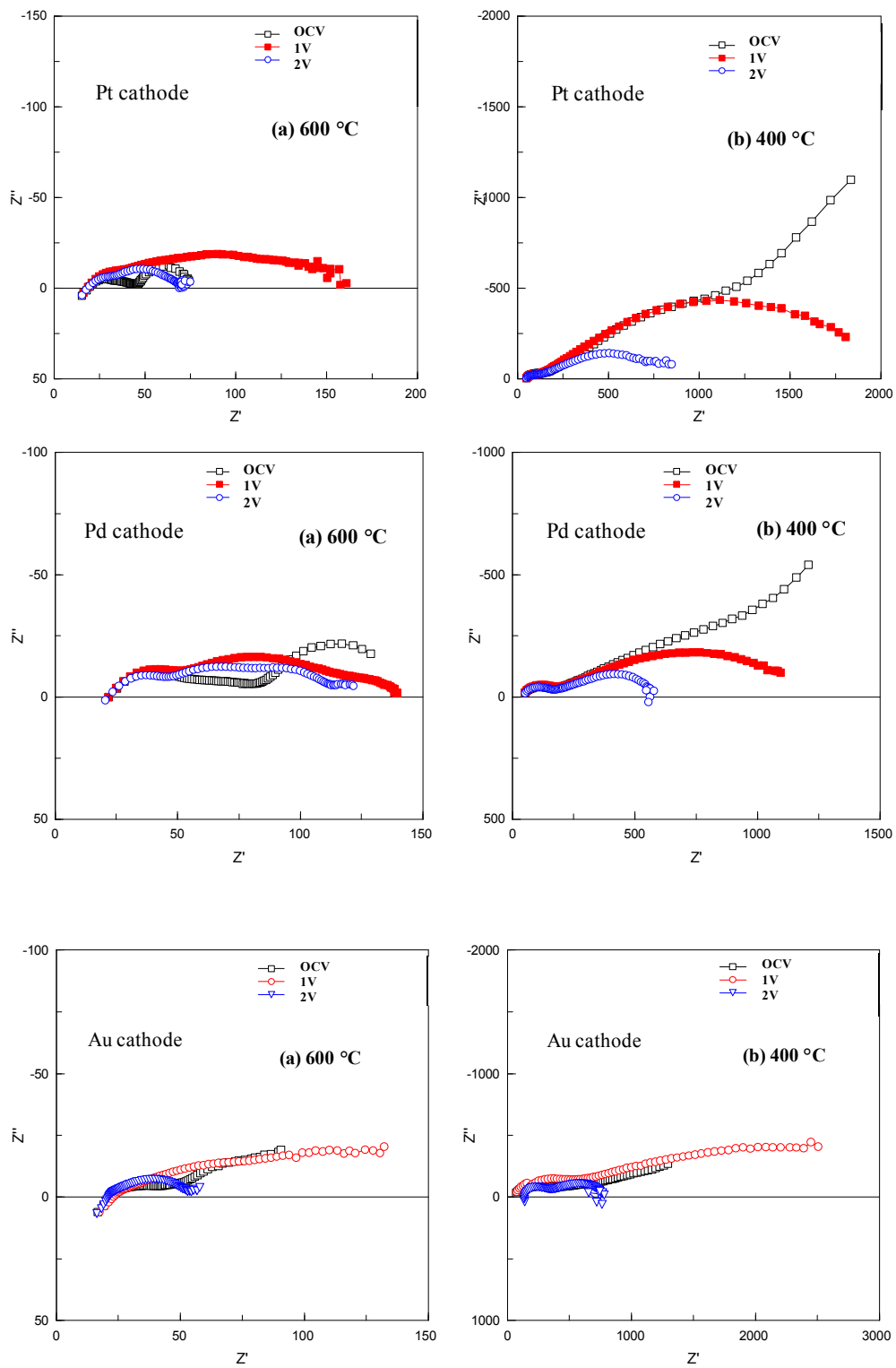


Figure 2.25 Impedance spectra of cells with various cathodes under DC loading at (a) 600 °C and (b) 400 °C in humidified 5 % H₂ and non-humidified N₂.

2.4.5.7 Ammonia formation rate

A significant amount of ammonia was produced when a constant potential was applied to the cell. The ammonia formation rates in Figure 2.26 indicate that the reaction requires current of at least 7 mA cm^{-2} in order to form ammonia. The formation rates tend to increase with increasing current and reach their maximum between $15\text{-}20 \text{ mA cm}^{-2}$. This study was performed in the temperature range of $450\text{-}600 \text{ }^\circ\text{C}$. At temperature higher than $600 \text{ }^\circ\text{C}$, the decomposition of ammonia may be pronounced and at temperature lower than $450 \text{ }^\circ\text{C}$, very high potential ($>3\text{V}$) was needed to generate enough current for the reaction.

The formation rates of ammonia from the three cathode materials are varied with temperature and type of the electrode. The Pt cathode provided highest formation rate of about $1.4 \times 10^{-9} \text{ mol s}^{-1} \text{ cm}^{-2}$ at $450 \text{ }^\circ\text{C}$. This corresponds to 2.7 % of current efficiency as shown in Figure 2.27. The current efficiencies of the cell with the Pt cathode are also higher than the Pd and Au, respectively.

The current efficiencies of ammonia formation tend to decrease with increasing current in the case of Pd and Au cathode. It is plausible that the formation reaction of H_2 is favourable on these electrodes at high current instead of ammonia formation. For example, the ammonia formation rate of the cell with the Au cathode at 24 mA cm^{-2} was close to zero while the highest H_2 evolution rate (shown in the next section) was attained. The results confirm that Au and Pd have poorer catalytic activity for ammonia formation reaction compared to Pt.

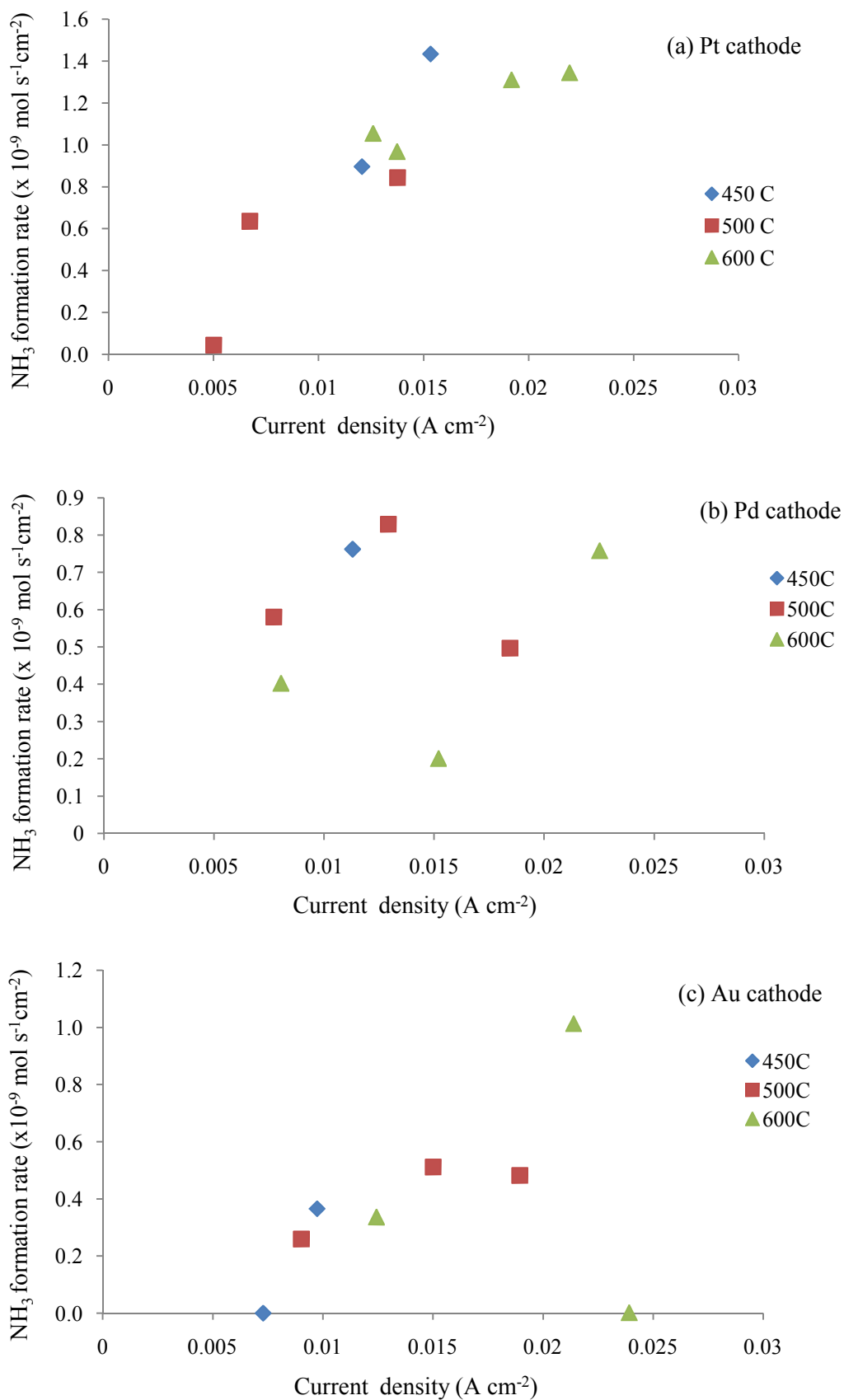


Figure 2.26 NH₃ production rate at different imposed currents and temperatures

(a) Pt cathode, (b) Pd cathode and (c) Au cathode

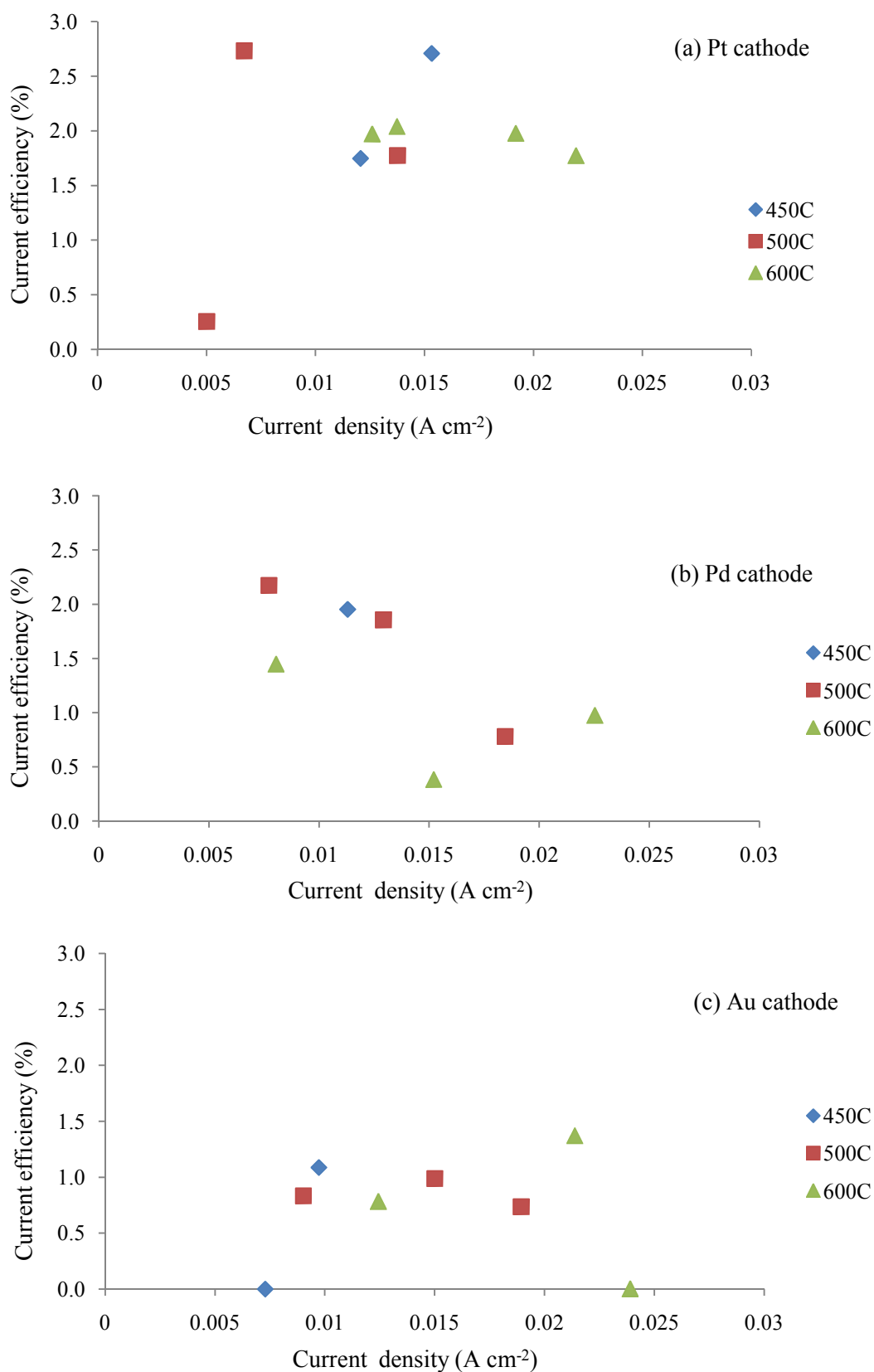


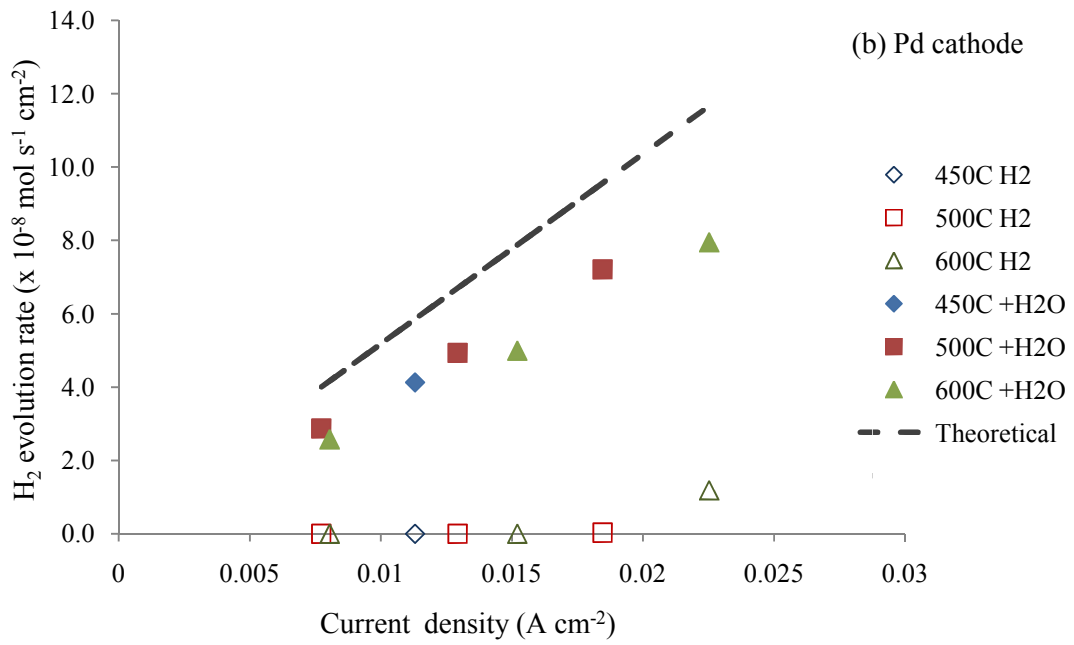
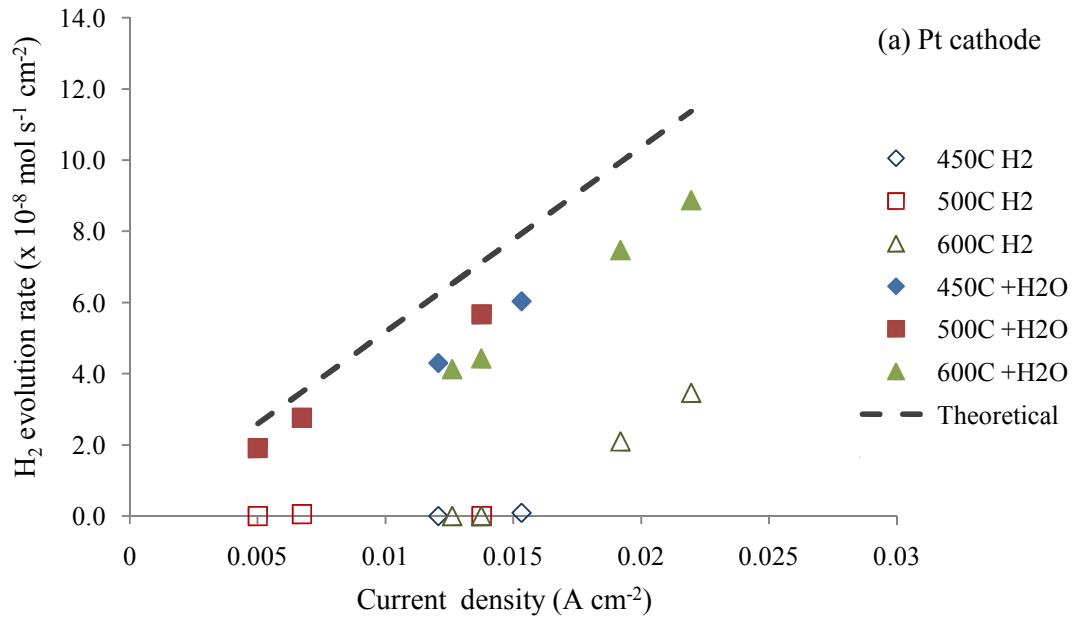
Figure 2.27 Current efficiencies of NH_3 formation versus current at various temperatures

2.4.5.8 H₂ evolution rate and overall current efficiency

During the closed circuit tests, a significant amount of H₂ was also detected along with ammonia. Figure 2.28 depicts the evolution rates of H₂ as a function of current. Note that the significant amount of O₂ (0.1-0.2 mol%) was usually detected in the cathode stream under open circuit condition. It may come from leakage within the apparatus or at the sealing area. Therefore under closed circuit, some evolved H₂ readily reacted with O₂ and formed H₂O. Consequently, the changes of H₂O or O₂ concentrations were used in the calculation of total amount of produced H₂.

At low current, it is hard to detect H₂ as most of it is used in the reaction with O₂. At higher current, a higher flux of protons was attained and the excess H₂ from the reaction with O₂ can be seen. However, the total H₂ produced is still lower than the theoretical value.

The loss in current efficiency is shown in Figure 2.29. The total current efficiencies including ammonia formation are just around 80%. The 20 % loss may concern the formation of the other side products or short circuits. Note that the internal short circuit occurred from electronic conduction of the electrolyte must be significant at 600 °C according to the lowest current efficiencies in all cells.



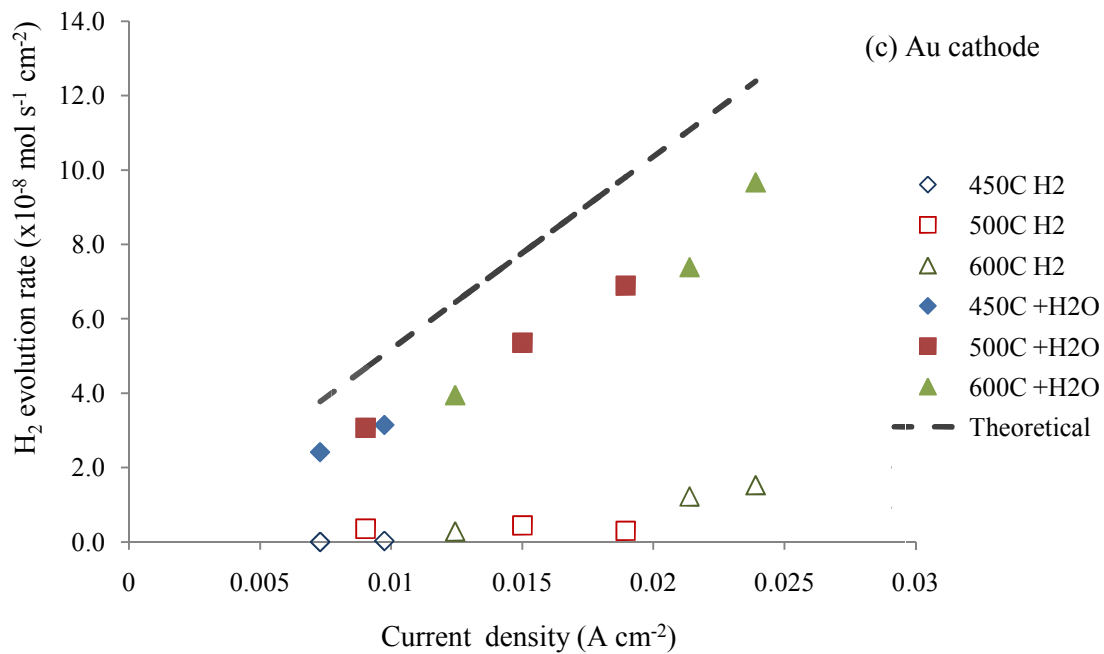
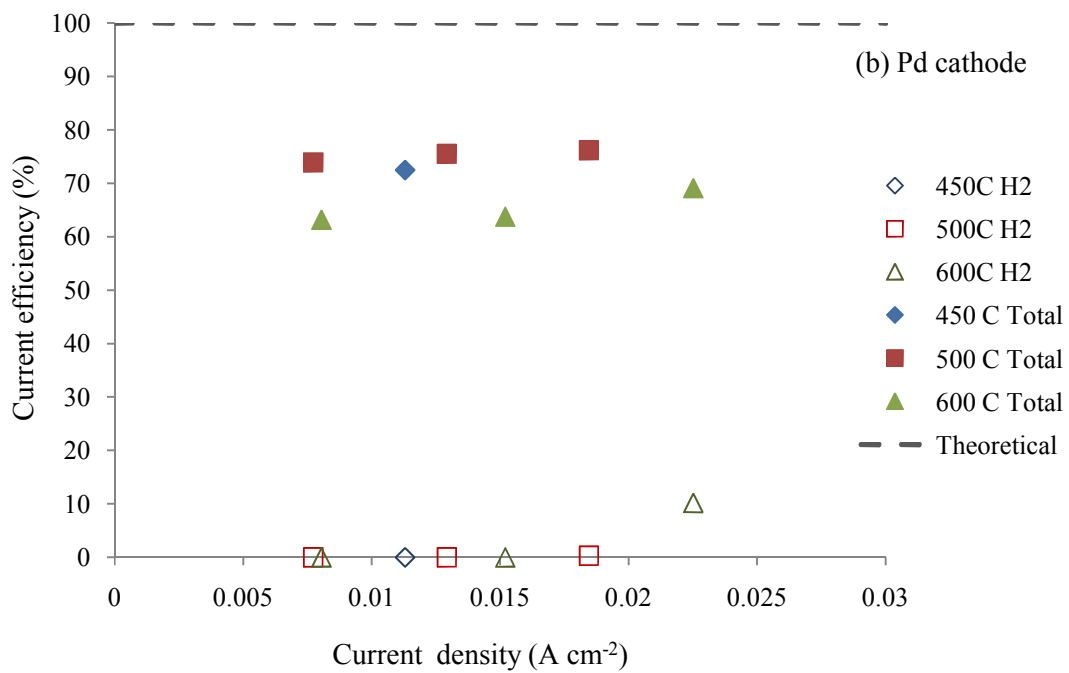
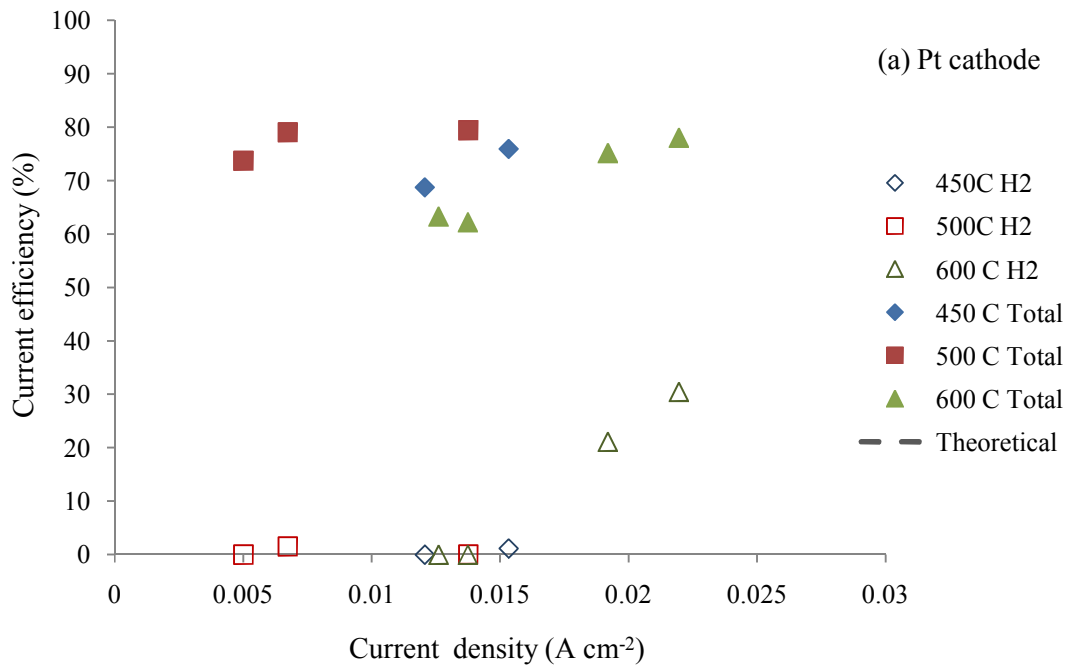


Figure 2.28 H₂ evolution rates at different imposed currents and temperatures (a) cell with Pt cathode, (b) cell with Pd cathode and (c) cell with Au cathode. Dashed lines are theoretical values. Open symbols for data derived from amount of H₂ detected by MS, Closed symbols for total amount of H₂ produced including H₂O formation.



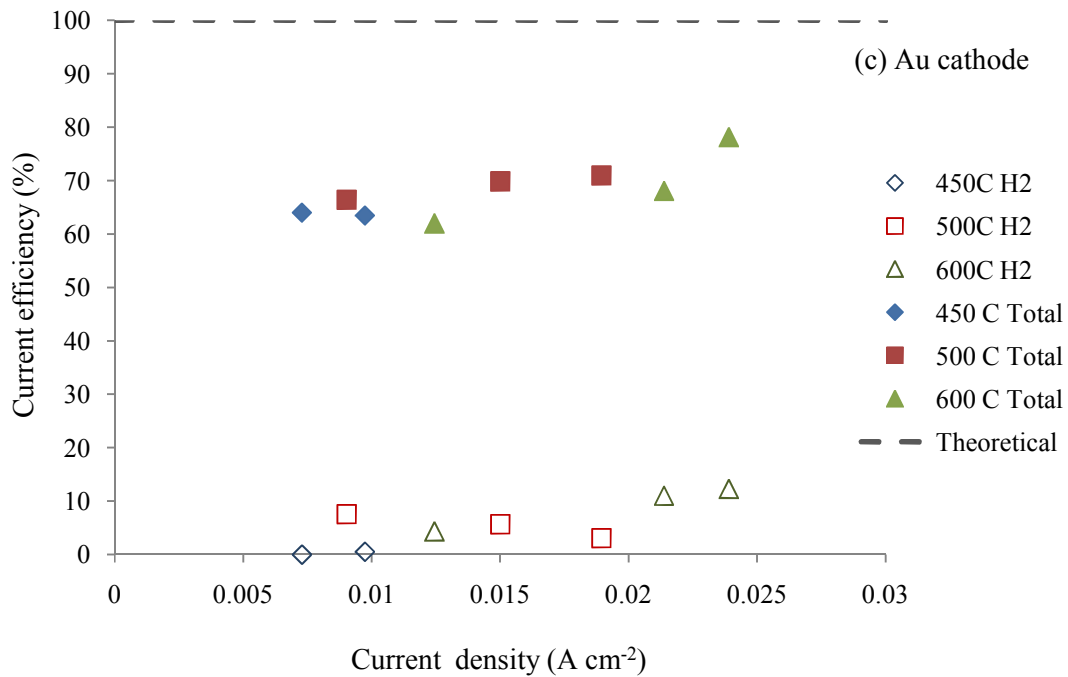


Figure 2.29 Current efficiencies at various temperatures evaluated from H₂ evolution rates (open symbols) and total product formation rates including H₂, H₂O and NH₃ (closed symbols).

2.5 Conclusions

A perovskite proton conducting oxide, $\text{BaCe}_{0.5}\text{Zr}_{0.3}\text{Y}_{0.16}\text{Zn}_{0.04}\text{O}_{3-\delta}$ (BCZYZ), was synthesised via solid state reaction. Sintering conditions and optimum thermal treatment were also determined. The BCZYZ 1 mm-thick pellet with high density (>90%) was attained by sintering at 1300 °C. Electrochemical characterisations of this ceramic electrolyte were performed. Under humidified 5% H_2 at the anode and non-humidified N_2 at the cathode, the performance of the cell is controlled by the diffusion processes that were observed as medium- and low-frequency impedance features. The improvement of cell performance by increasing the contact area between the electrolyte and the electrode proves the importance of the three-phase boundary (TPB) length. The performances derived from cells with metal electrodes (Pt, Au and Pd) are not sufficient for operating in electrolysis mode. High potential is needed to generate enough current for the reactions. The highest ammonia formation rate of $1.4 \times 10^{-9} \text{ mol s}^{-1} \text{ cm}^{-2}$ was obtained from a Pt cathode at 450 °C.

For further work, the cell components need to be improved. The ohmic resistance should be decreased by the reduction of the electrolyte thickness. The electrode component definitely required a greater TPB length.

References

1. A. R. West, Basic solid state chemistry, 2nd edition, John Willey & Sons, West Sussex (1999).
2. C. B. Carter, M. G. Norton, Ceramic materials science and engineering, Springer, New York (2007).
3. R. M. German, P. Suri, S. J. Park, J. Mater. Sci. 44 (2009) 1–39.
4. S. Tao and J. T. S. Irvine, Adv. Mater. 18 (2006) 1581–1584
5. A. Kruth, J. T. S. Irvine, Solid State Ionics 162–163 (2003) 83– 91.
6. F. Krug, T. Schober, Solid State Ionics 92 (1996) 297-302.
7. R. Kirk, D. Othmer, Encyclopedia of Chemical Technology, John Wiley & Sons, New York (1981).
8. E. Barsoukov, J.R. Macdonald, Impedance Spectroscopy; Theory, Experiment, and Applications, 2nd ed., Wiley Interscience Publications (2005).
9. J. T. S. Irvine, D. C. Sinclair, A. R. West, Adv. Mater. 2 (1990) 132-138.
10. X.-Z. Yuan, C. Song, H. Wang, J. Zhang, Electrochemical Impedance Spectroscopy in PEM Fuel Cells: fundamental and applications, Springer-Verlag, London (2010) p. 117.
11. A. J. Bard, L. R. Faulkner, Electrochemical methods: fundamentals and applications, John Wiley & Sons Inc, (2001)

Chapter 3

Fabrication of Thin BCZYZ Ceramic Membrane

3.1 Introduction	88
3.2 A brief overview of tape casting process	90
3.2.1 Tape slurry ingredients	91
3.2.1.1 Solvent	91
3.2.1.2 Dispersants/deflocculants	92
3.2.1.3 Binder	95
3.2.1.4 Plasticizers	96
3.2.2 Tape forming	98
3.2.3 Tape drying	99
3.2.4 Organics burnout	99
3.3 Experimental	101
3.3.1 Powder processing	101
3.3.2 Tape casting process	102
3.3.2.1 Lamination of ceramic green tape	103
3.3.2.2 Thermal decomposition of green tapes	105
3.3.2.3 Sintering support	106
3.3.2.4 Sintered body characterisation	107
3.4 Results and discussion	108
3.4.1 Thermal analysis of green tapes	108
3.4.2 Optimum heating treatment	111
3.4.3 Dense electrolyte layer	112
3.4.3.1 Slurry formulation	112
3.4.3.2 Effect of organic additive: Binder	114
3.4.3.3 Final slurry formulation	116
3.4.3.4 Microstructure of green electrolyte tape surface	116
3.4.3.5 Sintering conditions	118
3.4.3.5.1 Effect of sintering temperature	118
3.4.3.5.2 Thickness of the electrolyte layer	120
3.4.3.5.3 Sintering duration and final microstructure	121
3.4.4 Porous substrate layer	123
3.4.4.1 Porous structure optimisation	124
3.4.4.2 Effect of sintering temperature	125
3.4.4.3 Influence of pore former morphology	127
3.4.4.4 Microstructure of porous green tape surface	130
3.4.4.5 Effect of dispersant and binder contents	132
3.4.4.6 Phase identification of sintered porous BCZYZ layer	135
3.5 Conclusions	138
References	139

3.1 Introduction

The performance of an electrochemical cell is affected by many factors including ohmic losses, activation losses and concentration losses. Ohmic losses are influenced from the ionic and electronic conduction of electrolyte and electrode materials, activation losses are related to reaction kinetics, and concentration losses originate from the transportation of reactants and products in the cell. In high temperature solid oxide fuel cells, concentration losses mainly depend on the microstructure of porous electrodes, while ohmic losses can be limited by decreasing the electrolyte thickness. Losses associated with reaction kinetics can be improved by employing electrode materials with high electrocatalytic activity and by increasing the length of the three-phase boundary (TPB) where the electrochemical reactions take place^[1,2].

By decreasing the thickness of the electrolyte, the mechanical strength of the cell is also decreased. In this scenario, the electrode is used to provide the mechanical strength to the cell instead of the electrolyte, thus affording electrode-supported cells. Ceramic-metallic (cermet) composite electrodes are widely used for supporting thin electrolyte membranes. The presence of electrolyte phase (ceramic) in the electrode composite diminishes the thermal expansion mismatch between the electrode and the electrolyte components, especially when the electrode is reduced from metal oxide to metal in reducing atmospheres. A homogeneous and continuous structure of electrode and electrolyte materials in a porous cermet ensures good adhesion at the electrode-electrolyte interface and permits the conduction of ions, in this case protons, from the electrolyte to the deep parts of the electrode. This extends the TPB length available for the reaction leading to the lowering of polarisation losses^[2,3]. A possible drawback of cermet electrodes arises during sintering, when electrode and electrolyte materials

are mixed and co-sintered at high temperature in order to achieve a cermet framework. Therefore, this method is largely limited to electrode and electrolyte materials that have similar sintering temperatures and show no undesired reactions during high temperature sintering.

Ion impregnation or infiltration is a method for avoiding undesired reactions between electrode and electrolyte materials. Solutions containing salts of the metals that go to make up the desired electrode material are introduced into a well-established porous framework made from the electrolyte material. This method requires much lower firing temperatures compared to the cermet method. In addition, the impregnated electrode tends to deposit on the surface of the electrolyte scaffold, providing a non-random distribution that lowers the amount of electrode material required for good electronic conduction, and ensuring good connections between electrode-electrode, electrolyte-electrolyte and electrode-electrolyte phases^[4].

Tape casting is a method that has been widely used for preparing dense electrolytes and porous electrolyte frameworks for ion impregnation. The porosity of the porous layer can be conveniently controlled by the amount and type of pore formers. Importantly, good adhesion between dense and porous layer is also readily accessible using tape casting^[4-6].

In this study, the tape casting process was used to fabricate a 3-layer cell by sandwiching a dense electrolyte layer of BCZYZ with two porous layers made from the same material. The porous-dense-porous geometry is similar to a typical solid oxide fuel cell except for the presence of electrode materials. Electrocatalytic materials for anode and cathode were introduced into these porous frameworks by ion impregnation method, and this aspect of the study is considered in the later Chapters. In this Chapter, only the fabrication procedure of tape cast porous and dense films of

BCZYZ is considered. The final product should possess adequate open porosity within the porous layers, a dense and crack-free electrolyte layer, and good adhesion between layers.

3.2 A brief overview of tape casting process

Tape casting is a well known process for fabricating thin and flat sheets/films of ceramic and metallic materials. Large-area films with controlled thickness can be easily produced. The flexibility of unfired tapes allows them to be punched with holes, cut into various shapes or assembled into multilayered packages^[7]. Using this process, a multi-layer ceramic can be prepared by lamination and co-sintered at the same firing temperature. Therefore, it is possible to prepare a multi-layer ceramic composed of layers having different porosities. Porous ceramics can be generated by the addition of pore formers that may or may not be pyrolysed. The former type combusts during high-temperature treatment, while the latter type remains in the fired tape and needs a separate step for removing it e.g. acid leaching for NiO pore former^[8].

Slurry preparation usually involves two steps. The first step is called powder dispersion, when the ceramic powder is mixed with a dispersant in a solvent to create well-dispersed suspension. In the second step, binder is added to the suspension to ensure the cohesion between ceramic particles. In this step, some plasticizers are incorporated with the binder in order to increase the plasticity of the slurry before casting into desired tape form.

3.2.1 Tape slurry ingredients

In order to understand how ceramic particles and pore formers can be stabilised in a cast tape, brief details of tape slurry components are given below.

3.2.1.1 Solvent

The solvent plays an important role in providing fluidity to the powder by dissolving additives and allowing them to uniformly disperse throughout the powder^[9]. Therefore, the choice of solvent is based on the choice of binder and other additives^[7]. In tape casting, nonaqueous solvents are commonly employed due to their low latent heat of evaporation and low surface tension compared with water. Following the previous work of Irvine and co-workers^[10], a binary solvent system of methyl ethyl ketone (MEK)/ethanol was used here. Theoretically, a binary or ternary solvent may help to extend the solubility range for the different additives used in the tape slurry. At the same time, the physical properties of the solvent mixture, such as the evaporation rate, is also modified^[7,9]. For example, a tape casting slurry that contains only MEK may provide a quick drying cast tape due to the low heat of evaporation of MEK. However, the obtained cast tape tends to be inhomogeneous as a result of the drying out of the MEK solvent during the casting step. In addition, it is possible to create a solvent gradient within the cast tape due to the formation of a dried surface (a so-called ‘skin’) that blocks the evaporation of the solvent underneath it. By adding a solvent with higher heat of evaporation, such as ethanol, the evaporation rate of the solvent mixture decreases and allows the slurry to be processed and dried

homogeneously. Some physical and dielectric properties of ethanol and MEK are shown in Table 3.1.

Table 3.1 Physical and dielectric properties of ethanol and methyl ethyl ketone^[11].

Solvent	Boiling point (°C)	Dielectric constant at 293.2 K	Heat of evaporation (kJ/mol)
Ethanol	78	25.3	38.6
MEK	80	18.5	31.3

3.2.1.2 Dispersants/deflocculants

A dispersant/deflocculant is commonly used in the first step of tape casting. It helps break down soft agglomerates in the starting powder by preventing the particles from re-agglomerating. The dispersant/deflocculant works by holding dispersed particles in suspension and allowing the solvent to form a separating layer between particles, thus leading to a stable dispersed state. A well-dispersed suspension is required prior to the polymeric binder addition step. If agglomerates are present, the binder will wrap the whole group of particles instead of individual particles, making it difficult to destroy any remaining agglomerates (so-called zipper bag theory)^[7]. Particle agglomerates covered with binder will affect the density of sintered tapes by trapped air inside and uneven distribution of particles^[7].

Particle size and the attractive force (i.e van der Waal's force) between ceramic particles influence dispersion. If the particle size is too large or the attractive force is

too strong, undesired sedimentation of particles tends to happen easily. Consequently, a method for creating repulsive force between particles is required to overcome the attractive force. Some repulsive forces commonly found in a suspension are briefly reviewed.

1. Electrostatic forces

Particles can be stabilised in a suspension by employing a repulsive force from the charge developed at the solid-liquid interface. This charge covers the particle's surface and leads to a diffuse electrical double layer. The strength of this interparticle force relies on the surface potential induced on the interacting particles and the dielectric properties of the surrounding media^[12]. Details about DLVO theory (named after Derjaguin and Landau, Verwey and Overbeek) describing this interaction have been published elsewhere^[13]. In general, this type of interaction is significant in aqueous systems, although it is also possible to have electrostatic forces in non-aqueous solvent^[14].

2. Steric forces

Steric stabilisation created by the adsorption of organic molecules, normally as uncharged polymers, on the surface of a ceramic particle can be used in both aqueous and non-aqueous systems. These adsorbed molecules form an adlayer on the particle's surface and prevent particles bridging to one another at a separation distance less than twice that of the adlayer thickness^[12]. This coating adlayer must be stable against particle collisions during processing. Apart from the effect of coating a polymer on the particle's surface, the free polymer in the solvent also imparts steric stabilisation. This free polymer disperses in the solvent and prevents collisions between particles,

so-called depletion stabilisation. If the repulsion is not strong enough, flocculation may happen instead. In case the amount of polymer is not enough to cover the entire surface of the particles, the polymer may act as a bridge and bring particles close to each other instead. This type of flocculation is referred to as bridging flocculation. In another case, free polymer molecules between particles are excluded from the gap between particles, creating a concentration gradient and this generates a type of osmotic effect between particles. This effect is comparable to an attractive force and causes the flocculation called depletion flocculation^[9]. Figure 3.1 summarises steric forces and their influence on particle dispersion.

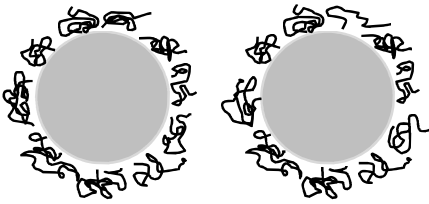
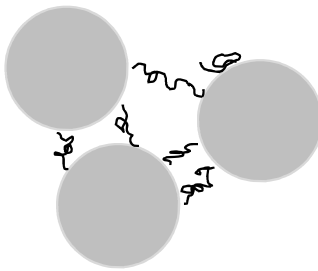
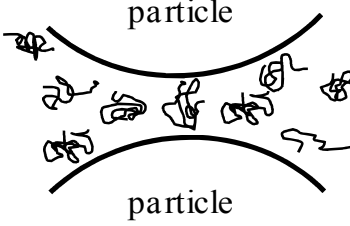
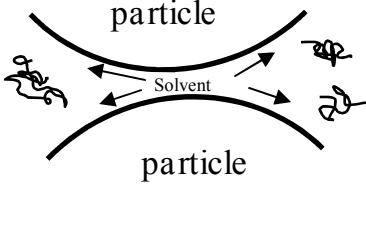
	Repulsion	Attraction
Adsorbing polymer	 <p>Steric stabilisation</p>	 <p>Bridging flocculation</p>
Nonadsorbing polymer	 <p>Depletion stabilisation</p>	 <p>Depletion flocculation</p>

Figure 3.1 Schematic illustration of steric forces occurring in the presence of uncharged polymer chains^[9].

In summary, the roles of a dispersant include:

- lowering the viscosity of a slurry and therefore allowing an increase in the solid concentration
- incorporating with solvent to break up aggregates and stabilise the primary particles by holding a fluid layer between them
- improving homogeneity of the suspension
- preparing the particles for addition of the binder and allowing the binder to attach to each particle separately

In organic solvent-based systems, the dispersion mechanism of most of the dispersants used is steric stabilisation. The dispersant used here was a polyphosphate ester which works very well in the MEK/EtOH system^[7,15]. This polyphosphate ester works by attaching one part of its chain molecule to the particle surface while the rest of its molecule interacts with the solvent. The barrier formed by the “tail” in the solvent prohibits particle-particle contact.

3.2.1.3 Binder

Binder is an important additive for the tape casting process. The binder function is to hold the entire chemical system together. It distributes strength, flexibility, laminatability, durability and smoothness to the green tape by encapsulating the powder in its continuous polymeric resin^[7]. Long chain polymers are usually employed as binders. Generally, a binder is introduced into the tape slurry after the dispersion step to avoid competitive adsorption with the dispersant on the particle's surface. In addition, the presence of high molecular weight binder increases the

viscosity of the slurry, which would not be suitable for particle dispersion step. The selection of a binder depends on the other components in the system. Factors such as solubility in the solvent, compatibility with the dispersant, burnout characteristics, glass transition temperature, viscosity, ash residue and cost are usually taken into account^[7,9]. Since the binder plays an important role in binding particles together, the amount of binder in a cast tape is considerably greater than the other additives. The molecular weight of the binder is also important. A polymer with lower molecular weight provides lower viscosity, high solid loading but lowers the mechanical strength of the cast tape. Higher molecular weight polymers provide high binding strength. However, glass transition temperature (T_g) also increases when molecular weight increases. The T_g is the temperature at which the polymer changes from a glassy state to a rubbery state. Green tapes containing a higher T_g binder will have higher strength, however lack flexibility.

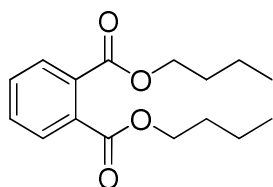
In this study, poly(vinyl butyral) (PVB) with molecular weight range of 40,000-70,000 g mol^{-1} was selected as a binder. The chemical structure of PVB is shown in Figure 3.2c. Since PVB has a T_g higher than room temperature ($T_g = 72\text{-}78\text{ }^\circ\text{C}$), this renders green tapes made using PVB alone brittle and rigid. In order to improve the plasticity of the cast tape, plasticizers are needed.

3.2.1.4 Plasticizers

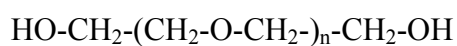
The role of plasticizers in tape slurries is to soften the binder in the dry state and improve flexibility of the green tape. These plasticizers are comprised of low molecular weight organic substances that can soften the binder effect by dissolving

homogeneously with the binder and inserting their small molecules inside the macromolecular network formed by the binder. This restrains the intermolecular interaction between adjacent polymeric chains of the binder, thereby causing an increase in the mobility of the chains that leads to a decrease in mechanical strength of the cast tape. However, the influence of plasticizer on the strength of the cast tape depends on the amount of organic phase and the pore volume of the tape^[16]. Two plasticizers suitable for the PVB binder used here are polyethylene glycol (PEG) and dibutyl phthalate (DBP), the structures of which are shown in Figure 3.2.

(a)



(b)



(c)

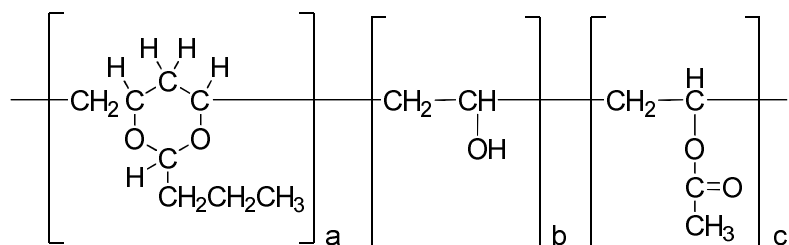


Figure 3.2 Chemical structures of (a) DBP, (b) PEG and (c) PVB^[17].

3.2.2 Tape forming

A typical tape caster is shown in Figure 3.3. It contains a slurry container (also called a reservoir), a stationary doctor blade and a moving carrier. In the casting process, the doctor blade is firstly adjusted to provide a gap between the blade and the carrier film. The slurry is then poured into a reservoir behind the doctor blade. When the carrier film is moving, the slurry will be pulled through the gap underneath the doctor blade and cast into a tape. In addition to gap height, the wet thickness of cast tapes is also influenced by viscosity of the slurry, speed of the carrier motion and level of slurry in the reservoir^[7].

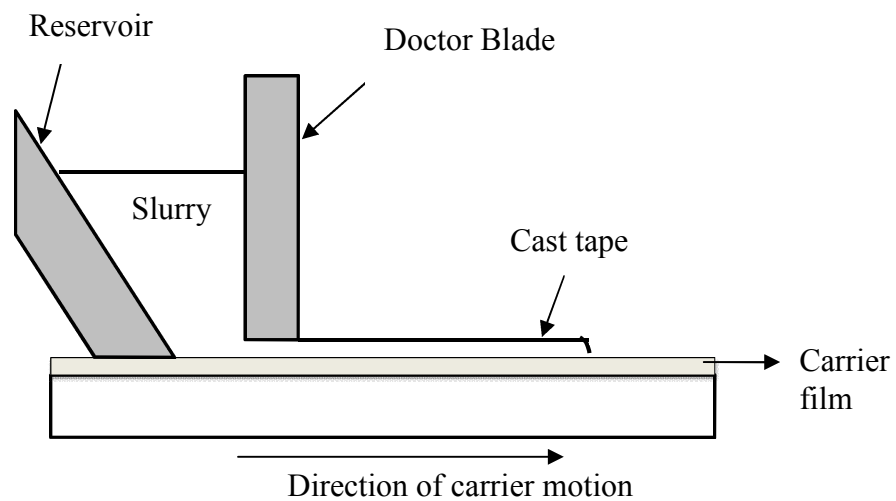


Figure.3.3 Schematic of a tape casting machine.

3.2.3 Tape drying

Once the tape has been cast, the drying process is started. The drying happens mainly through the surface of the cast tape due to its fine thickness and the presence of an impermeable carrier on the bottom. Drying process mechanisms mainly relate to the rate of capillary migration of solvent from the surface and the rate of solvent diffusion through the tape up to the surface, where the latter is much slower than the former.

The rate of surface evaporation is governed by the latent heat of evaporation of the solvent and the atmosphere above the tape surface. On the other hand, the rate of solvent diffusion through the green tape body is quite slow and limited by the body itself. All tape components i.e. particles, binder and plasticizers can retard the motion of solvent to the surface. The retarding effect becomes more severe as the tape shrinks with drying. This leads to some solvent remaining at the cast tape/carrier interface, although it is important to keep the solvent concentration throughout the tape as uniform as possible. During the drying stage, stresses from shrinkage can build up in the tape. Inappropriate drying rates can cause problems like cracks or a drying crust or skin on the tape surface^[7].

3.2.4 Organics burnout

In cast tapes, solid particles are held together by a significant amount of organic additives (up to 20 wt%). These organics should be completely removed from the green tape prior to ceramic sintering. Although there are many strategies to remove the organics, the most convenient method for this ceramic fabrication is thermal debinding. All organic additives chosen should be able to burn out under the same

atmosphere for sintering the desired ceramic and they must be completely removed at lower temperature than the sintering temperature of the ceramic. Organics burnout is a crucial step and it can affect the quality of the sintered tape, especially for multilayered-cast tapes. Cracks and large voids can be created in this step by the fast escape of gases generated from polymer decomposition. Both chemical and physical factors of the organics influence the burnout process. The chemistry of the organics i.e. molecular weight and interaction between them determines the decomposition temperature and the decomposition products. In addition, physical factors such as heat transfer into the body of the tape and the escape of decomposition products are involved in the decomposition process. These changes may cause problems for the quality of the final tape such as delamination, cracking or distortion when using inappropriate heat treatment. Usually, a slow heating rate (less than 1 °C/min) is used during decomposition and a fast heating rate may be used after the decomposition has been completed^[9]. Information about the thermal decomposition of organic additives and pore formers is usually obtained via thermal gravimetric analysis (TGA).

3.3 Experimental

3.3.1 Powder processing

According to Chapter 2, the starting powder used for preparing tape slurries was synthesised by solid-state reaction. Stoichiometric amounts of analytical grade BaCO_3 , CeO_2 , ZrO_2 , and Y_2O_3 were milled together in acetone for 2 hours using a planetary micro mill (Pulverisette 7, Fritsch). After acetone evaporation, the mixed powder was calcined in air at $1250\text{ }^\circ\text{C}$ for 4 h. In the final step, a stoichiometric amount of ZnO was milled with the as-calcined powder in acetone for 2 hours. The resulting powder was called BCZYZnO powder. The phase identification of this powder was determined by a powder X-ray diffractometer (see section 3.3.2.4). The XRD pattern of this powder shown in Figure 3.4 indicated that the powder contained mixed phases of barium cerate and barium zirconate (ICDD PDF No. 22-74 and 6-399, respectively)^[18,19].

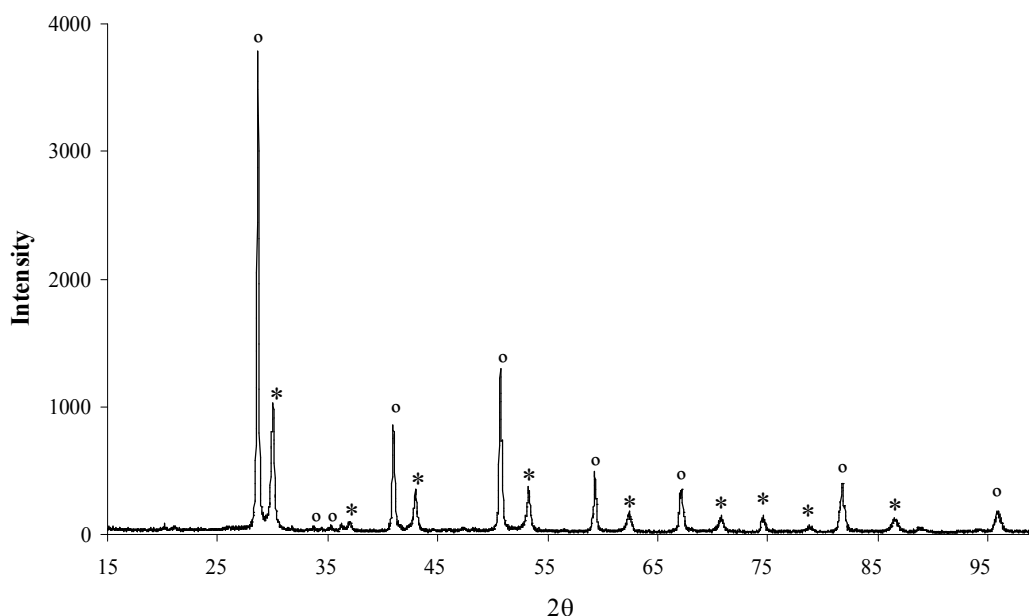


Figure 3.4 XRD pattern of BCZYZnO powder (° : BaCeO_3 peaks, * : BaZrO_3 peaks).

3.3.2 Tape casting process

The procedure for preparing tape casting slurries was based on a process for YSZ tapes that had been developed previously by the group of Prof Irvine and co-workers^[10]. The slurry was prepared by dissolving a dispersant (Triton QS-44, Sigma-Aldrich Ltd) with the solvent mixture of methyl ethyl ketone (MEK) and ethanol (60/40 % by weight) in a 125 cm³ Nalgene bottle (Sigma Ltd) before adding the BCZYZnO powder and grinding media (18x zirconia balls each of 8.8 mm diameter). The mixture was then milled for 18 h on a home-made ball mill with a speed of 160 rpm. This step allowed some soft agglomerates to be broken down and the powder particles to be mixed and dispersed homogeneously throughout the solvent. In the next step, PEG (Mn = 285-315, Sigma-Aldrich) and DBP (Fisher scientific) plasticizers and PVB (Butvar® B-98, Mw = 40,000-70,000, Sigma-Aldrich) binder were added to the dispersed mixture. Plasticizers with short chain polymer and low molecular weight should be added into the mixture before the long chain binder. This is to ensure that the plasticizers are fully dissolved in the solvent and ready to interact with the binder. Once the binder had contacted with the solvent in the mixture, it tended to agglomerate into lumps. Thus, the bottle was then vigorously shaken on a vibratory mixer for 20 min to deagglomerate binder lumps and to help dissolve the binder into the mixture. Most of the binder was dissolved at this stage but the mixing process was still continued on the ball mill for another 4 h using 100 rpm speed. In the last step, the homogeneous slurry was sieved through a piece of nylon net in order to remove the zirconia balls. The slurry in the new container was then rotated slowly on the ball mill for at least 18 h at a speed of 26 rpm for de-aeration. The slurry for porous BCZYZnO cast tape was prepared by the same procedure as mentioned above except that a certain amount of BCZYZnO powder was replaced by pore formers. The

pore formers used in this experiment were graphite (325 mesh, Alfa Aesar) and glassy carbon (10-20 μm , Alfa Aesar). The amounts of graphite and glassy carbon added to the slurry were varied in order to obtain optimised open porosity in the porous layer after sintering.

A TTC-1000 (Richard E Mistler Inc) tape caster was used for casting. The design of this tape caster is similar to the depiction in Figure. 3.1. The slurry was poured into a single 4 inch doctor blade reservoir which was set on a carrier film (silicon-coated Mylar). The gap height between the blade and the carrier film was kept at 0.012 cm (120 μm) for electrolyte tapes and at 0.030 cm (300 μm) for porous tapes. The slurry was cast by moving the carrier film at approximately 42 cm s^{-1} . The cast tapes were left to dry in air at room temperature for 30 min. The thickness of green tapes was ~ 70 μm for electrolyte tapes and ~ 280 μm for porous tapes.

3.3.2.1 Lamination of ceramic green tape

Although a thin electrolyte will provide low ohmic resistance, the mechanical strength of the cell also decreases. Therefore it is necessary to compromise between reasonable ohmic resistance and strength of cell for handling. One layer of BCZYZnO electrolyte cast tape provided about 50 μm of ceramic electrolyte thickness after sintering. This was quite fragile and had a strongly curling edge. Theoretically, the mechanical strength of the cell can be improved by increasing the thickness of the electrode part. Therefore porous tapes were in the first instance laminated in an attempt to increase the mechanical strength of the cell. Unfortunately, the results after several tests revealed that the mechanical strength of the cell mainly came from the dense part. There was no significant improvement in the mechanical strength when the thickness

of porous layers was increased and the sintered cell was still not flat. Consequently, the thickness of electrolyte tape had to be increased.

The lamination of green electrolyte tapes was performed with or without additional heat, depending on the condition of the green tape surface. In most cases, the green tape surface was covered with a thin film of residual solvent and the green tape was quite soft and sticky. This made the green tapes easily attach to each other and only a hand-rubber roller was needed to ensure adhesion. In some cases, the green tape surface was dried out after storage but the green tape body still had good flexibility. The tapes were then laminated using additional heat of ~ 50 °C generated using a household iron. The laminated tape was held at temperature for around 10 sec without additional pressure except the weight of the iron. The lamination process and tape configuration is shown in Figure 3.5.

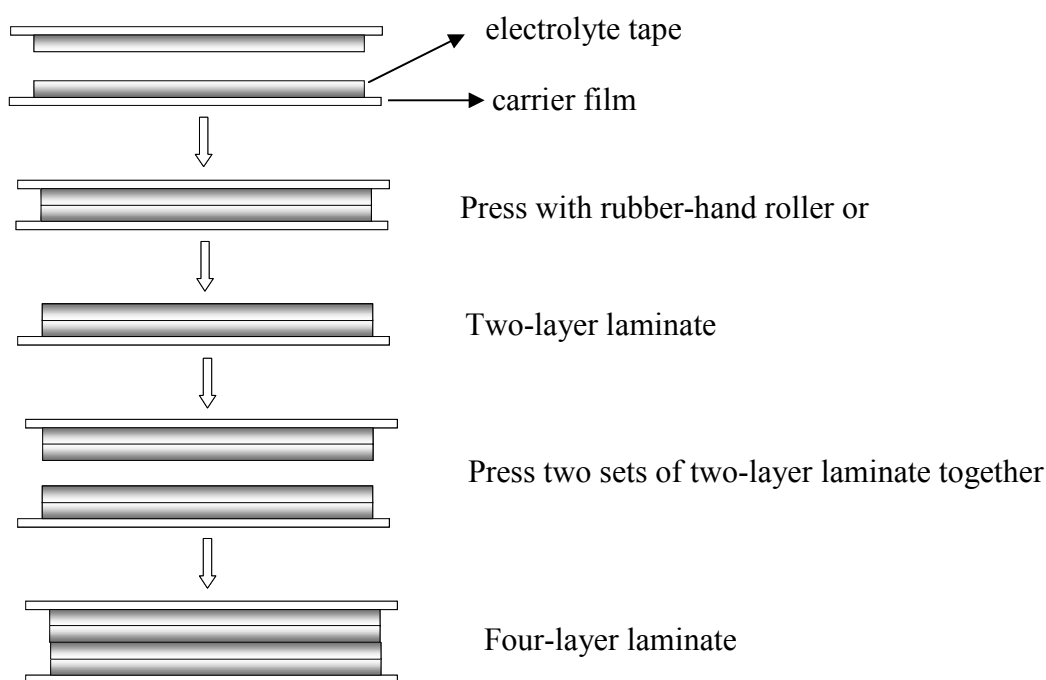


Figure 3.5 Green electrolyte tape lamination.

In the final step, the laminated electrolyte or porous tapes were punched into circular discs using steel punches. Two circular discs of porous BCZYZnO tape with one disc smaller than the electrolyte were then attached on both sides of the electrolyte disc. A schematic of a finished disc is shown in Figure 3.6. The porous layer with the same diameter of the electrolyte acts as a support for the electrolyte while the smaller one prevents cross-contaminations between the two electrode materials during the impregnation process.

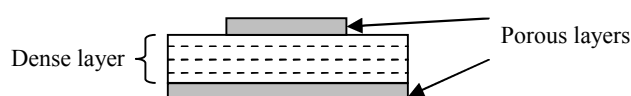


Figure 3.6 Geometric pattern of a three-layer green tape stack.

3.3.2.2 Thermal decomposition of green tapes

The thermal decompositions of organic components and pore formers were investigated using a Thermogravimetric Analyzer model TG 209 (NETZSCH-Geratebau GmbH, Germany). The sample weight of the dense or porous green tapes was about 10 mg in each experiment. All samples were tested in air flowed at a rate of 25 mL min⁻¹. The samples were heated up to 900 °C at a rate of 1 °C min⁻¹ then cooled down to room temperature with a cooling rate of 40 °C min⁻¹. Changes in the weight of samples under heating were recorded continuously.

3.3.2.3 Sintering support

As mentioned in Chapter 2, BCZYF was found to react with the alumina support at sintering temperature range of 1300-1400 °C. Therefore, a layer of sintered BCZYF powder was applied between the green tapes and the alumina support in order to minimise undesired reactions. In this case, the sintered powder was used for other purposes. Firstly, this powder helps diminish adhesion between green tapes and alumina support which causes deformation in final products. The powder assisted the shrinkage of green tapes, allowing them to shrink freely in x and y dimensions without surface friction with the alumina surface. Secondly, the gases generated by polymer and pore former combustion quickly escaped through the voids within the powder layer. Although some powder attached onto the sintered porous layer, removal was not difficult.

The environment in the sintering furnace was found to affect the quality of sintered products. The furnace used in this experiment was a chamber furnace (Carbolite, UK) with maximum operating temperature of 1400 °C. The silicon carbide heating elements are located on both sides of the chamber. The samples were placed between those elements and close to the lower elements. It was possible that the samples received heat directly radiated from the elements. As a result, the samples still had a distorted body after sintering. Sample flatness was improved by placing two sets of alumina plates and thin furnace bricks between the samples and heating elements, as shown in Figure 3.7.



Figure 3.7 Setup inside furnace chamber for sintering BCZYZnO green tapes.

3.3.2.4 Sintered body characterisation

Due to co-sintering of the porous layer with the dense layer, the porosity of the porous layer was considered from the geometry of a two-layer disc. After deducting the mass of the dense layer, the porosity of the porous layer can be obtained. The thickness of both dense and porous layers was evaluated from SEM images. Note that this measurement was applied to the specimen with reasonable flatness.

Phase purities of starting powder and sintered ceramic were examined by a Philips PW 1710 diffractometer operating in reflection mode using $\text{CuK}\alpha$ radiation (see Chapter 2 for details). The XRD data were collected using a continuous scan with a 2θ range of $15\text{-}100^\circ$, 0.02° step size and 1°min^{-1} scan rate.

SEM analysis (details in Chapter 2) was carried out on a JEOL 5600 scanning electron microscope using an acceleration voltage between 5kV and 20kV. Microstructures of both green and sintered tapes were investigated. For non-

conductive samples like green tapes or calcined-BCZYZnO powder, the samples needed to be coated by a thin layer of evaporated gold. In these cases samples were mounted onto specimen holders with silver paint (Agar Scientific Ltd) prior to gold evaporation using a home-made machine. For conductive samples such as graphite and glassy carbon, the samples were mounted onto specimen holders directly with electrically conductive carbon adhesive discs (Agar Scientific Ltd). For the sintered BCZYZ membrane, the cross-section microstructure was taken from fracture surface of the ceramic membrane without the need for gold coating.

3.4 Results and discussion

3.4.1 Thermal analysis of green tapes

The thermal decomposition of organic components and pore formers in green electrolyte and porous tapes prepared from the slurry formulations shown in Table 3.2 were studied. TG curves of those cast tapes are shown in Figure 3.8. In green electrolyte tapes, there are three apparent mass change regions. The first region with a small mass loss (~5%), starting from room temperature to around 80 °C, corresponded to evaporation of residual solvent in the matrix. According to the TGA data of each organic additive from Jones^[20], the decomposition temperatures of the two plasticizers used, DBP and PEG, start from 120 °C and 140 °C, respectively. The long-chain binder starts to decompose at the higher temperature of 220 °C. The initial burnout temperature of the dispersant is between those of the plasticizers and the binder. Only a small amount of the dispersant was used in the green tape (~1 wt%), and so it was quite difficult to notice. The organics in green electrolyte tapes started to decompose at 120 °C and were completely removed by 420 °C. The total mass loss was around 23%, which was in agreement with the amount of organic content of the green electrolyte tape formulation as shown in Table 3.2.

In green porous tapes, weight loss patterns were more complicated however were grouped into three main regions. Unlike the green electrolyte tapes, a negligible amount of solvent remained in the porous green tapes. This observation is consistent with the appearance of those tapes. The green electrolyte tape was quite flexible and a small amount of solvent was readily apparent on its surface, while green porous tapes

were much drier and stiffer due to high solid loading. The decomposition temperature for organic additives in porous tapes began at 110 °C and ended at around 400 °C. The last region, which was not present for green electrolyte tapes, was obviously due to the loss from the combustion of carbon pore formers. The different kinds of pore former provided different combustion temperatures. Glassy carbon (GIC) started to burn out earlier in the heating cycle (410 °C) compared to graphite (Gra) (500 °C). This difference in combustion temperatures could have been a result of the different particle size and shape of these pore formers. The SEM images in Figure 3.9 exhibit spherical particles of glassy carbon and plate-like particles of graphite. By mixing 10 wt% GIC into 40 wt% Gra, the initial burnout temperature shifted to lower temperature. It is likely that GIC with lower ignition temperature induced the graphite particles to burnout at a lower temperature. However, combustion in mixed pore formers still completed at the same temperature with 50 wt% graphite tape at 680 °C.

Table 3.2 Formulations of green tapes for thermogravimetric analysis.

Compositions		Formulations (g)			
		Electrolyte	50GIC	50Gra	40Gra10GIC
BCZYZnO powder		15.000	7.500	7.500	7.500
Pore formers	Graphite	-	-	7.500	6.000
	Glassy Carbon	-	7.500	-	1.500
Triton QS-44		0.142	0.112	0.100	0.246
PEG		1.208	1.044	1.395	1.412
DBP		1.007	1.004	1.117	1.071
Butvar (PVB)		1.800	2.500	1.680	2.000
Solvent		6.876	10.004	15.056	12.038

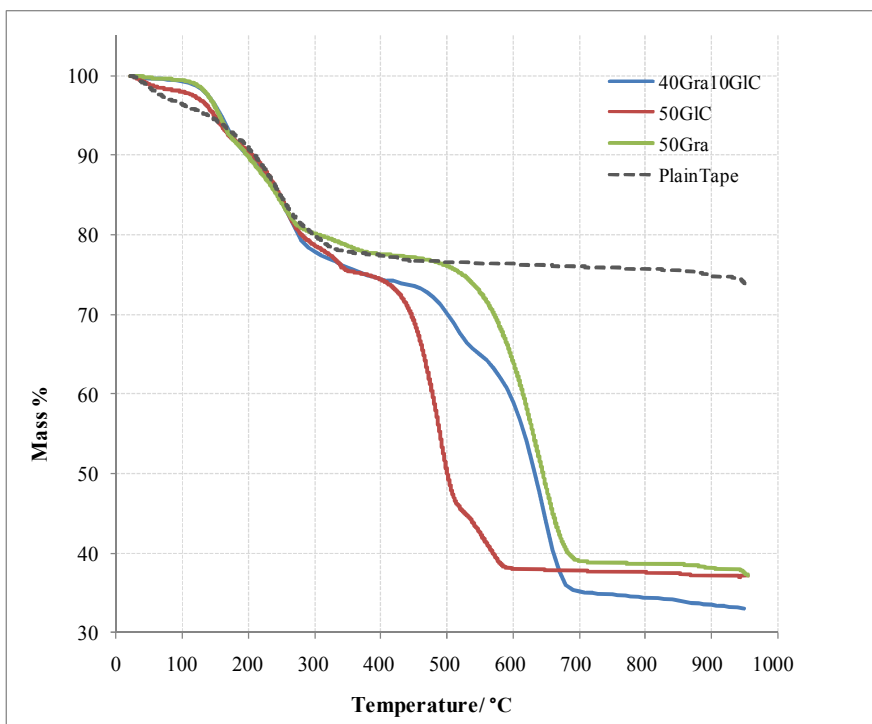


Figure 3.8 TG curves of green electrolyte and porous tapes with various pore former contents (50GIC: 50wt% glassy carbon, 50Gra: 50wt% graphite, 40Gra10GIC: 40wt% graphite+10wt% glassy carbon) at $1\text{ }^{\circ}\text{C min}^{-1}$ in air with flowing rate of 25 mL min^{-1} .

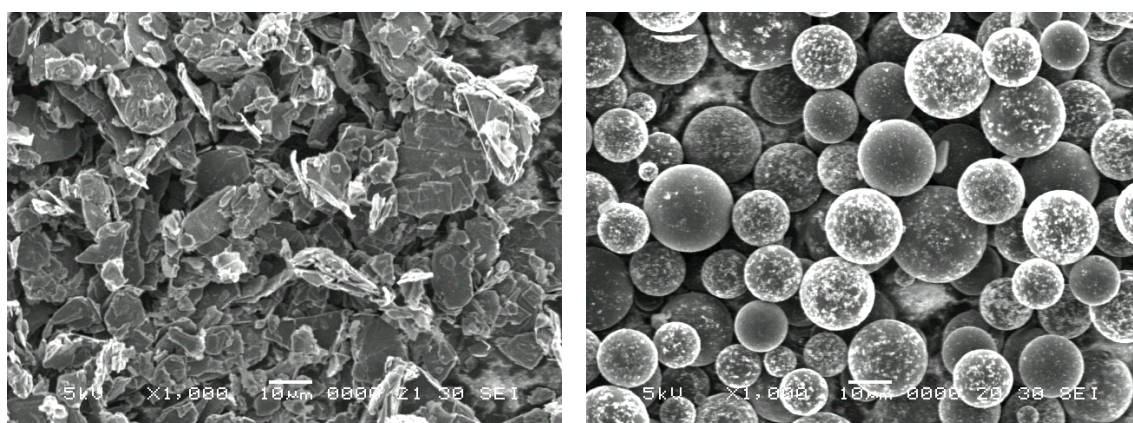


Figure 3.9 Microstructures of (a) graphite and (b) glassy carbon pore formers.

3.4.2 Optimum heating treatment

The heating rates for heat treatment were studied in order to obtain high density electrolyte layers and good adhesion between layers.

During the first heating step, organic additives start to deform and decompose. In order to avoid warping and edge curling, the heating rate needs to be slow. For example, samples with the heating rate of $1\text{ }^{\circ}\text{C min}^{-1}$ still revealed those problems. Hence, the most suitable heating rate for this first step was found to be $0.5\text{ }^{\circ}\text{C min}^{-1}$. Green tapes were heated up using this rate to $950\text{ }^{\circ}\text{C}$ in order to ensure that all organic additives and carbon pore formers had been completely burned out. After the organics burnout step, the tapes were heated up to the ceramic sintering temperature with a similar heat treatment as used for sintering the 1 mm thick BCZYZ pellet in Chapter 2. The optimum heat treatment for the BCZYZnO tape is shown in Figure 3.10.

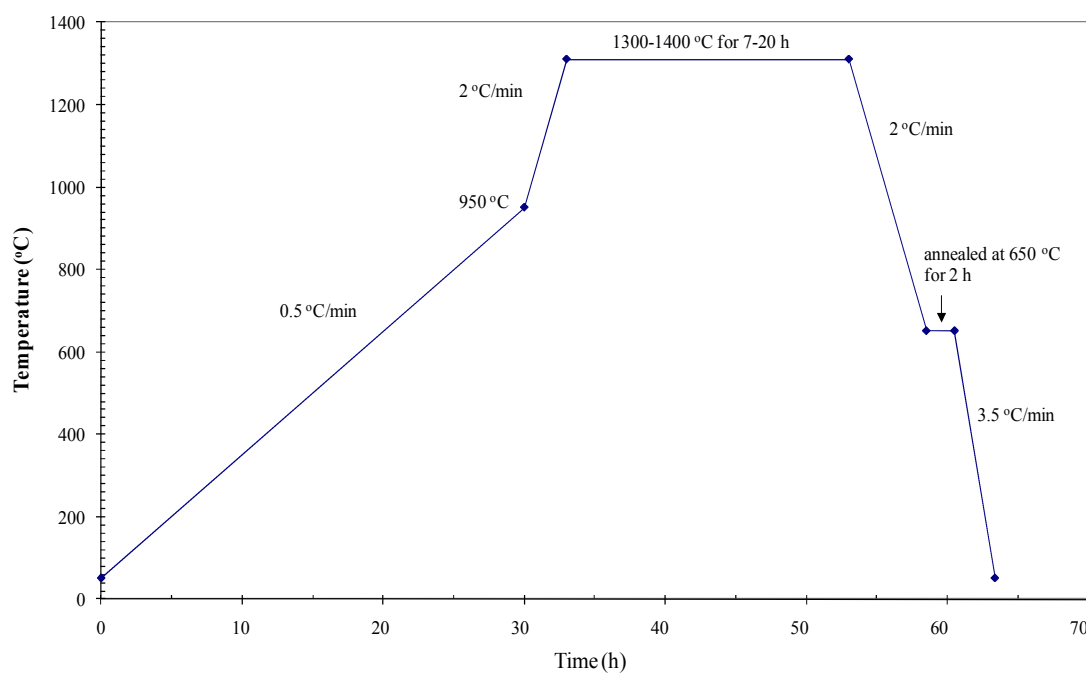


Figure 3.10 Optimum sintering treatments for laminated tapes.

3.4.3 Dense electrolyte layer

3.4.3.1 Slurry formulation

A high density green cast tape is required for sintering a high density electrolyte ceramic membrane. The proper amount of organic additives is a key to success. A good green electrolyte cast tape should have high bulk green density, smooth surface, good flexibility and laminatability. As mentioned before, the formulations for both electrolyte and porous layers were based on previous formulations reported by Jones^[20]. However, the difference in physical properties of the starting powder here required a few adjustments to the final formulation. The starting formulation for the electrolyte slurry and some modified formulations which were used in this experiment are summarised in Table 3.3.

Table 3.3 Starting formulation and modified formulations for BCZYZnO electrolyte slurries.

Chemicals	Formulations			
	(g)			
	As-started	A	B	Final
BCZYZnO	15.000	15.000	15.000	15.000
Triton QS-44	0.097	0.100	0.107	0.115
PEG	1.215	1.184	1.262	1.223
DBP	1.095	1.004	1.042	1.027
Butvar (PVB)	1.680	1.680	2.000	1.800
Solvent	7.000	6.454	7.075	6.850

All the electrolyte slurries prepared in this study showed a consistent homogeneous texture. By using the same formulation which was used for the YSZ powder, the starting slurry had quite low viscosity. This may have been because the surface area of the BCZYZnO powder ($1.893 \text{ m}^2 \text{ g}^{-1}$) was much lower than that of the YSZ powder ($7 \text{ m}^2 \text{ g}^{-1}$). Consequently, a highly porous sintered body was obtained from this slurry. By decreasing the amount of solvent, the viscosity of the slurry was increased, although the porosity of the sintered tape was still high. The SEM images of dense BCZYZ layers from as-started and formulation A are shown in Figure 3.11.

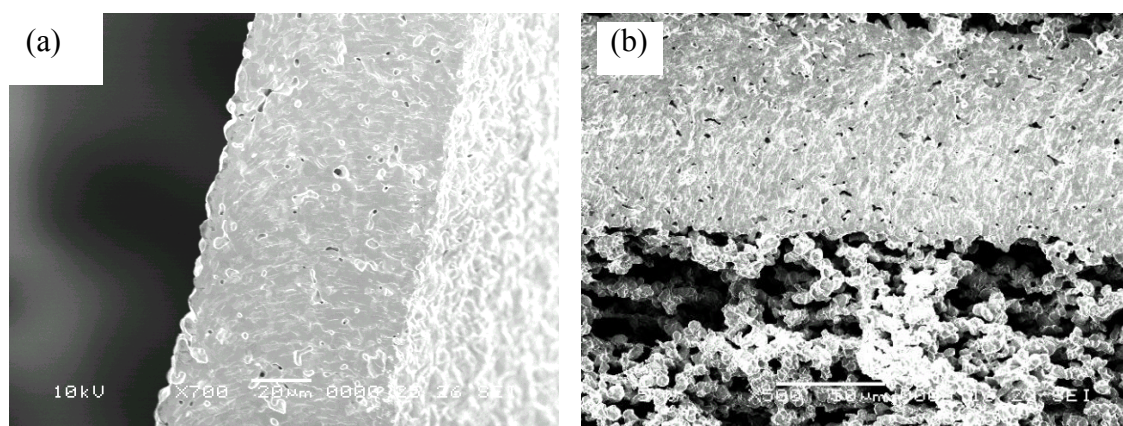


Figure 3.11 SEM images of cross section of dense BCZYZ layers from (a) as-started and (b) formulation A. The samples were sintered under similar sintering treatment at $1300 \text{ }^\circ\text{C}$ for 2 h and 7 h, respectively.

3.4.3.2 Effect of organic additive: Binder

In the tape casting process, the binder is the most important processing additive of the system, ensuring cohesion of the ceramic powder. In an attempt to raise the density, the amount of PVB binder was increased from 1.68 g to 2.00 g for 15 g of ceramic powder. Other additives were kept constant except that the amount of solvent was adjusted to allow the complete dissolution of the binder and homogeneity of the slurry. The results of samples with different binder contents are shown in Figure 3.12.

By increasing the amount of binder to 2.00 g, the pores seemed to be smaller and the number of pores was seemingly higher. However, the even distribution of pores in the microstructure of the sample with 2.00 g binder was a sign of an increase in the homogeneity caused by the additional binder. The small pores could form during the organic burnout step because of the excess of organic polymer presented.

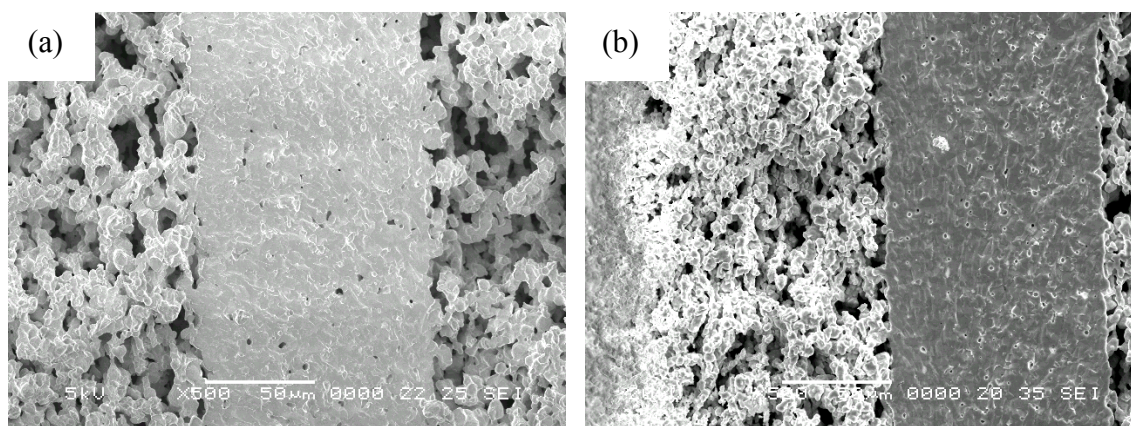


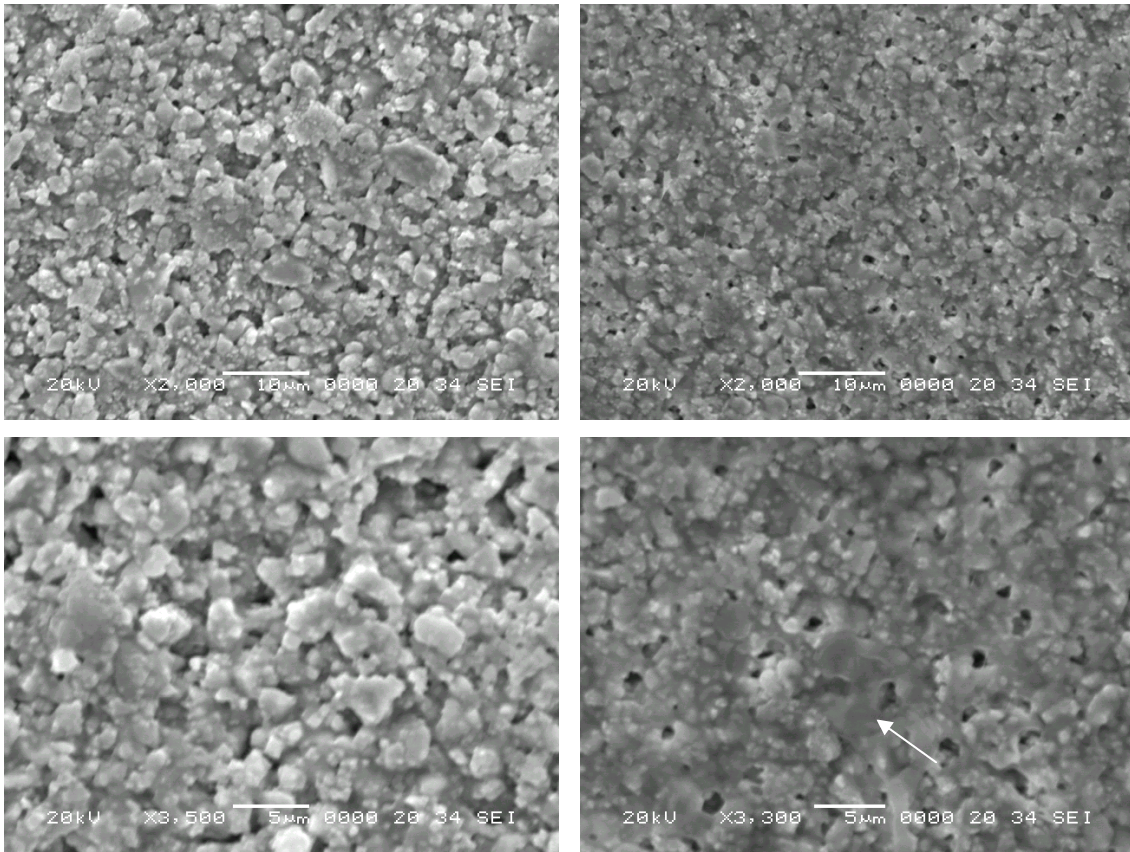
Figure 3.12 SEM images of dense electrolyte layer with different amounts of binder in the slurries (a) 1.68 g and (b) 2.00 g of the PVB binder. Samples were sintered under similar sintering treatment at 1350 °C for 15 and 12 h, respectively.

3.4.3.3 Final slurry formulation

After several adjustments, the slurry formulation was fine-tuned into the final formulation shown in Table 3.3. The green electrolyte tape using 1.8 g of binder possessed an adhesive surface, good plasticity and adequate mechanical strength for further handling.

3.4.3.4 Microstructure of green electrolyte tape surface

Microstructures of dried green tape surfaces prepared from the final formulation are revealed in Figure 3.13. The tape surfaces exhibited well-dispersed microstructures of BCZYZnO powder. The BCZYZnO particles were closely packed together. Small open pores with diameter up to 1 μm in the upper side and less than 1 μm in the carrier film side were illustrated. These pores were created by solvent evaporation and shrinkage of dried organic contents. Therefore, the upper side that was left exposed to air revealed higher porosity than the side which was in contact with the carrier film. The higher content of the organic phase in the carrier side is a result of the limitation of solvent evaporation by the impermeable carrier film. The presence of a significant amount of organic phase made this side smoother and shinier than the upper side as was observed with the naked eye. The SEM image of primary BCZYZnO powder in Figure 3.14 reveals some agglomerates of small particles among some large particles. From the electrolyte green tape surface, the small particles from agglomerates were well dispersed. This confirmed the success of this tape casting process both in deagglomeration and particle binding steps for this green electrolyte tape.



(a) upper side

(b) carrier side

Figure 3.13 SEM images of the dried green tape surface (a) upper side and (b) carrier side. An arrow in Figure 3.13b indicates an example of low electron density area scattered from the organic polymer.

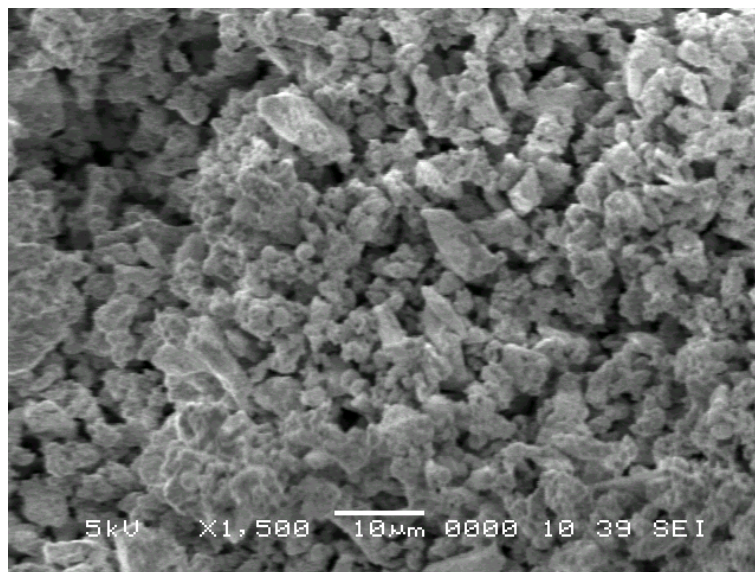


Figure 3.14 SEM image of BCZYZnO starting powder.

3.4.3.5 Sintering conditions

During the slurry optimization process, the sintering conditions and the optimum thickness of the dense layer were simultaneously investigated.

3.4.3.5.1 Effect of sintering temperature

The effect of sintering temperature on the microstructure of sintered samples is illustrated in Figure 3.15. These samples were prepared from the same formulation green tapes and sintered under the same heating treatment. The SEM image of the fracture surface of the sample sintered at 1400 °C exhibits dense microstructure with isolated large grains (up to 10 μm) surrounded by small grains. The grain sizes in the sample sintered at 1300 °C were much smaller and more uniform with a grain size of around 5 μm. There was no significant difference in porosity between sintering temperatures. Although a larger grain size microstructure will present lower grain boundary resistance, the non-uniform microstructure will decrease the mechanical strength and thermal shock resistance of the membrane.

Another aspect that needs to be considered is the chemical reaction between BCZYZnO tape and Al₂O₃ support. The results showed that the sample sintered at 1400 °C severely reacted with Al₂O₃ support while only a trace of the reaction could be seen at 1300 °C. Therefore the optimum temperature for sintering BCZYZnO green tapes was determined to be 1300 °C.

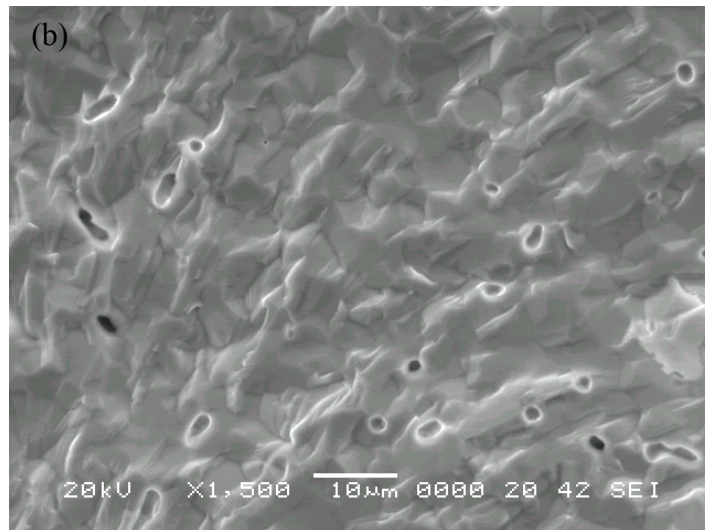


Figure 3.15 SEM image of fracture surface of BCZYZ electrolyte sintered at different temperatures (a) 1400 °C and (b) 1300 °C, each for 10 hrs. The dotted circle shows a large grain compared with the surrounding grains indicated by an arrow. Both samples were prepared from slurry formulation B.

3.4.3.5.2 Thickness of the electrolyte layer

The thickness of the electrolyte layer was varied by multi-layer lamination of green tapes. Theoretically, the thickness of electrolyte layer should be as thin as possible in order to minimise ohmic resistance while at the same time possessing adequate mechanical strength for handling and being gas tight when sealing in the testing apparatus. The experimental results revealed that the mechanical strength and flatness of this BCZYF ceramic disc was mainly derived from the electrolyte part. This meant that the thickness of this part needed to be optimised. The disc containing one layer of electrolyte ($\sim 50 \mu\text{m}$) showed strong edge curling and lack of mechanical strength. When the electrolyte thickness was increased to $\sim 100 \mu\text{m}$, the mechanical strength was improved but the specimen still exhibited poor flatness and strength. The specimen with $\sim 200 \mu\text{m}$ thick electrolyte had good flatness and reasonable mechanical strength. Figure 3.16 shows photographs of sintered specimens with 50, 100, 150 and 200 μm thick electrolyte layers. Note that all specimens were sintered under the same conditions and co-sintered with porous layers.

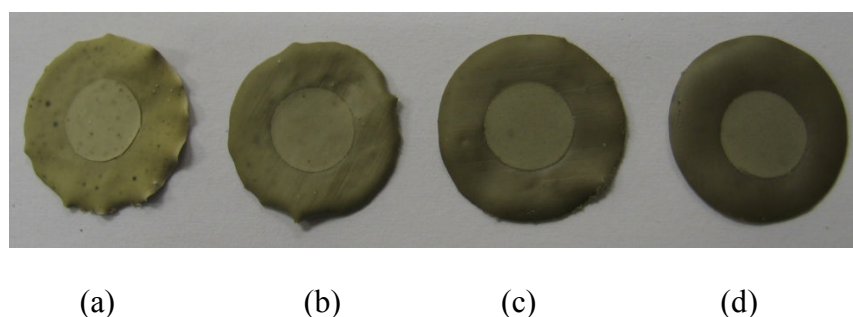


Figure 3.16 Sintered specimens with different electrolyte thicknesses. (a) 50 μm (b) 100 μm (c) 150 μm and (d) 200 μm . All samples were sintered in air at 1300°C for 10 h.

3.4.3.5.3 Sintering duration and final microstructure

The sintering duration was varied from 2 h to 15 h along with the variation of binder and solvent content. At this stage of the investigation, the microstructure of the electrolyte part still contained a significant amount of isolated porosity. Accordingly, the sintering duration was increased to 20 h in order to attain higher density. This condition and the final green tape formulation were utilised thereafter. The microstructures of the dense layer prepared from this formulation are shown in Figure 3.17.

The laminated dense layer was fully sintered and showed no sign of interfacial defects. The residual pores could be seen all over the fracture surface of the specimen, however tended to be concentrated in the middle area. The intense residual porosity at the middle may have been due to a more sluggish organics removal process compared to the edge. In Figure 3.17a, around 20 μm depth from the edge of this layer is almost fully dense and denser than the middle area. Higher magnification of the middle area (Figure 3.17b) revealed dense microstructure with small isolated pores (around 1-2 μm in diameter). The porosity is located mostly at the joint between grains and rarely found within the grain. This kind of porosity can be diminished by further optimisation. The fracture surface shows both intergranular and transgranular fractures. Transgranular fracture paths through the grains made it quite difficult to determine the grain size due to lack of sharp edges. Therefore the grain size was estimated to be around 4 μm from grains that were exposed by intergranular fracture. Nevertheless, the sintered density of this layer was quite high at around 95% of the theoretical density.

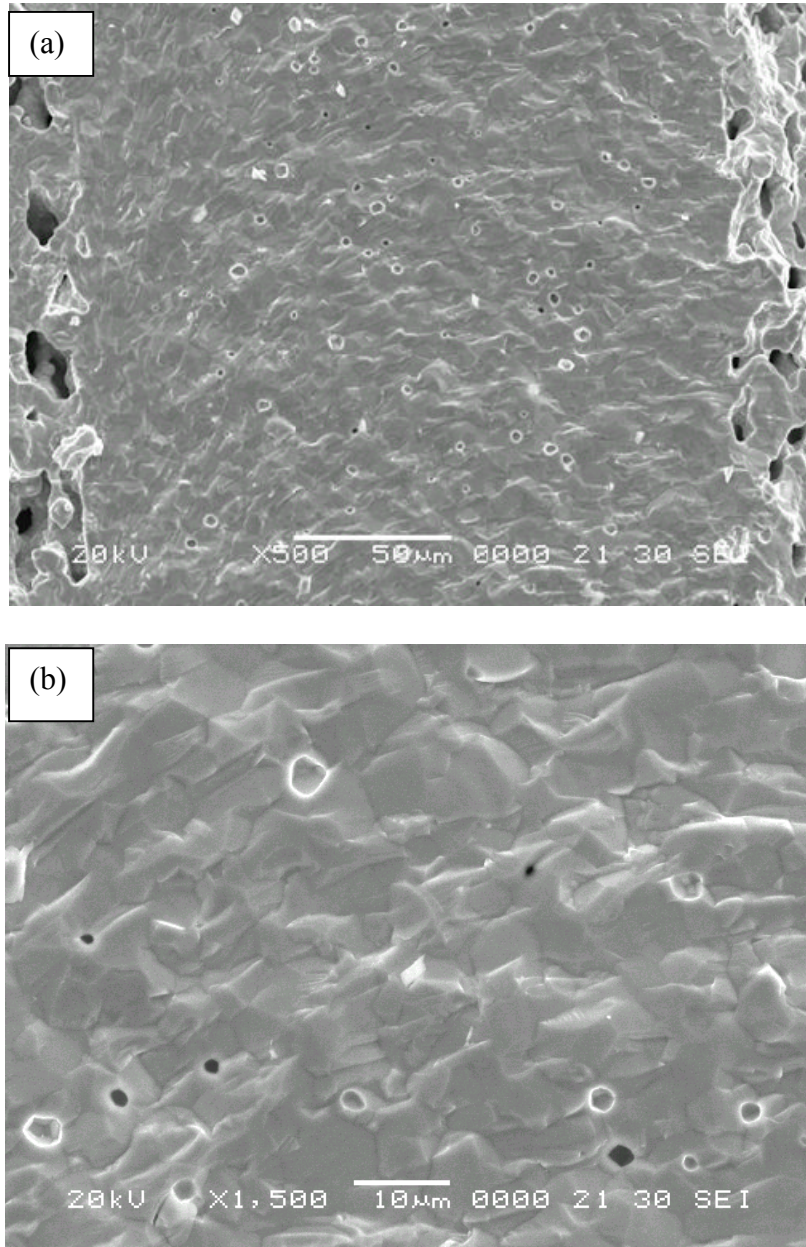


Figure 3.17 SEM images of fracture cross section of 4-layer laminated dense layer at different magnifications (a) x500 and (b) x1500. The sample was sintered in air at 1300 °C for 20 h.

3.4.4 Porous substrate layer

Porous BCZYZ frameworks achieved with the addition of pore formers into BCZYZnO green tapes importantly served as supports for impregnated electrode materials. In the same time, this BCZYZ framework also provided an extension of the TPB length from the electrolyte-electrode interface deep into the electrode structure. The porosity of the porous layer is of utmost important for allowing reactant gases to transport to the TPB site, with porosity of around 40 % being optimal^[1]. In addition, pores should be interconnected and open to the surface. Porosity can be determined in several ways, however most methods focus on a porous sample that can be sintered alone. Unfortunately, the BCZYZ porous layer could not be sintered alone without the dense electrolyte layer since calcination of green porous tapes resulted in a powder-like layer. This may have been a result of the large particle size and loose packing of the particles that made the nucleation difficult to process. However, the porous layer was successful sintered on the dense layer. It is plausible that dense layer acts as a substrate and promotes the nucleation of BCZYZnO grains in porous layer from its surface. Therefore, the porosity of the sintered porous layer was examined by measuring mass and volume of 2-layer disc containing dense and porous layers. Then the subtraction of the dense electrolyte layer mass from the 2-layer disc provided the porous layer mass. The thickness of each layer was obtained from SEM images. Hence, sample discs required good flatness for this measurement. As mentioned in section 3.4.3, most samples in the early stage of the experiments experienced poor flatness. Therefore, the optimum slurry formulation for the porous layer was mostly evaluated by structure determination using SEM.

3.4.4.1 Porous structure optimisation

In this study, graphite was the main pore former component while the addition of glassy carbon was to disrupt layered packing of the graphite.

The slurry formulation for the porous layer was adapted from the formulation for the dense electrolyte. The total amount of solid powder in the slurry was kept constant. The amount of pore formers added was in wt% of total solid content (15 g). In most cases, dispersant and plasticizer contents were not changed. In some cases, the amount of solvent and binder were varied in order to achieve an acceptable viscosity. In tape slurry formulation process, pore formers were added in the first step along with BCZYZnO powder and dispersant. Comparing to the tape slurry without pore former, the substitution of pore former (e.g. 50 wt% of graphite) into the BCZYZnO powder dramatically increased the viscosity due to its high surface area. Therefore, the amount of solvent was increased until the mixture reached enough fluidity for a good dispersion. After adding plasticizers and the binder, most of the slurries reached a satisfactory viscosity and presented a homogeneous suspension. Consequently, all green porous tapes produced in this experiment had good flexibility with a smooth and crack-free surface. Table 3.4 presents selected formulations for the porous tape slurries.

Apart from the adjustments of the organic contents, the amount and shape of pore formers were also varied in order to reach an optimum porous microstructure with adequate and interconnected porosity. A well-sintered porous structure with moderate size scaffold is desired for low grain boundary resistance and high mechanical strength.

Table 3.4. Selected formulations for porous BCZYZnO tape slurries

Chemicals		Formulations(g)		
		P1 50 wt% Gra	P2 30 wt% Gra	P3 40 wt% Gra + 10 wt% GIC
BCZYZnO		7.500	10.500	7.500
Pore formers	Graphite	7.500	4.500	6.000
	Glassy carbon	-	-	1.500
Triton QS-44		0.100	0.100	0.127
PEG		1.395	1.278	1.298
DBP		1.117	1.109	1.108
Butvar (PVB)		1.680	2.000	1.700
Solvent		12.000	10.000	10.500

3.4.4.2 Effect of sintering temperature

There are several factors that influence the microstructure of the porous layer. Sintering temperature is one of them since the rate of grain growth relies on temperature. The influence of the sintering temperature on the microstructure of the porous layer is clearly shown in Figure 3.18. Samples prepared from the same green tape containing 30 wt% of graphite were sintered at two different temperatures. The SEM images of fracture surfaces of both samples demonstrated well-sintered porous structure with high porosity and relative uniformity. As expected, the sample sintered at the higher temperature possessed a denser microstructure. The temperature affected

the density of the sintered ceramic by increasing the rate of grain growth, thereby caused higher shrinkage in the structure. Such high shrinkage could have made it difficult to control the porosity and microstructure of the porous layer. Moreover, the reaction between BCZYF and Al_2O_3 support was also accelerated at the higher temperature. Therefore, the sintering temperature was chosen at around 1300 °C.

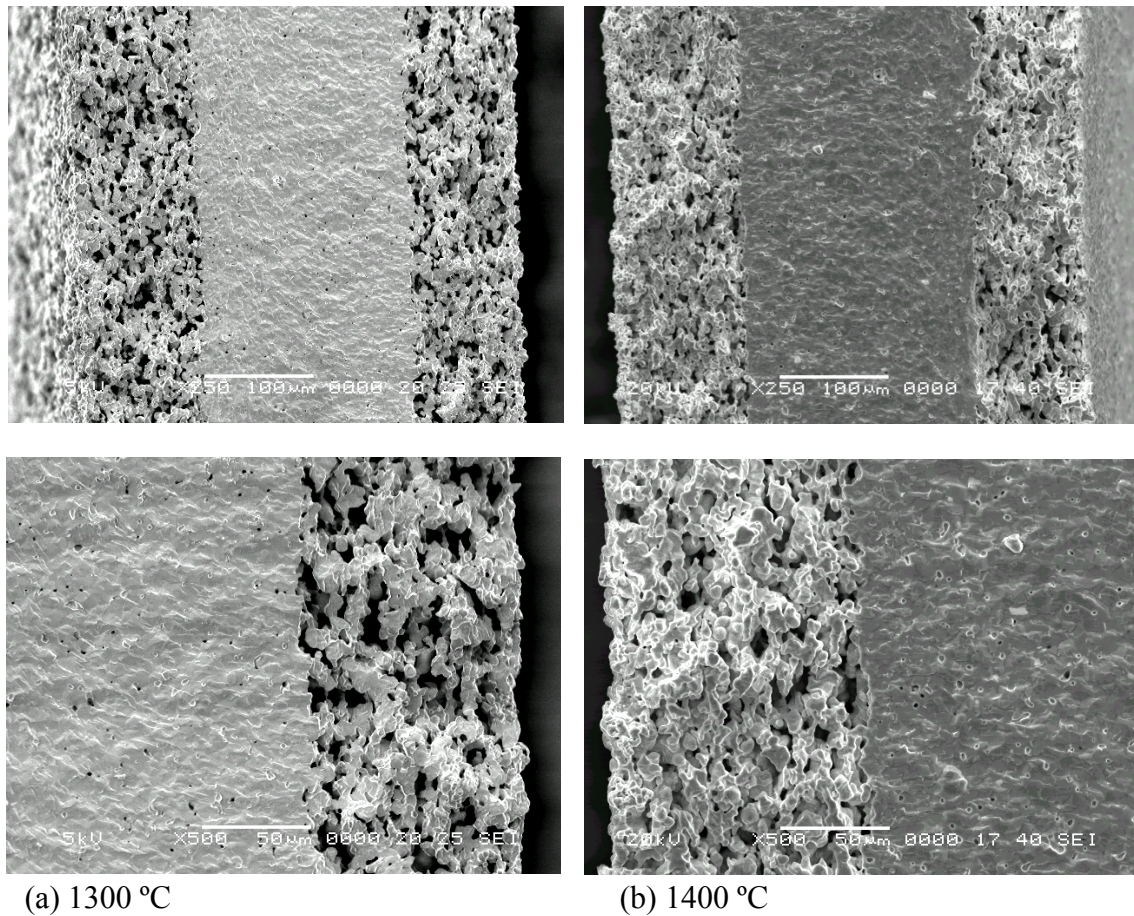


Figure 3.18 SEM images of specimens prepared from tapes containing 30 wt% graphite sintered for 10 h at different temperatures.

3.4.4.3 Influence of pore former morphology

Many researchers have suggested that pore size and microstructure of porous ceramics are influenced by the morphology and amount of pore former used^[8,20-22]. The influences of pore former morphology and amount in green tapes are considered here. Green tapes containing only graphite or a mixture of graphite and glassy carbon were prepared. SEM images of the fracture surface of sintered tapes are presented in Figure 3.19. All samples demonstrated well-connected networks of the sintered BCZYZ scaffold and open porosity. The images also indicate good adhesion at the interface between porous and dense layers, which is important for transporting H⁺ ions from the electrolyte membrane to the TPB sites in the porous electrode matrix.

In Figure 3.19a, the cross-section of the sample with 30 wt% graphite reveals the pores with long and narrow shapes lying parallel to the surface. The morphology of the pores is in agreement with the morphology of the graphite particles. The uniform and open porous network in the porous layer suggests that both BCZYZnO and graphite particles were well-dispersed and they both formed their own percolating network throughout the green tape.

When the graphite content was increased to 50 wt%, (Figure 3.19b), the pore size became larger and the size of the BCZYZ scaffold decreased. These observations were obviously due to segregation of the graphite particles, which hindered the packing of the BCZYZnO particles. In addition, porosity also increased with the increase of the graphite content, as expected

From the two cases described above, the sample with 30 wt% graphite provided good size of the BCZYZ scaffold but poor porosity, while the sample with 50 wt% graphite provided good porosity but a quite thin scaffold, which could cause problems for ionic

transport and mechanical strength. Therefore, a modification to the microstructure was expected with the addition of spherical glassy carbon into the graphite matrix. Figure 3.19c reveals the porous microstructure created from the mixture of 40 wt% of graphite and 10 wt% of glassy carbon. As a result, the porous microstructure was improved, exhibiting a moderately sized BCZYZ scaffold and a mixture of large and small pores. This was attributed to the different shape of spherical glassy carbon, which prevented the segregation of graphite particles. At this point in the study, the mixture of glassy carbon with graphite had a positive effect on the microstructure of the porous layer, so that this mixture was used as a starting point for further organic additive adjustments.

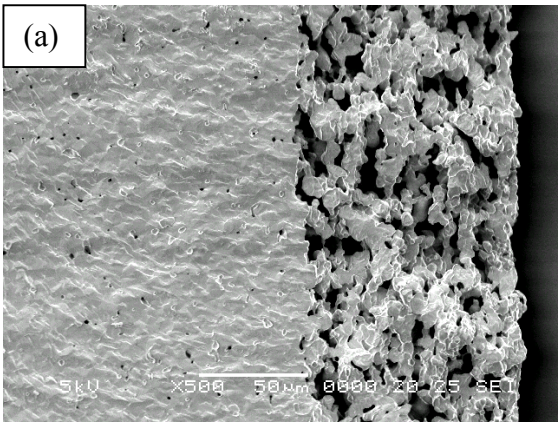
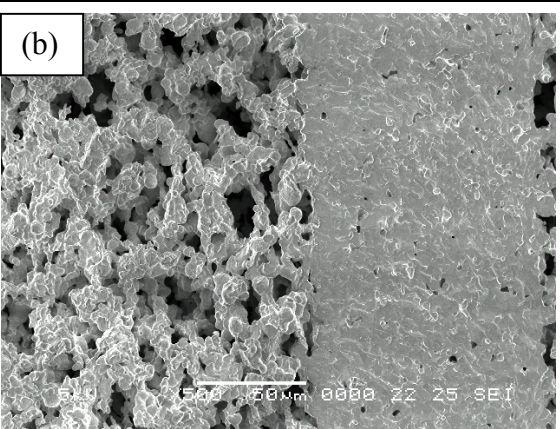
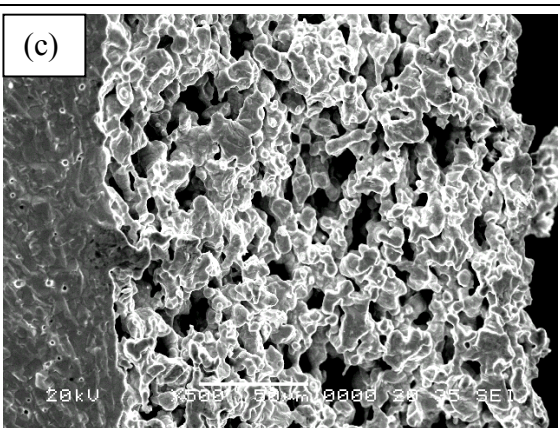
	<p>Contents: 30 wt% graphite, 2 g binder</p> <p>Sintering condition: 1300 °C for 10 h</p> <p>Features: relatively uniform porosity with long and narrow pore shape, which is similar to graphite's shape. The scaffold was thick and dense.</p>
	<p>Contents: 50 wt% graphite, 1.68 g binder</p> <p>Sintering condition: 1350 °C for 15 h</p> <p>Features: larger pores, thin scaffold</p>
	<p>Contents: 40 wt% graphite + 10 wt% glassy carbon, 1.7 g binder</p> <p>Sintering condition: 1350 °C for 20 h</p> <p>Features: combination of large and small pores with moderate scaffold</p>

Figure 3.19 SEM images of fracture surface of sintered BCZYZ porous layers prepared from various amounts and types of pore formers.

3.4.4.4 Microstructure of porous green tape surface

In order to confirm the behaviour of pore formers in the green tape, the microstructure from the surface of a green porous tape containing 40wt% graphite and 10wt% glassy carbon was investigated. The SEM images in Figure 3.20 reveal the packing of the pore former particles within the BCZYZnO powder. Similar to the case of the dense electrolyte tape, the BCZYZnO powder were disaggregated, revealing small and well-dispersed primary particles. In contrast to the dense electrolyte tape, there was no sign of residual organics on both upper and bottom side surfaces. However, the results from TGA measurements of green porous tapes in section 3.4.1 exhibited a significant weight loss at 120-350 °C corresponding to the weight loss from the decomposition of organic contents. It is possible that the solvent quickly evaporated via the highly porous created by the pore former particles, leaving only dried organics between the particles which were hardly noticeable with SEM.

Regarding the upper side surface, the BCZYZnO powder was well-dispersed among the graphite and glassy carbon particles. The graphite particles packed down parallel to the surface and allowing the BCZYZnO powder to situate among them. This hindered the BCZYZnO particles from closely packing and was the probable cause of the failure in sintering this layer alone without a dense supporting layer.

A sediment layer of the BCZYZnO particles was found on the bottom side surface, as evidenced in Figure 3.20b. Due to the high solid loading of the pore former, it is possible that some of the BCZYZnO particles, which are much smaller than the pore former particles, were repelled from the pore former matrix. Note that most of the precipitate particles were forming a connecting particle network. As such this powder layer could be used as a sintering base in order to promote the adhesion between the

porous layer and the dense electrolyte interface by attaching this bottom side to the dense green tape during lamination.

The TGA data of the green porous tapes with various pore formers in section 3.4.1 suggests that all pore formers were removed from the green tape up to 700 °C, before the densification of the BCZYZnO powder. By considering the influence of pore former morphology to the pore structure, obviously the key role of pore formers is to serve as templates for the porous structure.

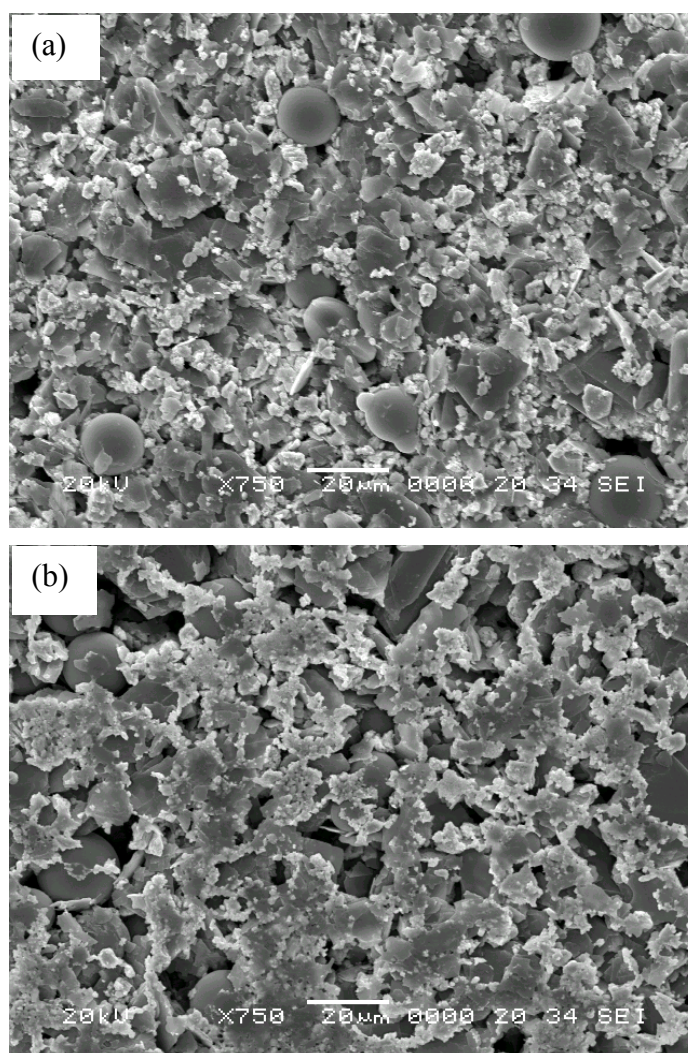
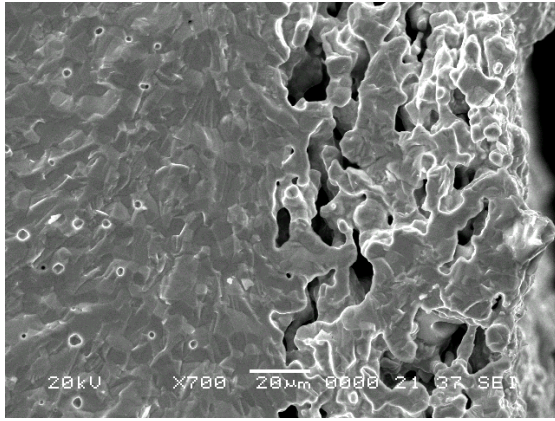


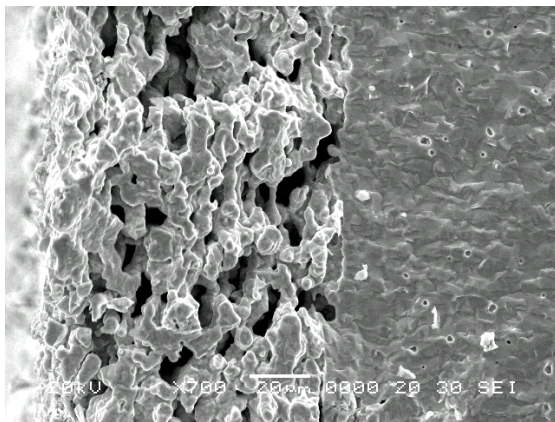
Figure 3.20 SEM images of green porous tape surfaces for tape containing 40 wt% graphite + 10 wt% glassy carbon (a) upper side and (b) bottom side.

3.4.4.5 Effect of dispersant and binder contents

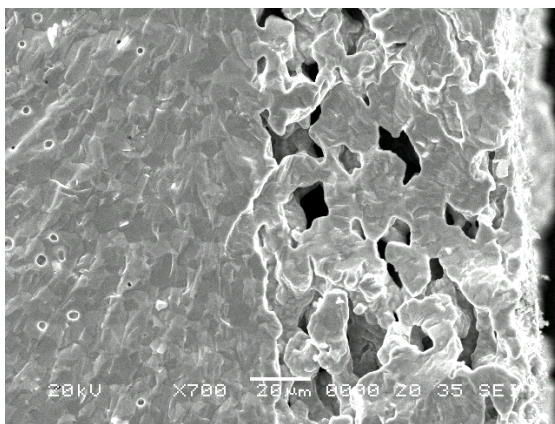
By modifying the P3 formulation in Table 3.4, the effects of dispersant and binder contents on sintered porous film microstructure were examined. Considering their roles in tape slurries, the dispersant helps separate groups of particles and disperse them homogeneously during the dispersion step. The binder then brings the particles close to each other, and this applies to both BCZYZnO and pore former particles. Regarding influences on particle distribution, the effect of the dispersant and binder contents on porous microstructure is investigated in this section. The amount of pore former used was fixed at 40wt% of graphite + 10wt% of glassy carbon. The microstructures of the sintered bodies with various dispersant and binder contents are shown in Figure 3.21. Comparing samples with the same amount of binder, the sample with higher dispersant content exhibited a porous microstructure with finer scaffold and more uniform pores. Accordingly it is possible that the amount of the dispersant of 0.12 g that was used for preparing the dense electrolyte tape was not enough to disperse all pore former and BCZYZnO particles. Figure 3.21c indicates that higher binder and dispersant contents dramatically increased the thickness of the scaffold. This dense microstructure is in accordance with the increase of binding effect from the additional binder. Consequently, the microstructure obtained from using 0.25 g dispersant and 1.7 g binder was chosen as a suitable microstructure for further impregnation process. The final formulation for the porous tape slurry is shown in Table 3.5 and an example microstructure of a sample sintered from this formulation is exhibited in Figure 3.22.



a) 0.12 g dispersant, 1.7 g binder



b) 0.25 g dispersant, 1.7 g binder



c) 0.25 g dispersant, 2 g binder

Figure 3.21 SEM images of fracture surface of samples prepared using various amounts of dispersant and binder. All samples were sintered at 1300 °C for 20 h.

Table 3.5 Final formulation for the porous tape slurry.

BCZYZnO (g)	Graphite (g)	Glassy carbon(g)	Triton QS-44 (g)	DBP (g)	PEG (g)	PVB (g)	Solvent (g)
7.5	6.0	1.5	0.25	1.0	1.24	1.7	10.5

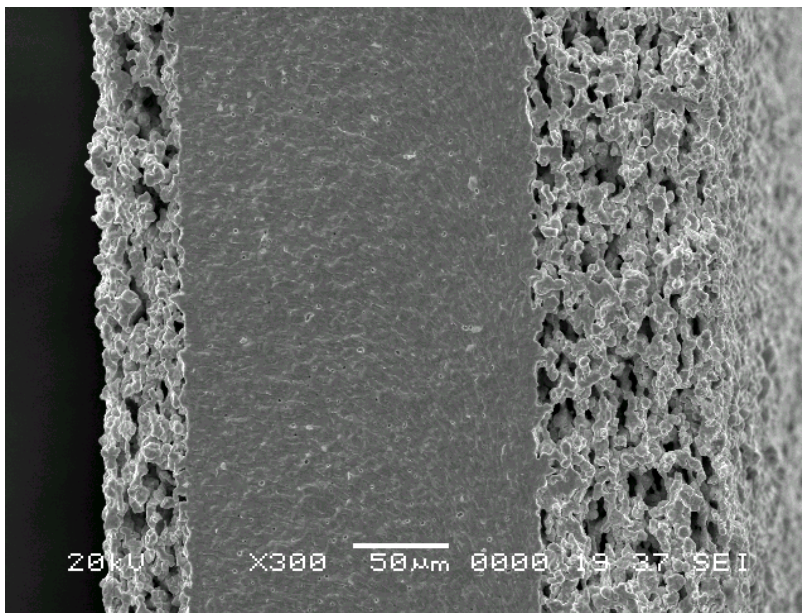
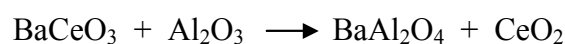


Figure 3.22 SEM image of fracture surface of sample prepared from final slurry formulation for both dense and porous layers.

3.4.4.6 Phase identification of sintered porous BCZYZ layer

During sintering, 3-layer discs were fired by facing the larger diameter porous side down against the Al₂O₃ support, with a layer of sintered BCZYZ powder acting as a buffer between the sample and the support. Surfaces of the dense and porous layers were examined by reflection mode XRD. From Figure 3.23, the XRD pattern of a BCZYZ disc without porous layer indicated a single perovskite phase. The XRD pattern of the upper side porous layer from the 3-layer disc also revealed a single perovskite phase, however the XRD pattern of the bottom porous layer, which was sintered while in contact with the Al₂O₃ support, revealed several weak peaks. Most of these peaks were consistent with of the presence of CeO₂, which could have come from the reaction between BCZYZ and Al₂O₃ according to the following reaction suggested by Chen et al.^[23]:



If the porous BCZYZ layer reacted with the Al₂O₃ support, the sintered powder buffer layer that was in direct contact with the Al₂O₃ support should have had a more severe reaction. The XRD spectrum of the sintered powder buffer layer in Figure 3.24 confirms that Al₂O₃ did react with the BCZYZ sintered powder, although the reaction was not severe and the main phase was still a perovskite phase. In order to prevent this reaction from happening, the buffer layer of sintered BCZYZ powder should be quite thick. The shortening of sintering duration could be another way to decrease the extent of reaction between these two materials. Figure 3.25 shows the XRD spectrum for a sample sintered at 1300 °C for 10 h. No sign of impurities was found, thereby

confirming that the weak peaks observed in the 20 h sintered sample came from the reaction between BCZYF and the Al_2O_3 support.

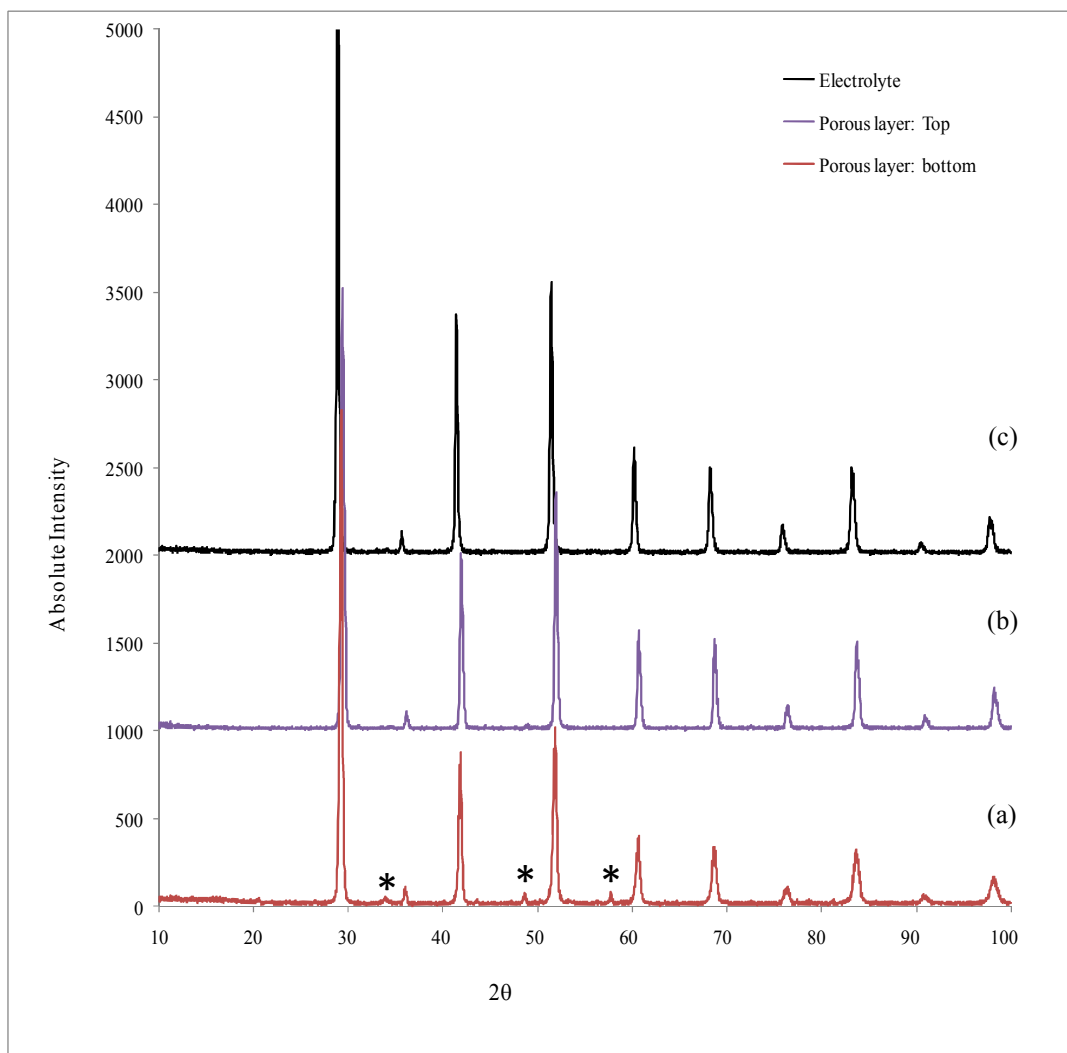


Figure 3.23 XRD patterns of sintered porous layers (a) porous bottom layer (b) porous top layer and (c) electrolyte layer. Sample was sintered at 1300°C for 20 h.

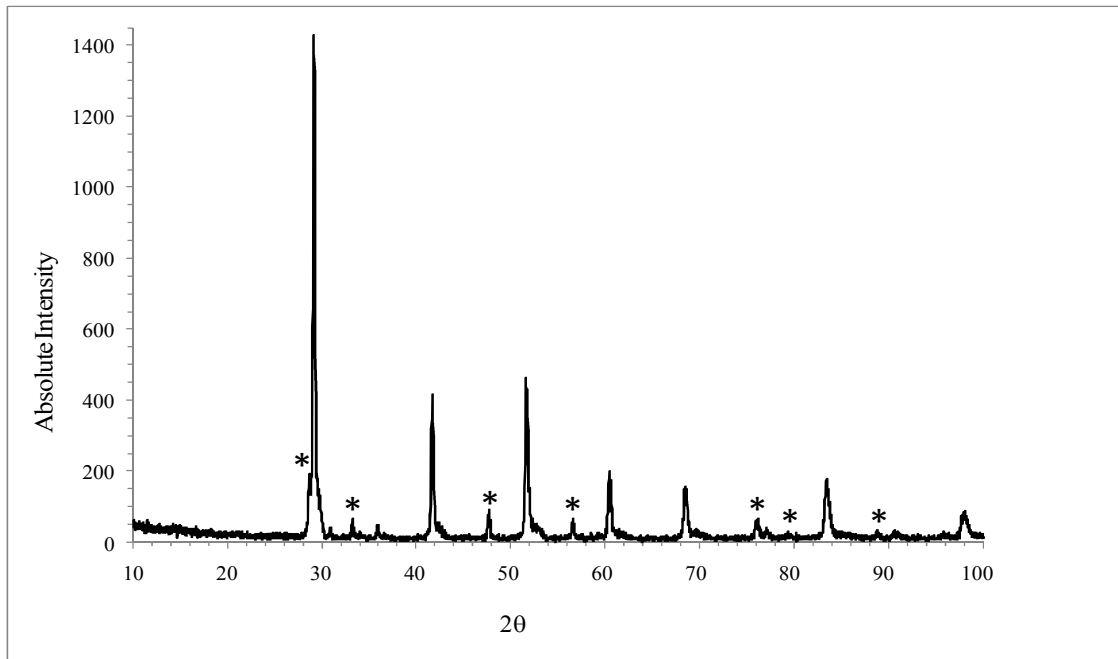


Figure 3.24 XRD data of BCZYZ powder buffer layer after use as a sintering support at 1300 °C.

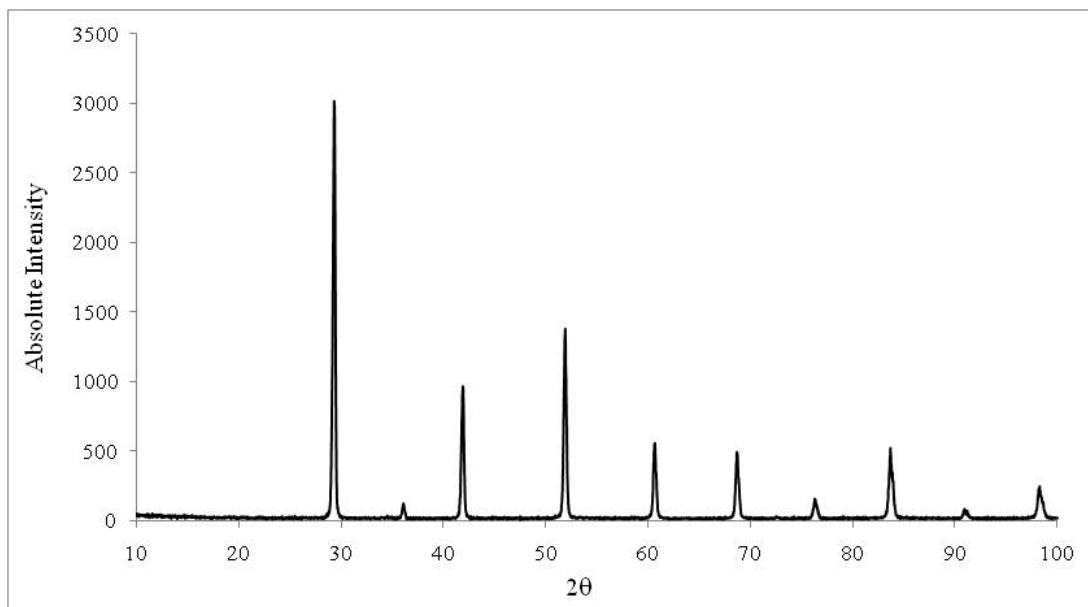


Figure 3.25 XRD pattern of bottom porous layer sintered at 1300 °C for 10 h showing the absence of peaks due to reaction with Al_2O_3 .

3.5 Conclusions

Tape casting procedures and slurry formulations developed by Prof Irvine and co-workers for commercial YSZ powder can be readily applied to the house-made barium cerate/zirconate (BCZYZnO) powder. The 3-layer cast tape of BCZYZnO powder, porous-dense-porous, was successfully co-sintered in air at 1300 °C. The optimised slurry formulation provided a maximum green body density of 3 g cm⁻³ for electrolyte tape, which is almost 50% of the theoretical density of sintered electrolyte. The electrolyte layer with an appropriate thickness of ~200 μm maintains adequate mechanical strength to the whole sintered body. This 200 μm thick electrolyte was fabricated by 4-layer lamination and showed a homogeneous body without any appearance of defects between laminated layers after sintering. The density of the electrolyte layer was normally in the order of ~ 95 % of the theoretical density. Porous BCZYZ layers were achieved by the addition of graphite and glassy carbon pore formers. The morphology of the pores was related to the morphology of pore former particles and other slurry components. However, the optimum porous microstructure was obtained using 40 wt% graphite together with 10 wt% glassy carbon in the green BCZYZnO tape. The porosity in the sintered porous layer was open and pores well interconnected. This confirms that both BCZYZnO and pore former particles were well-dispersed and linked into networks. The removal of pore formers before reaching the ceramic sintering temperature had no adverse effect on the BCZYZnO particle network. A porosity of the final product of about 50% was normally obtained. Porous layers were adhered very well with underlying dense layers, an important requirement for transporting H⁺ ions from the electrolyte to the electrode matrix.

References

1. R. O'Hayre, S. W. Cha, W. Colella, F. B. Prinz, Fuel cell fundamentals, John Willey & Sons, New York (2006).
2. R.J. Gorte, J.M. Vohs, Current Opinion in Colloid & Interface Science 14 (2009) 236.
3. W. Z. Zhu, S. C. Deevi, Mater. Sci. Eng. A362 (2003) 228.
4. H. He, Y. Huang, J. Regal, M. Boaro, J. M. Vohs, R. J. Gorte, J. Am. Ceram. Soc. 87 (2004) 331.
5. S. Park, R. J. Gorte, J. M. Vohs, J. Electrochem. Soc. 148 (2001) A443.
6. S. I. Lee, J. M. Vohs, R. J. Gorte, J. Electrochem. Soc. 151 (2004) A1319.
7. R.E. Mistler, E.R. Twiname, Tape Casting Theory and Practice, The American Ceramic Society, Westerville (2000).
8. M. Boaro, J. M. Vohs, R. J. Gorte, J. Am. Ceram. Soc. 86 (2003) 395.
9. M. N. Rahaman, Ceramic processing and sintering, 2nd edition, CRC Press, Florida (2003).
10. F. G. E. Jones, J. T. S. Irvine, Ionics 8 (2002) 339.
11. D. R. Lide, Handbook of Chemistry and Physics, 76th edition, CRC Press, Florida (1995) p. 6-115.
12. J. A. Lewis, J. Am. Ceram. Soc. 83 (2000) 2341-2359.
13. T. Cosgrove, Colloid Science: Principles, Methods and Applications, Blackwell Publishing (2005) 20 January 2010
from <http://lib.myilibrary.com/Browse/open.asp?ID=121483&loc=40>
14. U. Paik, V. A. Hackley, S. C. Choi, Y. G. Jung, Colloid Surf. A: Physicochem. Eng. Aspects 138 (1998) 77-88.

15. T. Chartier, T. Rouxel, J. Eur. Ceram. Soc. 17 (1997) 299.
16. M. Descamps, G. Ringuet, D. Leger, B. Thierry, J. Eur. Ceram. Soc. 15 (1995) 357-362.
17. D. H. Kim, K. Y. Lim, U. Paik, Y. G. Jung, J. Eur. Ceram. Soc. 24 (2004) 733.
18. PDF (Powder Diffraction file) number 22-74, BaCeO₃, produced by ICDD (International Center for Diffraction Data)
19. PDF (Powder Diffraction file) number 6-399, BaZrO₃, produced by ICDD (International Center for Diffraction Data)
20. F. G. E. Jones, Tape casting, co-firing and electrical characterisation of a novel design solid oxide fuel cell: SOFCRoll, Ph.D. thesis, University of St Andrews (2005).
21. A. Sanson, P. Pinasco, E. Roncari, J. Eur. Ceram. Soc. 28 (2008) 1221-1226.
22. S. F. Corbin, J. Lee, X. Qiao, J. Am. Ceram. Soc. 84 (2001) 41-47.
23. F. Chen, O. T. Sørensen, G. Meng, D. Peng, J. Mater. Chem. 7(3) (1997) 481-485.

Chapter 4

Electrochemical Characterisations of Anode and Cathode Materials

4.1 Ion Impregnation of Electrode Materials	142
4.2 Experimental	143
4.2.1 Impregnation procedure	143
4.2.2 SEM and EDS elemental analysis	144
4.2.3 X-ray diffraction	145
4.2.4 Details of electrode materials and catalysts	145
4.2.5 Single-atmosphere testing apparatus	146
4.2.6 Cell with painted Pt electrode as a reference cell	148
4.3 Results and discussion	149
4.3.1 Decomposition temperature of metal nitrates	149
4.3.2 Phase compositions of impregnated electrodes	153
4.3.3 Performances of Ni impregnated anodes in H ₂ atmospheres	154
4.3.3.1 Ni electrodes without catalyst addition	155
4.3.3.2 Degradation of Ni impregnated electrodes	158
4.3.3.3 Ni electrodes with CeO ₂ addition	160
4.3.3.4 NiO-CeO ₂ electrodes in different H ₂ partial pressures	162
4.3.3.5 Stability of NiO-CeO ₂ electrodes	165
4.3.3.6 NiO-CeO ₂ electrode in different regimes of H ₂ O contents	168
4.3.3.7 Comparison of Ni impregnated electrodes and painted Pt electrode	169
4.3.3.8 Microstructure of Ni impregnated electrodes after testing	172
4.3.4 Cathode material: impregnated Fe oxide	175
4.3.4.1 Cell with 1:1 Fe oxide:BCZY electrode	175
4.3.4.2 Microstructure of Fe oxide impregnated electrode	177
4.3.4.3 Cell with 25 wt% Fe oxide-BCZY electrode	178
4.3.4.4 Behaviour of 25wt% Fe electrode in non-humidified atmospheres	181
4.3.5 Comparison between conductivities of cells with various electrodes	184
4.4 Conclusions	185
References	186

In this chapter, electrochemical measurements of cells fabricated by tape casting and ion impregnation were investigated in order to select the proper anode and cathode materials for ammonia synthesis. The contents of this chapter include the investigations of the promising anode and cathode materials which were performed individually in a single-atmosphere apparatus. Symmetrical cells of the anode or cathode materials were tested in H₂ and N₂-containing atmospheres, respectively.

4.1 Ion Impregnation of Electrode Materials

Ion impregnation is one of the most effective methods for preparing an electrode-electrolyte composite. Typically, the electrode material is prepared in a solution form and then impregnated into a porous scaffold made from the same material of the electrolyte. So, the porous scaffold should act as an extension that builds upon a dense electrolyte base. This extends the ionic-conductive path from the electrolyte/electrode interface deep into the electrode matrix. When the impregnated electrode is deposited on the surface of the porous scaffold, an electronic conducting path will be created. Therefore, this method ensures not only the contact between the electrode and the electrolyte but also the connection between electrode-electrode and electrolyte-electrolyte phases. It was found that the impregnation of the electrode material onto the porous support can reduce the amount of electrode needed to reach the percolation threshold. Like the cermets, this method provides a good adhesion between the electrode/electrolyte interface and is capable to extend the length of triple-phase boundary (TPB) between the electrolyte, electrode and reactant gas phase into the electrode matrix. Unlike the cermets, the electrode-electrolyte composite can be assembled without the need of high temperature sintering which probably would

cause sintering and grain growth of the electrode and/or electrolyte phases in the cermet^[1]. Low firing temperature in the impregnation process provides an advantage for the usage of electrolyte and electrode materials with different sintering temperature requirements and also reduces the intercomponent reactivity. A well-known example of this advantage has been demonstrated by Gorte et. al^[2,3] in the replacement of Ni with Cu which has lower sintering temperature than NiO and YSZ in a hydrocarbon SOFC. This versatile process is also suitable for modifying the surface of a well-sintered porous electrode with an additional catalyst^[1] or allowing a complex combination of two or more metal electrodes to be easily established^[4].

4.2 Experimental

4.2.1 Impregnation procedure

The solution of the electrode materials was prepared by dissolving nitrate salts of the metal electrodes in absolute ethanol in order to obtain a solution with low surface tension and rapid evaporation. The concentration of the solution was about 1 M. Although a solution with higher concentration may reduce the numbers of repeated-impregnation, it tends to produce larger metal oxide particles which are likely to deposit near the surface of the porous support. These particles will be agglomerated after repeated the impregnation leading to blockages in some areas on the surface. It is important to ensure that the metal solution is uniformly distributed and reaches the electrode-electrolyte interface where the electrochemical reactions occur intensively. The metal nitrate solution was introduced drop-wise onto the porous BCZYZ layer

using a 1 ml syringe fitted with a needle. The impregnated sample was dried in an oven at 80 °C for 10 minutes and the process was repeated until the porous substrate reached a saturated point. Then, the sample was transferred to the furnace where the nitrate decomposition was performed in a stagnant air. The heating treatment consisted of a fast heating rate of 8 °C/min to 650 °C and dwelling at this temperature for 30 min before cooling down to room temperature at a rate of 5 °C/min. The technique of fast drying provides uniform distribution of the metal particles. Slow drying tends to cause the migration of the metal salt upward and accumulate near porous layer surface^[5]. After the heating treatment, the metal oxides of the electrode material should deposit on the BCZYZ porous scaffold surface. The desired loading of the electrode oxide was achieved after repeating the process about 5-10 times in each porous support. Phase composition and metal oxide distribution inside the porous substrate were investigated by SEM-EDS.

4.2.2 SEM and EDS elemental analysis

The distribution of the metal oxide inside the porous structure was investigated by a JEOL 5600 scanning electron microscope (SEM) equipped with EDS system using a voltage of 20kV, working distance of 20 mm and a spot size around 30. Without gold sputtering on their fracture surfaces, small pieces of specimens were attached directly on a specimen holder using electrically conductive carbon adhesion discs (Agar Scientific Ltd). The EDS elemental analysis was applied to investigate the percolation and distribution of the impregnated electrode inside the porous matrix.

4.2.3 X-ray diffraction

Phase composition of the impregnated composites was examined on a Philips PW 1710 diffractometer operating in reflection mode using $\text{CuK}\alpha$ radiation. The XRD data were collected using a continuous scan with a 2θ range of $15\text{-}100^\circ$, 0.02° step size and $1^\circ 2\theta/\text{min}$ scan rate.

4.2.4 Details of electrode materials and catalysts

Table 4.1 presents anode, cathode and catalyst precursors employed in this study. For the anode, Ni metal was a candidate electrode due to its excellent catalytic activity of hydrogen oxidation and good electronic conductivity. In addition to the Ni metal, CeO_2 catalyst was added into the Ni electrode in order to improve the stability of the electrode and prevent the growth of Ni particles.

For the cathode, the Fe metal was selected due to it is normally employed as a catalyst for ammonia synthesis. However, in order to apply the Fe metal into an electrochemical cell as an electrode, factors such as stability of Fe in operating conditions and electronic conductivity have to take into account. Therefore, the proper amount of the Fe impregnated electrode and performance of Fe was determined in both N_2 and H_2 -containing atmospheres. The addition of catalyst onto Fe cathode was carried out only in two-chamber experiment for ammonia synthesis (Chapter 5). The amount of the impregnated electrode was reported in the weight percentage of metal oxide to the weight of BCZYZ porous layer.

Table 4.1 List of electrode and catalyst precursors used in this experiment.

Anode		Catalytic additive	
Ni	Ni(NO ₃) ₂ ·6H ₂ O (98%, Alfa Aesar)	CeO ₂	Ce(NO ₃) ₃ (99+%, Fisher Scientific)
Cathode		Catalytic additives	
Fe	Fe(NO ₃) ₃ ·9H ₂ O (98+%, Sigma-Aldrich)	Pd	5 % Pd solution (NH ₃) ₄ Pd(NO ₃) ₂ (Alfa Aesar)
		Ru	0.3 M Ru(NO)(NO ₃) ₃ (Alfa Aesar)

4.2.5 Single-atmosphere testing apparatus

The experiment in single atmosphere was designed for studying the electrochemical reaction of a particular electrode in a symmetrical cell configuration. The symmetrical cell comprised of two electrodes with the same composition but different in size. The circular ceramic disc with two electrode sizes of 1.5 and 0.7 cm in diameter was employed in this experiment. The difference in size of both electrodes prevents cross-contamination during impregnation which can cause short-circuit under testing condition. The active electrode area was considered from the small electrode which was $\sim 0.4 \text{ cm}^2$. On the top of each electrode was the current collector which was prepared by painting metal paste as a mesh pattern, allowing a good connection on the exposed electrode surface and adequate gas transportation through the electrode composite. Different kinds of metal current collectors were also studied. For the Ni-based electrode, only Au and Pt current collectors were chosen while Au, Pt and Pd current collectors were employed in the case of the Fe-based cathode. After painting, the current collector was fired in air at 900 °C for 1 h to decompose organic additives

and obtain good adhesion with the electrode composite. The finished cell was placed in a testing apparatus as shown in Figure 4.1. This two-electrode apparatus consisted of two Pt leads and beads for electrical connection with total resistance of $\sim 1 \Omega$, gas inlet and outlet tubes and a thermocouple. This testing jig was sealed in a quartz tube allowing a single atmosphere testing. Within this set up, only AC impedance measurement under open circuit was performed.

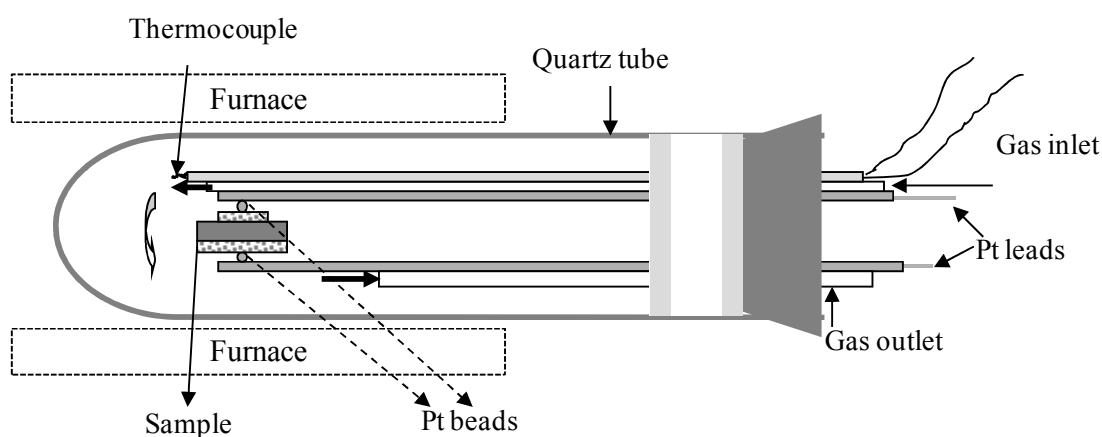


Figure 4.1 Schematic of experimental set up for single atmosphere test

The AC impedance measurements were carried out on a frequency response analyzer (Solartron 1255, UK) coupled with an electrochemical interface (Solartron 1287, UK) using a frequency range of 0.1 Hz to 1 MHz and amplitude of 20 mV. The temperature range for the measurements was 400-700 °C with intervals of 50 °C. The equilibration time was at least 30 min or until the steady state had been reached.

The thickness of tape cast electrolyte was between 200-250 μm . Both electrode composites had thicknesses of $\sim 100 \mu\text{m}$ with porosity around 57% before impregnation. The actual thickness of each component was examined by SEM after electrochemical testing. The atmospheres used for anode or cathode material testing are summarised in Table 4.2.

Table 4.2 A summary of testing atmospheres for anode or cathode materials

Anode (Ni-based)	Cathode (Fe-based)
1. humidified 5% H_2 (3% H_2O /Ar/4% H_2)	1. humidified 5% H_2 (3% H_2O /Ar/4% H_2)
2. humidified pure H_2 (3% H_2O /97% H_2)	2. humidified mixed 5% H_2 / N_2
3. non-humidified 5% H_2 (5% H_2 /Ar)	3. humidified pure N_2 (3% H_2O /97% N_2)
	4. non-humidified 5% H_2 (5% H_2 /Ar)
	5. non-humidified mixed 5% H_2 / N_2
	6. non-humidified pure N_2 (99.998% N_2)

4.2.6 Cell with painted Pt electrode as a reference cell

The usage of Pt paste as a current collector on the Ni impregnated electrode raises some concerns due to the catalytic activity of the Pt for the H_2 oxidation reaction. However, the catalytic activity of Pt depends on several factors such as its surface area and particle size. In order to indicate the catalytic activity of this Pt paste on the H_2 oxidation, a cell with a Pt electrode was prepared by painting Pt paste on thin BCZY electrolyte disc and firing under the same condition with the Pt current collector. The results provided a comparison between the polarisation resistance of Pt alone and that of the Ni impregnated electrode with a layer of Pt current collector on the top. The Pt | BCZY | Pt cell was tested only in humidified 5% H_2 /Ar from 400-700 °C.

4.3 Results and discussion

4.3.1 Decomposition temperature of metal nitrates

Firstly, the firing conditions for the impregnation of the Ni electrode were investigated. According to the literatures^[7,8], the thermal decomposition of $\text{Ni}(\text{NO}_3)_2 \cdot 6\text{H}_2\text{O}$ in air begins at 300 °C. With an intention to prevent any thermal shock that may happen in this fairly strong ceramic membrane after repeated impregnation, the decomposition temperature of the impregnated nickel nitrate was set at 350 °C with dwell time of 30 min. However after several impregnation cycles, the impregnated samples were completely disintegrated and delaminated. The SEM images in Figure 4.2 show a significant change in the microstructure of both dense and porous layers, especially in an area that directly contacted with the impregnation solution. In this area, the intergranular fracture which usually happens in weak grain boundaries was observed. The high magnification image in Figure 4.3d reveals the faceted individual grains. It was found that the change of the microstructure appeared deep into the dense BCZY layer where it was not directly in contact with the solution. It seems that the impregnation solution can diffuse into the grain boundary and continuously react with the BCZY dense layer.

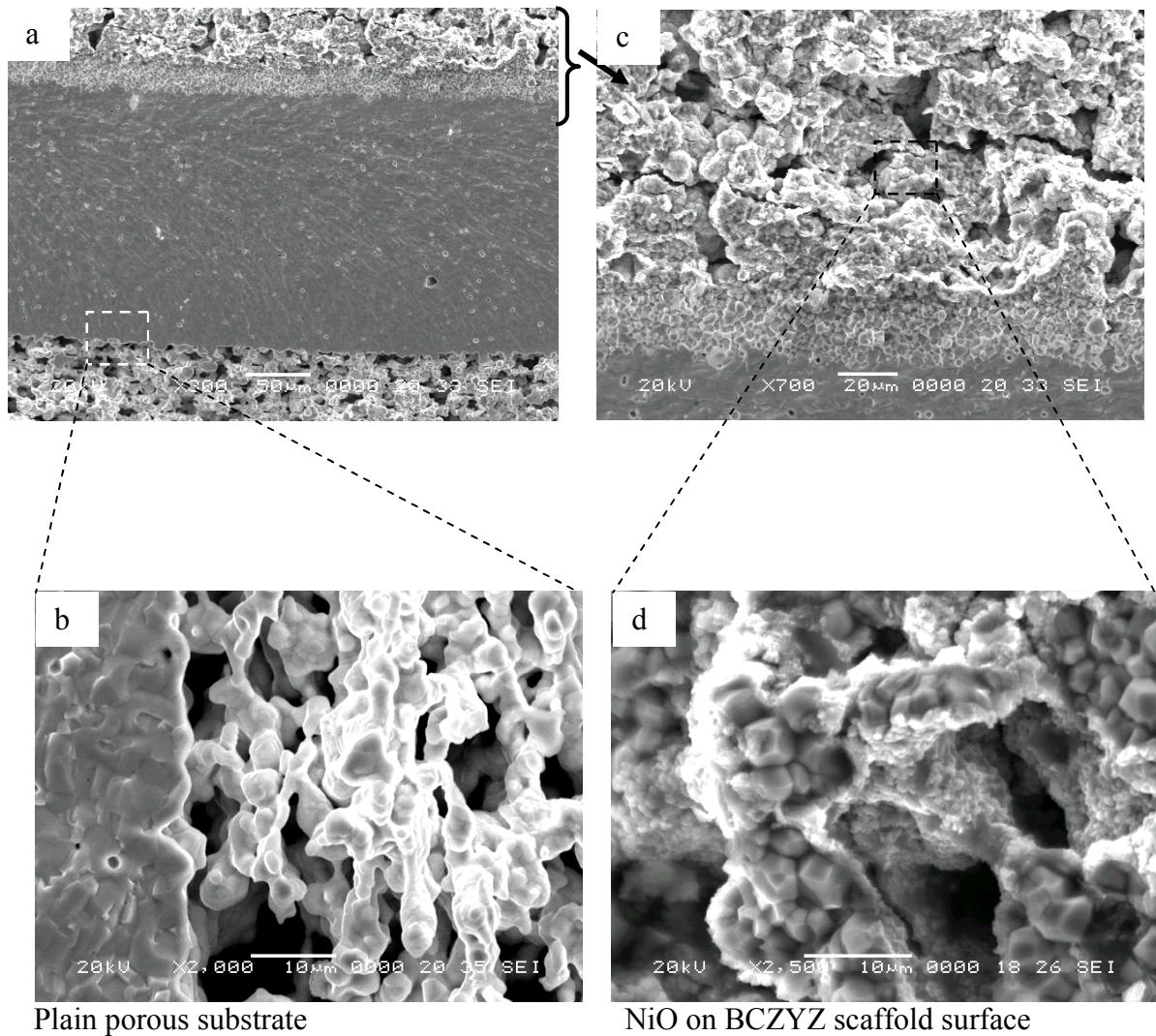


Figure 4.2 SEM images of fracture-cross section of three-layer BCZYZ membrane with an impregnated porous layer. (a) porous-dense-porous membrane with Ni-impregnated layer on top layer, (b) higher magnification of porous layer without impregnation, (c) and (d) higher magnifications of Ni-impregnated layer.

It was speculated that water of crystallisation in hydrated nickel nitrate may react with the BCZYZ ceramic and cause the degradation. Bhide and Virkar^[9] studied the effect of boiling water on the chemical stability of barium cerates. They reported that the degradation of these oxides in contact with the boiling water was severe and the kinetics of the decomposition should be proportional to the surface area. Therefore, the reaction seems to take place at the grain boundary as the sample became porous after being exposed to the boiling water. The reaction between water and the barium cerates was proposed as follows^[9].



Although the firing temperature in this study of 350 °C is much higher than the boiling water, it is possible that the above reaction is still favourable at this temperature.

Based on the idea of water attacking the grain boundaries still occurring at 350 °C, an increase of the firing temperature would completely remove the water out of the ceramic structure. Hence, the firing temperature was increased to 650 °C and the SEM results in Figure 4.3 show no sign of degradation in BCZYZ ceramic after repeating the impregnation more than 10 times. The NiO particles are evenly distributed on the BCZYZ surface with particle sizes in the range of hundred of nanometres as usually found in impregnated particles^[10].

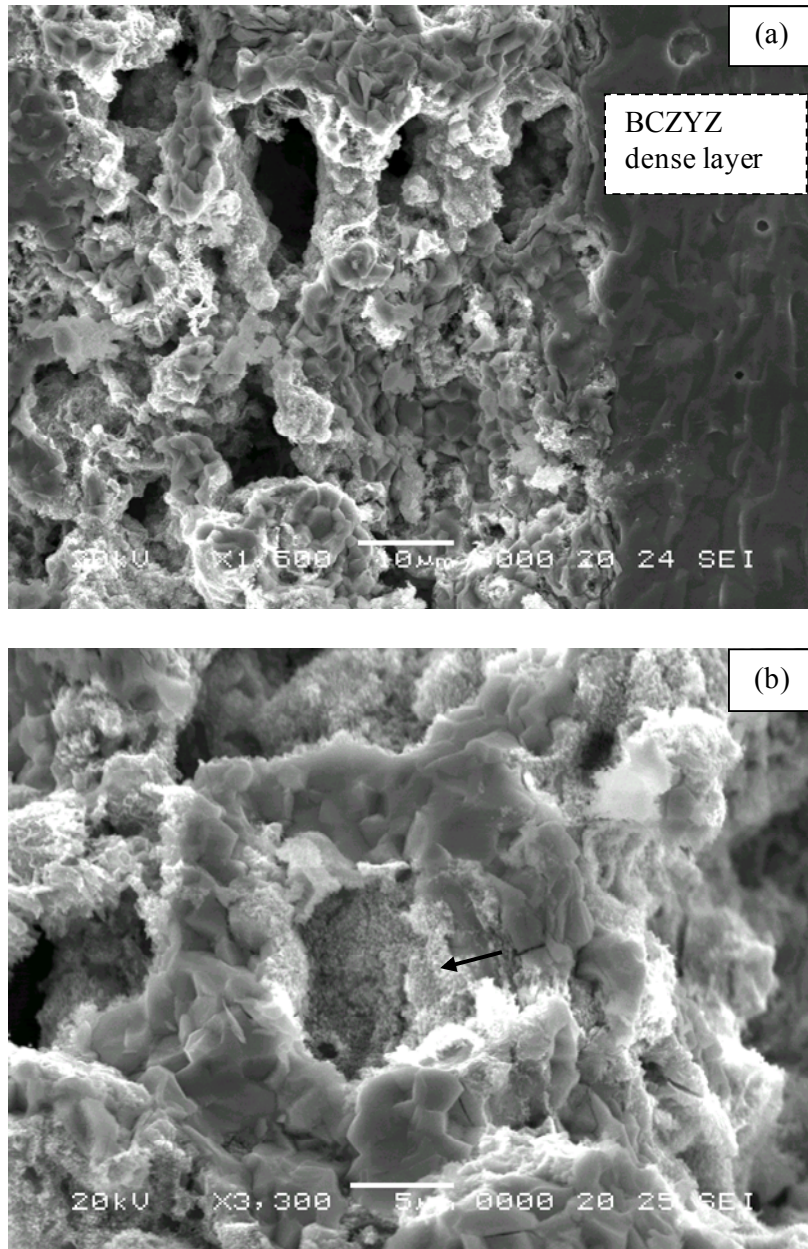


Figure 4.3 SEM images of fracture surface of Ni impregnated sample when using firing temperature at 650 °C (a) x1500 and (b) x3300. The arrow indicates NiO particles deposited on BCZYZ porous skeleton.

4.3.2 Phase compositions of impregnated electrodes

Phase identification of three impregnated electrodes prepared from metal nitrates was determined by X-ray diffraction (XRD). Figure 4.4 displays the XRD patterns from the surfaces of three electrode composites comprising of Ni, Ni with CeO₂ addition (NiCe) and Fe electrodes. For comparison, an XRD pattern of the BCZYZ porous layer is also included. After the decomposition of nitrates at 650 °C, XRD peaks of NiO (PDF no. 4-835), a mixture of CeO₂ (PDF no. 34-394) and NiO and Fe₂O₃ (PDF no. 33-664) were revealed in Ni, NiCe and Fe impregnated electrodes, respectively.

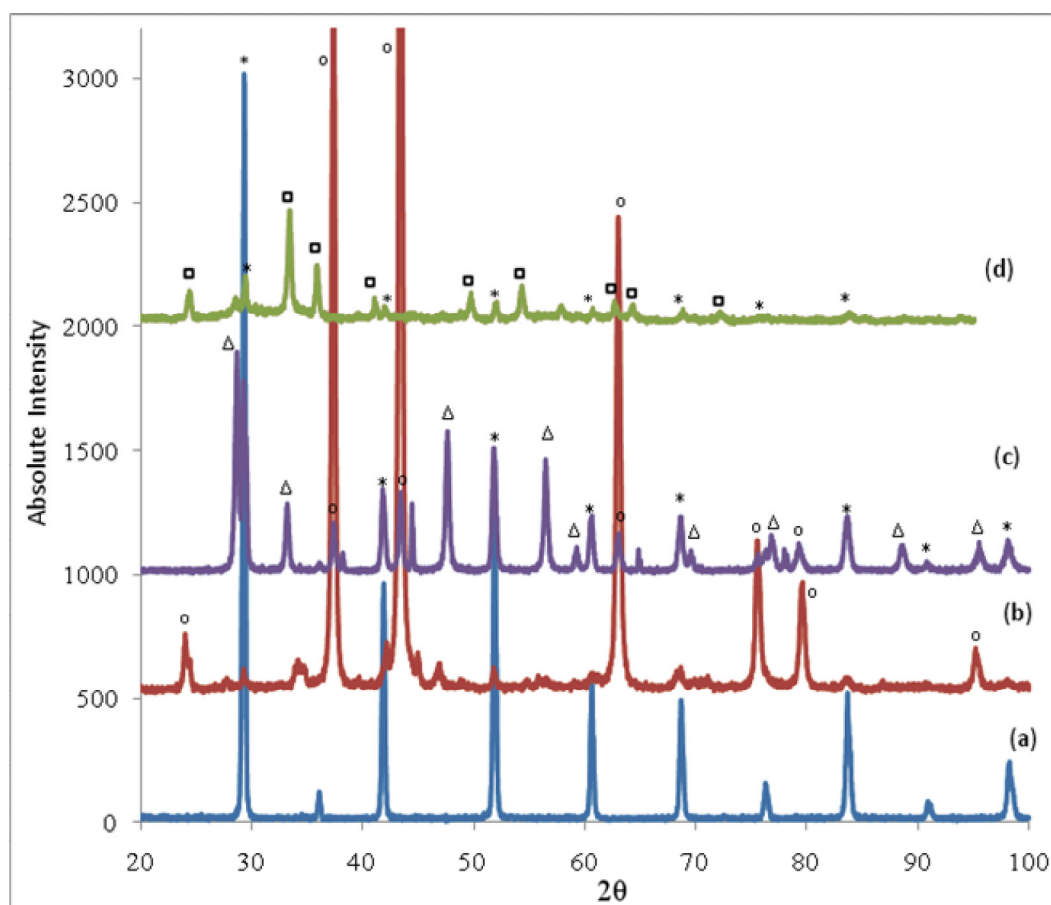


Figure 4.4 XRD patterns of impregnated electrodes before testing (a) BCZYZ porous substrate (b) Ni electrode (c) NiCe electrode and (d) Fe oxide electrode. The symbols indicate: (*), BCZYZ; (o), NiO; (Δ), CeO₂; and (□), Fe₂O₃ peaks.

4.3.3 Performances of Ni impregnated anodes in H₂ atmospheres

Various contents of NiO in the electrode composites were investigated. Also, the metal that is capable of being a current collector was also demonstrated. The current collector plays an important role in providing efficient electric contact between electrode and electrical connections. However, it should neither react with the electrode material nor suppress the catalytic activity of the electrode.

For the Ni-based electrode, two kinds of metal current collectors, Pt and Au, were studied. The results showed that the painted Au reacted with the Ni electrode after testing in reducing atmosphere. Pt was much more stable than Au, therefore it was used as the current collector throughout the experiment. The electrode polarisation of cells with varying contents of the impregnated NiO was investigated in humidified and non-humidified 5% H₂ or pure H₂ atmospheres. The AC impedance data were plotted using Zview software. So far, only a few detailed studies has been published for electrochemical characterisation of Ni-proton conductor composite electrodes^[11-13]. Therefore, the interpretation of the observed data will be compared with the information obtained from the experiments on Ni-YSZ composites in the literature.

4.3.3.1 Ni electrodes without catalyst addition

Symmetrical cells with 1:1, 0.5:1 and 0.3:1 w/w of NiO:the BCZYZ porous support were prepared. Figure 4.5 exhibits the AC impedance spectra of these cells plotted as a function of temperature in humidified (3% H_2O) 5% H_2 /Ar after correction for Pt leads resistance of 1 Ω . Most of the impedance plots consist of at least three major contributions, an ohmic resistance and two overlapping depressed semicircles. The ohmic resistance (R_s) which includes the resistances from electrolyte and electrode materials can be estimated from the high frequency intercept at the real axis. Hence, the polarisation resistance (R_p) of the electrode occurs at lower frequencies than the ohmic resistance and can be estimated from the intercepts of high- and low-frequency contributions with the abscissa. For a symmetrical cell, the attained R_p value must be divided by two as the correction for two identical electrodes used in the cell. From the impedance spectra, the associated capacitance of each electrode response can be interpreted by fitting the spectrum with an equivalent circuit using Zview software. In this experiment, an equivalent circuit, $LRs(R_1CPE_1)(R_2CPE_2)$, is one of several possible circuits corresponding to the impedance data. The circuit consists of an inductance (L) introduced by the instrument, the ohmic resistance (R_s) and two sets of a resistor (R_1 and R_2) in parallel with a constant phase element (CPE_1 and CPE_2). The χ^2 values were in the range of 10^{-5} - 10^{-6} . This circuit is consistent with the behaviour of the impedance suggesting at least two rate-limiting processes exist in the electrode reactions and can be applied to the impedance data obtained at 450-700 $^\circ\text{C}$ for all Ni-BCZYZ electrodes. However at 400 $^\circ\text{C}$, the typical equivalent circuit above could not be fitted with the impedance of 1:1 NiO:BCZYZ electrode and an additional set of R in parallel to CPE was required. This additional contribution presents at high

frequency (10^5 Hz) and its capacitance of 1.3×10^{-9} Fcm⁻¹ corresponding to the grain boundary response which usually appears at low temperature. This grain boundary response was also noticed in 0.5:1 NiO:BCZYZ electrode at the same temperature. An equivalent circuit for NiO:BCZYZ electrodes is shown in Figure 4.6.

For all Ni-BCZYZ electrodes, the higher frequency arc shows stronger temperature dependence than the lower frequency arc. This is due to the fact that the size of the high-frequency arc decreased significantly with the increasing temperature and the summit frequency shifted to the lower frequencies. Note that the capacitance of the high-frequency arc also increased with temperature. For example in the case of the 1:1 NiO:BCZYZ electrode, the capacitances of the electrode contribution at high frequency increase from 4×10^{-5} F/cm² to 9×10^{-3} F/cm² with temperature increased from 400 to 600 °C while the capacitances of the low frequency arc are quite constant with temperature with slightly increasing values from 3×10^{-3} F/cm² to 3×10^{-2} F/cm² at 400 to 600 °C. For lower NiO contents, the behaviour of both high- and low-frequency arcs was similar to the high NiO content but their sizes were greater by a factor of 20. Considering its capacitance and behaviour, the high frequency arc which strongly depends on temperature may arise from the charge transfer process at the electrode/electrolyte interface^[14,15]. However, the overlap between high and low frequency arcs makes it difficult to specify the rate-limiting process for the low frequency contribution.

In this Ni-BCZYZ electrodes, the lowest Rs and Rp values were obtained from the cell with 1:1 NiO:BCZYZ. The Rs and Rp values of this cell at 500 °C are $3.3 \Omega \text{ cm}^2$ and $0.35 \Omega \text{ cm}^2$, respectively. Higher Rs and Rp values were attained from 0.3:1 NiO:BCZYZ electrode, the Rs value was 4 times higher and the Rp value was about 30 times greater than those of 1:1 NiO:BCZYZ electrode. An increase in ohmic

resistances of the lower Ni content electrodes may be attributed to the rise of contact resistance between Ni particles due to lower Ni percolation in the composite. The influence of Ni contents on R_p values suggests the changes in microstructure of Ni electrodes that affects the catalytic activity.

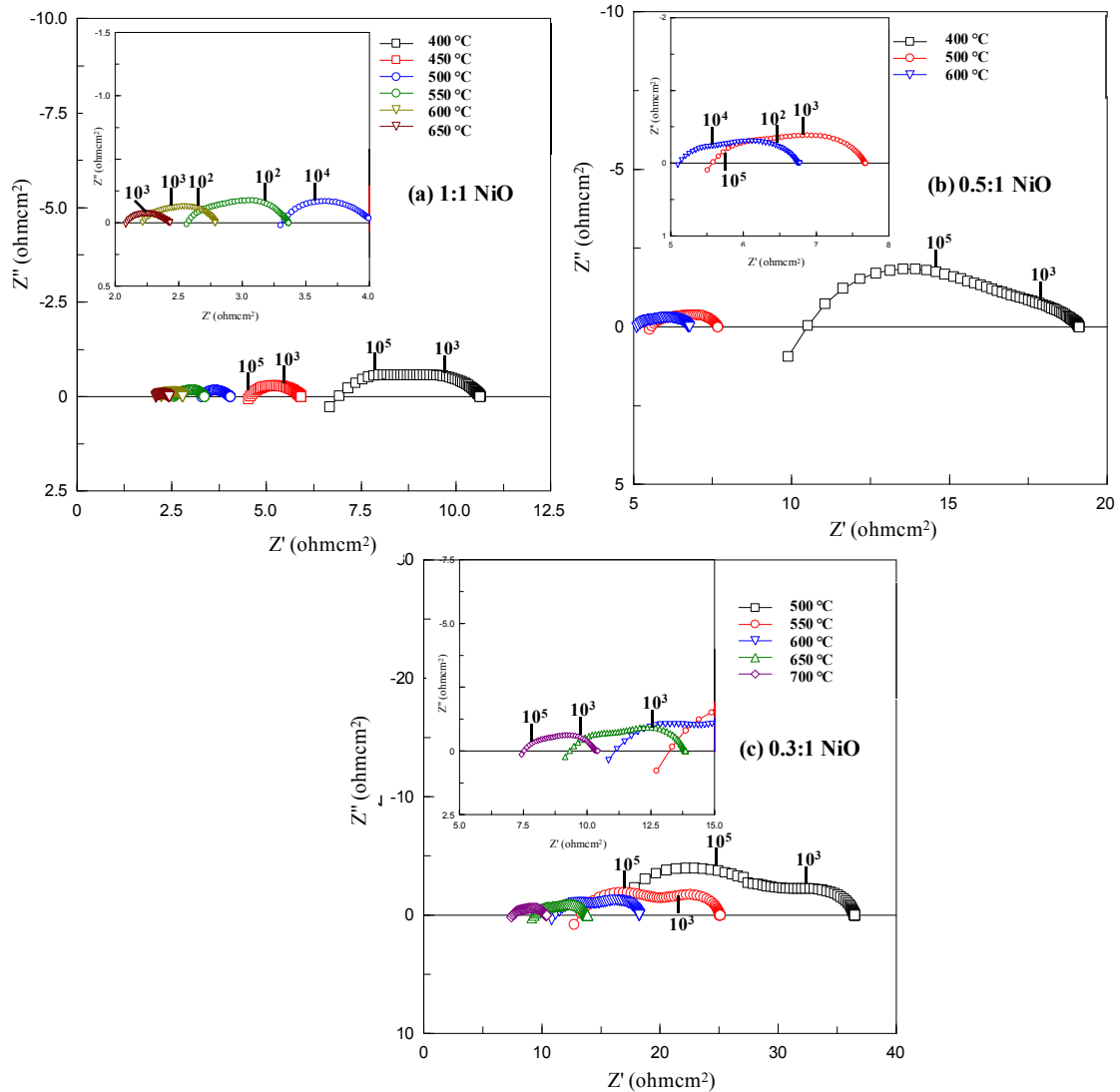


Figure 4.5 AC impedance data under open circuit from the cells with Ni impregnated electrodes in humidified 5% H_2 /Ar (a) 1:1 (b) 0.5:1 and (c) 0.3:1 w/w NiO:BCZYZ porous layer. Thicknesses of electrolyte membrane in those cells are 220, 227 and 212 μm , respectively. The numbers (10^n) indicate frequency in Hz.

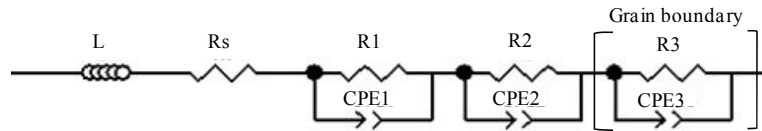


Figure 4.6 An equivalent circuit for the impedance from cells with Ni electrodes

4.3.3.2 Degradation of Ni impregnated electrodes

Although the cells with Ni impregnated electrodes provided reasonable performances, the degradation of these cells with time and thermal cycling was notable. Figure 4.7 shows the selected impedance data of cells with 1:1 and 0.5:1 w/w NiO:BCZYZ electrodes after a deterioration testing. The cell with 1:1 NiO:BCZYZ electrode was tested under three thermal cycles from 400 to 650 °C. The results show increasing in both ohmic and polarisation resistances. Obviously, the impedance at 400 °C was strongly affected by the cell degradation. After two thermal cycles, the R_s value increased by 50% and the R_p value was greater by a factor of 6 at 400 °C. Not only the thermal cycle that affects the impedance, the cell with 0.5:1 NiO:BCZYZ electrode that was kept at 600 °C for 70 h also showed significant changes in the impedance spectra with greater resistances in both high-and low-frequency contributions. It is possible that the acquired NiO particles via the ion impregnation were in nano-size and easily sintered or agglomerated in reducing atmosphere at these working temperatures. Therefore, the stability of Ni electrode needs to be improved. By introducing another phase such as an oxide which is stable in reducing atmosphere into NiO matrix, the sintering problem of Ni particles should be resolved. CeO_2 is one of oxides that can be used to improve the distribution of Ni particles^[17].

Advantageously, the catalytic activity of CeO_2 for the redox reactions has been proved to enhance the cell performance^[16-18].

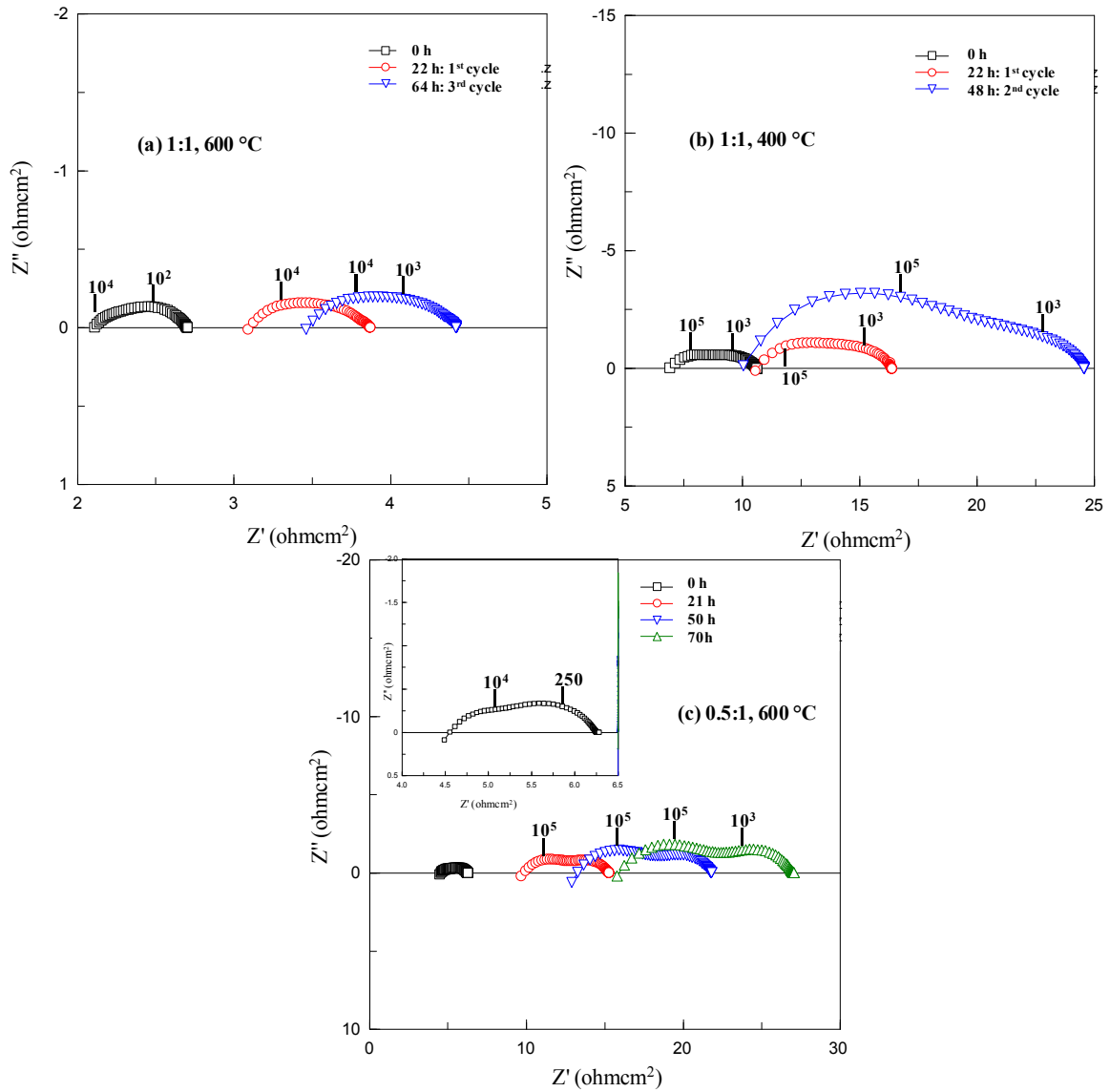


Figure 4.7 Comparison of cell degradation of symmetrical cells with NiO:BCZYZ electrodes in humidified 5% H_2 /Ar (a) 1:1 at 600 °C (b) 1:1 at 400 °C and (c) 0.5:1 at 600 °C. The numbers (10^n) indicate frequency in Hz.

4.3.3.3 Ni electrodes with CeO₂ addition

The mixed solutions of Ce(NO₃)₃ and Ni(NO₃)₂ in different ratio were used for the impregnation. Two different compositions of the NiO and CeO₂ mixtures were NiO 35wt% + CeO₂ 15 wt% (35Ni15Ce) and NiO 25 wt% + CeO₂ 10 wt% (25Ni10Ce), with respect to the weight of BCZYZ porous support. Figure 4.8 shows the impedance spectra of these cells which were similar to those of cells with the Ni electrodes. At lower temperatures (400-450 °C), the equivalent circuit suggested three electrode responses, LR_s(R₁CPE₁)(R₂CPE₂)(R₃CPE₃). When increasing the temperature, the electrode response at higher frequency became smaller. Therefore, only two electrode responses were notified.

The high frequency contribution with associated capacitance of $9 \times 10^{-6} - 1 \times 10^{-4}$ F/cm² which disappears at higher temperature may result from the charge transfer process. The contributions at mid-and low-frequencies also depend on temperature. The corresponding capacitances of these contributions were close to each other within the range of $3 \times 10^{-3} - 5 \times 10^{-2}$ F/cm² from 400-600 °C. Note that when increased the temperature to 650-700 °C, the medium- and low-frequency arcs were no longer separated and an additional arc with summit frequency at 4-6 Hz was emerged. The capacitance of this additional arc of 2-4 F/cm² indicates that another type of electrode process had emerged. It can probably be attributed to the concentration polarisation in the gas above the electrode structure that is usually observed at high temperatures^[19].

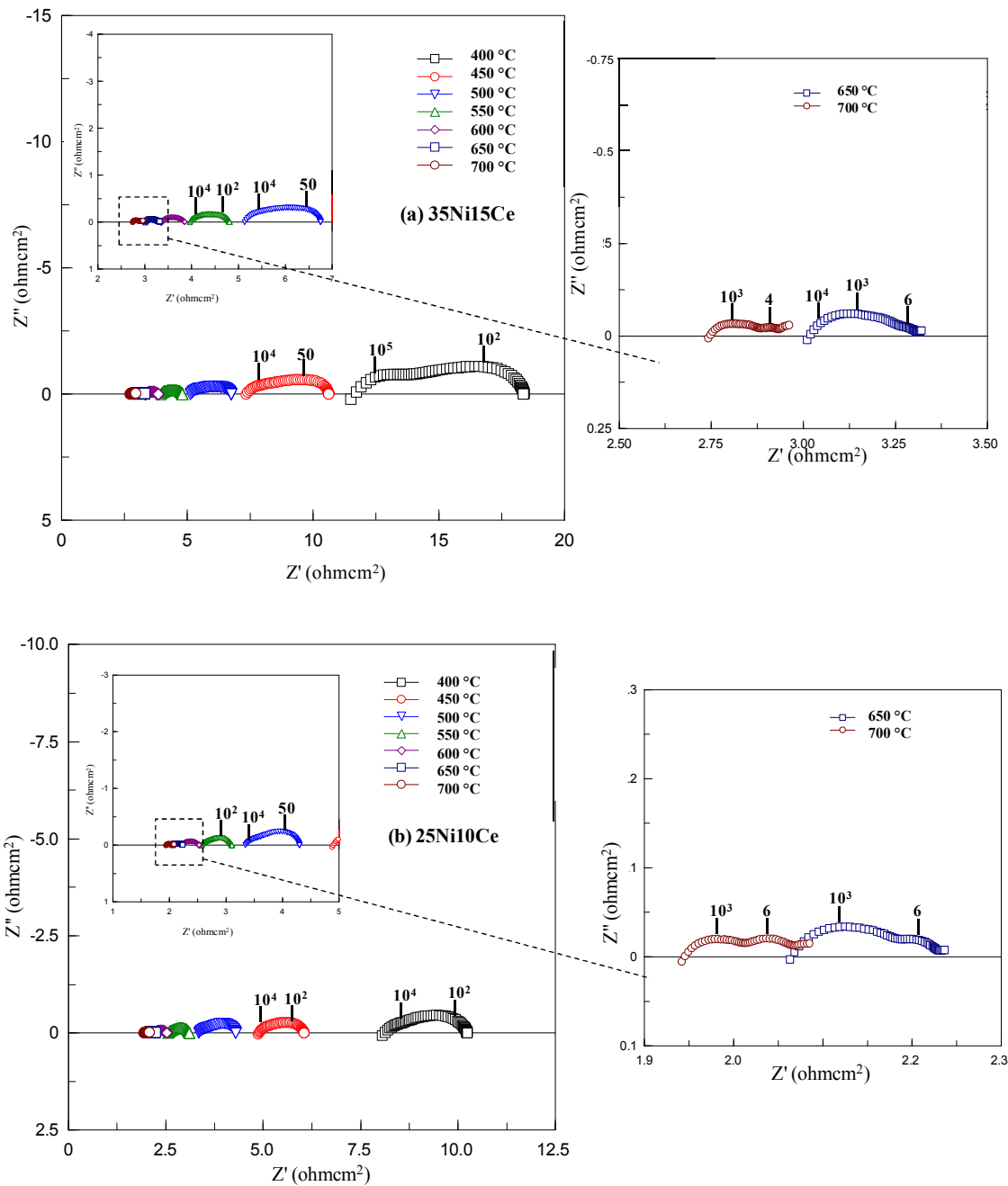


Figure 4.8 AC impedance data under open circuit from the cells with CeO₂-NiO co-impregnated electrodes at different temperatures in humidified 5%H₂/Ar. (a) 35Ni15Ce and (b) 25Ni10Ce. Thicknesses of those cells were 250 μ m. The numbers (10^n) indicate frequency in Hz.

4.3.3.4 NiO-CeO₂ electrodes in different H₂ partial pressures

In this study, the H₂O content was kept constant while the H₂ gas was switched from 5%H₂/Ar to pure H₂. With increasing H₂ partial pressure, the impedance dramatically decreased. Typical impedance spectra shown in Figure 4.9 represent a significant reduction of the low frequency contribution when operating in pure H₂ for both 35Ni15Ce and 25Ni10Ce cases. At 450 °C, the dependence on H₂ partial pressure of the lower frequency arc indicates that this arc with the summit frequency of 100-200 Hz would involve hydrogen adsorption/ diffusion processes on the electrode surface^[15]. At 650 °C, the arc with the summit frequency of 4-6 Hz observed in 5%H₂ was invisible when operated in pure H₂. The limiting process of this arc must be the gas conversion limitation which depends on gas concentration and can be observed only at high temperature.

The plots of R_s and R_p values obtained from these cells are shown in Figure 4.10. A cell with 25Ni10Ce electrode showed better performance than a cell with 35Ni15Ce electrode in both 5%H₂ and pure H₂. With increasing temperature, the polarisation resistance of the 25Ni10Ce electrode dramatically decreased from 0.35 Ω cm² at 450 °C to 0.02 Ω cm² at 650 °C. Comparing with Ni/YSZ anodes, the polarisation resistance for conventional Ni/YSZ cermet anode in humidified H₂ was in the order of 0.16 Ω cm² at 850 °C^[20], 8 times higher than the results reported here. The key factor for this high electrode performance could be CeO₂ that provides electronic conduction while preventing Ni particles from agglomerating. It is also possible that the presence of CeO₂ may enhance the catalytic activity of Ni for H₂ oxidation reaction. Comparing between 25Ni10Ce and 35Ni15Ce, the higher Ni content may cause poorer microstructure that depresses electrode performance.

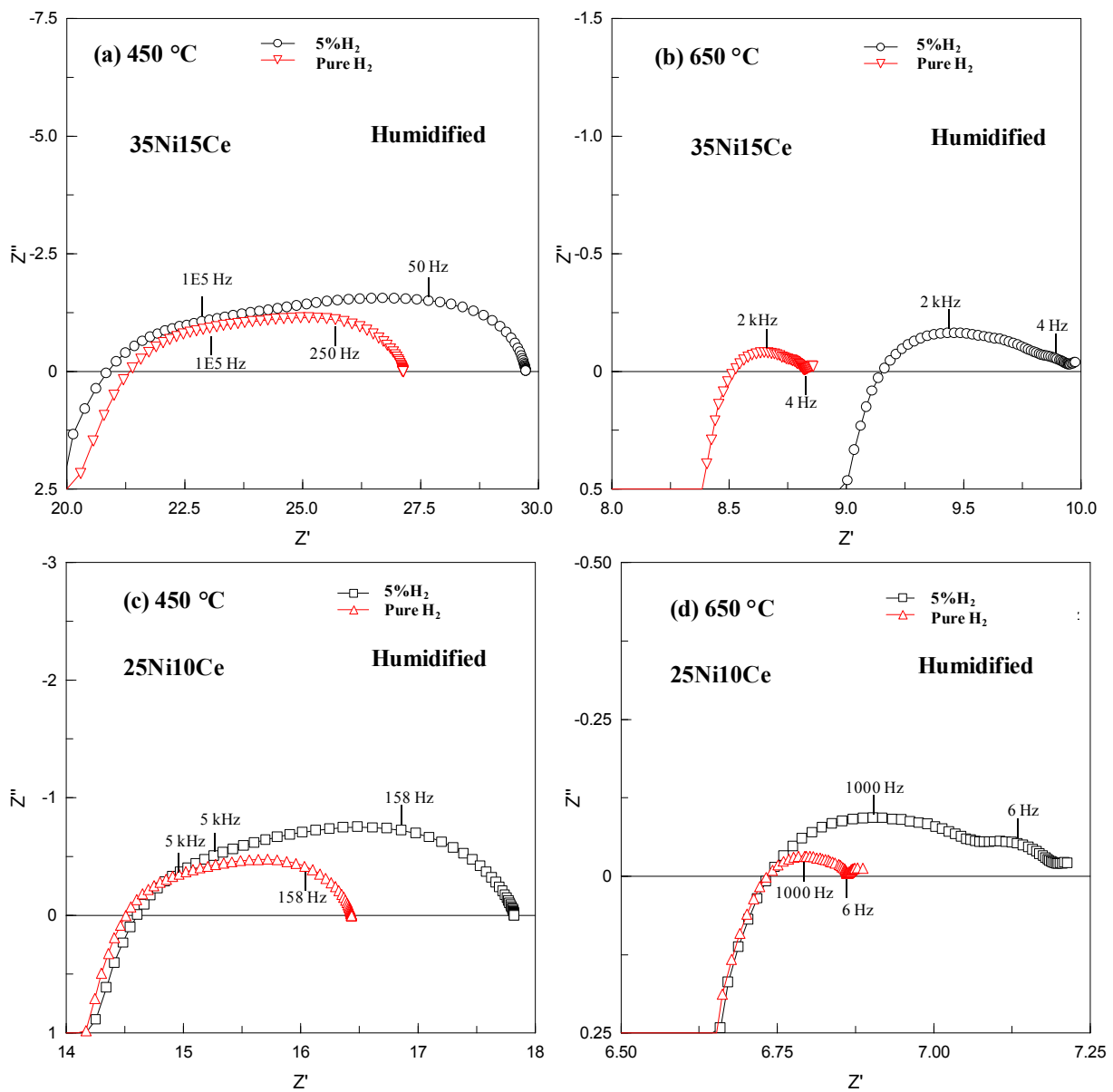


Figure 4.9 Comparison of the impedance spectra of cells with 35Ni15Ce electrode and 25Ni10Ce electrode in humidified 5%H₂ and pure H₂ at (a) 450 °C and (b) 650 °C for 35Ni15Ce electrode and at (c) 450 °C and (d) 650 °C for 25Ni10Ce.

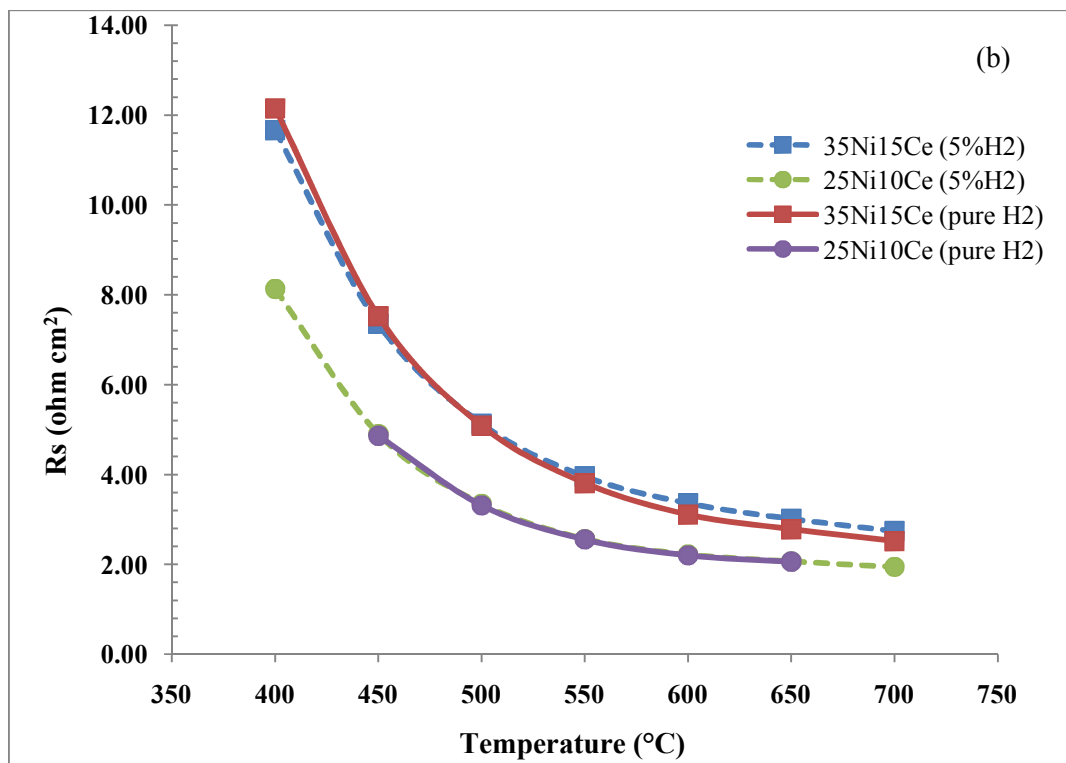
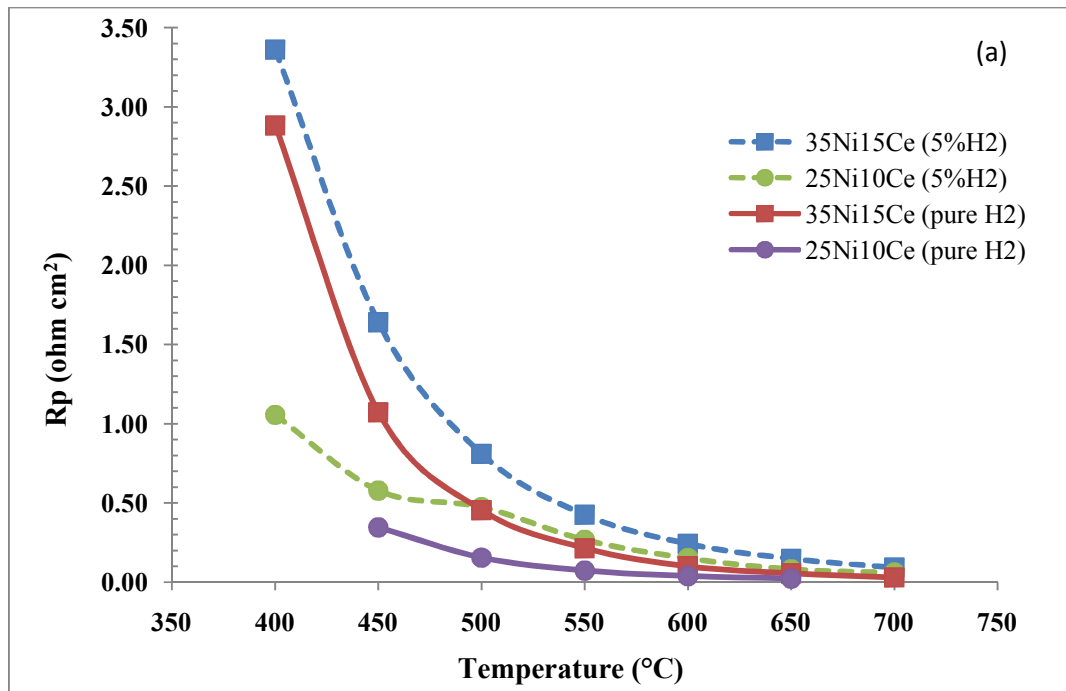


Figure 4.10 Temperature dependences of (a) the polarisation resistances and (b) the ohmic resistances of 35Ni15Ce cell (\square) and 25Ni10Ce cell (\circ) in humidified 5% H₂ (---) and pure H₂ (—).

4.3.3.5 Stability of NiO-CeO₂ electrodes

Comparing between 25Ni10Ce and 1:1 NiO:BCZYZ electrodes, 25Ni10Ce electrode showed slightly better performance but much greater stability than the 1:1 NiO:BCZYZ electrode. The stability tests were carried out under similar conditions with those performed in NiO:BCZYZ electrodes. The sample was kept in humidified 5% H₂ and the temperature was decreased from 600 to 400 °C before increased back to 600 °C for one thermal cycle. Impressively, the 25Ni10Ce electrode exhibited excellent stability, much better than the 35Ni15Ce electrode as shown in Figure 4.11. The low stability of 35Ni15Ce electrode may relate to the higher content of Ni in the composite. For the Ni-based electrode, it is difficult to avoid sintering and coarsening of Ni particles under reducing atmosphere, especially at high temperature.

Comparing to the 1:1 NiO:BCZYZ electrode, the R_s and R_p values from the stability tests of 1:1 NiO:BCZYZ and 25Ni10Ce cells are plotted as a function of operating duration in Figure 4.12. Obviously, the cell with 25Ni10Ce electrode provides superior performances and stability, especially when operated at low temperature (400 °C).

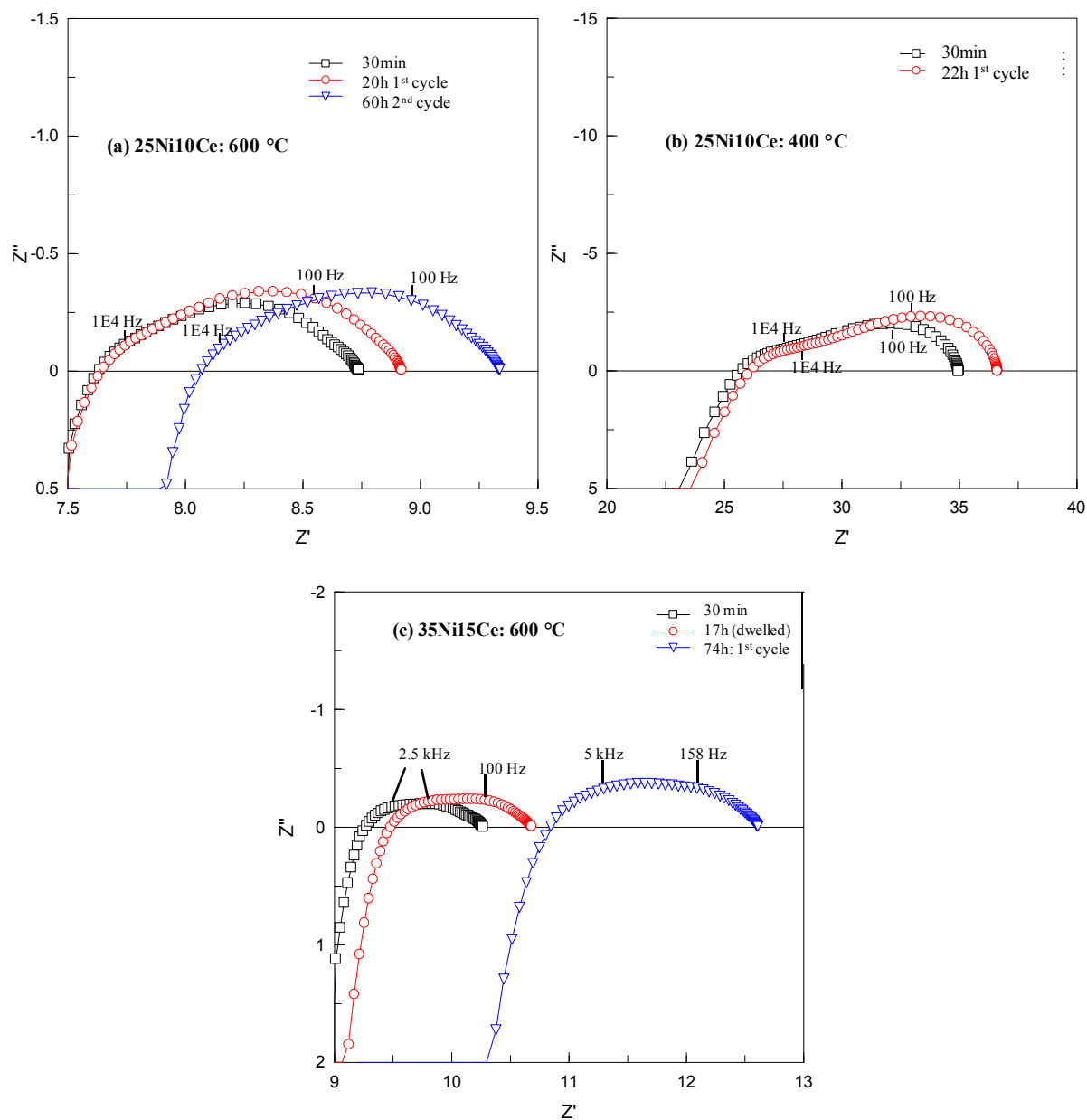


Figure 4.11 Comparison of cell degradation as function of time and thermal cycle from 600 to 400 °C in cells with different NiO-CeO₂ electrodes. (a) and (b) 25Ni10Ce electrode at 600 °C and 400 °C, respectively and (c) 35Ni15Ce electrode at 600 °C.

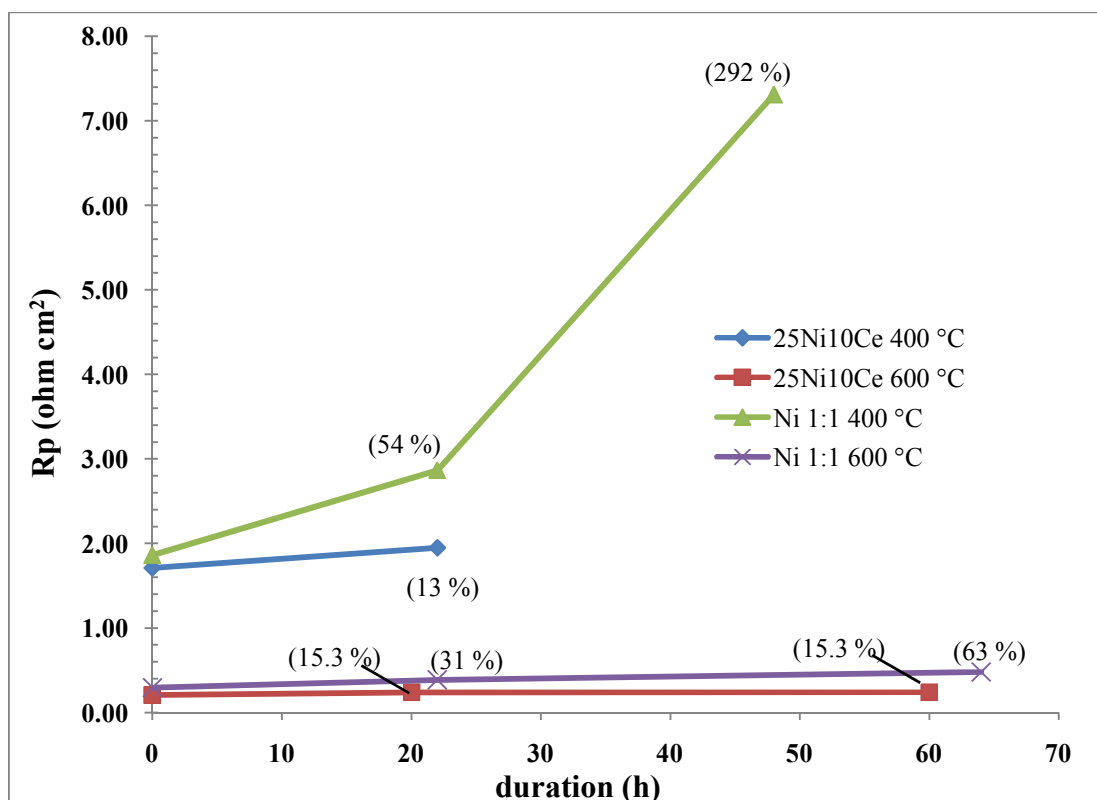
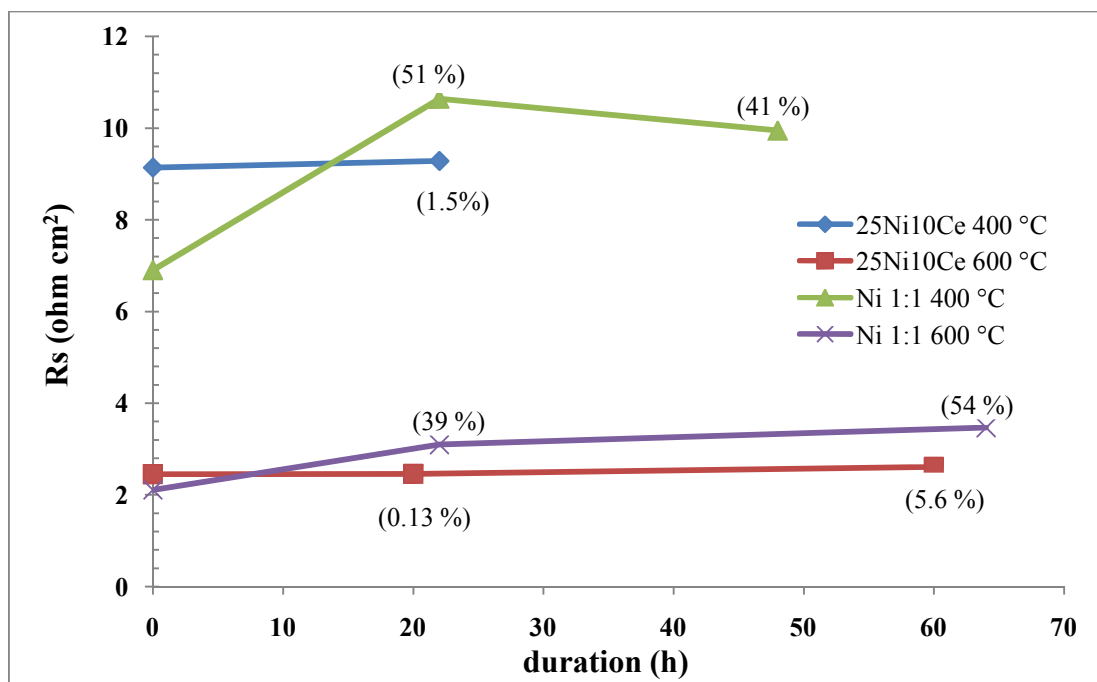


Figure 4.12 Plots of R_s and R_p values versus time comparing electrode stabilities in humidified 5% H_2 of pure Ni electrode (1:1 NiO:BCZYZ) and NiO-CeO₂ electrode (25Ni10Ce) at 400 and 600 °C. The number in the brackets indicates the increased percentage of each resistance compared to the starting values.

4.3.3.6 NiO-CeO₂ electrodes in different regimes of H₂O contents

The cell with 25Ni10Ce electrode in 5%H₂/Ar was tested under different water content atmospheres in order to confirm the appearance of proton conduction in this BCZYZ membrane cell. In the presence of the water vapour, protons from water also take part in the electrolyte conductivity of the proton conductor.

The measurement was performed from 600 to 400 °C. The sample was kept in humidified 5%H₂ before changing to non-humidified 5%H₂ and then switching back to humidified condition again. Note that the impedance was carried out periodically until reaching a steady state in each atmosphere. Normally, the equilibration time was more than 1 h. Figure 4.13 depicts that the impedance spectra in non-humidified 5%H₂/Ar have higher ohmic resistance than in humidified atmosphere. This is related to the loss of protons from the crystal lattice under low partial pressure of water. The increase in R_s value under non-humidified condition was obvious at higher temperature. It is possible that the kinetics of diffusion of protons out of the electrolyte lattice is faster at higher temperature. After switched back to humidified atmosphere, the ohmic resistance was set back to its original value which confirms that the H₂O uptake is a reversible process. For the polarisation resistance, the change in the water content did not affect the shape of the impedance curves but decreased the size of the low frequency contribution. The dependences of the low frequency contribution on the fraction of H₂ and water vapour suggest that adsorption/dissociation of H₂ or surface diffusion of hydrogen species on the Ni-based electrode could be the rate-limiting processes for this low frequency contribution^{[15,21-}

22]

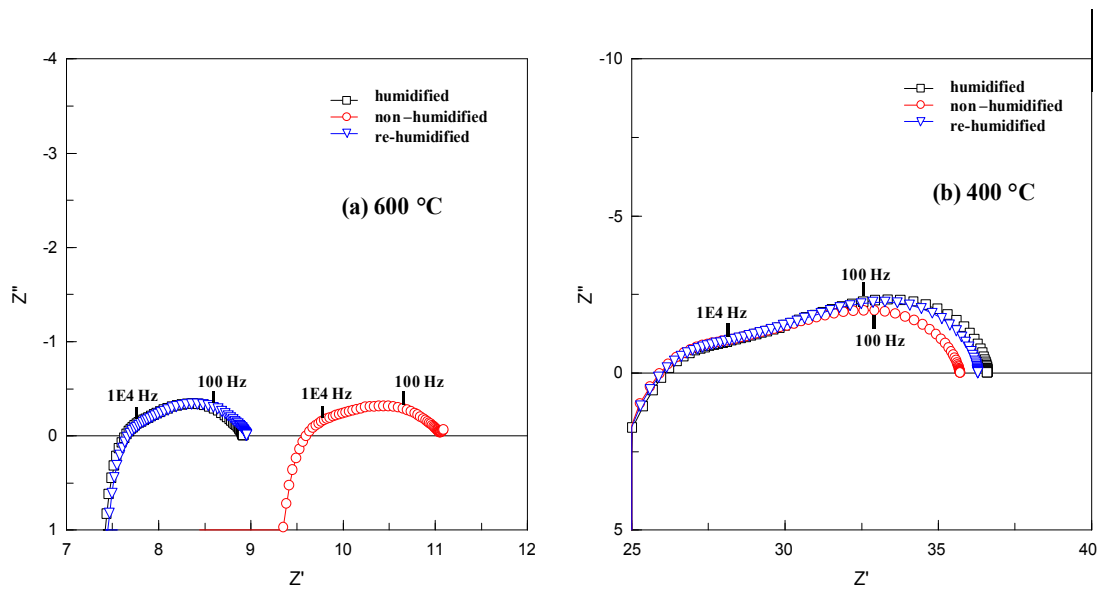


Figure 4.13 Behaviour of 25Ni10Ce electrode under the atmospheres with different water contents at (a) 600 °C, (b) 450 °C, and (c) 400 °C. (□) Humidified 5% H₂ and (○) non-humidified 5% H₂.

4.3.3.7 Comparison of Ni impregnated electrodes and painted Pt electrode

It is known that Pt is a good catalyst for H₂ oxidation. The presence of Pt as a current collector on the Ni-based electrode would interfere the catalytic activity of the interesting electrode. Therefore, the catalytic activity of Pt morphology used in this experiment needed to be clarified. A symmetrical cell with Pt electrodes was prepared by painting the Pt paste directly on the BCZYZ electrolyte dense membrane. The results of this cell in humidified 5% H₂ are shown in Figure 4.14. The impedance spectra of the Pt electrode show large polarisation arcs with at least two rate-limiting processes similar to that of the Ni electrodes but are much larger in size by almost two orders of magnitude. The high-frequency contribution shows strong temperature

dependence. Nevertheless, being ~200 times higher in the polarisation resistance of the Pt electrode confirms that the excellent catalytic activity that caused low polarisation resistance in the 25Ni10Ce electrode definitely came from the composite itself.

Figure 4.15 displays the plots of polarisation resistances as a function of temperature from the Ni impregnated electrodes, 1:1 NiO:BCZYZ and 25Ni10Ce, and painted Pt electrodes. From the slope of the plots, the activation energies of the H₂ oxidation reaction on Pt, 1:1 NiO:BCZYZ, and 25Ni10Ce electrodes are 0.56, 0.54 and 0.61 eV, respectively. These values were consistent with the value of 0.7 eV obtained from Pt and Ni metal electrodes in a point contact with a proton conductor, SCY, at various H₂ contents and 600-800 °C^[23]. Comparing with YSZ, these values are much lower than the values of the Ni-YSZ electrode which are in the range of 0.7-1.3 eV^[19]. The lower activation energy of the Ni-BCZYZ electrode probably comes from the presence of BCZYZ in the electrode composite as it may take part in the catalytic reaction of the H₂ oxidation.

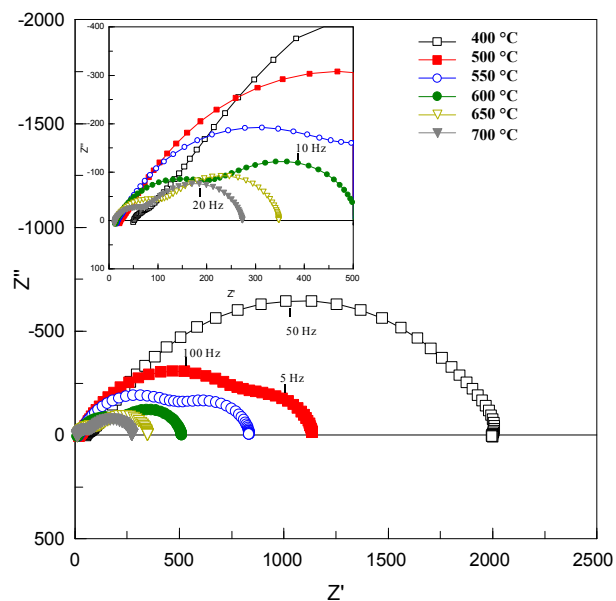


Figure 4.14 Impedance spectra of thin BCZYZ electrolyte cell with Pt electrodes tested as function of temperature in humidified 5% H₂/Ar. Electrolyte thickness is 230 μm and electrode active area is 0.24 cm².

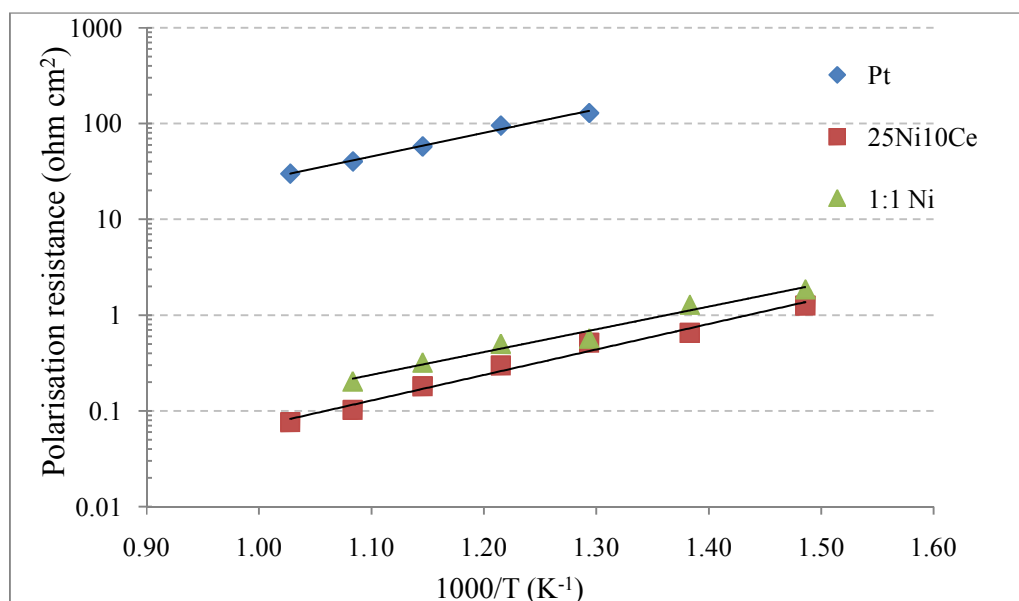
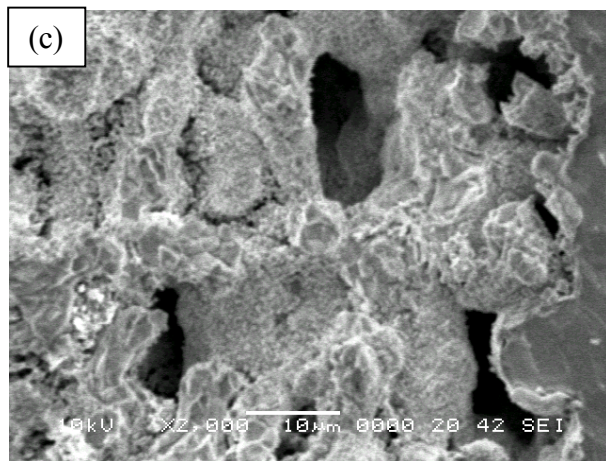
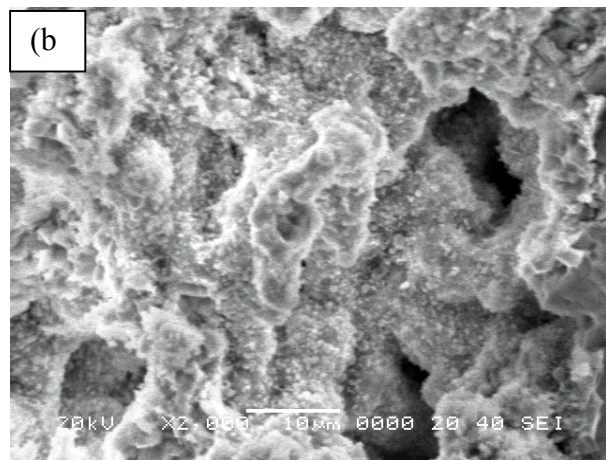
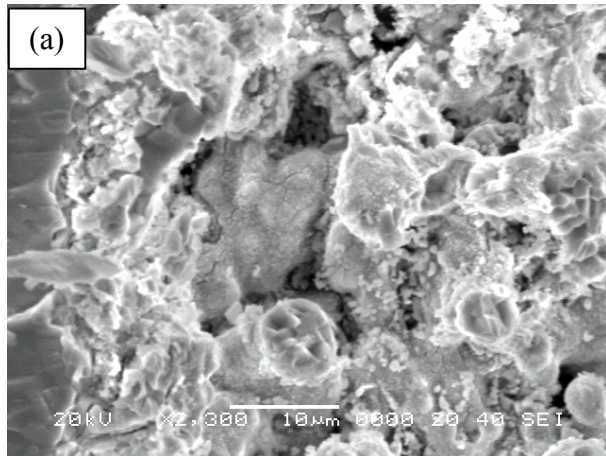


Figure 4.15 Comparison of polarisation resistances as a function of temperature tested in humidified 5% H₂ from (♦) Pt, (■) 25Ni10Ce, and (▲) 1:1 NiO:BCZYZ electrodes.

4.3.3.8 Microstructure of Ni impregnated electrodes after testing

The microstructures of the Ni impregnated electrodes after testing were revealed in Figure 4.16. Comparing to the microstructure of NiO crystallites before testing in Figure 4.3, there is a significant change in the microstructure of Ni particles after tested in reducing atmospheres. The thin, flake-like NiO crystallites had changed into small Ni clusters with less than 1 μm in diameter. The clusters of the Ni particles became larger in the higher Ni content electrodes. The Ni-CeO₂ electrodes show distinct microstructures. In 35Ni15Ce electrode, a layer of the electrode on BCZY surface was found instead of particle clusters. In the 25Ni10Ce electrode, an even distribution of fine Ni-CeO₂ clusters was revealed which seems to be the reason for its superior electrode performance. Certainly, the proper CeO₂ content promotes the nucleation and limits the growth of the Ni particles. Figure 4.17 illustrates the even distribution of Ni and CeO₂ inside the 25Ni10Ce electrode composite using EDS elemental analysis.



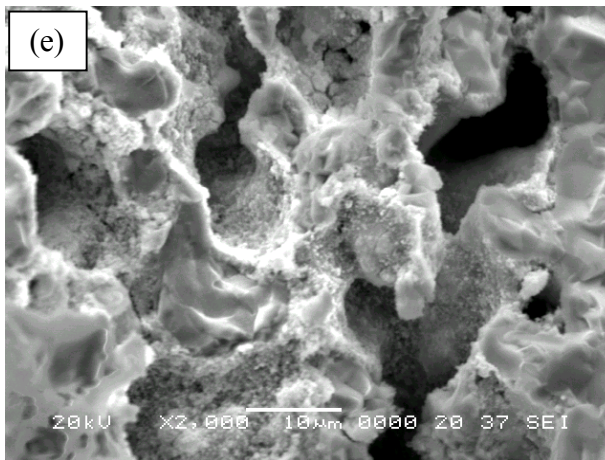
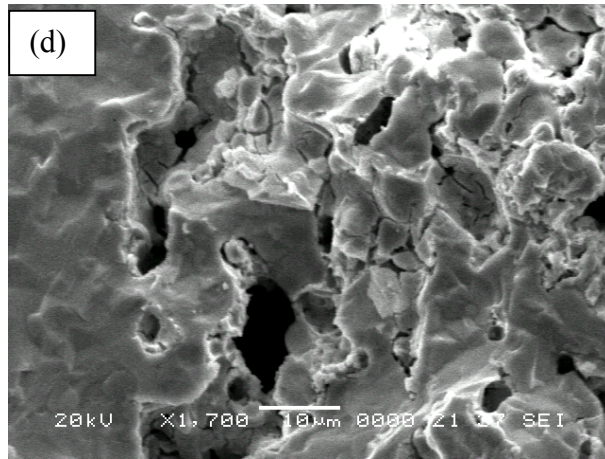


Figure 4.16 SEM images of Ni and Ni-CeO₂ impregnated electrodes after testing. (a) 1:1, (b) 0.5:1, (c) 0.3:1 NiO:BCZYZ, (d) 35Ni15Ce and (e) 25Ni10Ce.

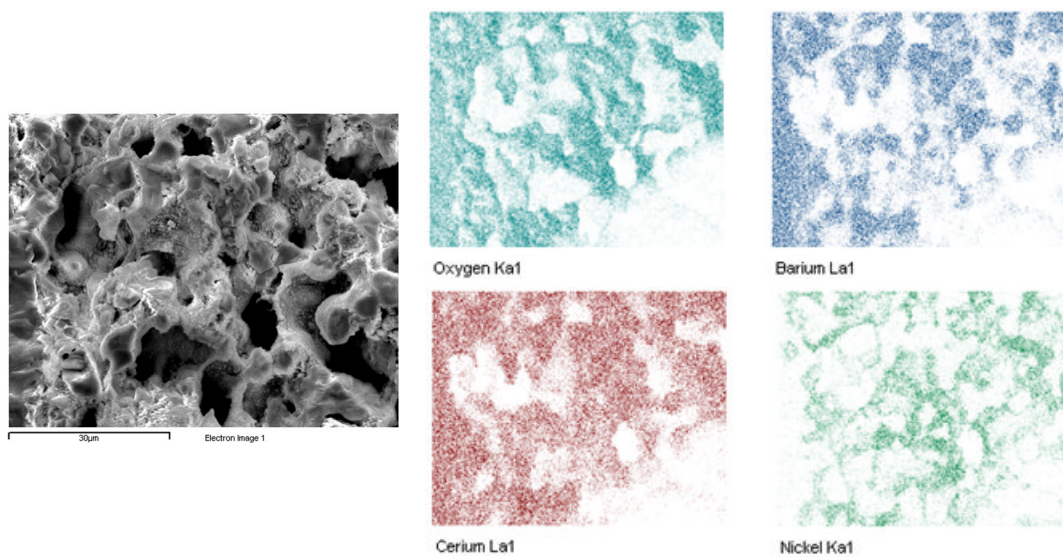


Figure 4.17 EDS elemental analysis of 25Ni10Ce impregnated electrode after testing

4.3.4 Cathode material: impregnated Fe oxide

4.3.4.1 Cell with 1:1 Fe oxide:BCZYZ electrode

A symmetrical cell with 1:1 by weight of Fe oxide: BCZYZ porous substrate was first considered. In this cell, three kinds of metal paste (Au, Pt or Pd) were applied as a current collector. As observed in the Ni impregnated electrodes, Au paste was found reacted with the impregnated Fe after testing. Thus, Pt or Pd paste was used as a current collector in this experiment.

Figure 4.18 shows an example of the impedance spectra from the cell with the 1:1 Fe oxide:BCZYZ electrode using painted Pt as current collector in different regimes of H₂ contents at 550 °C. In humidified 5%H₂/Ar, the impedance data show a small imperfect semicircle at high frequency and a low-frequency spike. When decreased the H₂ content by mixing N₂ along with the 5%H₂, there was no significant change in the size of the high frequency contribution but that of the low-frequency spike was slightly increased. When switched to pure N₂, both high- and low-frequency contributions became dramatically greater with time but the impedance characteristics were still unchanged. It is plausible that the electroactive species for this electrode were hydrogen species, thus the atmosphere with very low H₂ content directly suppressed the electrochemical processes on the Fe surface leading to the increase in polarisation resistance. The low H₂ content atmosphere affected both high- and low-frequency contribution which are related to charge transfer and hydrogen adsorption/diffusion processes, respectively.

The increase of R_s value by a factor of 10 when switching from humidified H₂ to humidified N₂ seems to be incredibly high for the ionic resistance of a 200 μm-thick

BCZYF membrane. It is likely that the increase of R_s value stems from the formation of Fe oxide when operated in N_2 atmosphere. From Ellingham-Richardson diagram, metallic Fe tends to be oxidized in an atmosphere which has an oxygen partial pressure (pO_2) of 10^{-6} Pa or greater^[25]. Data from another instrument containing pO_2 sensor has confirmed that pO_2 of pure N_2 gas is around 10^{-5} Pa at 550 °C. It is likely that a non-conductive Fe oxide layer may be formed at the surface of the Fe electrode resulting in the rise of the contact resistance as exhibited in Figure 4.18. Perhaps, the poor conductance of the Fe/FeO_x dramatically increases the lateral resistance of the electrode reducing the effective contact area.

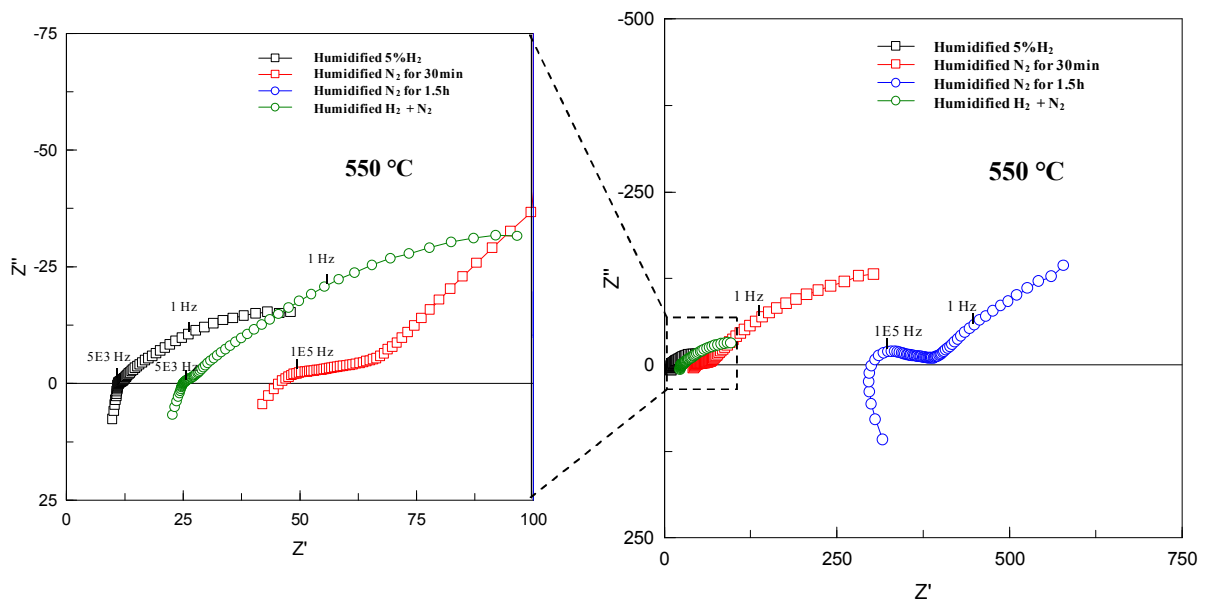


Figure 4.18 AC impedance data of cell with 1:1 Fe:BCZYF electrode in various H_2 content atmospheres at 550 °C. Active area of this cell was 0.35 cm².

4.3.4.2 Microstructure of Fe oxide impregnated electrode

SEM images of Fe oxide electrode before and after testing in Figure 4.19 reveal a dense layer of Fe oxide covering the BCZYF surface. The SEM images of Fe oxide before reduction show an even distribution of large Fe oxide crystallites. After testing, small white particles which are likely to be Fe metal particles appeared all over the Fe layer. The dense morphology of the impregnated Fe may be responsible for large R_p value when operating in humidified N_2 . The dense layer of the impregnated Fe probably blocks the diffusion of the reactant gas and the transport of charge between the electrode/electrolyte interface.

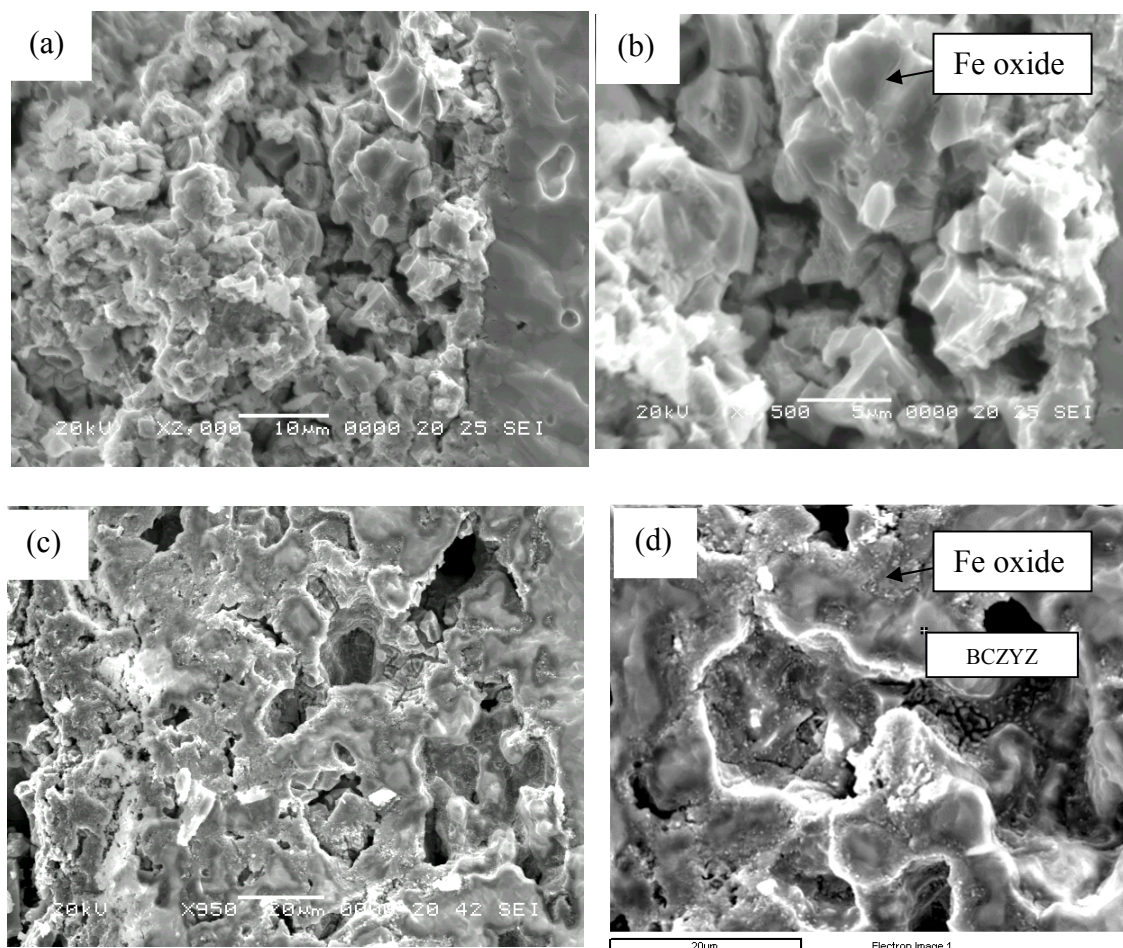


Figure 4.19 SEM image of a fractured cross-section of 1:1 Fe:BCZYF electrode (a)-(b) before and (c)-(d) after testing.

4.3.4.3 Cell with 25 wt% Fe oxide-BCZYZ electrode

With the concern over the additional resistance arisen from the oxidation of Fe, a small content of the impregnated Fe oxide such as 25% by weight of the BCZYZ porous layer was employed. Figure 4.20 displays the impedance spectra under open circuit of the cell with 25 wt% Fe oxide using Pt as current collector. In hydrogen-containing atmospheres, the impedance curves comprise of an imperfect arc at higher frequencies and low frequency spike which were similar to that of the 1:1 Fe oxide:BCZYZ electrode. When increasing temperature, the high frequency arc became smaller and the low-frequency spike turned over into a depressed semicircle. After switching to humidified N₂, the impedance spectra show the increase in both ohmic and polarisation resistances. Apparently, the R_s value in humidified N₂ is 5 times smaller than that found in the 1:1 Fe oxide:BCZYZ electrode and close to the theoretical value. The small R_s value of this 25 wt% Fe electrode in humidified H₂ confirms a good connection between the Fe particles that adequate to reach the percolation threshold. The high frequency contribution with the summit frequency of 1x10⁴ Hz shows strong dependences on both H₂ content and temperature. The charge transfer process between the Fe electrode and the BCZYZ electrolyte interface could be a rate-limiting process for this contribution. For the low-frequency spike which also depends on temperature and H₂ content, the rate-determining process for this contribution could be either the hydrogen adsorption/diffusion or gas concentration polarisation.

Along with the Pt current collector, the impedance data of a cell with 25 wt% Fe oxide electrode using Pd as a current collector are shown in Figure 4.21. The Pd

current collector slightly improved both ohmic and polarisation resistances. It must be the microstructure of these current collectors that affects the performance.

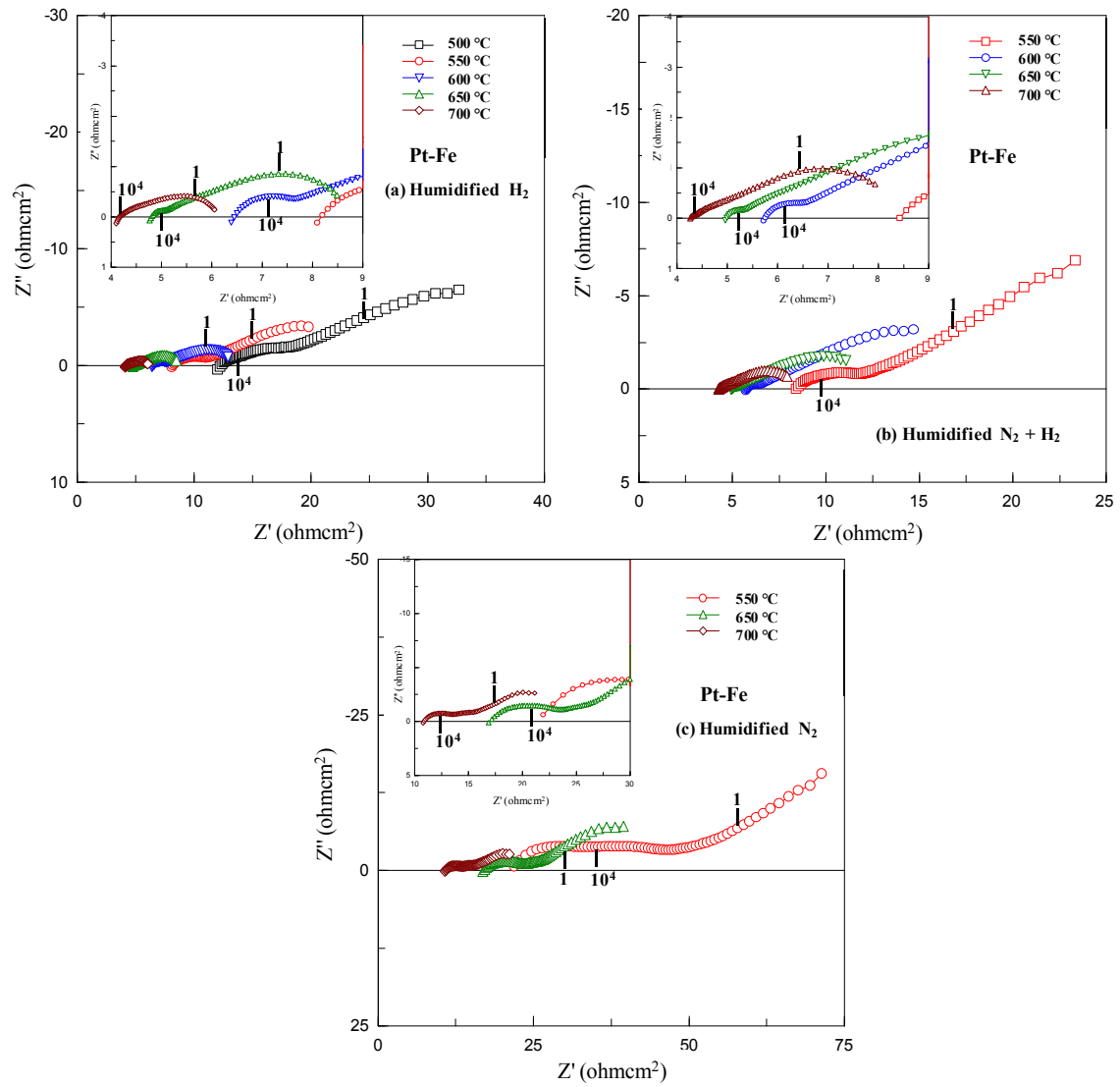


Figure 4.20 AC impedance spectra under open circuit of cell with 25 wt% Fe oxide electrode with Pt current collector in humidified atmospheres as a function of temperature. The numbers (10^4) indicate frequency in Hz.

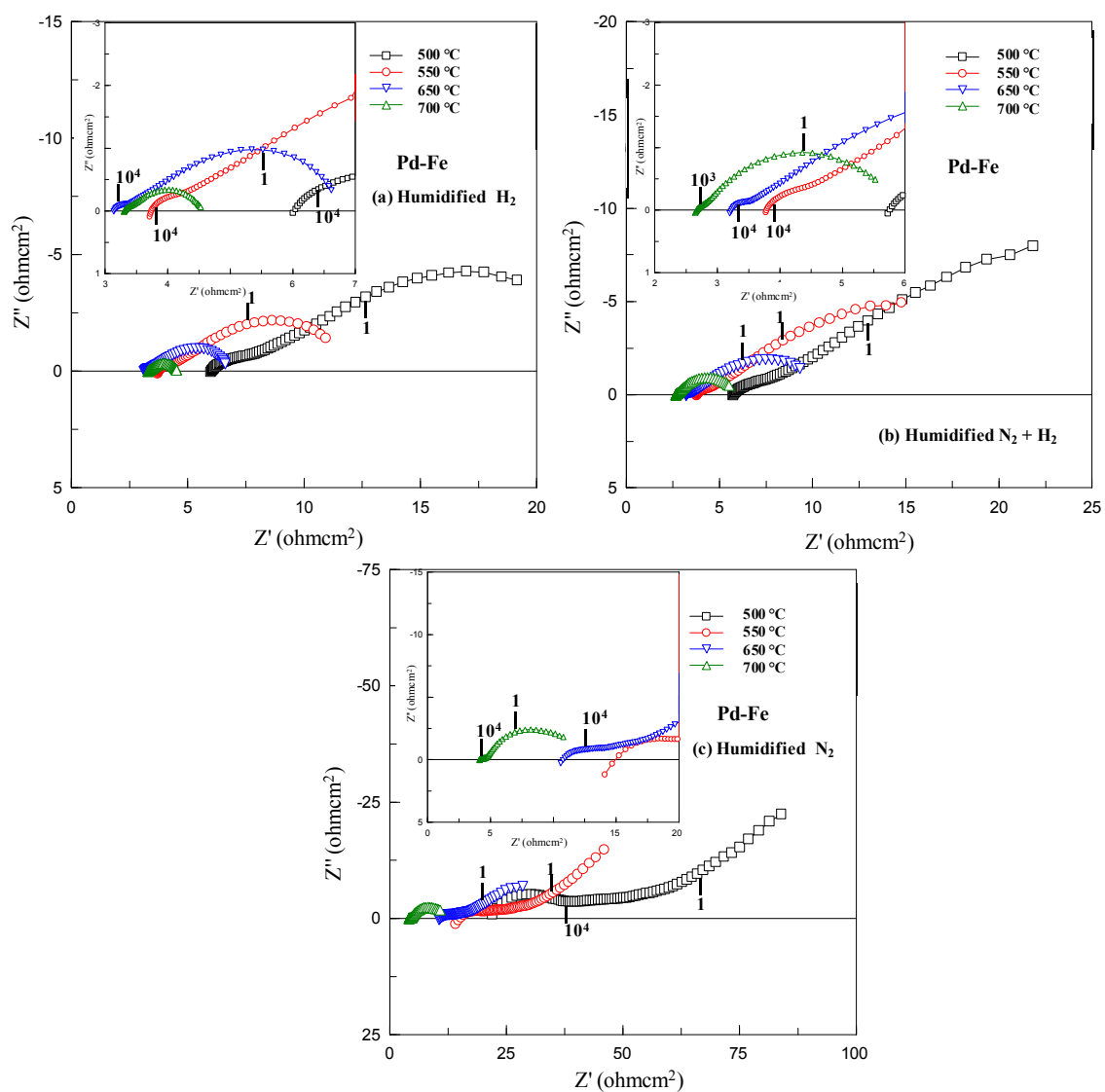


Figure 4.21 AC impedance spectra under open circuit of cell with 25 wt% Fe oxide electrode with Pd current collector in humidified atmospheres as a function of temperature. The numbers (10^n) indicate frequency in Hz.

4.3.4.4 Behaviour of 25wt% Fe electrode in non-humidified atmospheres

Under the real condition for ammonia synthesis, the Fe cathode will be operated in non-humidified N₂. Actually, a significant amount of H₂ will be electrochemically pumped from the anode to the cathode under closed-circuit conditions. Therefore, the behaviours of the 25 wt% Fe oxide electrode in non-humidified atmospheres with varying H₂ contents were investigated. The results in Figure 4.22 exhibit that the behaviour and shape of the impedance spectra in non-humidified atmosphere were similar to those in the humidified atmospheres. The reduction of the H₂O content did increase the ohmic resistance by ~ 10%. The polarisation resistances were slightly better than those in the humidified atmospheres. It could be the catalytic activity of Fe that was improved in the non-humidified atmosphere.

As the Fe cathode will be operated in redox atmospheres, the stability of the Fe impregnated electrode after being reduced and oxidized is shown in Figure 4.23. The sample was switched between N₂, N₂ mixed with H₂ and H₂ atmospheres before being switched back to N₂ within 26 h at 600 °C. The impedance of the cell in non-humidified N₂ before and after being reduced and oxidised showed no significant changes in the ohmic resistance. A small improvement in the electrode polarisation in the low frequency contribution could be a result of the sintering of the impregnated electrode after being reduced in H₂ atmosphere. The improvement in the stability of the 25 wt% Fe oxide electrode compared to the 1:1 Fe oxide:BCZYZ electrode may be influenced by the improvement of the electrode microstructure by lowering the Fe oxide content.

The microstructure of the 25 wt% Fe oxide electrode after testing is displayed in Figure 4.24. The SEM images reveal small Fe clusters anchored on BCZYZ surface

providing a number of active TPB sites as both Fe electrode and BCZY electrolyte were in good contact and exposed to the gas phase.

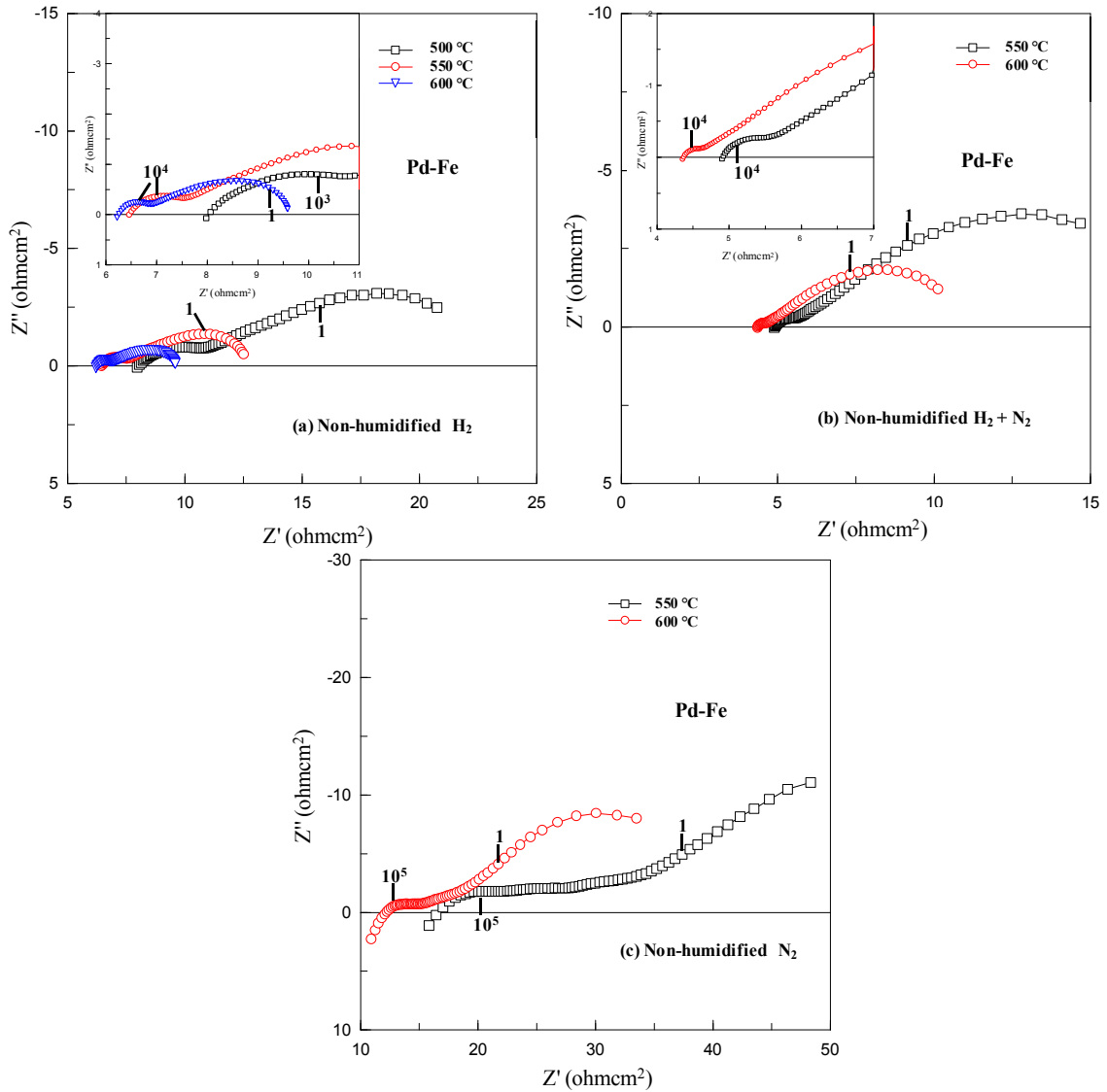


Figure 4.22 Impedance spectra of cell with 25 wt% Fe oxide electrode in non-humidified atmospheres as a function of temperature. Painted Pd was used as current collector.

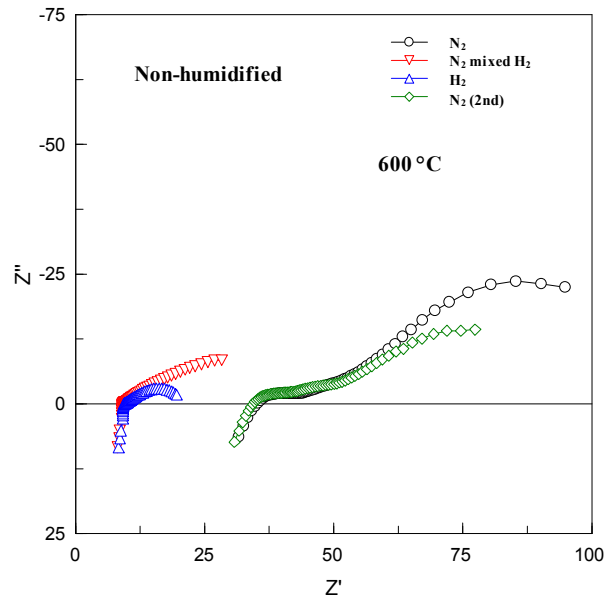


Figure 4.23 Stability of 25 wt% Fe oxide impregnated electrode at 600 °C in non-humidified atmosphere with various H_2 contents.

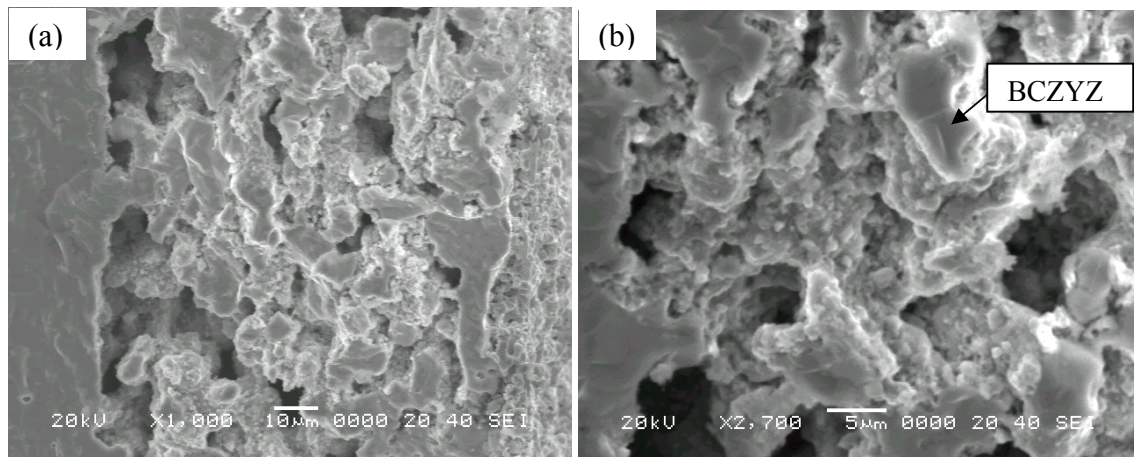


Figure 4.24 SEM images of a fractured cross-section of 25 wt% Fe oxide impregnated electrode after testing. (a) x1000 and (b) x2700 magnifications.

4.3.5 Comparison between ohmic conductivities of cells with various electrodes

The conductivities derived from the R_s values of cells with different kinds of electrode are plotted as a function of reciprocal temperature in Figure 4.25. The results show that the ohmic conductivities of the cell with 25 wt% Fe oxide impregnated electrode with Pt current collector were 2 times lower than that of the cell with the 25Ni10Ce impregnated electrode. The activation energies from cells with the painted Pt (reference cell with painted Pt electrode) and the 25Ni10Ce impregnated electrode were 0.40 eV which were slightly lower than that of cells with 25 wt% Fe oxide impregnated electrodes (0.45 eV). However, these values are in agreement with the value of 0.48 eV from the previous work for $\text{BaCe}_{0.5}\text{Zr}_{0.35}\text{Sc}_{0.1}\text{Zn}_{0.05}\text{O}_{3-\delta}$ ^[26].

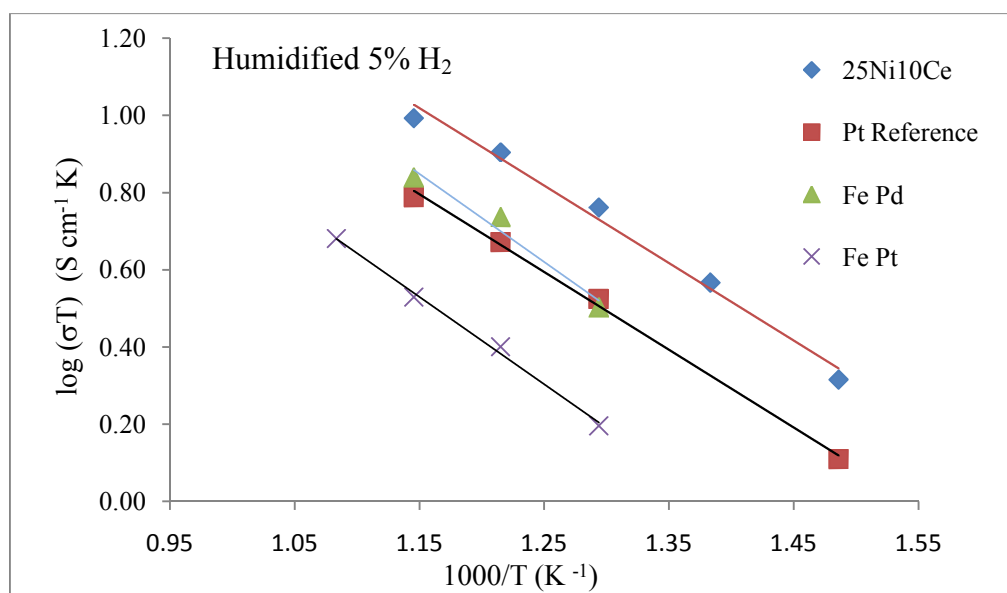


Figure 4.25 Arrhenius plots for ohmic conductivities of cells with various electrodes; impregnated 25Ni10Ce (◆), painted Pt (■), impregnated 25 wt% Fe with Pd current collector (▲), and impregnated 25 wt% Fe with Pt current collector (×).

4.4 Conclusions

A proton conducting oxide membrane cell with Ni-based anode and Fe-based cathode has been developed by tape casting and ion impregnation. The electrode compositions have been individually investigated in order to attain the suitable electrode composites for the real working conditions in ammonia synthesis. For the anode, the high Ni content electrode, i.e. 1:1 NiO:BCZY, provided better performance than the low Ni content electrodes. However, the Ni impregnated electrode suffered severely from the sintering of Ni particles during operation. Hence, CeO₂ was co-impregnated with Ni in order to improve the sintering problem. As expected, the performance of Ni-CeO₂ impregnated electrode was higher than Ni impregnated electrode. The best performance was achieved from the combination of 25 wt% NiO and 10 wt% CeO₂ with the lowest polarisation resistance of 0.02 Ω cm² at 650 °C in humidified H₂. In the temperature range of 400-500 °C which tends to be the working range for ammonia synthesis, the reasonable R_p values of 1-0.45 Ωcm² in humidified 5%H₂ were obtained. For the cathode, it was found that the re-oxidation of Fe in N₂ atmospheres affected the performance of the high Fe oxide content electrode. However by decreasing the content of the impregnated Fe oxide to 25 wt%, the electrode exhibited a fair performance and an excellent stability in non-humidified N₂.

References

1. S. P. Jiang, Y. Y. Duan, J. G. Love, *J. Electrochem. Soc.* 149 (2002) A1175-A1183
2. R. J. Gorte, S. Park, J.M. Vohs, C. Wang, *Adv. Mater.* 12 (2000) 1465.
3. S.-I. Lee, K. Ahn, J.M. Vohs, R.J. Gorte, *Electrochem. Solid-State Lett.* 8 (2005) A48.
4. W. Wang, R. J. Gorte, J. M. Vohs, *Chem. Eng. Sci.* 63 (2008) 765-769.
5. G. C. Bond, *Heterogeneous catalysis: Principles and application*, 2nd edition, Oxford University Press, New York (1987) p.79.
6. A. J. Bard, L. R. Faulkner, *Electrochemical methods fundamentals and applications*, 2nd edition, Wiley & Sons, Haryana (2006) p. 421.
7. Y. Shanmugam, F. Y. Lin, T. H. Chang, C. T. Yeh, *J. Phys. Chem. B* 107 (2003), 1044-1047.
8. W. Brockner, C. Ehrhardt, M. Gjikaj, *Thermochimica Acta* 456 (2007) 64–68.
9. S. V. Bhide, A. V. Virkar, *J. Electrochem. Soc.* 146 (1999) 2038-2044.
10. S. P. Jiang, *Mater. Sci. Eng. A* 418 (2006) 199-210.
11. A. Essoumhi, G. Taillades, M. Taillades-Jacquín, D.J. Jones, J. Rozière, *Solid State Ionics* 179 (2008) 2155-2159.
12. G.C. Mather, F.M. Figueiredo, J.R. Jurado, J.R. Frade, *Electrochim. Acta* 49 (2004) 2601-2612.
13. G.C. Mather, F.M. Figueiredo, J.R. Jurado, J.R. Frade, *Solid State Ionics* 162-163 (2003) 115-120.
14. J. T. S. Irvine, D. C. Sinclair, A. West, *Adv. Mater.* 2 (1990) 132-138.
15. S. P. Jiang, S. P. S. Badwal, *Solid State Ionics* 123 (1999) 209-224.

16. J. Qiao, K. Suna, N. Zhang, B. Suna, J. Kong, D. Zhoua, J. Power Sources 169 (2007) 253–258.
17. M. Cimenti, J. M. Hill, ESC Transactions 7 (2007) 1591-1600.
18. S. Park, R. J. Gorte, J. M. Vohs, Appl. Catal. A Gen. 200 (2000) 55–61.
19. M. Brown, S. Primdahl, M. Mogensen, J. Electrochem. Soc. 147 (2000) 475-485.
20. S. Primdahl, M. Mogensen, Solid State Ionics 152– 153 (2002) 597– 608
21. A. Ringuede, D. Bronine, J. R. Frade, Electrochim. Acta 48 (2002) 437-442.
22. J. Mizusaki, H. Tagawa, T. Saito, T. Yamamura, S. Ehara, et al., Solid State Ionics 70-71 (1994) 52.
23. D. Kek, N. Bonanos, Vacuum 61 (2001) 453-457.
24. P. J. Gellings, H. J.M. Bouwmeester, Catal. Today 58 (2000) 1-53.
25. D. R. Gaskell, Introduction to the Thermodynamics of Materials, 3rd ed., Taylor & Francis (1973) p. 370.
26. A. K. Azad, J. T. S. Irvine, Solid State Ionics 179 (2008) 678-682.

Chapter 5

Electrocatalytic ammonia synthesis

5.1 Components of a membrane cell for electrocatalytic ammonia synthesis	189
5.2 Experimental	190
5.3 Results and discussion	192
5.3.1 Effect of cathode current collector on ammonia formation	192
5.3.2 Investigations of single cells with and without catalyst addition	194
5.3.2.1 AC impedance measurements under open-circuit condition	195
5.3.2.2 Polarisation properties under closed-circuit condition	198
5.3.2.3 The relationship between applied potential and cell resistance	202
5.3.2.4 Overall overpotentials of cells with and without catalyst addition	204
5.3.2.5 Changes in the gas compositions during <i>V-I</i> measurement	207
5.3.2.6 Microstructure of single cells with catalyst impregnated Fe	209
5.3.3 Ammonia production	212
5.3.3.1 Ammonia formation rate	216
5.3.3.2 H ₂ evolution rate and overall current efficiency	221
5.4 Conclusions	225
References	226

5.1 Components of a membrane cell for electrocatalytic ammonia synthesis

With the proper compositions for anode and cathode materials from the results in Chapter 4, a single cell for electrocatalytic ammonia synthesis were assembled. The geometry of a single cell along with its components is displayed in Figure 5.1.

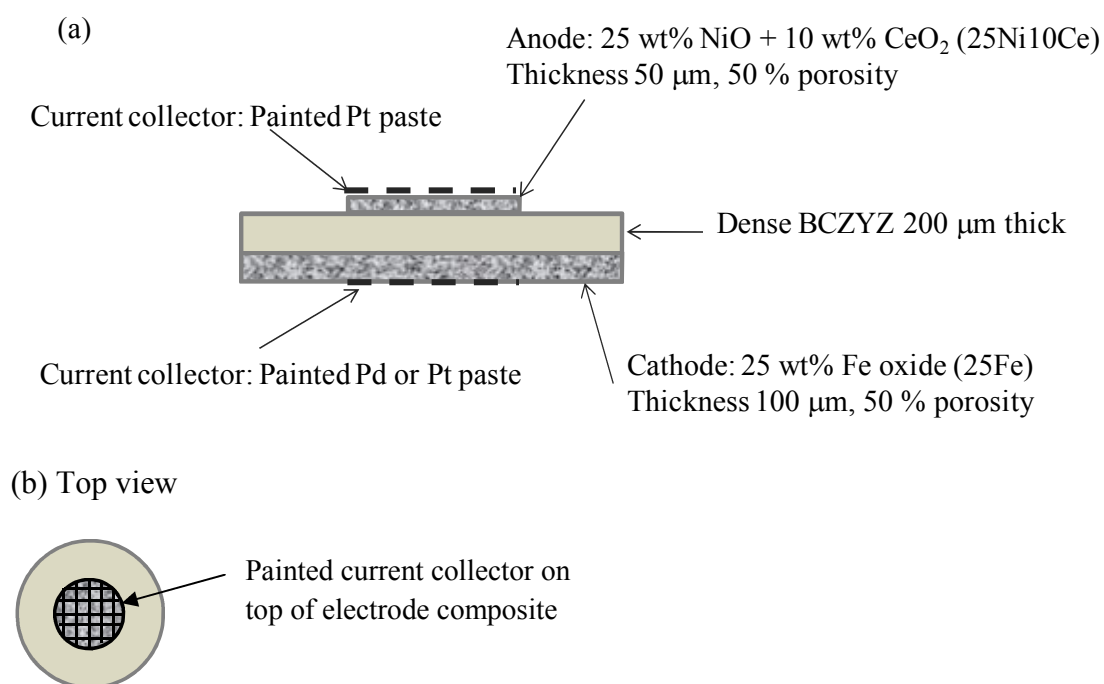


Figure 5.1 Schematic of the components of a single cell prepared for electrocatalytic ammonia synthesis. (a) cross-section view and (b) top view.

5.2 Experimental

The electrocatalytic synthesis of ammonia was carried out in two-chamber jig at 400-600°C under atmospheric pressure. The thickness of the anode layer was reduced from 100 µm in symmetrical cell testing to 50 µm. The reduction of anode thickness was expected to improve gas diffusion and catalyst utilization. Despite the sluggish reactions at the Fe cathode, the thickness of this layer was kept at 100 µm in order to provide higher catalyst loading and probably increase the TPB length. The superficial surface areas of the anode and cathode layers were 0.4 and 1.8 cm², respectively. The active area of the cell was considered to be equal to the surface area of the anode. The membrane cell was tested in a two-chamber reactor as shown in Figure 5.2. The cell was sealed between two alumina tubes by a ceramic adhesive (P-24, Toku ceramic). The testing atmosphere was kept constant. The anode was fed by humidified 5%H₂ which was obtained by bubbling 5%H₂/Ar gas through room-temperature water resulting in a gas mixture of 3 % H₂O and 4 % H₂ in Ar. The flow rate of 5% H₂/Ar gas was 30 mL/min. In the cathode, a constant flow of non-humidified N₂ was required. The flow rate of pure N₂ gas of 38 ml/min was controlled by a mass flow controller (Model 5850S, Brooks instrument). However, the actual flow rate of the cathode outlet was checked periodically by a glass soap bubble flow meter.

The electrical connections were established by attaching Ag wire and Ag paste directly to each electrode as shown in Figure 5.2. The electrochemical measurements were carried out using a frequency response analyzer (Solartron 1255, UK) coupled with an electrochemical interface (Solartron 1287, UK). The voltage-current (*V-I*) measurement was performed by sweeping potentials across the cell using a scan rate of 2 mV/sec with the applied potentials from 0-3 V with respect to the OCV. The AC-

impedance measurement was obtained in a frequency range of 0.1 Hz to 1 MHz and potential amplitude of 20 mV under open-circuit condition. In some cases, the polarisation under applied potential was also investigated.

For ammonia synthesis, a constant potential was imposed against the open circuit voltage through the cell for a transient period of 20 min. During the closed-circuit, the amount of evolved ammonia was continuously detected by a mass spectrometer (MS) (Prolab 300, Thermo Scientific). Along with the ammonia concentration, the changes in concentration of O_2 , H_2O and H_2 were also recorded and used for evaluating total current efficiency from all competitive reactions. The concentrations of those gases detected from the MS were in unit of mol%. The differences in concentrations of those gases under open circuit and closed circuit were used in the calculations of formation rate and current efficiency. The details about these calculations have been explained in Chapter 2, section 2.3.4.4.

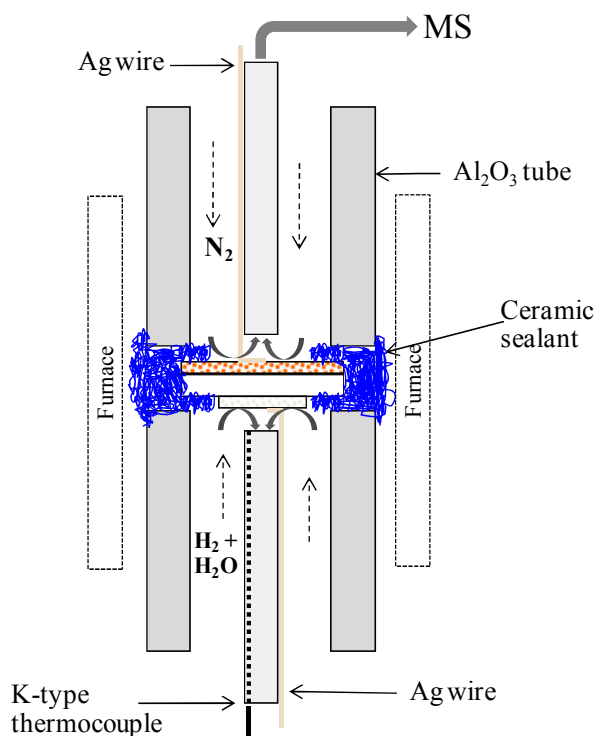


Figure 5.2 Two-chamber testing apparatus.

5.3 Results and discussion

5.3.1 Effect of cathode current collector on ammonia formation

The impedance spectra under open circuit of single cells containing 25Ni10Ce anode and 25Fe cathode with different current collectors, Pd or Pt, on the Fe cathode are shown in Figure 5.3. The impedance of these single cells showed a similar behaviour with the impedance of a symmetrical cell with Fe oxide electrode in non-humidified N₂. However, the ohmic resistance seems to be smaller than that of the symmetrical cell due to the presence of H₂ and H₂O in the anode side. It is likely that the polarisation resistance was mainly influenced by the cathodic polarisation regarding to the fact that the polarisation resistances of the 25Ni10Ce electrode in humidified 5% H₂ at 400-500 °C were much smaller than that of the Fe electrode which are only 1-0.45 Ωcm², respectively.

During the closed-circuit condition, the amount of H₂ emerged at the cathode with Pd current collector was much lower than the cell with the Pt current collector and the expected values. The current efficiency calculated from the total amount of H₂ and H₂O produced with respect to the theoretical value derived from the imposed current was only 30-50% at 500-400 °C. Importantly, there was no sign of NH₃ being produced although high potential was imposed. According to the results from Chapter 2, cell with painted Pd electrode also produced a small amount of H₂. This may be due to the catalytic activity of Pd on the reaction of hydrogen and oxygen.

Therefore, Pt paste was used as current collector on the Fe cathode for the rest of the experiment. Although Pd current collector used to provide better performance than Pt current collector in the symmetrical cell tests, the impedance data achieved from cells

with Pt or Pd current collector in Figure 5.3 show that there was no significant difference between those cells in the single cell testing. Instead, the electrode performance of the single cell with Pt current collector was better than that of Pd current collector at lower temperature.

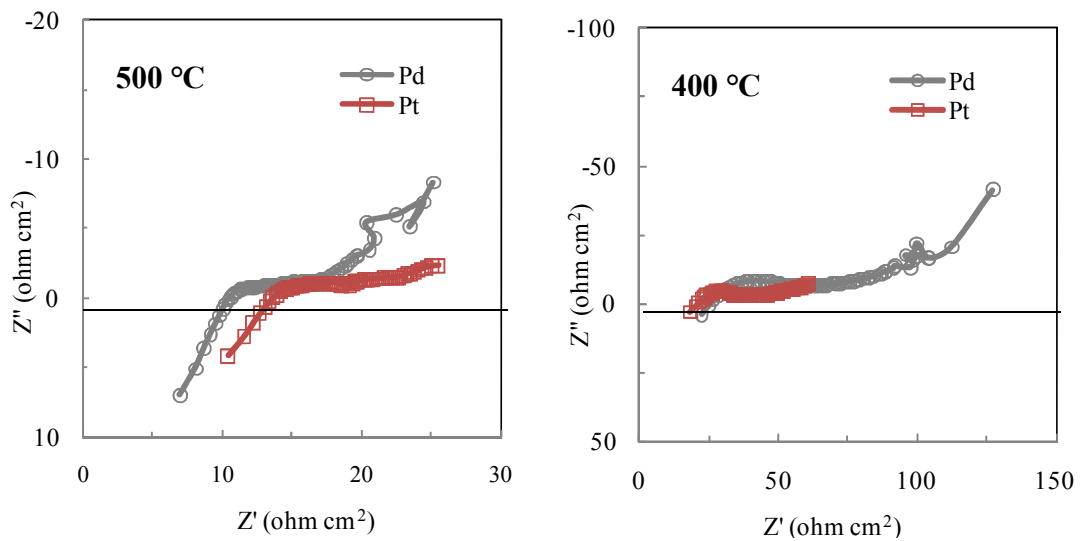


Figure 5.3 Impedance spectra under open circuit from single cells, humidified 5% H_2 , $25\text{Ni}10\text{Ce} \mid \text{BCZYZ} \mid 25\text{Fe}$, N_2 with Pd or Pt current collector on Fe cathode at (a) 500 °C and (b) 400 °C.

5.3.2 Investigations of single cells with and without catalyst addition

Single cells with 25 wt% NiO + 10 wt% CeO₂ (25Ni10Ce) anode and 25 wt% Fe₂O₃ (25Fe) cathode using Pt current collector on both sides was tested for electrolytic ammonia synthesis. Note that the working temperature was in the range of 400-500 °C in order to prevent the decomposition of ammonia at high temperature^[1]. When operated at temperature higher than 500 °C, the formation rate of ammonia was obviously unstable and sharply decreased with time. In addition, the results from the Chapter 2 (section 2.4.5.1) suggested the increase of the electronic conduction in the BCZY electrolyte at high temperature which resulted in the loss of the current efficiency.

Apart from the study of the catalytic activity of the Fe electrocatalyst, the Fe surface was modified by two kinds of catalysts i.e., Pd and Ru. By impregnating the catalysts onto the Fe surface, the amount of the catalyst loading was fixed at 10wt% with respect to weight of the Fe oxide.

Pd catalyst addition

Like other platinum-group metals, Pd has been used widely as a catalyst for several reactions such as hydrogenation or dehydrogenation of H-containing compounds^[2,3], hydrogen sensors and hydrogen separation^[4,5]. Its strong interaction with hydrogen makes Pd become a promising catalyst for electrochemical ammonia synthesis. It is expected that the presence of Pd catalyst on the Fe electrode could facilitate the

transportation and adsorption of hydrogen (both H^+ and H_{ad}) allowing them to react with adsorbed N at Fe surface and form NH_3 .

Ru catalyst addition

Metallic Ru is another active catalyst for ammonia synthesis and has been employed in the ammonia industrial production for many years^[6,7]. The performance of Ru in ammonia synthesis is better than Fe leading to the possibility to operate under milder conditions. In oxide form, RuO_2 with its metallic conductivity is widely used in polymer electrolyte fuel cells or electrolyser as an electrocatalyst^[8-10]. Therefore, the addition of RuO_2 onto the Fe electrode is possible to improve the conductivity of the Fe cathode under open circuit while the nanoparticles of Ru metal, which arise under closed circuit may enhance the catalytic activity of the Fe electrode on ammonia formation reaction.

5.3.2.1 AC impedance measurement under open-circuit condition

Figure 5.4 displays the impedance spectra of cells with and without catalyst addition at different temperatures under the open circuit. The behaviours of the impedance of cells without catalyst and with Pd addition were similar with at least three electrode responses at high frequency (10^5 Hz), medium frequency (10 Hz) and low frequency (1 Hz). A large depressed arc at high frequency which was assigned as the charge transfer response in the impedance of Fe symmetrical cell seemed to dominate the electrode process in these cells. An imperfect arc at medium frequency and a spike at

low frequency suggested that the adsorption/dissociation and diffusion of nitrogen or oxygen on the Fe electrode could be responsible for these contributions.

By impregnating 10 wt% PdO on the Fe oxide cathode, the R_s and R_p values were higher than those of the unmodified cell by a factor of 2. The rise of R_s values may result from the increase of the contact resistance at the electrolyte/electrode interfaces due to the presence of resistive PdO particles. Moreover, it seems that the presence of PdO on the Fe surface obstructed the electrode processes and caused a significant increase in polarisation resistance especially for the high-frequency contribution.

The addition of 10 wt% of RuO₂ into the Fe cathode exhibited quite interesting results. The impedance spectra obtained from this cell under open circuit showed the lowest R_s values and different electrode polarisation characteristics to the unmodified cell. The electrode responses were composed of a high-frequency contribution which is much smaller than in the case of the unmodified and Pd-modified Fe cell. The low frequency contribution appeared as a straight line with almost 45° angle to the real axis. The straight line tends to turn down to the real axis with the increasing temperature indicating the dominant process became more favourable at higher temperature. The improvement of the impedance by the addition of the Ru catalyst is related to the metallic conductivity and catalytic activity of RuO₂ that overwhelms the electrode properties of the Fe oxide. At 500 °C, the ohmic conductivity of 2 mScm⁻¹ obtained from both unmodified cell and Ru-modified Fe cell which were determined from the high-frequency intercept were close to the ionic conductivity of the symmetrical cell with the Fe electrode measured in humidified 5% H₂ at the same

temperature. The ohmic conductivities of Pd-modified cell, however were 2 times lower than that of the unmodified Fe cell.

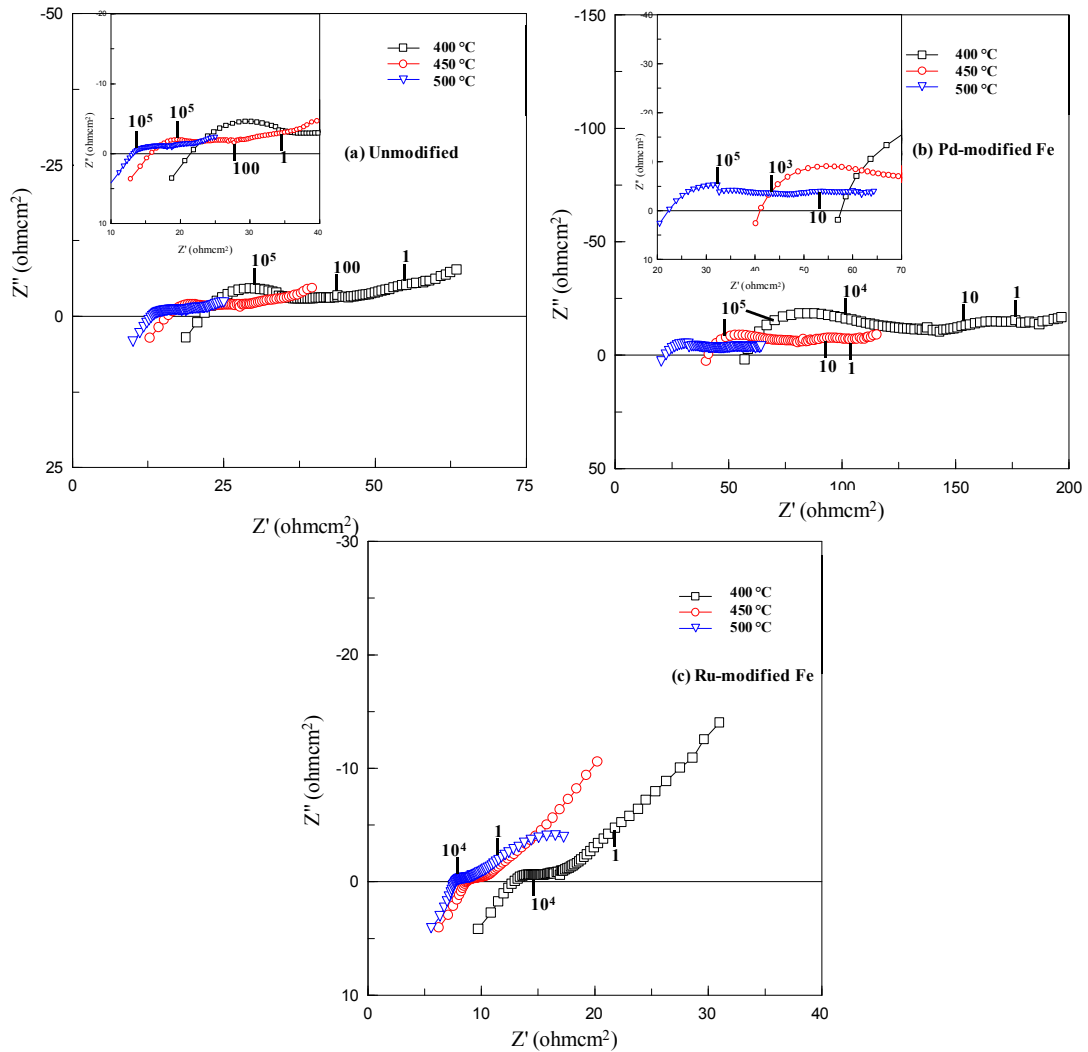


Figure 5.4 AC impedance spectra under open circuit of humidified 5% H₂, 25Ni10Ce | BCZYZ | 25Fe, N₂ cell with and without catalyst addition on the Fe cathode at different temperatures. (a) unmodified Fe, (b) Pd-modified Fe and (c) Ru-modified Fe. Electrolyte thicknesses of those cells are 268, 198 and 192 μm for cells (a), (b), and (c), respectively.

5.3.2.2 Polarisation properties under closed-circuit condition

The polarisation response of cells under closed-circuit condition was studied by sweeping various potentials from 0 to 3 V with respect to open circuit voltage (OCV) across the cells. The polarisation characteristics were considered from plots between the swept potential and corresponding current density ($V-I$ curve) as shown in Figure 5.5. Unexpectedly, the OCV of all three cells under humidified 5% H_2 /Ar in the anode and non-humidified N_2 in the cathode were as high as -1.05 V. This high OCV may arise from the reversible reaction between humidified 5% H_2 /Ar in the anode side and ~ 0.1 mol% of O_2 that was usually found in the cathode chamber and this OCV value was in agreement with the theoretical value calculated from the Nernst equation. The typical gas compositions of the cathode outlet stream during open-circuit condition are presented in Table 5.1.

Table 5.1 Gas composition from the cathode outlet stream under open circuit.

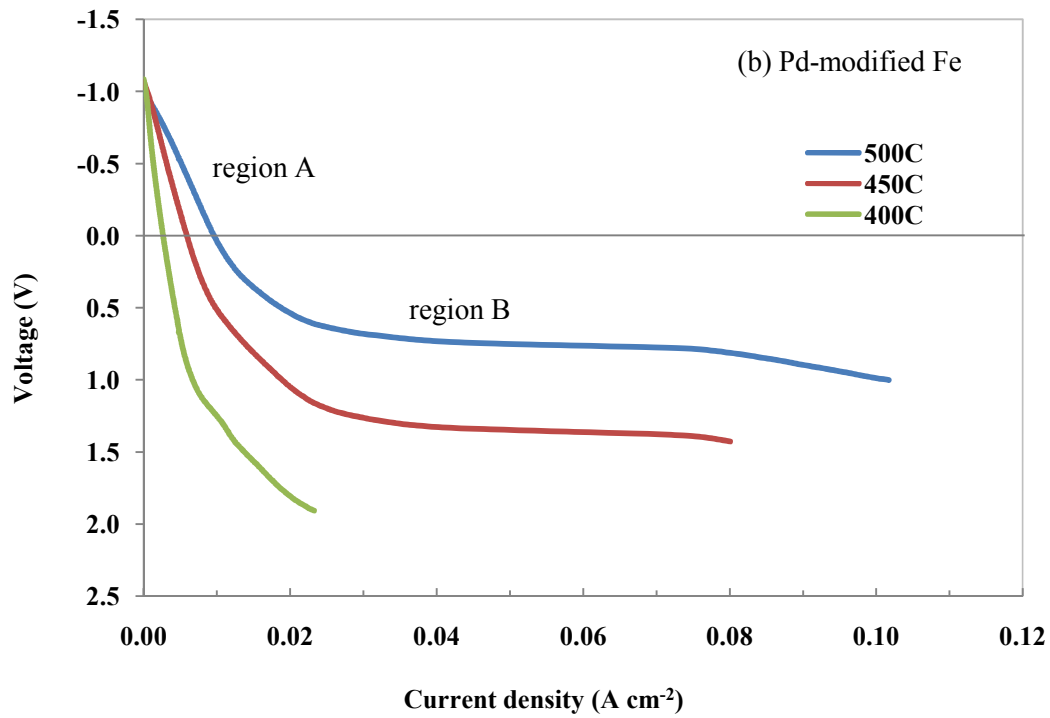
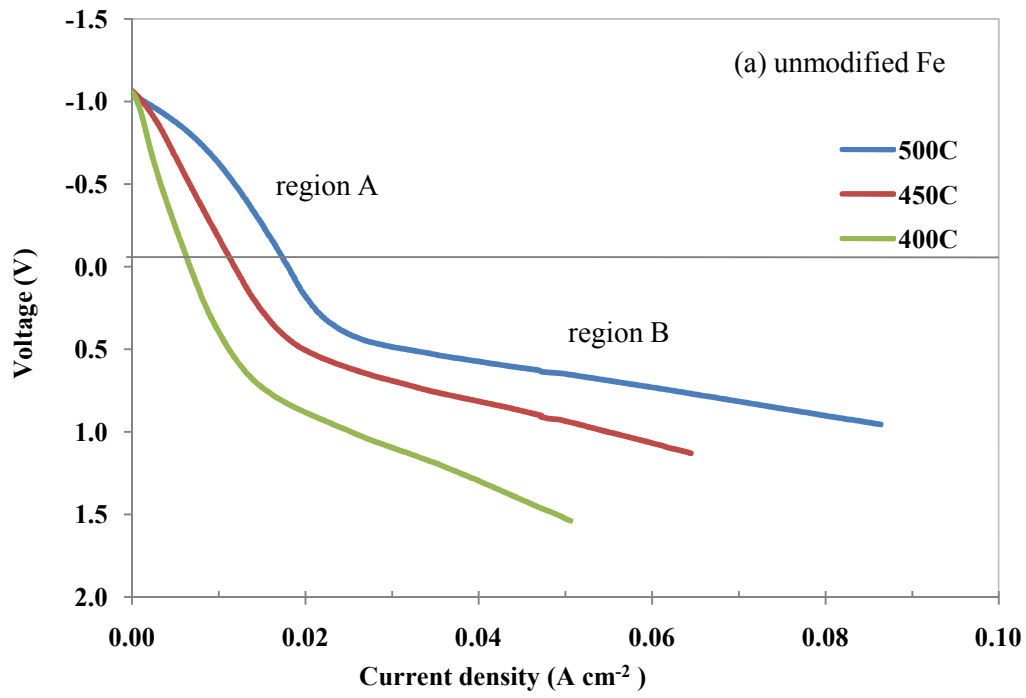
Gas	Concentration (mol%)
Ar	0.3-0.4
H_2O	0.1-0.2
O_2	0.1-0.15
H_2	0-0.001
CO_2	8-10 ppm

The small amount of O_2 in the cathode stream may come from some air leakage inside the cathode chamber. At the same time, the presence of O_2 in the cathode chamber would be a driving force for the reaction between H_2 and O_2 and responsible for the presence of H_2O . As a proton conducting membrane cell, it has been reported that

steam diffusion in a proton-conducting oxide can happen in a water vapour concentration cell. However, this phenomenon is pronounced at 900-1000 °C according to Coors's study for Y-doped barium cerate^[11]. Estimating from his data, the amount of H₂O that can be transported from the anode is just around 0.02 mol% at 600 °C and the rate of steam diffusion tends to decrease exponentially with decreasing temperature. Within the working temperature of 400-500 °C, the steam diffusion phenomenon would be negligible.

Polarisation properties of this cell at different temperatures in Figure 5.5 indicate that the Ru-modified Fe cell with the lowest ohmic and polarisation resistances provided the highest corresponding current density when applying the same potential range compared to the other cells, as might be expected. The Ru-modified Fe cell provides the current density of 0.16 A cm⁻² when a potential of 2 V was applied at 500 °C which was 30% and 100% higher than those of cells with Pd catalyst and without catalyst, respectively.

The correlation between the polarisation curve and AC impedance under high potential loads was observed. After deducting R_s values from the impedance spectra, the changes in electrode responses of the cell without catalyst addition under the potential loads are revealed in Figure 5.6. By applying 1 V, the polarisation resistance became greater than under open circuit due to the enlargement of the low frequency contribution. When higher potentials were applied, the polarisation resistances became much smaller and gave an unusual dependence. The reduction of total cell resistance was consistent with the small cell resistance observed in region B of the corresponding *V-I* curve in Figure 5.5. The improvement of electrode polarisation suggests that the ammonia formation reaction at the cathode might be achieved by applying potentials in the range of region B of the *V-I* curve.



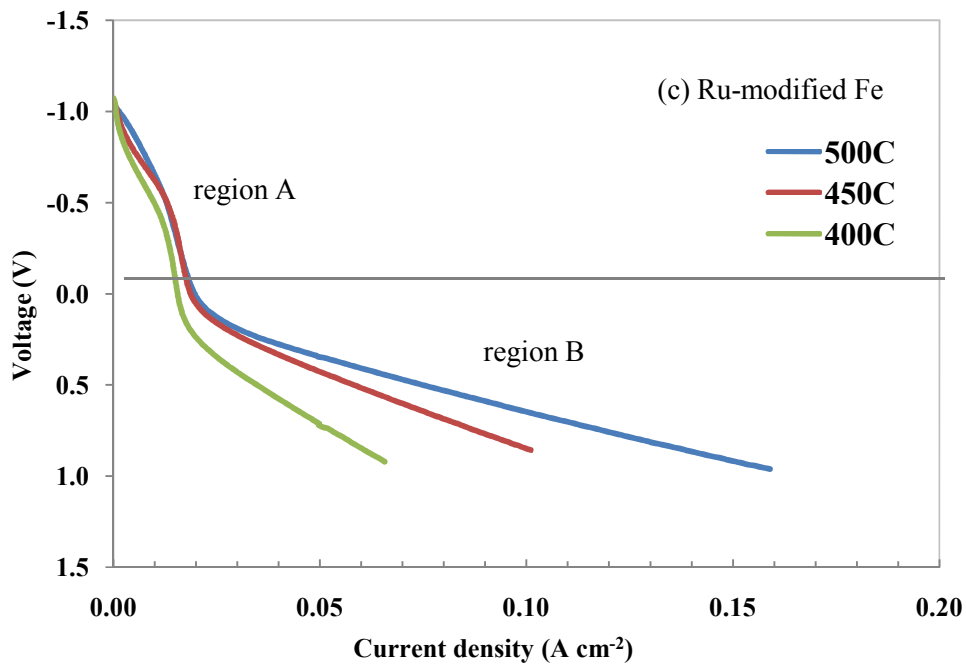


Figure 5.5 Polarisation curves of humidified 5% H₂, 25Ni10Ce | BCZYZ | 25Fe, non-humidified N₂ cells at various temperatures. (a) without catalyst addition, (b) Pd addition, and (c) Ru addition.

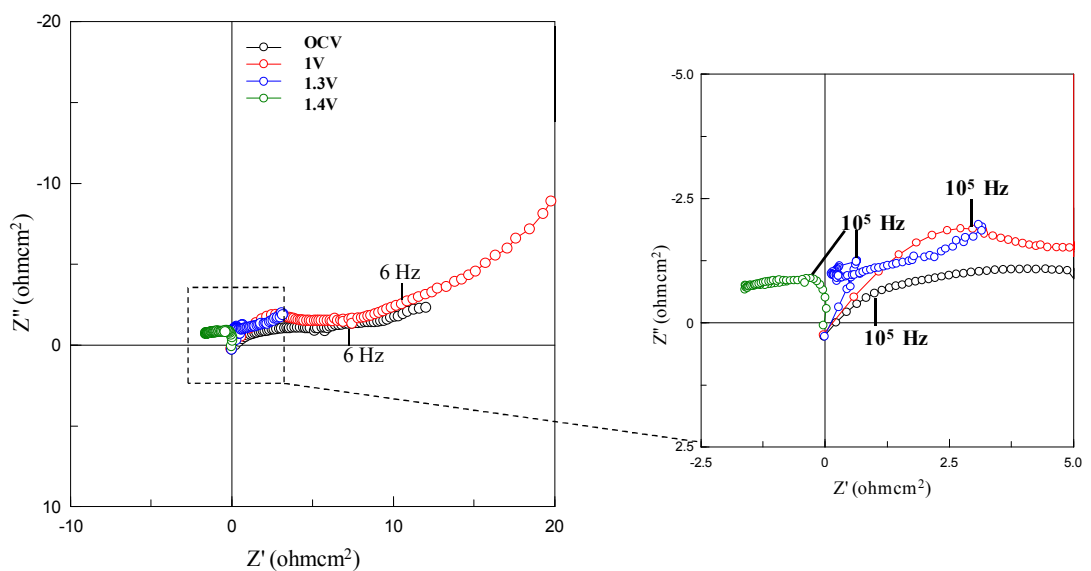


Figure 5.6 AC impedance spectra of cell without catalyst addition at Fe cathode measured at OCV and under loading.

5.3.2.3 The relationship between applied potential and cell resistance

The value from the slope of the V - I curve (dE/dI) evaluated from the linear region of the curve indicates the changes of the cell resistance at non-steady state conditions. From Figure 5.5, the polarisation curves of all cells show two linear regions with different slopes and the slopes of these regions are summarised in Figure 5.7. The region A at lower imposed voltages contains high dE/dI values while the dE/dI values from region B were much smaller. The relationship between applied potentials and the cell resistances can be explained in two stages. First, cells under open-circuit condition have more negative anode and positive cathode related to the spontaneous reactions that take place at both electrodes. At OCV, these following reactions are in equilibrium.



When potentials were applied across the cell, the anode became less negative and cathode became more negative as a number of electrons were driven to the cathode by the external power source. In this region which is called region A, the cell resistances (dE/dI) were higher than expected from the impedance spectra under open circuit in cases of unmodified and Pd-modified cell due to the additional resistances from the charge transfer of driven electro-active species. There is no change in the cell resistances of the Ru-modified cell since the resistance from the charge transfer process in this cell was negligible. In the second stage when the applied voltage was increased until the region B is reached, the dE/dI values of all cells were significantly

decreased suggesting that the reactions at the electrodes were enhanced by applying this range of potentials.

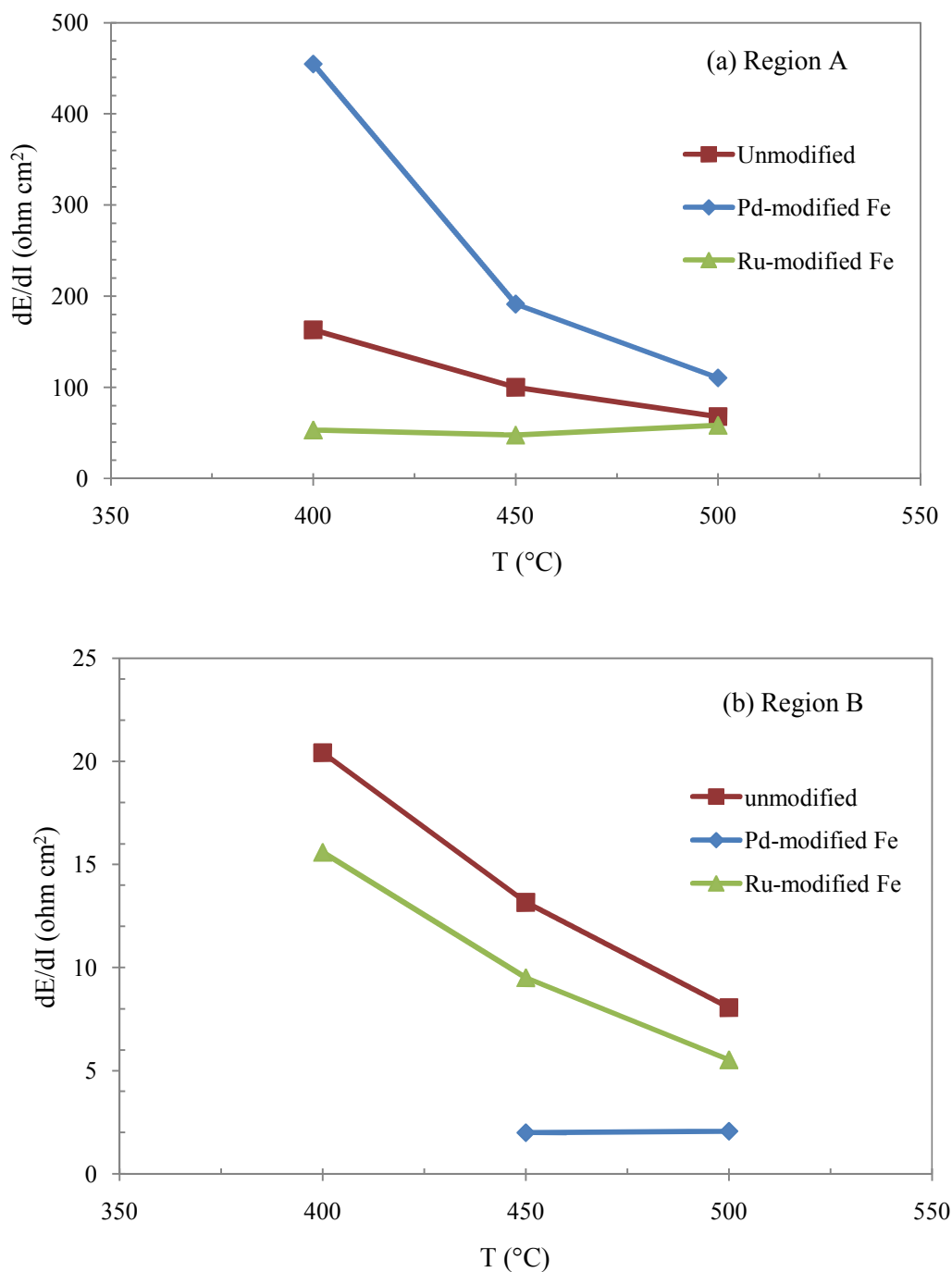
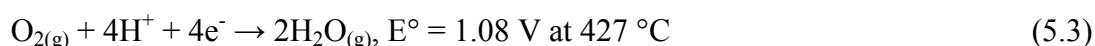


Figure 5.7 Plots of dE/dI values evaluated from the slopes in polarisation curves in (a) region A and (b) region B of cells with and without catalyst addition as a function of temperature.

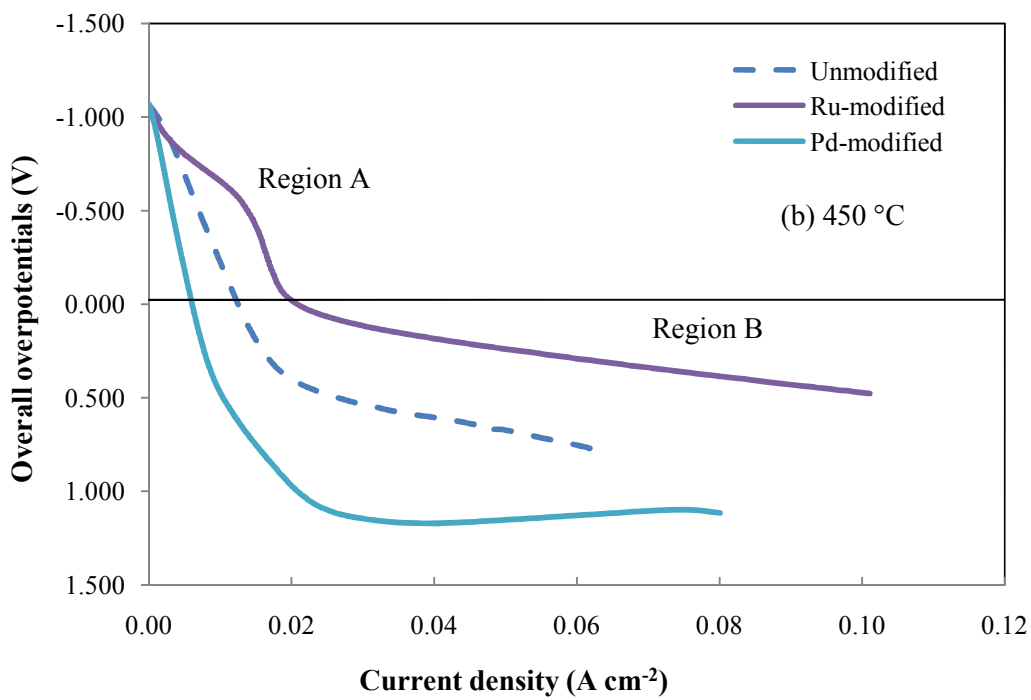
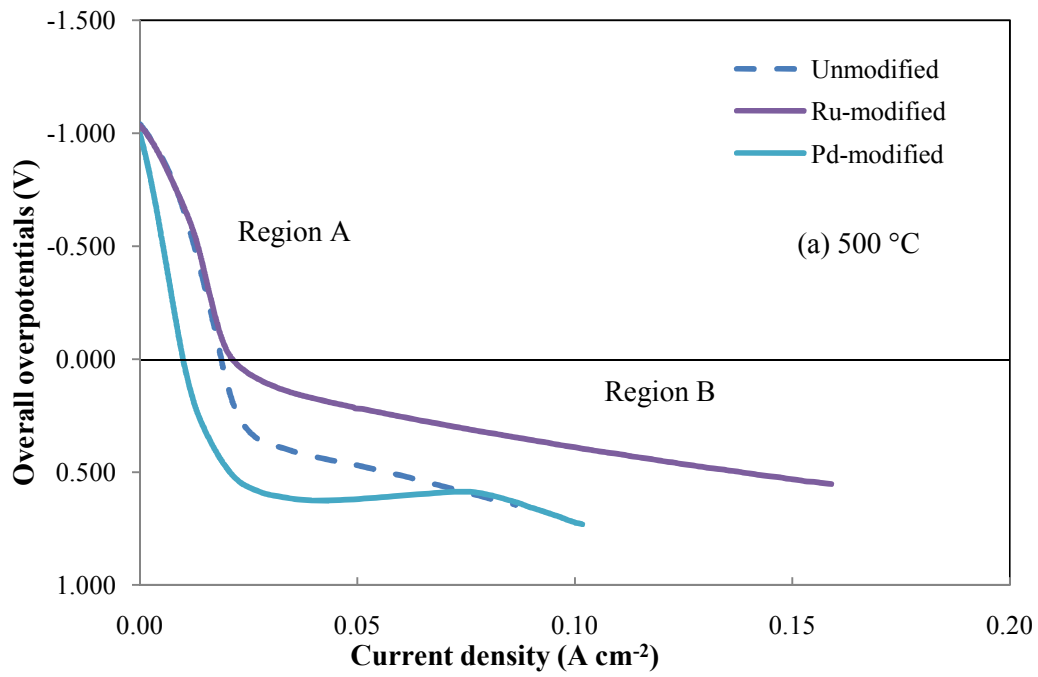
5.3.2.4 Overall overpotentials of cells with and without catalyst addition

Overall overpotentials (η_{overall}) of these three cells were considered by deducting the loss from ohmic resistance (iR_{ohmic}) from the V - I curves. R_{ohmic} corresponding to the electrolyte resistance was evaluated from the ohmic conductivity of the cell with 25Ni10Ce electrode which showed the best electrode performance in order to minimise the inclusion of the electrode resistance in the ohmic conductivity. The plots of the overpotentials versus the current density are shown in Figure 5.8. According to the thermodynamic data, the standard reduction potentials (E°) of NH_3 formation reaction are -0.07, -0.089 and -0.1 V at 400, 450 and 500 °C, respectively. These values were smaller than those of O_2 reduction and H^+ reduction reactions^[12],



When a potential is applied to the cell, the reduction reaction with higher E° usually proceeds first. Hence, O_2 should be reduced before H^+ and N_2 , respectively. The overpotential values in the region A may derive from the O_2 reduction reaction as those were close to 1 V for the Ru-modified cell while the other cells consumed higher overpotentials. The difference in overpotential values for different catalysts and temperature suggests that the kinetics of the reaction plays a role on the overpotential characteristics.

Note that the proof for the order of the reactions at the cathode was performed by recording the change in the cathode gas compositions during continuously applied potential to the cells. The results are discussed in the following section.



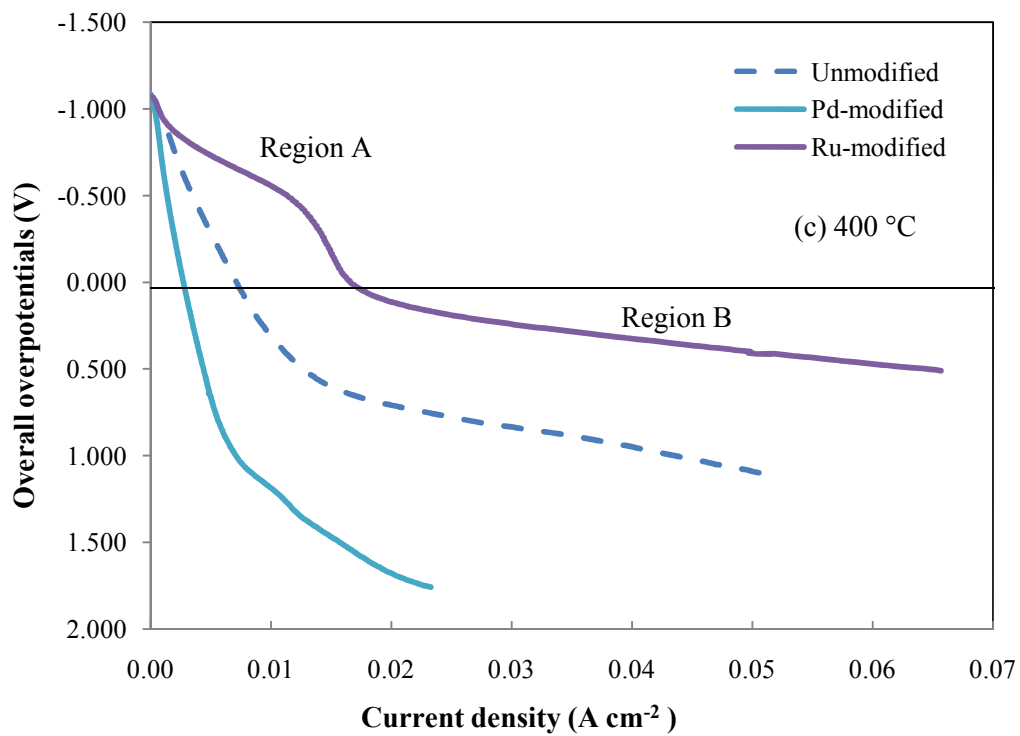


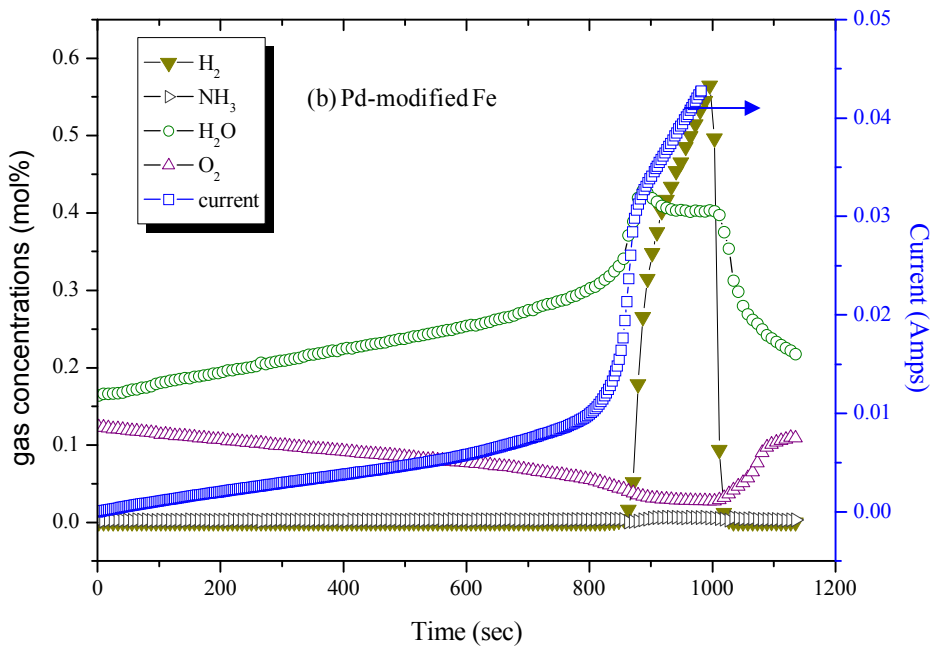
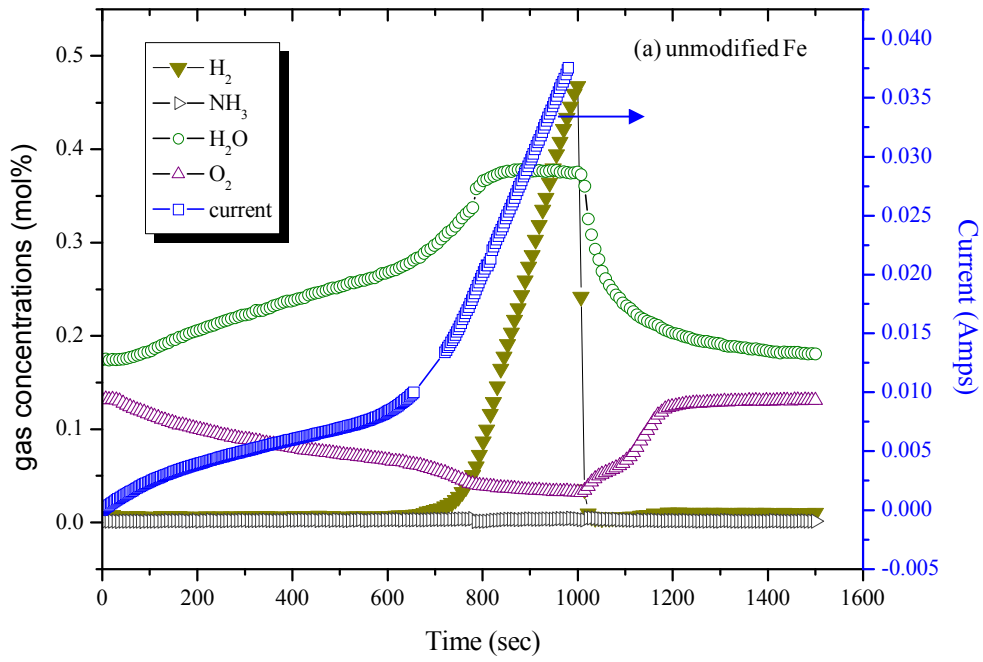
Figure 5.8 Plots of overpotentials (IR_{ohmic} -free) versus current density of cells with and without catalyst addition.

5.3.2.5 Changes in the gas compositions during *V-I* measurement

Along with the *V-I* measurement, the changes in concentration of cathode gases were monitored by the mass spectrometer. Figure 5.9 shows the plots of the concentrations of H₂, O₂ and H₂O gases and the corresponding current as a function of time. Once the current had been produced, the reaction between H⁺ (at anode) and O₂ (at cathode) via the proton conducting electrolyte was instantly activated resulting in the increase of H₂O and the reduction of O₂ which was in agreement with the order of E° values as mentioned in previous section. However, the development of the ammonia formation was also observed. This suggests that the ammonia formation reaction is not strongly dependent upon applied potential and it is not kinetically sluggish. Therefore, the nature of catalyst and the number of active sites more or less govern the reaction. Note that the ammonia formation rate was increased sharply with the concentration of H₂ revealing the dependence of this reaction on the reactant concentration.

As the current increased, the amount of H⁺ driven from the anode through the cathode was also increased significantly. A new equilibrium between H₂ and O₂ reaction was also observed due to the limit concentration of O₂ in the system. When the current was stopped, the concentration of H₂ was suddenly decreased as the concentration of O₂ was gradually increased back to the original value.

Cell with the Ru-modified Fe cathode which had the lowest cell resistance provided the highest corresponding current and also the highest amount of produced H₂.



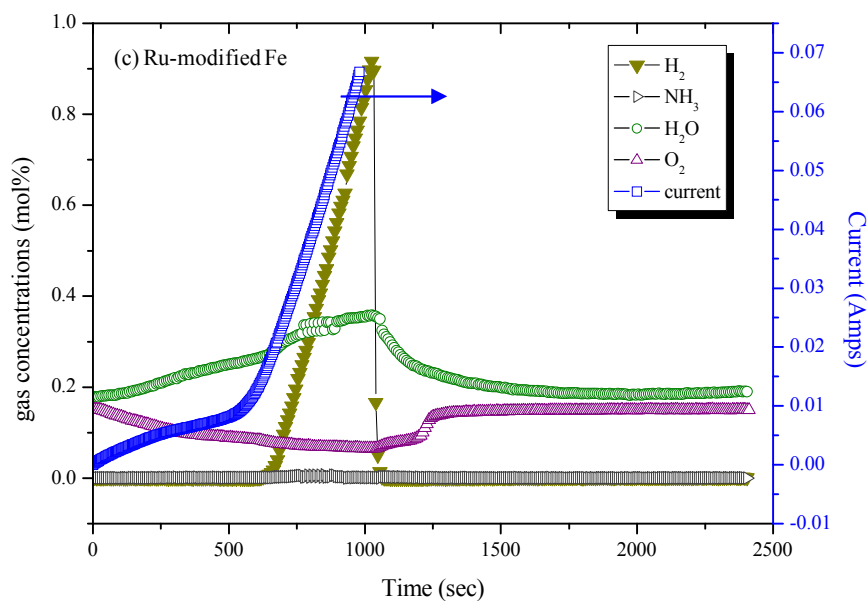


Figure 5.9 Correlation between electrolytic current and changes in concentrations of gases in cathode outlet stream during potential sweep at 2mV/s. (a) without catalyst addition, (b) Pd addition, and (c) Ru addition.

5.3.2.6 Microstructure of single cells with catalyst impregnated Fe

The microstructures of the membrane cells after testing were investigated by SEM. The SEM images in Figure 5.10 exhibit that all cells have similar electrode microstructures. With the attempt to investigate the difference in microstructure of Fe electrode with and without the addition of the catalyst, the SEM images at higher magnification on the Fe-BCZYF electrode side were taken as shown in Figure 5.11. There is no significant change in the microstructure of the porous layer or on the Fe surface. The EDS elemental analysis was performed on these electrodes in order to investigate the distribution of Pd or Ru on Fe surface. Unfortunately, the amount of the Pd or Ru catalyst on the Fe electrode was inadequate to provide a clear element map of the catalyst.

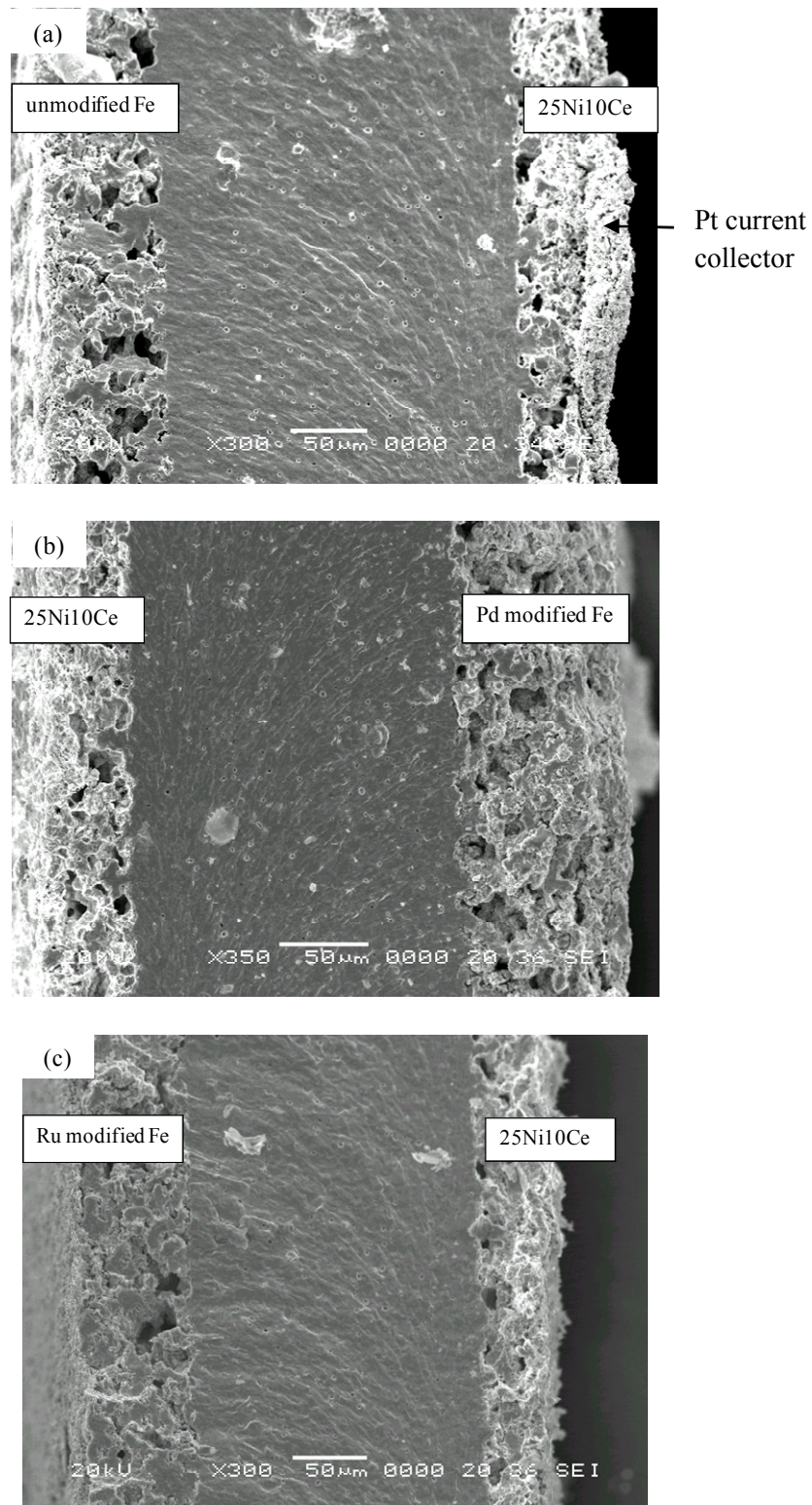


Figure 5.10 SEM image of a fractured cross-section of 25Ni10Ce | BCZYZ | 25Fe cell without catalyst addition after testing. Note that Pt was used as current collector for both electrodes.

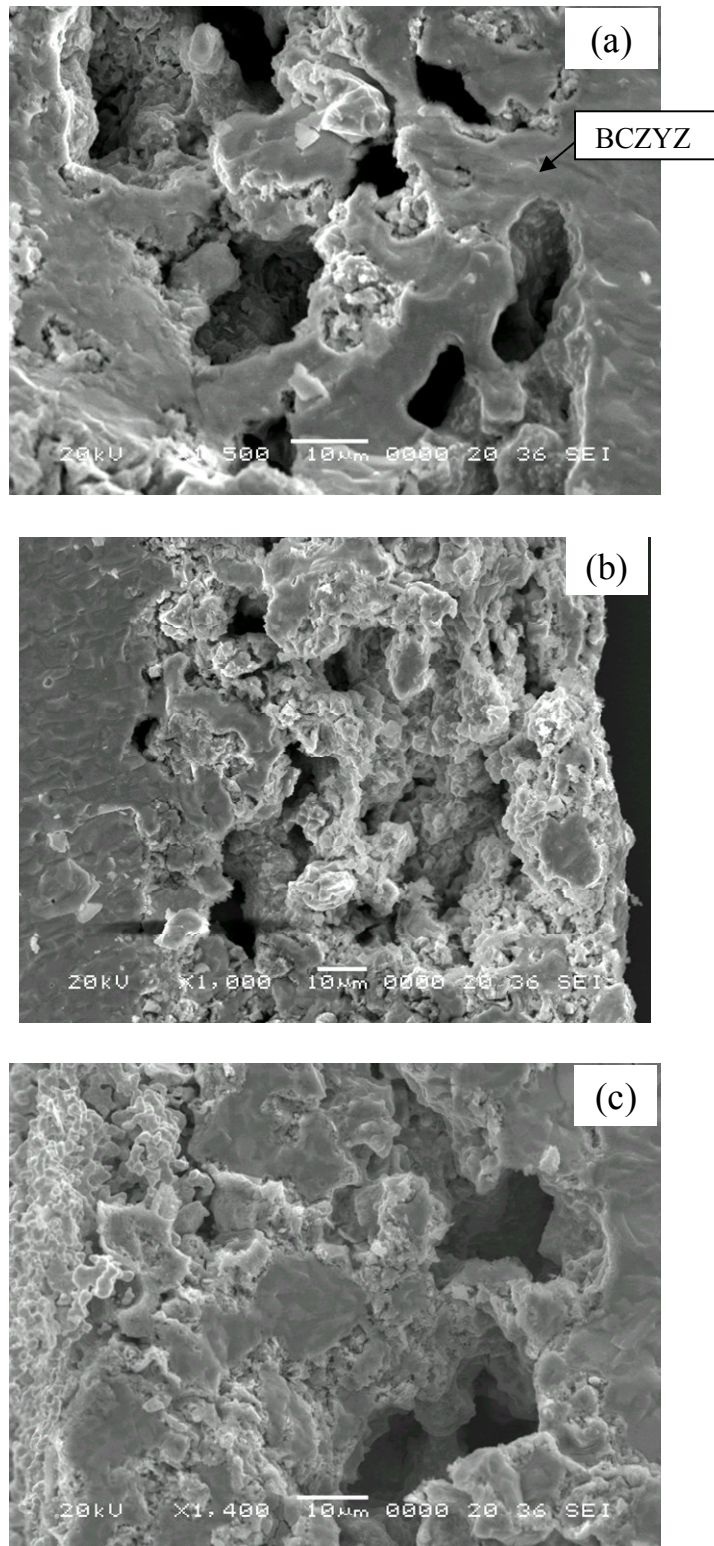


Figure 5.11 SEM images of fractured cross-section of Fe-BCZYZ impregnated electrode after testing (a) unmodified Fe, (b) Pd modified Fe and (c) Ru modified Fe. The electrode particles are in granular form (lighter colour) situated on BCZYZ surface.

5.3.3 Ammonia production

In this section, the ammonia formation rates obtained from the cells with and without catalyst addition on Fe-BCZY electrode are discussed. Typical MS data analysed from the outlet gas during closed-circuit condition is shown in Figure 5.12. The changes in concentrations of H₂, O₂, H₂O, and ammonia were online-monitored. When a constant potential was applied across the cell, a certain amount of protons is electrochemically driven from the anode through the electrolyte to the Fe cathode. These protons are expected to react with adsorbed N atoms (N_{ads}) on Fe electrocatalyst.



On the other hand, H⁺ may incorporate electrons and evolve as H₂ molecules.



As a significant amount of O₂ was always found in the system, the partial amount of evolved H₂ may instantly react with O₂ that produced H₂O.



From Figure 5.12, the increase of H₂, NH₃ and H₂O was immediately observed once the potential was applied as results of the reactions above. The formation rates of the H₂, NH₃ and H₂O were increased until reaching their new equilibriums. The formation rate of H₂O was in proportion with the reduction of O₂ and reached its equilibrium after applying the potential for 200 sec. The formation of ammonia was slower than that of H₂O and reached its equilibrium at 300 sec at the same time with that of the

evolved H_2 . By varying the potential, it was found that the formation rates of H_2 , NH_3 and H_2O before reaching their equilibria depends on the applied potential and the corresponding current. Higher applied current increased the formation rate of the products. The concentrations of the products (H_2 , NH_3 and H_2O) at equilibrium were used in calculation of current efficiency with respect to the applied current.

It is worthy noticing that the applied potentials were considered from the $V-I$ curves and were in the range of region B (low dE/dI region). Therefore, the ranges of potentials applied to these cells are exhibited in Figure 5.13. Normally in order to achieve 10-30 mA, the potentials of 1-3 V were needed. However, only the potentials of 1-2 V were enough to generate that range of the current in the case of Ru-modified Fe cell.

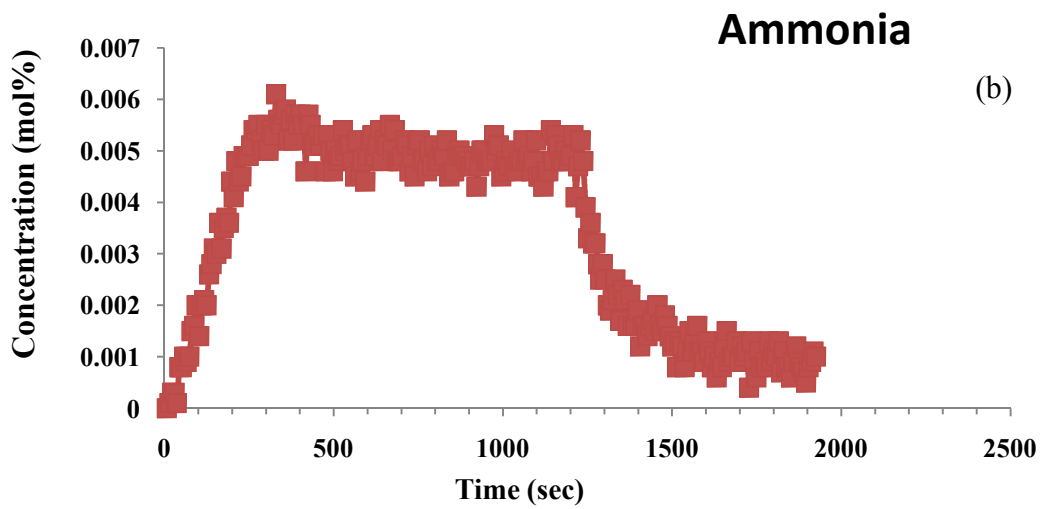
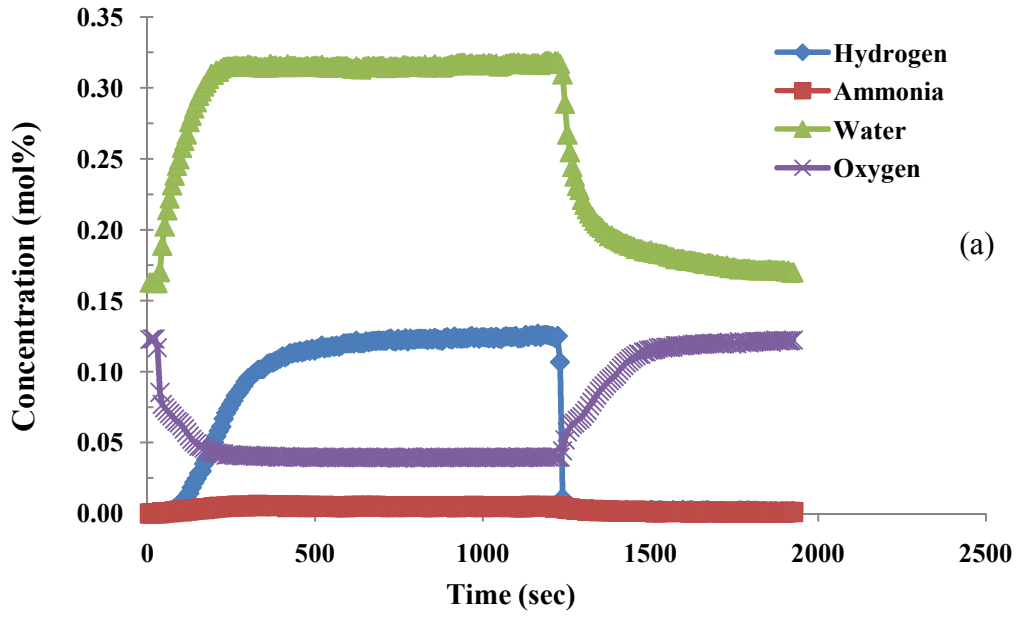


Figure 5.12 typical data obtained from the cathode outlet stream recorded by Mass spectrometer. The data received from cell without catalyst addition at 400 °C, imposed potential of 2.23V, corresponding current of 15.7 mA and transient time of 20 min.

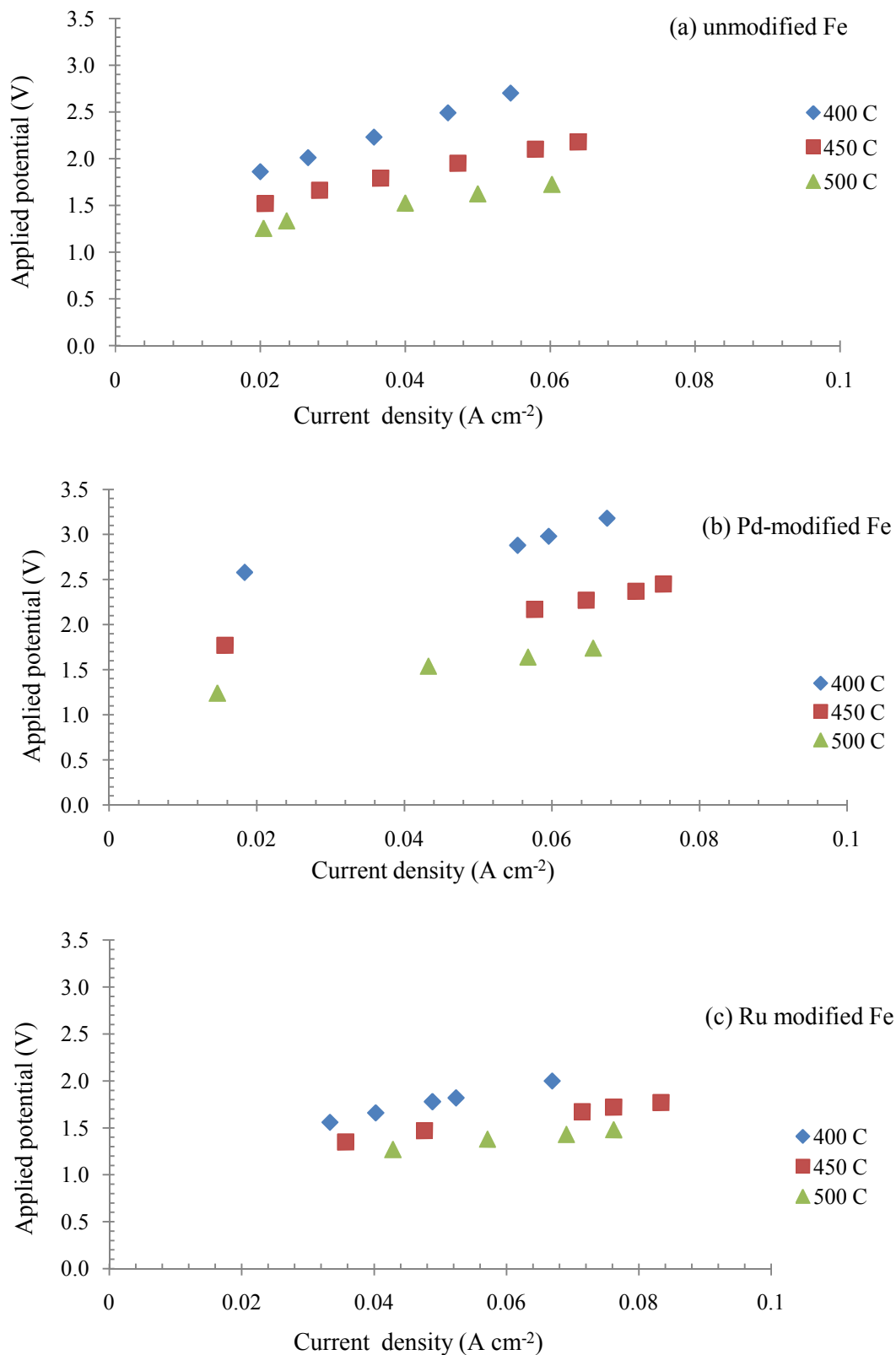


Figure 5.13 Correlation between applied potential and corresponding current employed for ammonia synthesis in cell with (a) unmodified Fe, (b) Pd-modified Fe, and (c) Ru-modified Fe.

5.3.3.1 Ammonia formation rate

Under open circuit, a very small amount of ammonia was frequently detected along with a small amount of H₂ in the cathode stream. Hence, the rate of ammonia formation was considered from the difference of concentrations between open-circuit and closed-circuit conditions. The plots of ammonia formation rate versus current density from cells with and without catalyst addition are shown in Figure 5.14. For the cell without catalyst addition, the rate of NH₃ formation decreased with the increasing temperature which may result from the decomposition of NH₃ at higher temperatures. The cell with Pd-modified Fe cathode exhibited similar results and provided the lowest NH₃ formation rate at 500 °C. However at 450 °C, the NH₃ formation rate of this cell overcame the decomposition rate and resulted in the highest NH₃ formation rate with the value of $4 \times 10^{-9} \text{ mol s}^{-1} \text{ cm}^{-2}$.

In principle, the NH₃ formation rate should increase with the applied current or the amount of protons. In these cases, the formation rate reached the maximum value at the current density around 0.06 A cm^{-2} . This limitation is in agreement with the fact that the NH₃ formation rate must be restricted by a limited number of N₂ dissociation sites on an Fe surface^[13].

For the Ru-modified cell, the NH₃ formation rates show less temperature and current dependences and the attained values are in the same range as the unmodified cell.

From Faraday's law, the current efficiency for the NH₃ formation can be calculated based on theoretical values, I/nF where n is equal to 3 for the number of electrons

involved in the reaction and I is the corresponding current. The plots of the current efficiency versus the current density are depicted in Figure 5.15.

Cells with unmodified and Pd-modified Fe cathode provided current efficiencies in the range of 2.5-0.5 % while the current efficiencies for the cell with Ru-modified Fe were in the range of 1.5-0.7%. Although the current efficiency is quite small, these NH_3 formation rates and current efficiencies are promising.

The limitation of the number of active site for N_2 dissociation is one of the possible reasons for the small NH_3 formation rate. Dahl et al.^[13] suggested that the number of active sites used for the N_2 dissociation on a multipromoted iron-based catalyst at 350 °C and atmospheric pressure is around $4 \mu\text{mol g}^{-1}$. The amount of the impregnated Fe oxide used in the present experiment was about 0.01 g. Therefore on the unmodified Fe, the expected number of the active sites must be less than 2×10^{-8} mol. Moreover, the number of available active sites could be decreased by the poisoning effect of O_2 and H_2O ^[14,15]. On the other hand, the coverage of hydrogen or NH_x intermediates ($x=0, 1, 2, 3$) on the catalyst surface also affects the ammonia formation rate^[13,16]. Therefore, the value of $4 \times 10^{-9} \text{ mol s}^{-1} \text{ cm}^{-2}$ for the highest NH_3 formation rate attained from Pd-modified Fe cell at 450 °C was close to the theoretical value. The poisoning effects of those species seem to be minor. It is likely that the formation rate would be increased by the increasing of the active sites on the catalyst.

In previous works, the electrocatalytic ammonia synthesis using proton conducting oxide electrolyte has been investigated using Pd electrodes on $\text{SrCe}_{0.95}\text{Yb}_{0.05}\text{O}_3$ (SCY) electrolyte^[2,17], Ag-Pd electrodes on various electrolyte oxides^[18-22] and an industrial

iron catalyst on metallic Fe for $\text{SrZr}_{0.95}\text{Y}_{0.05}\text{O}_{3-\alpha}$ electrolyte^[23]. Compared to those previous works; it seems that the results obtained in this study were close to those from painted Pd and Ag-Pd electrodes and much higher than that of the combination of industrial iron catalyst on Fe layer which was around $6.3 \times 10^{-12} \text{ mol s}^{-1} \text{ cm}^{-2}$.

To confirm that the formation of ammonia occurred electrochemically at Fe surface, a gas mixture of H_2 and N_2 was fed into the Fe cathode side. The results show that no significant amount of ammonia was produced directly from the gas mixture of H_2 and N_2 in this reactor and the ammonia formation should happen electrochemically on the catalyst surface.

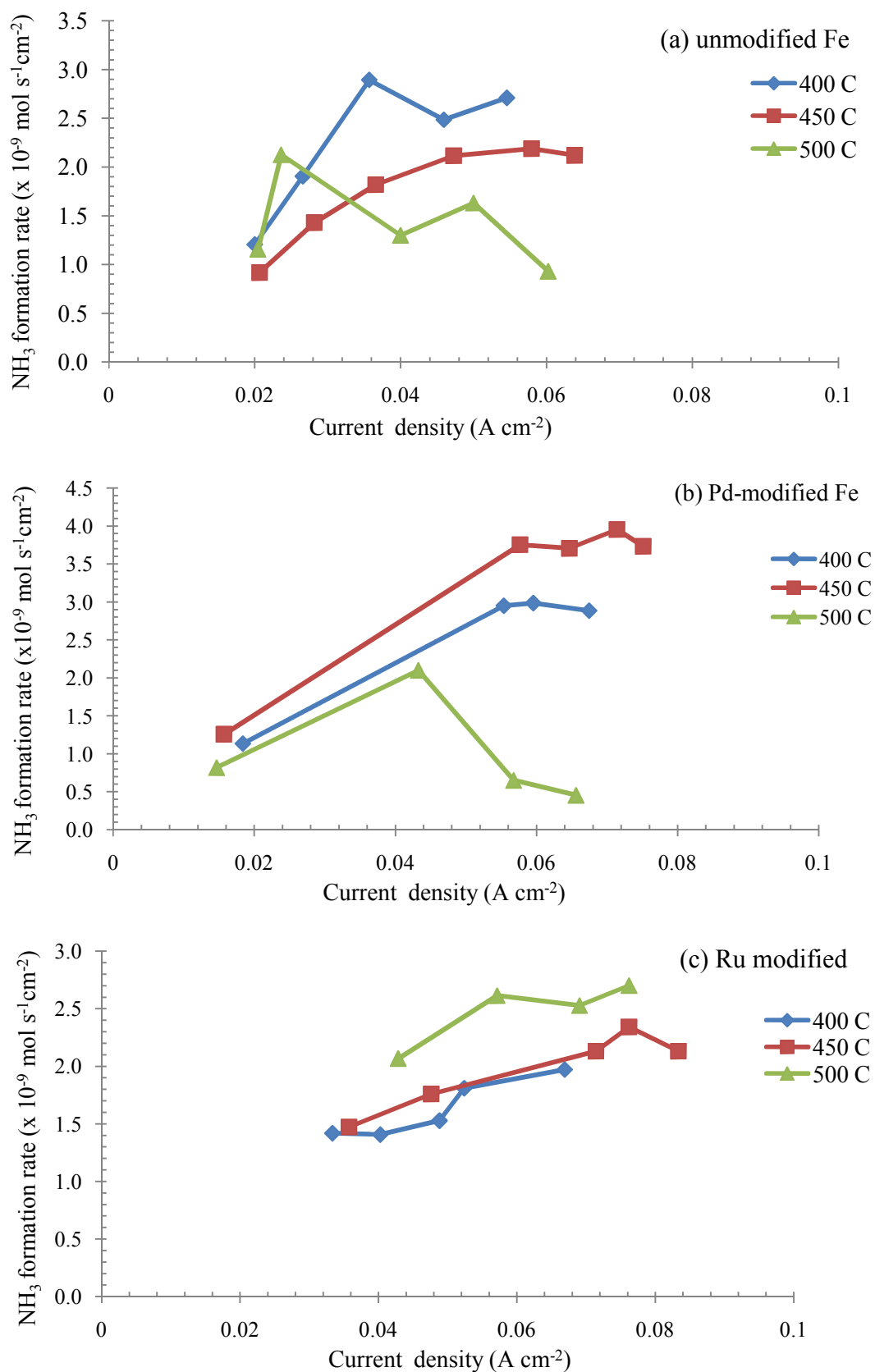


Figure 5.14 NH₃ production rate at different imposed currents and temperatures.

(a) cell without catalyst, (b) cell with Pd addition and (c) cell with Ru addition

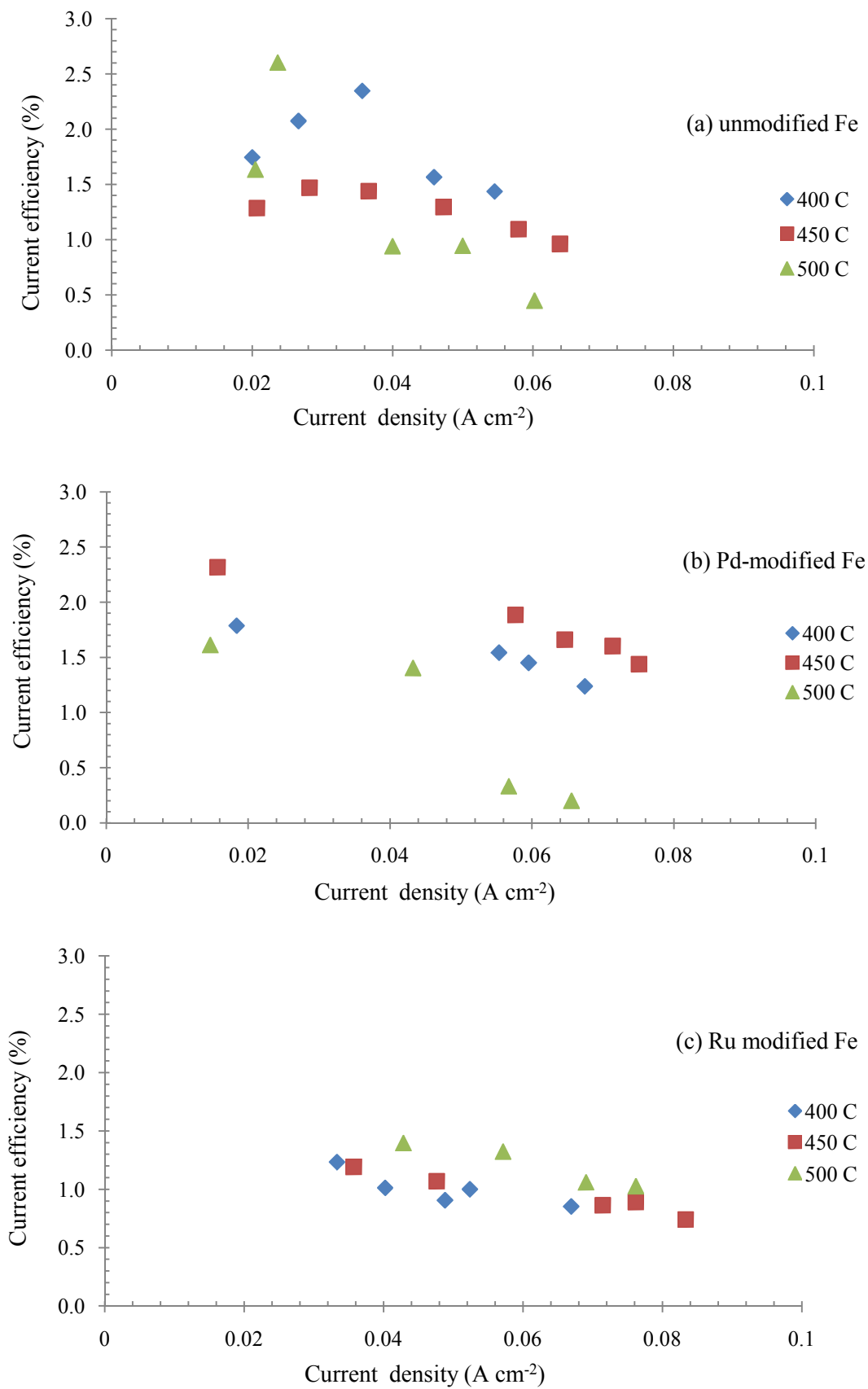


Figure 5.15 Current efficiency for NH₃ formation versus current density.

5.3.3.2 H₂ evolution rate and overall current efficiency

From the MS data, a significant amount of H₂ was generated during closed circuit. The evolution rates of H₂ in Figure 5.16 are plotted against the current density from cells with and without catalyst addition at various temperatures. The results show that there is no difference between the H₂ evolution rates from each cell. The evolution rate seems to depend on only the applied current and has no dependence on type of catalyst. Comparing with theoretical values calculated from I/2F (dashed lines), the evolution rates of H₂ were varied from 0-60 % of the applied current. The losses in the current efficiency could be due to some misdirected electrons participating in other competitive reactions including NH₃ and H₂O formation reactions. The amount of H₂ consumed in the competitive reaction with O₂ was calculated from the increase in the concentration of H₂O during closed circuit. From the experiment, the amount of produced H₂O was approximate 2 times higher than the reduction of the amount of O₂ which is consistent with the coefficients of O₂ and H₂O in the following reaction.



The significant amount of H₂ consumed in this reaction is related to the loss in current efficiency of the H₂ evolution reaction. Considering all reactions including the NH₃ formation reaction, the total current efficiencies at the cathode are displayed in Figure 5.17. The cell with Pd-modified Fe shows the highest current efficiency (close to 100%) while the other cells experience the current efficiency losses of 10-20%. These losses may stem from the consumption of the current in the partial reduction of Fe oxide. In the case of the Pd-modified Fe, a Pd catalyst was found to help accelerate the reduction of the Fe oxide under a reducing atmosphere^[24]. Hence, the presence of the Pd catalyst on the Fe oxide could diminish the loss of the current.

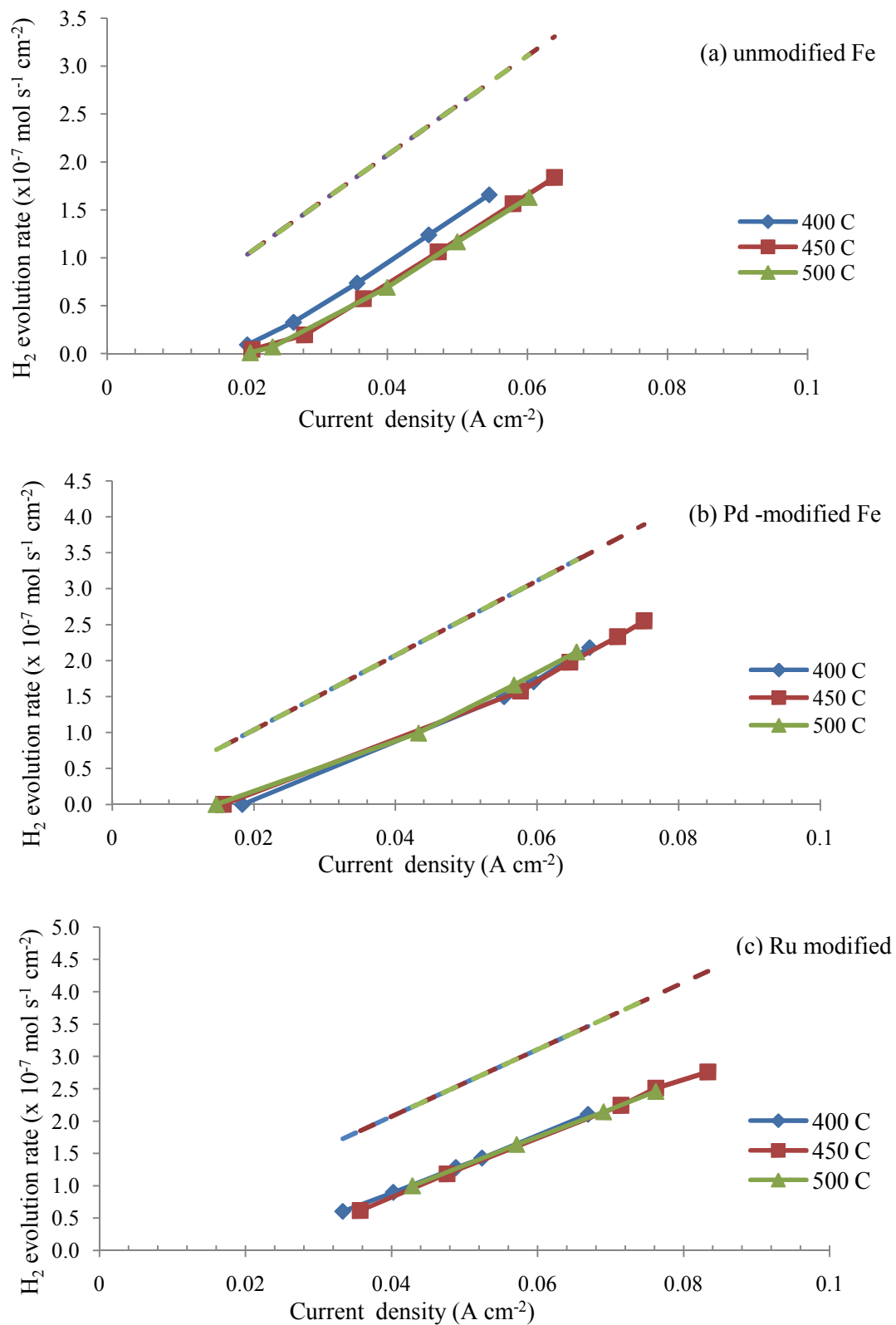
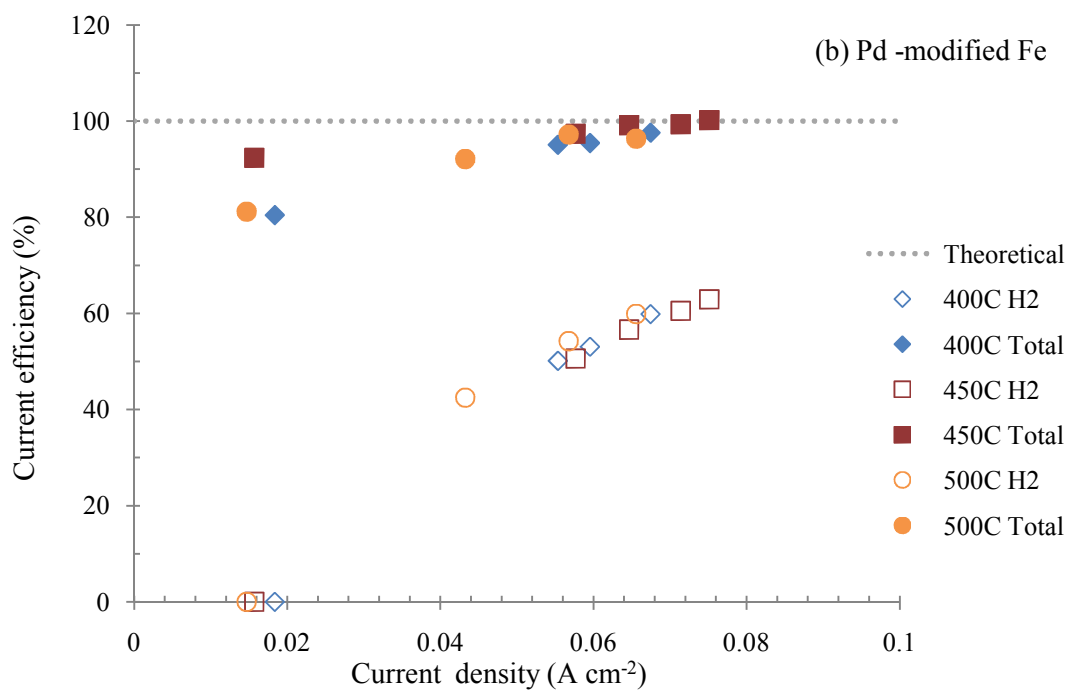
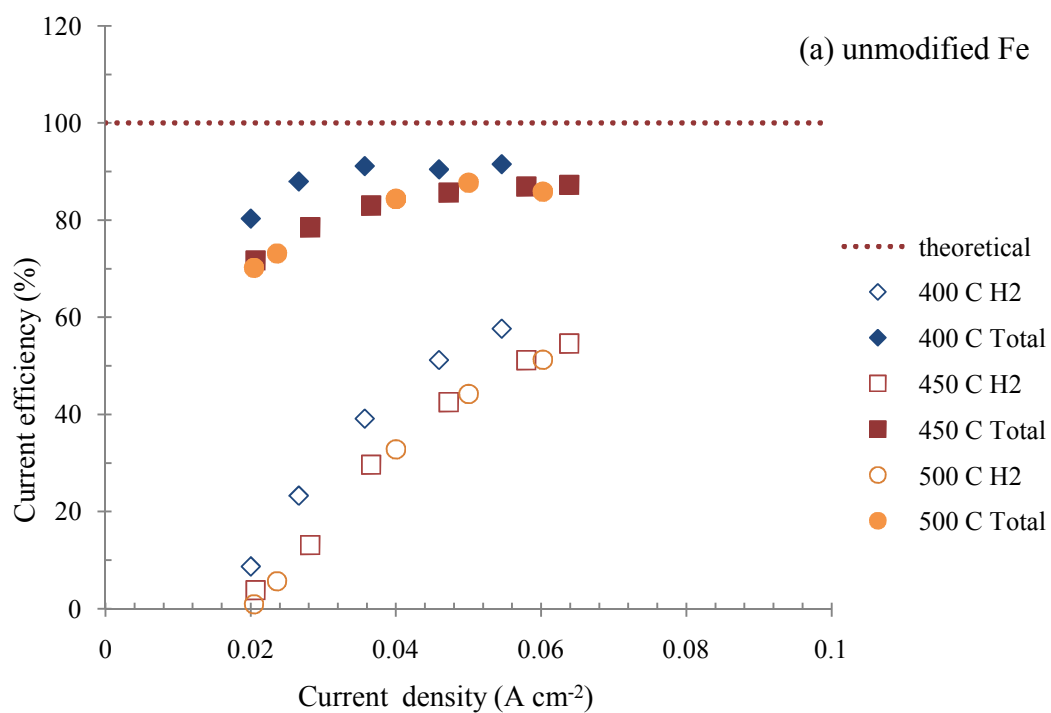


Figure 5.16 H₂ evolution rate at different imposed currents and temperatures (a) cell without catalyst, (b) cell with Pd catalyst and (c) cell with Ru catalyst. Dashed lines are theoretical values.



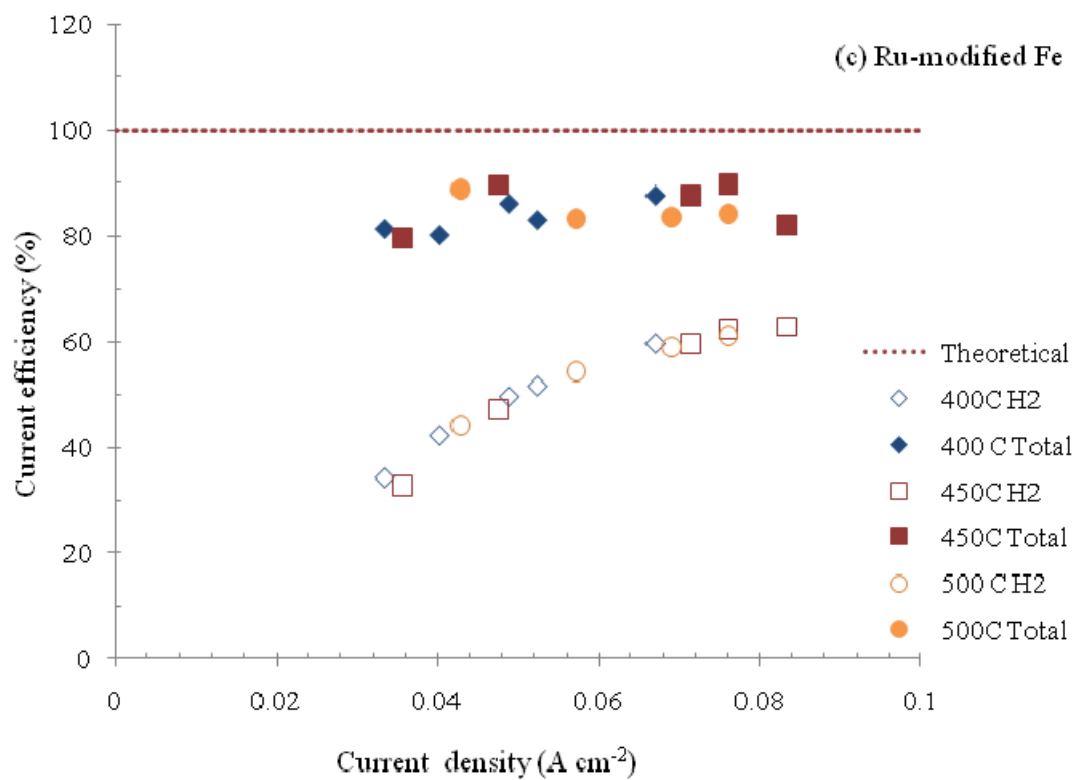


Figure 5.17 Total current efficiency evaluated from (open symbol) H₂ evolution rate and (closed symbol) total amount of H₂ and H₂O formation rate including NH₃ production rate.

5.4 Conclusions

The application of impregnated Ni-CeO₂ and Fe electrodes in a single cell provided interesting results for electrocatalytic ammonia synthesis at 400-500 °C. As expected, the impedance behaviour of the single cell was similar to that of the symmetrical cell with Fe oxide impregnated electrode but the R_s and R_p values in the single cell were slightly better due to the incorporation of the 25Ni10Ce impregnated anode.

The highest ammonia formation rate of a single cell without catalyst addition of $2.9 \times 10^{-9} \text{ mol s}^{-1} \text{ cm}^{-2}$ was attained at 400 °C. The ammonia formation rate was increased by the addition of 10 wt% PdO onto the Fe cathode. The increase of the formation rate of 34% suggests that Pd catalyst must take part in the catalytic activity for the ammonia formation reaction. Pd is a well-known metal for hydrogen adsorption. The affinity between Pd and hydrogen may create a high H⁺ density area in the vicinity of the active site for N₂ dissociation and encourage H⁺ to react with N_{ads} on the Fe surface.

The addition of RuO₂ did improve the electrode performance but there is no significant change in the ammonia formation rate. It is possible that only metallic Ru is active for ammonia synthesis and this metallic form may be not achieved under these testing conditions.

References

1. J. M. Thomas, W. J. Thomas, Principle and practice of heterogeneous catalysis, VCH, the Federal Republic of Germany (1997) p. 549.
2. G. Marnellos, M. Stoukides, Science 282 (1998) 98-100.
3. S. R. G. Carrazan, R. Mateos, V. Rives, P. Ruiz, Catal. Today 112 (2006) 161-164.
4. M. Wang, Y. Feng, Sens. Actuators B 123 (2007) 101–106.
5. G. Zhang, S. Dorris, U. Balachandran, M. Liu, Electrochem. Solid-State Lett. 5 (2002) J5-J7.
6. F. Rosowski, A. Hornung, O. Hinrichsen, D. Herein, M. Muhler, G. Ertl, Appl. Catal. A Gen. 151 (1997) 443-460.
7. A. Hellman, K. Honkala, I.N. Remediakis, A. Logadottir, A. Carlsson, S. Dahl, C.H. Christensen, J.K. Nørskov, Surf. Sci. 603 (2009) 1731-1739.
8. S. Trasatti, Electrochim. Acta 45 (2000) 2377–2385.
9. A. Velazquez, F. Centellas, J. A. Garrido, C. Arias, R. M. Rodriguez, E. Brillas, P. L. Cabot, J. Power Sources 195 (2010) 710-719.
10. A. T. Marshall, R. G. Haverkamp, Electrochim. Acta 55 (2010) 1978–1984.
11. W. G. Coors, Solid State Ionics 178 (2007) 481–485.
12. D. R. Lide, Handbook of Chemistry and Physics, 76th edition, CRC Press, Florida (1995) p. 5-68.
13. S. Dahl, Appl. Catal. A Gen. 222 (2001) 19-29.
14. R. Kirk, D. Othmer, Encyclopedia of Chemical Technology, 3rd edition, John Wiley & sons, New York (1981).

15. C. N. Satterfield, *Heterogeneous Catalysis in Practice*, McGraw-Hill, New York (1980).
16. A. Hellman, K. Honkala, I.N. Remediakis, A. Logadottir, A. Carlsson, S. Dahl, C. H. Christensen, J. K. Nørskov, *Surf. Sci.* 600 (2006) 4264-4268.
17. G. Marnellos, S. Zisekas, M. Stoukides, *J. Catal.* 193 (2000) 80-87.
18. Y. Guo, B. Liu, Q. Yang, C. Chen, W. Wang, G. Ma, *Electrochem. Commun.* 11 (2009) 153-156.
19. C. Chen, G. Ma, *J. Alloys Compd.* 485 (2009) 69-72.
20. Z. J. Li, R. Q. Liu, Y. H. Xie, S. Feng, J. D. Wang, *Solid State Ionics* 176 (2005) 1063–1066.
21. J. D. Wang, Y. H. Xie, Z. F. Zhang, R. Q. Liu, Z. J. Li, *Mater. Res. Bull.* 40 (2005) 1294–1302.
22. R. Q. Liu, Y. H. Xie, J. D. Wang, Z. J. Li, B. H. Wang, *Solid state Ionics* 177 (2006) 73-76.
23. M. Ouzounidou, A. Skodra, C. Kokkofitis, M. Stoukides, *Solid State Ionics* 178 (2007) 153-159.
24. K. Urasaki, N. Tanimoto, T. Hayashi, Y. Sekine, E. Kikuchi, M. Matsukata, *Appl. Catal. A Gen.* 288 (2005) 143–148.

Chapter 6

Conclusions and Future Work

6.1 Conclusions

The application of $\text{BaCe}_{0.5}\text{Zr}_{0.3}\text{Y}_{0.16}\text{Zn}_{0.04}\text{O}_{3-\delta}$ (BCZYZ) as a proton conducting electrolyte in an electrocatalytic cell for ammonia synthesis has been explored. The project firstly addressed the study of the electrolyte ceramic sintering and the improvement of cell performance via tape casting and ion impregnation.

The electrochemical characterisations of the electrolyte material were performed on 1 mm-thick BCZYZ pellets with Pt metal as anode and Pt, Pd or Au as cathode. These cells contributed low cell performance with high polarisation resistances. So, there were two major problems found in these cells. First, the adhesion between the metal electrode and the electrolyte surface was quite poor, and second, the metal cathodes had low catalytic activity in non-humidified N_2 which may relate to the sintering or agglomeration of the metal particle during electrode firing. However, only a small amount of ammonia was detected along with a significant amount of H_2 when operating these cells under electrolysis mode. These results definitely confirm the proton conduction in this electrolyte material. In this experiment, the highest rate of ammonia formation of $1.4 \times 10^{-9} \text{ mol s}^{-1} \text{ cm}^{-2}$ was obtained from the cell with Pt cathode at $450 \text{ }^\circ\text{C}$. Most of the cells cannot be operated at $400 \text{ }^\circ\text{C}$ because the cell resistance increased dramatically at low temperature and high potential was needed for generating adequate proton fluxes for the reactions.

The improvement of cell performance was carried out by decreasing the thickness of the electrolyte and utilising a high catalytic activity electrode. The tape casting method was employed in order to reduce the electrolyte thickness and prepare porous ceramic support for the electrode material. The electrode materials were introduced into porous BCZYZ support by ion impregnation technique and a composite electrode/electrolyte was achieved. For the anode, the combination of Ni and CeO₂ provided the best electrode performance. The symmetrical cell with 25wt% NiO and 10 wt% CeO₂ (25Ni10Ce) impregnated electrode exhibited low polarisation resistances of 1-0.45 Ωcm² at 400-500 °C, respectively in humidified 5% H₂/Ar. Compared to the painted Pt electrode in the same conditions, the R_p values from the 25Ni10Ce electrode were smaller than those of Pt electrode by ca. 300 times. For the cathode, 25wt% Fe₂O₃ (25Fe) impregnated electrode displayed a reasonable performance in non-humidified N₂.

Then the tape cast membrane cell with 25Ni10Ce impregnated anode and 25Fe impregnated cathode was employed in electrocatalytic ammonia synthesis. Compared to 1 mm-thick cell with painted Pt electrode, the performance of the membrane cell was ~10 times improved.

The addition of catalysts, i.e. Pd or Ru, into Fe impregnated cathode improved the cell performance in different ways. The Pd catalyst enhanced the catalytic activity of ammonia formation reaction whereas the Ru catalyst decreased the cell resistance with its high electronic conductivity.

The highest ammonia formation rate was attained from the cell with Pd modified Fe cathode. The formation rate of 4 x 10⁻⁹ mol s⁻¹ cm⁻² was achieved at 450 °C. In most cases, the current efficiency of the ammonia formation was around 1-2.5 % while the

rest was consumed in the H₂ evolution reaction. Note that the highest formation rate of ammonia from this experiment was 18 times higher than the expected rate calculated from the equilibrium constant, K_{eq} , of the reaction of gaseous N₂ and H₂ at the same conditions.

It can be concluded that there are several factors that control the formation of ammonia. A specific range of applied current or potential is also crucial. By applying too low potential, the amount of current may not be enough to force the reaction to occur but with too high potential, the reaction mainly undergoes H₂ evolution instead. The number of active sites could be another factor. The results from the Pd modified cathode suggested that the cathode with appreciable proton conduction is preferable for the electrocatalytic ammonia reaction.

6.2 Future work

The results from the formation rate of NH₃ and H₂ suggests that a vital factor that controls the rate of NH₃ formation would be the number of active sites on the cathode catalyst. Therefore, the increase of the electrode active area should provide the higher amount of NH₃ and lower the amount of H₂ produced by the same applied current. This can be done by increasing size of the button cell or changing the geometry of the cell to a tubular cell which can be easily performed via tape casting process.

Although Fe oxide showed a reasonable performance, the cell resistance was quite high comparing to the cell with Ru-modified Fe. The improvement of the cathode material needs to be carried on. The cathode material that can transport H⁺ would be an ideal cathode for electrocatalytic ammonia synthesis. For further work, the

25Ni10Ce anode with high catalytic activity and stability is likely to be tested in a gas mixture with higher steam content. Steam electrolysis is expected to happen at this anode. However, a small amount of H₂ is still required in order to keep the Ni anode in a metallic form at this low working temperature.